Optimizing the Interfacial Electron Transfer Rates in Ru(II)-, Os(II)-, Re(I)-polypyridyl Based Sensitizer-TiO_2 Ensembles

Thesis Submitted to AcSIR for the Award of
the Degree of
DOCTOR OF PHILOSOPHY
in
Chemistry

By

Tanmay Banerjee

10CC11J26133

Under the guidance of

DR. AMITAVA DAS

Organic Chemistry Division
CSIR-National Chemical Laboratory
Pune - 411008, Maharashtra, India

October 2013

National Chemical Laboratory
Dr. Homi Bhabha Road, Pune: 411008, Maharashtra, India

Dr. Amitava Das, F.A.Sc, F.N.Sc.
Sr. Principal Scientist
Organic Chemistry Division

Date – 21.10.2013

CERTIFICATE BY THE SUPERVISOR

This is to certify that the contents of this thesis entitled **“Optimizing the Interfacial Electron Transfer Rates in Ru(II)-, Os(II)-, Re(I)-polypyridyl Based Sensitizer-TiO_2 Ensembles”** is the original research work of **Tanmay Banerjee** carried out under my supervision.

I further certify that the work has not been submitted either partly or fully to any other University or Institution for the award of any degree.

Amitava Das

Amitava Das

Fax: +91-020-25902629; Phone: +91-020-25902385; E-Mail: a.das@ncl.res.in

CANDIDATE'S STATEMENT

I hereby declare that the work incorporated in the present thesis is original and has not been submitted to any University/Institution for the award of a Diploma or a Degree. I further declare that the results presented in the thesis and the considerations made therein, contribute in general to the advancement of knowledge in **Chemistry** and in particular to "**Optimizing the Interfacial Electron Transfer Rates in Ru(II)-, Os(II)-, Re(I)-polypyridyl Based Sensitizer-TiO_2 Ensembles**".

Tanmay Banerjee

21-10-2013

Tanmay Banerjee

Acknowledgements

I express my deepest sense of gratitude to Dr. Amitava Das, my research supervisor, for introducing me to the present field of work. I am extremely grateful to him for the freedom he granted me. I am equally indebted to Dr. Hirendra Nath Ghosh of Radiation and Photochemistry Division, BARC and Dr. Bishwajit Ganguly, CSIR-CSMCRI for their guidance, encouragement and continuous support throughout these years.

I am thankful to Dr. P. K. Ghosh and Dr. Sourav Pal, Directors, CSIR-CSMCRI and CSIR-NCL, respectively, for providing me the infrastructure necessary to carry out my research work and would also wish to convey my gratefulness to Dr. R. I. Kureshy, Dr. P. Paul and Dr. H. C. Bajaj for their appreciative comments and continuous guidance. I am thankful to Dr. Sandeep Verma, Dr. Sreejith Kaniyankandy, Dr. Sachin Rawalekar, Pallavi Singhal, Partha Maity, Tushar Debnath and Jayanta Dana of BARC for their support. I am also immensely indebted to all the scientists of the Analytical Science Division, CSIR-CSMCRI and Organic Chemistry Division, CSIR-NCL, and my labmates, co-workers and friends for all their help extended.

Above all, I would like to thank DAE-BRNS and CSIR for financial support.

Index

Chapter	Section	Title	Page No.
		Summary of the Thesis	1
1		**Introduction**	3
	1.A	Photovoltaics	5
	1.A.1	Global position	5
	1.A.2	The present PV technologies	6
	1.B	The dye sensitized solar cell	8
	1.B.1	Semiconductor	9
	1.B.2	Electrolyte	11
	1.B.3	The dye	12
	1.B.3.A	Metal complexes as sensitizers	13
	1.B.3.A.1	Basic photophysics	13
	1.B.3.A.2	Absorption and electrochemical properties	14
	1.B.3.A.3	Anchoring groups	16
	1.B.3.A.4	Peripheral groups	18
	1.B.3.A.5	Selected examples of ruthenium complex based sensitizers	19
	1.B.3.B	Examples of other metal complex based sensitizers	26
	1.B.3.C	Other sensitizers	29
	1.B.3.D	Perovskite based sensitizers	31
	1.B.4	Dynamics of interfacial electron transfer	32
	1.B.4.A	The excited state time scales	32
	1.B.4.B	Electron Injection	33
	1.B.4.B.1	Injection from the excited state	34

1.B.4.B.2 Distance dependence of electron injection 38

1.B.4.B.3 Can '*hot*' injection be harvested? 42

1.B.4.B.4 MPCT and reduced sensitizer injection 42

1.B.4.C Sensitizer regeneration and charge recombination 43

1.B.4.C.1 Intramolecular sensitizer regeneration 45

1.B.4.C.2 Distance dependence of charge recombination 48

1.B.4.D The interfacial electron transfer dynamics of catechol bound metal polypyridyl dyes 48

1.C Scope of the present thesis: An afterword 53

1.D References 54

2 **Effect of Electron Donating Groups on the Interfacial Electron Transfer Dynamics of Catecholate Bound Ru(II) Polypyridyl Based Sensitizers on TiO_2 Nanoparticle Surface** 67

2.A Foreword 69

2.B Experimental Section 69

2.B.1 Synthesis 69

2.C Results and Discussion 72

2.D Conclusions 81

2.E References 82

3 **Studies of *Resorcinol* Bound Ruthenium(II), Osmium(II), Rhenium(I)-polypyridyl Complexes on Nano-TiO_2 Surface** 85

3.A Synthesis, steady state and femtosecond transient absorption studies of ruthenium(II) and osmium(II)-polypyridyl complexes on nano-TiO_2 surface in water 87

3.A.1 Foreword 87

3.A.2 Experimental Section 87

3.A.2.A Synthesis of TiO_2 nanoparticles 87

3.A.2.B Synthesis 88

3.A.3 Results and Discussion 90

3.B Ru(II)- and Re(I)- polypyridyl complexes on oleic acid capped TiO_2 in non-aqueous solvent: prolonged charge separation and substantial thermalized ^{3}MLCT injection 104

3.B.1 Foreword 104

3.B.2 Experimental Section 105

3.B.2.A Analytical Methods 105

3.B.2.B Preparation of sample solution 105

3.B.2.C Synthesis of oleic acid capped TiO_2 nanoparticles 105

3.B.2.D Synthesis 105

3.B.3 Results and Discussion 106

3.B.3.A Synthesis 106

3.B.3.B Electrochemical studies 107

3.B.3.C Steady state and transient spectral characterization 107

3.B.3.D Electron Injection 111

3.B.3.E Charge Recombination 114

3.C Regulating interfacial charge recombination of Os(II)-polypyridyl-resorcinol complex on TiO_2 surface by controlling density of semiconductor surface traps 117

	3.C.1	Foreword	117
	3.C.2	Experimental Section	117
	3.C.2.A	Computational methodology	117
	3.C.3	Results and Discussion	118
	3.C.3.A	Steady state and transient spectral characterization	118
	3.C.3.B	Transient spectral characterization	119
	3.C.3.C	Electron Injection	120
	3.C.3.D	Back electron transfer	122
	3.D	Conclusion	126
	3.E	References	128
4		**Superior Grafting and state-of-the-art Interfacial Electron Transfer Rates for Newly Designed Geminal Dicarboxylate Bound Ru(II)- and Os(II)-polypyridyl Dyes on TiO_2 Nanosurface**	135
	4.A	Foreword	137
	4.B	Experimetal Section	138
	4.B.1	Computational Methodologies	138
	4.B.2	Synthesis	139
	4.C	Results and Discussion	143
	4.D	Conclusion	160
	4.E	References	162
5		**Optimal Interfacial Electron Transfer Rates for *dye-spacer-anchor* Arrangement in Newly Designed Acetylacetonate Based Ru(II)- and Os(II)-polypyridyl Sensitizer**	165

5.A Foreword 167

5.B Experimental Section 168

5.B.1 Synthesis of TiO_2 nanoparticles 168

5.B.2 Computational Methodologies 168

5.B.3 Synthesis 168

5.C Results and Discussion 171

5.D Conclusion 181

5.E References 182

Appendix A: Common Experimental Methods 185

Appendix B: Selected ^1H NMR and ESI-MS Spectra 189

Publications 201

Conferences and Symposia 203

Abbreviations

APCE	Absorbed Photon-to-Current Efficiency
BET	Backward Electron Transfer
BODIPY	Boron Dipyrromethene
bpy	2,2'-bipyridine
CB	Conduction Band
CD	Cyclodextrin
CT	Charge Transfer
CTRW	Continuous Time Random Walk
dcb	2,2′-bipyridyl-4,4′-dicarboxylic acid
DFT	Density Functional Theory
DMSO	Dimethyl Sulphoxide
DPSS	Diode Pumped Solid State
DSSC	Dye Sensitized Solar Cell
EDOT	Ethylene-dioxythienyl
EJ	Exajoule
ESI-MS	Electrospray Ionisation – Mass Spectrometry
FC	Frank – Condon
FT	Fourier Transform
FWHM	Full-width-at-half-maxima
HOMO	Highest Occupied Molecular Orbital
IPCE	Incident photon-to-current Conversion Efficiency
IR	Infrared
IRF	Instrument Response Function
ISC	Intersystem Crossing
LF	Ligand Field
LUMO	Lowest Unoccupied Molecular Orbital
MC	Metal Centered

MLCT	Metal-to-ligand Charge Transfer
ND	Neutral Density
NHE	Normal Hydrogen Electrode
NMR	Nuclear Magnetic Resonance
OA	Oleic Acid
OD	Optical Density
PCM	Polarizable Continuum Solvation Model
PV	Photovoltaics
PVA	Poly(vinyl) Alcohol
PTZ	Phenothiazine
SAED	Specific Area Electron Diffraction
SCE	Saturated Calomel Electrode
tct	4',4′′,4′′′-tricarboxylic acid-tpy
TEM	Transmission Electron Microscopy
THF	Tetrahydrofuran
TLC	Thin Layer Chromatography
TMS	Tetramethylsilane
tpy	2,2′:6′,2′′-terpyridine

Summary of the Thesis

Over the recent years, dye-sensitized solar cells have emerged as the major cost effective alternative for efficient harvesting of solar power. The efficiency of such devices is a cumulative imprint of an array of factors, of which the stability of the dye-semiconductor linkage and optimum interfacial electron transfer rates in this dye-semiconductor assembly are perhaps the most important ones.

The present thesis aims at the design of new Ru^{II}-, Os^{II}-, Re^{I}- polypyridyl dyes, having anchoring groups which increase the aqueous stability of the dye-semiconductor linkage till significantly high pHs, and subsequent optimization of the interfacial electron transfer parameters.

The introductory chapter provides a comprehensive account of the basic architecture and functioning of a dye sensitized solar cell; it also provides a thorough survey of the available literature on the various attempts made by the researchers worldwide towards the development of efficient solar dyes and consequent efforts towards the optimization of interfacial electron transfer parameters.

Chapter 2 describes an attempt to supersede the deleterious backward electron transfer rates of catechol bound dyes by incorporation of secondary electron donating groups, tyrosine and phenol. In an early time scale, backward electron transfer rate is found to correspond exactly to the donor ability of the secondary donating groups.

In chapter 3, an innovative ruthenium(II)-, osmium(II)-, rhenium(I)-polypyridyl-based sensitizer system containing resorcinol, instead of catechol, as the enediol anchor has been developed. For the ruthenium (II) complex, electron injection is found to be biexponential. The backward electron transfer rate is significantly slower for the ruthenium(II) and rhenium(I) based systems, than the corresponding catechol based dyes. The results have been explained in terms of a wider and weaker overlap of the electron donating bipyridine orbital with the TiO_2 conduction band manifold.

In chapter 4, two new Ru^{II}-/Os^{II}-polypyridyl based sensitizer dyes with *geminal* dicarboxylic acid group as the new binding unit for superior grafting of the dye to TiO_2 have been designed and synthesized. The electron injection rates are extremely fast in spite of multiple saturated C-C linkages present and are suggested to be probably due to electron injection through space or through bond by a superexchange tunnelling mechanism. Also, the charge recombination rates are considerably slower.

In chapter 5, similar to that in the last chapter, two new Ru^{II}-/Os^{II}-polypyridyl based sensitizer dyes with acetylacetone group as the binding unit, known to be stable towards hydrolysis reactions over a wide pH range, have been synthesized. Electron injection is again biexponential and is very fast for saturated spacer(s) based binding and the back electron transfer is exceedingly slow. This study, along with the examples discussed in chapter 4, irrefutably prove the efficacy of the *dye-spacer-anchor arrangement* in educing optimal electron transfer rates.

Chapter 1

Introduction

1.A. Photovoltaics

1.A.1. Global position

Our world currently relies heavily on coal, oil and natural gas for its energy needs. Such fossil fuels are non-renewable, *i.e.* they draw on finite resources that will eventually dwindle and are each day becoming too expensive or too environmentally damaging to retrieve. Also, with ever increasing constraints placed by environmental issues on such already very limited fossil fuels, in order to maintain social and economical development, our society *must* find alternative ways to cater to the global energy needs which is no less than 4.7×10^{20} J per annum.[1]

Renewable energy sources thus comprise no less than 13% of global energy consumption.[2,3] Of the available renewable energy sources, solar power is perhaps the most cheap and elegant one. The total solar energy absorbed by Earth's atmosphere, oceans and land masses is of the order of 3,850,000 EJ per year.[4] In 2002, this was more energy in one hour than what the world used in one whole year. The amount of solar energy reaching the surface of the planet is cosmic; in one year it is about twice as much as will ever be obtained from all of the Earth's non-renewable resources of coal, oil, natural gas and mined uranium combined.[5]

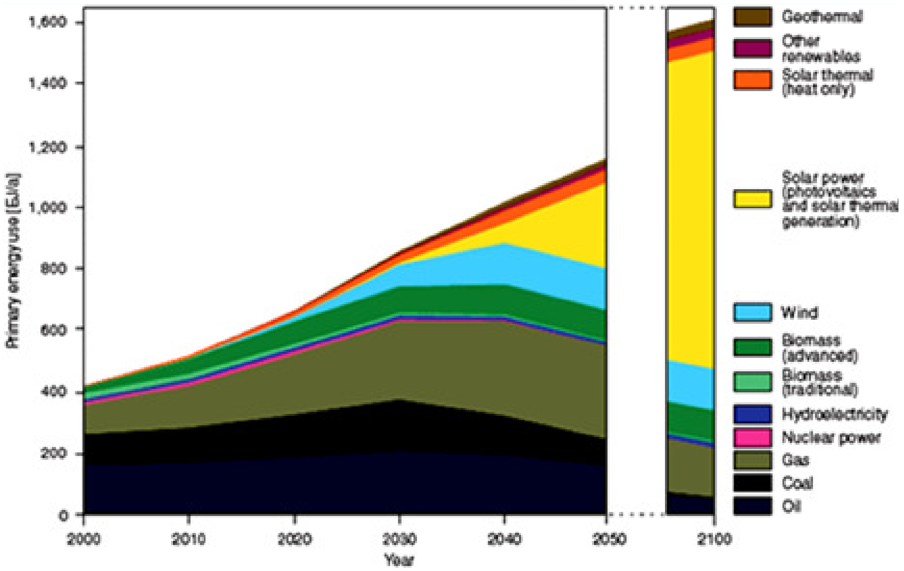

Figure 1: A forecast of the sources of global energy supply till 2050/2100. (Taken from Figure 1, reference 3).

PV thus are predicted to account for no less than 1% of global energy production by 2030. Continued PV growth is presently based on government support mainly, as solar PV energy costs are not yet competitive. Nevertheless, the fact that PV cells are free from chemical and noise pollution, their power output is flexible and uniquely portable makes such devices a very elegant and attractive choice (Figure 1).[3]

1.A.2. The present PV technologies

The inception of the first modern PV solar cells, silicon (Si) p/n, dates back to 1954 by Chapin *et al.* at Bell Laboratories.[6] Several improvements in terms of efficiency and reliability occurred with time and the use of solar cells has grown slowly but steadily.

i. Mono and polycrystalline silicon (**mc–Si** and **pc–Si**, respectively): Such solar cells have totally dominated the global PV market so far. An important point to note is that silicon is not the ideal material for PV conversion.[7] For 90% light absorption while it takes only 1 μm of GaAs (a direct semiconductor), it takes 100 μm of crystalline Si! This is because of the fact that silicon is an indirect band gap material and so if the film is made any thinner then light would simply pass through. Now, the photogenerated carriers have to reach the p-n junction which is mostly near the front surface. Thus, for high efficiencies, the diffusion length of minority carriers has to be 200 μm or at least twice the silicon thickness. The material has thus to be of very high purity and of high crystalline perfection. The chief reason for market dominance of crystalline Si, in spite of these physical limitations and besides its natural abundance, very low toxicity and an established processing technology, is the supply of rejected materials from the high-tech semiconductor industry to the manufacturers. This situation has consequently created a dependency of the PV industries on semiconductor industries which can only sustain itself if the electronic silicon industry grows at the same rate as the PV industry. Unfortunately, this is not the case.

A typical crystalline silicon solar cell is constituted by three layers: the n-type, the p-type and the p-n junction which is formed between the n-type and the p-type layers. The n-type layer is doped with group V elements, normally phosphorous, because it has extra electrons and works as the donor (anode); the p-type layer, in contrast, is doped with group III elements, commonly boron and therefore has a need of electrons and consequently becomes the receptor (cathode). Photons absorbed in the p-n junction generate electron–hole pairs by exciting electrons from the junction valence band to the conduction band. Electrons are driven to the negative layer while ‘‘holes’’ are left as positive. This leads to different potentials in the anode and cathode, creating an electron flow and hence electricity. Champion cells achieve up to 24.4% efficiency under standard reporting conditions.[8]

ii. Amorphous silicon cell (**a–Si**): Amorphous silicon cell (a–Si) first appeared in 1976.[9] Compared to crystalline cells, amorphous silicon cell has a higher rate of absorption of light. Thus, light can be absorbed with a very thin layer of photo-electrically active material. Material requirements are therefore less and with current technologies being capable of large-area deposition of a-Si, the scalability of this type of cell is high. However, since the structure is amorphous, significant inherent disorders and dangling bonds are present in the structure which makes it a bad conductor of charge carriers. These dangling bonds act as recombination centers and reduce the carrier lifetime significantly. Development of a–Si has been further clogged by the Staebler–Wronski light induced degradation effect;[10] a photoelectronic effect that causes loss of cell efficiency by about 50% or more upon light exposure.

iii. Polycrystalline CdTe: CdTe solar cells are typical hetero-junction solar cells with CdTe being the n-type component.[11] CdTe has an appropriate energy band gap of 1.5 eV and a high optical absorption coefficient. Maximum efficiency of 16.5% has been reported with such architectures.[12] CdTe toxicity is a major concern for such type of cells.

iv. Chalcopyrite solar cells: This class is characterized almost solely by CIGS solar cells. CIGS is a I-III-VI_2 type semiconductor substance composed of copper, indium, gallium and selenium.[13] A solid solution of copper indium selenide and copper gallium selenide, with a chemical formula of $CuIn_xGa_{(1-x)}Se_2$, is the actual material. The band gap varies continuously from 1.0 to about 1.7 eV. Such cells have a very high absorption coefficient for 1.5 eV and higher energy photons. Confirmed maximum efficiency is 19.2% which is a record for any thin film solar cell.[12] High quality cell fabrication is still very difficult and very challenging. An additional problem is the toxicity of the composite.

v. III–V semiconductor solar cells: These cells show better results in multijunction, with semiconductors showing different energy band gaps for using the whole solar spectrum. Such multijunction solar cells do not possess the upper efficiency limit of ~34%, the well known Shockley-Quiesser limit for single junction solar cells.[14] Double and triple junction cells are currently being commercialized; the most common three junction cell is GaInP/GaAs/Ge with a record efficiency of 32%.[12] In space applications where cost is not the major problem, multijunction cells have replaced silicon cells. However, economically viable terrestrial transition is impeded by raw materials cost and high-purity demands.

vi. Molecular and polymer organic solar cells: These are straightforward devices that are made from organic semiconductors, including polymers, sandwiched between two electrodes. Energy conversion efficiencies achieved till date using such organic semiconductors are low compared to inorganic materials. Since these cells can be processed from solution, the possibility of a simple roll-to-roll printing process, leading to inexpensive, large scale production is obvious. A great deal of attention is now being given to the development of such solar cells, particularly now that the 5% efficiency obstacle has been crossed.[15,16]

vii. Quantum dot solar cells: Such cells consist of using quantum dot as the light harvesters. The tunability of the band gap in such quantum dots by simple variation of sizes renders these extremely beneficial for the development of multijunction cells. A maximum efficiency of 7.0% has been reported recently by Sargent and co-workers using PbS quantum dots.[17]

viii. Dye sensitized solar cells (DSSCs): Such cells present a very promising cost effective alternative. Champion DSSCs regularly achieve more than 12% efficiency.[18,19] The highest efficiency reported till date is ~ 15% using inorganic-organic hybrid perovskite-based light harvesting materials on TiO_2.[20] These high efficiencies are accompanied by commendable performance under any atmospheric condition and solar incidence angle and very low irradiance as in cloudy days. Such cells operate on principles analogous to photosynthesis in green plants; the photoreceptor and the charge carriers are different elements unlike conventional silicon based PV devices where the semiconductor assumes both these functions. As a result of a separation of these functions there is a lesser requirement of purity of the raw materials and hence the costs are low. Other notable advantages of such architectures are that the raw materials are environment friendly and the cells can be semi-transparent and offer multi colour range possibilities (Figure 2).

Sensitization got started to be used for photoelectrochemical purposes in the late twentieth century. Significant contributions were made in this direction by Tributsch,[21] Fujishima and Honda,[22] and Tsubomura.[23] Grätzel and co-workers had already published quite a number of articles on TiO_2 sensitization in the late 1980s[24-26] but it was not until the seminal work published in 1991,[28] reporting an efficiency as high as 7% by the innovative use of mesoporous TiO_2 particles and a judicious choice of a ruthenium complex as the light absorber, that generated the still increasing impetus.

Figure 2: "Hana-Akari" lanterns powered by the dye-sensitized solar cells. Courtesy: www.sony.net

It must be noted that each of the non crystalline-silicon technologies discussed above have their own *pros and cons*. None of the renewable energy sources would be able to solve the energy crisis alone. Likewise, no particular PV technology would be able to stand alone and subsequent development of all possible technologies is necessary.

1.B. The dye sensitized solar cell

At the heart of a DSSC is a mesoporous oxide layer composed of nanoparticles sintered together to allow electronic conduction (Figure 3).[28] TiO_2 (anatase) has been the material of choice though alternative wide band gap materials such as ZnO and Nb_2O_5 have also been investigated. To the surface of the nanocrystalline semiconductor film is attached a monolayer of the dye. Photo-excitation of the dye results in injection of an electron from the dye LUMO to the conduction band of the semiconductor. The dye is

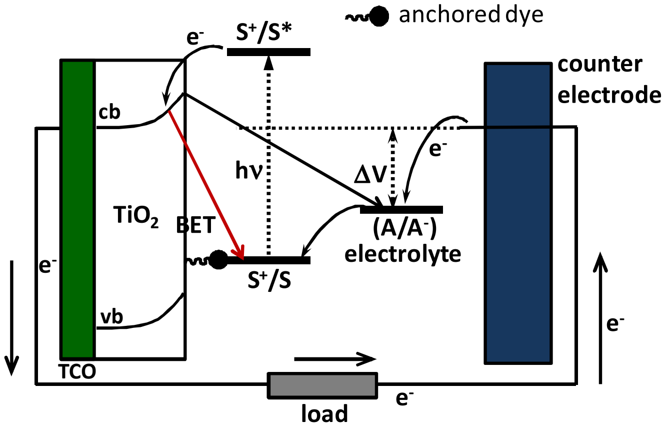

Figure 3: Principle of operation of a DSSC.

subsequently re-reduced by the electrolyte which is usually an organic solvent containing a redox system, such as the I^-/I_3^- couple. Iodide, on the other hand, is regenerated by the reduction of triiodide at the counter electrode, typically platinum. The circuit is completed *via* electron migration through the external load. Solar energy is converted into electrical energy primarily by a kinetic-based process; the voltage generated equals the difference between the Fermi level of the electron in the semiconductor and the redox potential of the electrolyte, with no chemical species consumed overall.

1.B.1. Semiconductor

Owing to a surge in ecological and environmental consciousness, preferences in the choice of semiconductor are for inert and non-toxic compounds. The ideal semiconductor layer should also have a nanostructured mesoscopic morphology, crucial for a high specific surface area. Logically, the objective is to obtain the maximum area available for dye adsorption using a minimum quantity of the semiconductor. Consequently, preparation of nanoparticles, as they are called, must not be very cumbersome a process. Also, thin film preparation techniques must be wieldy. TiO_2 meets these requirements adequately.[29]

Anatase, a crystalline form of TiO_2, has been widely used because it has a high band gap (3.2 eV, and absorbs only below 388 nm) making it transparent to most of the solar spectrum, reducing the recombination rate of photo-injected electrons. Additionally, it has good thermal stability, is chemically inert, non-toxic and relatively cheap. Rutile, another crystalline form of TiO_2 can also be employed. However it has a higher dark current ($E_g = 3.0$ eV) and so it is less effective and also photon excitation within the band gap generates holes that act as oxidants making it less chemically stable.[30] TiO_2 is known as an n-type semiconductor, which contains donor-type defects such as oxygen vacancies and titanium interstitials.[31]

Thin films of TiO_2 can be prepared by many different physical and chemical techniques such as thermal oxidation, sputtering or chemical vapor deposition while screenprinting and doctor-blading are two most prevalent deposition techniques.[28]

Electron transport in sintered nanocrystalline TiO_2 film depends on the properties of the individual nanoparticles, namely, the extent of particle connectivity, electronic coupling between the particles, the geometrical configuration of the assembly *etc*.[32] The exciton Bohr diameter of TiO_2 is close to 1.5 nm, below which it exhibits quantum size effects, *i.e.* splitting of the electronic band into discrete electronic levels occurs. The nanocrystalline film composed of 10-25 nm particles can be considered therefore as a network of bulk crystals with a band of extended electronic states. The surface states in nanomaterials, which usually lie within the band gap, arise from unsaturated bonds, deviations in the bond lengths and bond angles from that of the bulk materials, and presence of impurities *etc*.[33] The diffusion coefficient of nanocrystalline TiO_2 is very poor and has been explained under the framework of multiple trapping mechanism. Under this mechanism, electron transport is slowed down by trapping–detrapping events. An electron normally passes through ~ 10^7 trapping events in nanocrystalline TiO_2 which ultimately reduces the diffusion coefficient.[34] The density of trap states influences the kinetics of electron transport.[35] The photocarrier transport measurements through TiO_2 nanoparticles show TiO_2 to be a material of high trap density and indicate that the electrons move through the mesoporous network by trap filling, *i.e.* by trapping and detrapping events as said before.[36]

Though TiO_2 has been the preferred semiconductor in DSSCs, some promising properties are offered by other metal oxides like ZnO and Nb_2O_5 as well.

ZnO is a wide-band gap semiconductor of the II-VI semiconductor group which crytsallizes either in cubic zinc-blende, cubic rocksalt or hexagonal wurtzite structure. The zinc-blende phase can be stabilized only by growth on cubic substrates and the rocksalt structure forms at relatively high pressures. The hexagonal wurtzite is the lowest energy structure of ZnO and has a band gap of 3.0-3.2 eV much like the anatase form of TiO_2.[28] Hagfeldt and colleagues studied the electron transport in nanostructured ZnO and discussed their findings under the framework of the multiple trapping diffusion model similar to that applied for TiO_2.[37] The density of traps is reported to be less for ZnO compared with that of TiO_2. This lower trap density allows electrons to move faster through the ZnO nanoporous network and the carrier life time in ZnO is longer than that in TiO_2.[37] Despite the superior transport properties of ZnO, the DSSCs constituted using ZnO give inferior performance and maximum efficiencies so far reported are 6.6% only.[38] Several reports suggest that dye adsorption is the main problem in dye-sensitized ZnO solar cells.[28,31] Cells with high dye loading tend to be inefficient, whereas cells with lower dye loading show good quantum efficiencies.[28] These problems are mainly related to the high acidity of the (carboxylic acid) binding groups of the dyes that can lead to dissolution of ZnO and precipitation of dye-Zn^{2+} complexes, leading to a poor overall electron injection efficiency of the dye.[39,40]

Also, Nb_2O_5 could be a more suitable candidate than TiO_2 and other semiconductors in view of its wider band gap and higher conduction band edge, comparable electron injection efficiency, as well as better chemical stability.[41] While Nb_2O_5 nanoparticles, nanobelts, and nanofibre networks have been studied for the development of DSSCs, their photocurrents and photoconversion efficiencies have not reached those of TiO_2-based DSSCs due to the reduction in their dye-loading sites.[42,43] It has been suggested that the large unit cell dimension of orthorhombic Nb_2O_5, in comparison to anatase TiO_2, makes it a challenging task to obtain the optimum Nb_2O_5 morphology for DSSC applications.[31]

One dimensional nanostructures of the aforesaid semiconductor materials and some ternary compounds such as $SrTiO_3$ and Zn_2SnO_4 have also been tested for their use as photo-electrodes in DSSC.[44-47]

Throughout the thesis discussion is based primarily on the use of TiO_2 as the semiconductor, unless otherwise noted.

1.B.2. Electrolyte

The electrolyte is a crucial part of all DSSCs. It is responsible for carrying charge between the electrodes in solution – it is the hole transport material. With the charge collected at the counter electrode, it incessantly regenerates the sensitizer dye at the anode. There are three different kinds of hole transport materials employed in DSSCs: liquid electrolytes (the electrolytes in which the redox mediators are dissolved in organic solvents, water or electrolytes composed of ionic liquids), quasi-solid-state electrolytes and solid electrolytes.[48] In all these cases, the electrolyte must have a high conductivity to permit fast electron transfer from the counter to the working electrodes and efficient dye regeneration. For the same reason, the ionic species present in the electrolyte must have a high diffusion coefficient. The electrolyte should also be thermally, optically, chemically and electrochemically stable to avoid dye degradation or desorption from the metal oxide surface. Furthermore, the redox mediator should have adequate redox potential to allow efficient dye regeneration. It is also important that the electrolyte does not absorb in the visible region of the spectrum, since it would reduce light absorption by the sensitizer.

Interestingly, after more than more than 15 years of intense research since the 1991 *Nature* paper by Grätzel and O'Regan, the same categories of nanoparticles, dyes, and electrolytes are still being used even today. The best results are obtained with the triiodide/iodide (I_3^-/I^-) redox couple in an organic solvent, generally acetonitrile.[3,49] However, the two major issues regarding the use of I^-/I_3^- are the severe corrosion problems for the device-sealing materials which causes difficulties in device sealing and stability, and the complicated electrochemistry arising from the two-electron redox couple. In addition, triiodide shows partial absorption of visible light. Alternative redox mediators such as Br^-/Br_3^-,[50] $SCN^-/(SCN)_2$,[51] $SeCN^-/(SeCN)_2$,[52] Fc^+/Fc,[53] Cu^I/Cu^{II} complexes,[54] Ni^{III}/Ni^{IV} complexes[55] *etc.* have been tested in DSSCs. Several complexes of Co^{II}/Co^{III} have also been tried.[56] Compared to iodide, their advantage is that they are non-volatile, non-corrosive and have the benefit of being easy for molecular modifications. However, the current exchange rate at the counter-electrode is much smaller and leads to voltage losses.[57]

Several organic solvents have been used, like methoxypropionitrile,[58] butyronitrile[59] or methoxyacetonitrile[60] among others. The most recurrent solvent is acetonitrile, particularly when one wishes to maximize cell efficiency. Most recently, mixtures of acetonitrile and valeronitrile have become popular. Virtually hundreds of chemical compounds can be experimented with as long as they fulfill most of the following requirements: low volatility at the expected cell operating temperature, low viscosity, resistance to decomposition over long periods of time, good redox-couple solubility, low toxicity and low cost.[61]

In recent years the development of ionic liquid electrolytes has been one of the most dynamic research fields within DSSCs. The development of viscous electrolytes to avoid known sealing and stability problems has had very promising results.[62] Suitable room temperature ionic liquids being explored must have good chemical and thermal stability, negligible vapor pressure, non-flammability, high ionic conductivity and a wide electrochemical window.[63] Ionic liquids might end up working simultaneously as the iodide source and as the solvent.

The regular liquid electrolyte can also be replaced by a p-type semiconductor layer with the sensitized semiconductor matching the n-type layer, and the sensitizer the p–n junction. The main difficulty in optimizing the interface between the sensitized semiconductor and the electrolyte is that it is very difficult to achieve a close contact, without voids, among particles due to the roughness of the former and the impossibility of high-temperature depositions of the latter.

1.B.3. The dye

As one of the crucial parts in DSSCs, the photosensitizer should fulfill some essential characteristics:

(1) It should have strong absorption in the visible region and should preferably absorb in the near-infrared region as well.

(2) It must have anchoring groups to bind the dye strongly to the semiconductor surface.

(3) The excited state must be higher in energy than the conduction band edge of the concerned n-type semiconductor (for n-type DSSCs). This will ensure that electron injection into the conduction band of the semiconductor is thermodynamically possible.

(4) For efficient regeneration, the ground redox level of the (oxidized) dye must be more positive than the redox potential of electrolyte.

(5) It should preferably have an optimized molecular structure to prevent aggregation on the semiconductor surface. Co-adsorbers can also be added to prevent this. In some cases, dye aggregates can be controlled (H- and J-aggregates) to result in an improved performance as compared to the monomer.

(6) It must be electrochemically, thermally and photochemically stable.

(7) Electron injection into TiO_2 must be faster in comparison with decay to the ground state of the dye.

Based on these requirements, many different photosensitizers including metal complexes, porphyrins, phthalocyanines and metal-free organic dyes have been designed in the past decades.

1.B.3.A. Metal complexes as sensitizers

1.B.3.A.1. Basic photophysics

The major emphasis on the choice of sensitizers has been on polypyridyl complexes of transition metals and particularly on those of Ru^{II}. In the last few decades enormous literature has developed on the photophysics and photochemical properties of such complexes.[64] Quantitative investigation of the spectral, electrochemical and photophysical properties of innumerable complexes have led to lucid understanding of the CT transitions involved so that it is now possible to design complexes having desired properties. In Ru^{II}-polypyridine complexes, the MLCT transitions are responsible for nearly all of the absorption in the visible range.[64]

As the name itself implies, absorption of light in such transitions promotes an electron from the metal d orbitals to the ligand π* orbitals, d(π) - π*. A number of electric-dipole-allowed CT transitions are observed which give rise to intense absorption bands in the visible region with reasonable extinction coefficients. An important point to be noted is that there is no formal spin for the excited states due to heavy-atom spin–orbit coupling from the transition-metal centre (especially for 4d and 5d metals) which must be taken into account in order to rationalize the relative oscillator strengths and hence the absorption spectra.[65,66] As a result of this spin-orbit coupling, the excited state is correctly described only by the symmetry label of the molecular point group to which it belongs and not the spin and an orbital individually.[65]

The typical example of a compound with such MLCT transitions is $Ru(bpy)_3^{2+}$ (bpy is 2,2'-bipyridine) which is perhaps one of the most explored coordination compounds (Figure 4). The lowest-energy state of this compound is three-fold symmetric and belongs to the symmetry label D_3. The excited state formed immediately after excitation should have the same structural symmetry as the ground state, following Franck–Condon principle.[67-69] So, if Jahn–Teller distortions and/or solvent-induced fluctuations are not involved, then this initial FC excited state formed could consist of a delocalized electronic wave function on all the three bipyridine ligands with each of them formally possessing one-third of an electronic charge. From this FC excited state, the first excited state is formed. Since molecules with D_3 symmetry do not possess an electric dipole, and since the ground state MLCT absorption features of such molecules have solvent dependent features (though minor), this initial excited-state electron is thought to localize on a single bipyridine ligand and there are compelling experimental evidences to show such localization in nanosecond and longer time scales.[70,71] This localized excited state has the reduced-symmetry designation C_2 and it has an estimated dipole moment of about 10 Debye.[70] This lowest-energy excited state, 1E′, as discussed above, has a predominantly triplet character[72-73] and the transition from the initial FC state

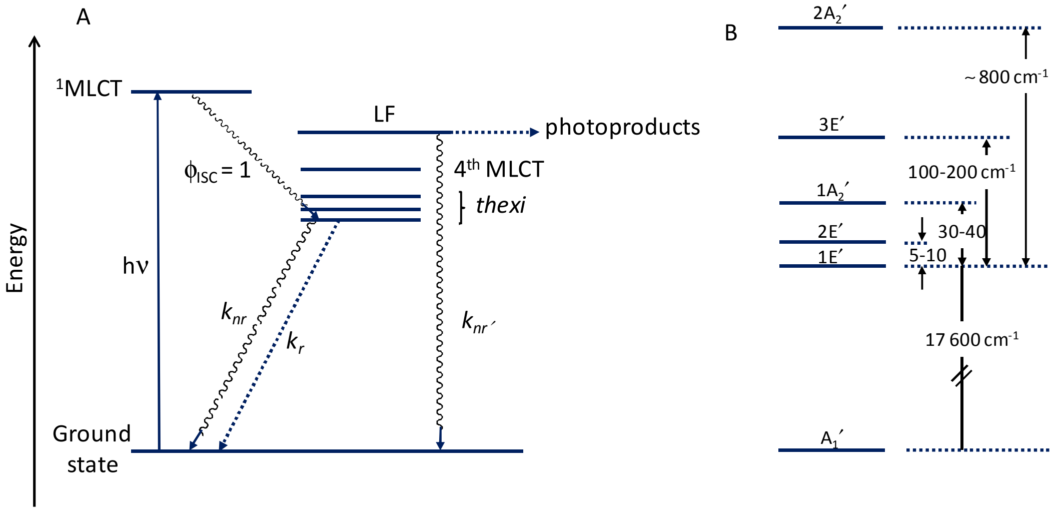

Figure 4: (A) Jablonski-type diagram showing the manifold of excited states of Ru(bpy)$_3^{2+}$, and (B) Energy level diagram of the emitting states.

having singlet character is termed ISC which has been shown to occur with a quantum yield near unity in fluid solutions. These states are therefore labelled as ^{3}MLCT and ^{1}MLCT, respectively. The photoluminescence of Ru(bpy)$_3^{2+}$ arises from three closely spaced electronic states (these states are ~ kT apart) which are in thermal equilibrium and thus having significant Boltzmann population so that photoluminescence occurs from what seems to be a single thermally equilibrated excited state, the *thexi* state.[74] A fourth MLCT excited state and a distorted ligand field state, LF, [$(d\pi)^5(d\sigma^*)^1$] lie higher in energy. It is this *thexi* → LF surface crossing that is responsible for ligand loss photochemistry, shortened and temperature-dependent lifetimes and quantum yields.[75]

1.B.3.A.2. Absorption and electrochemical properties

For $d\pi^6$ coordination compounds, the absorption and the electrochemical properties can be easily tuned. The energy of the MLCT absorption can be tuned by altering the substituents on the bipyridine based ligands or by controlling the extent of $d(\pi)$-π^* back-bonding donation to nonchromophoric ligands. The MLCT transition energy can be reduced either by tuning t_{2g} or the π^* level.[29] The t_{2g} energy level is determined largely by the electron density at the metal centre. Hence, electron-donating substituents (such as –NMe$_2$ or –OMe) on the bipyridine moieties raise this level and thereby decrease the energy associated with the MLCT transition. Electron-withdrawing groups (such as –COO$^-$), on the other hand, lower the level.

Very obviously, one would like to use a dye that absorbs at all possible wavelengths of the solar spectrum. With the solar spectrum having high intensities in the IR region (*ca.* 1200 nm), it is desirable to shift the absorption threshold to as low energy as possible. However, the energy of the photon decreases as one moves further into the IR region.

With thus an aim to shift the absorption to higher energies, the ligand SCN$^-$ had been incorporated and this resulted in the development of one of the most efficient solar dyes, **N3** (Figure 5).[76] The visible absorption spectrum of this dye exhibits two distinct absorption bands which occurs due to a shift in the HOMO electron density from Ru^{II} to the isothiocyanate ligands.

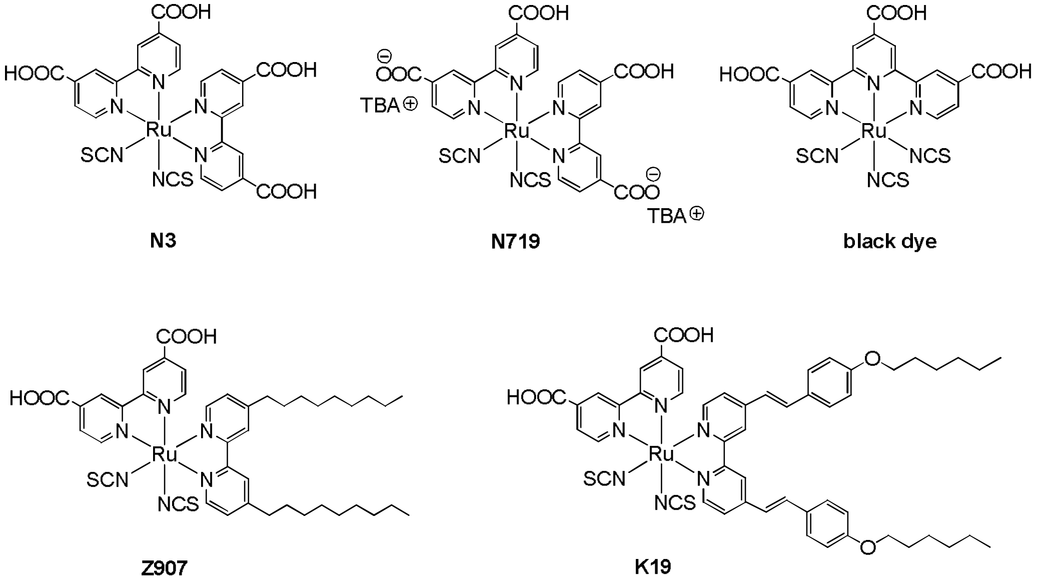

N3 **N719** **black dye**

Z907 **K19**

Figure 5: Molecular structures of **N3** dye and its analogues.

However, **N3** gains red absorption over $Ru(dcb)_3^{2+}$ at the expense of the ground state E^0 value and thus means loss in the driving force for dye regeneration. However, **N3** dye and its analogues still remain the champion dyes for DSSC applications (Figure 5). Another successful dye developed was $[Ru(tct)(NCS)_3]^-$ (also called the '**black dye**'). As compared to the classical **N3** dye, this has a significantly higher absorption on the red side.[77] However, as a result of a low extinction coefficient throughout the visible range, its overall efficiency is low.

For most of the tris-heteroleptic Ru^{II} compounds, the photophysical and electrochemical properties are fairly insensitive to the environment.[70,78] However, this is not the case for compounds of the type $[M(bpy')(X)_4]^{2-,2+}$ or $[cis\text{-}M(bpy')_2(X)_2]^{0,2+}$ with X = CN^- or NH_3 and M = Ru, Os.[78] $[Ru(dcb)(CN)_4]^{2-}$ is a highly solvatochromic compound because of a shift of its $E^0(Ru^{III}/Ru^{II})$ value as a result of outer-sphere interactions with the cyano ligands.[79]

A problem with the MLCT transitions is that they have significantly lower extinction coefficients as compared to $\pi \rightarrow \pi^*$ transitions found in organic photosensitizers. Thus, TiO_2 films as thick as 6-10 μm are required for efficient solar harvesting. The preparation of high extinction coefficient **N3** derivatives, where one of the dcb ligands is replaced by a 4,4'-disubstituted bipyridine having low lying π orbitals to enhance MLCT extinction coefficients is therefore an extremely active area of research.[80-82]

Antenna effect can also be employed to increase the light harvesting efficiency of such complexes. Multiple chromophoric centres can be so arranged that these can absorb light and vectorially transfer their energy to the central unit which can then inject the

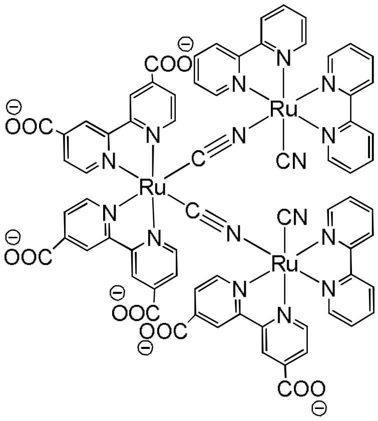

Figure 6: Example of an antenna-sensitizer polynuclear complex.

electrons into the semiconductor nanoparticles. The work carried out by Scandola and co-workers can be cited as an early example (Figure 6).[83]

Another very important criterion in regard to the design of efficient sensitizers is that (and as discussed before) the LUMO of the dye must be sufficiently high in energy for efficient charge injection into TiO_2, and the HOMO must be sufficiently low in energy for efficient regeneration of the oxidized dye by the redox electrolyte. Electron transfer from the dye to TiO_2 must also be rapid in comparison with decay to the ground state of the dye. This is because if the excited state charge injection is kinetically slow, other processes in the excited state manifold such as non-radiative decay, cross-over to metal-centred excited states become important in determining the efficiency of charge injection and stability of the dye. This also implies that the dye excited state should be long lived enough to ensure efficient electron injection without any ardent competition from the excited state decay processes discussed above.[84]

1.B.3.A.3. Anchoring groups

In order to develop efficient DSSCs, the dye must possess an anchoring group, which should react with the surface hydroxyl groups of the semiconductor oxide to form chemical bonds.[85] In earlier times, the dye molecules were adsorbed on semiconductor films by physisorption. This was done by dipping the cast films in a solution of the dye and then drying them in air. It was soon obvious that it was important to better control the binding process and already in the 1970s researchers started preparing dyes with anchoring groups that could bind covalently to semiconductor surfaces.[86-88] These efforts have indeed borne fruit in having led to significantly improved stable sensitized films with higher surface coverages, minimal dye desorption in addition to a highly controlled and even distribution of the dyes on the semiconductor to form monolayer coverages.[85] The anchoring groups provide control of the electronic coupling strength and their roles can be deduced directly by studying interfacial electron transfer rates (*vide infra*).

A range of anchoring moieties has been explored for probable use and Figure 7 lists some of them for binding dyes onto oxide semiconductor surfaces. Groups such as silanyl,[89] amide, carboxyl, phosphonato *etc*. have been shown to form stable linkages.[29,64,85] For phosphonates and carboxylates the binding is reversible with high equilibrium binding constants ($K \sim 1 \times 10^5$ M^{-1} for ruthenium-polypyridine complexes attached through -COOH groups) and high saturation surface coverages.[85] It has been shown that chemisorption of the -COOH groups to TiO_2 can occur though a variety of binding modes[85] (Figure 8) and the adopted mode depends on the structure of the dye, the binding groups, the pH, and the semiconductor preparation.

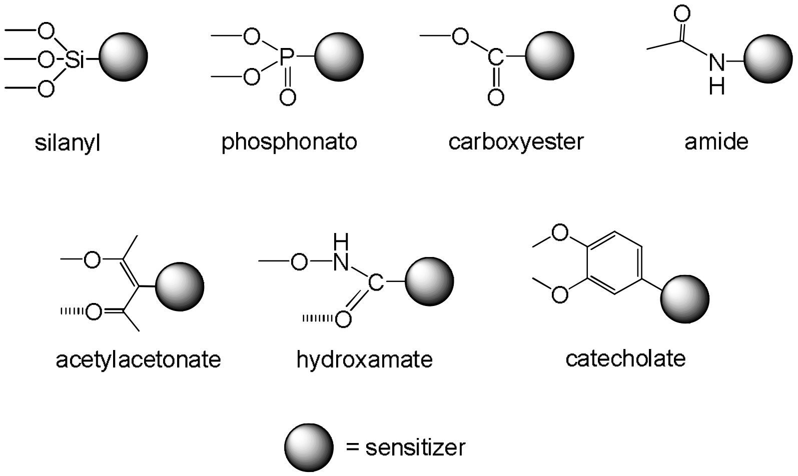
silanyl
phosphonato
carboxyester
amide
acetylacetonate
hydroxamate
catecholate
= sensitizer

Figure 7: Binding moieties explored for anchoring dyes onto oxide semiconductor nanoparticles.

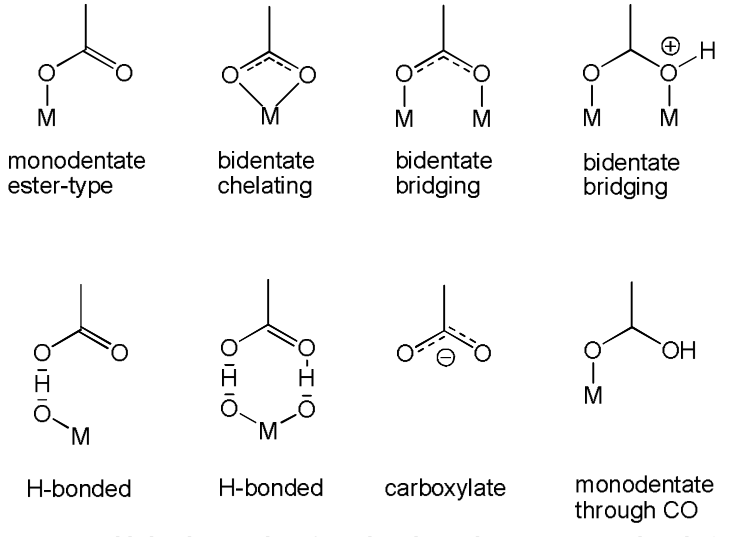
monodentate ester-type
bidentate chelating
bidentate bridging
bidentate bridging
H-bonded
H-bonded
carboxylate
monodentate through CO

Figure 8: Possible binding modes of a carboxylic acid group to a metal oxide (TiO_2).

However, carboxylate bound dyes are easily desorbed from the films in presence of water and so the stability of this linkage is limited to a certain pH range only (pH ≤ 4.5) due to the associated protolytic equilibrium.[29] In aqueous solutions of higher pH values, hydrolysis and subsequent de-chelation can occur from the surface. Most often, this equilibration takes place quite slowly so that the effects are seen in limited long-term stability tests. The pH range where the devices can be used in aqueous media is rather limited for this reason.

Phosphonic acids have therefore been explored as pH stable anchoring groups, since the corresponding phosphonato esters are reported to be stable till pH ≤ 8.5. Studies into phosphonic acid linkers report some of the highest efficiencies (≥ 8%) for any dye with a non-carboxylic acid linker (*e.g.* **Z955**, Figure 9).[90] In this case, modification of the linker from carboxylic acid group to phosphonic acid group resulted in a series of changes; *e.g.*, a blue shift was observed in the absorption maxima along with good stability of the device accompanied with slower charge-recombination kinetics relative to the analogous dye **Z907** (Figure 5). The greater number of protons on the phosphonic acid group as compared to carboxylic acid group has been suggested as a factor in the observed changed in performance of the dye, as it has been observed that the efficiency of the solar cell can be influenced by changing the protonation of the acid groups. This effect is also apparent in the dye **N719** (Figure 5), which being deprotonated, gives a higher cell efficiency than its protonated analogue **N3**.[91]

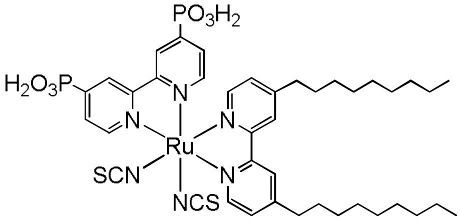

Z955

Figure 9: Molecular structure of **Z955** dye.

More recently, hydroxamic acids[92] and acetylacetones[93] have been proposed in order to overcome this pH stability problem. However, much further development is needed in order to establish dyes based on such anchoring groups as prospective alternatives to the classical ones. Also reported is the binding unit catechol whose ground state *pKa* is known to be > 9.6 and so the pH stability issue is overcome.[94,95] However, as a result of a very strong binding of the catechol moiety with TiO_2, the deleterious BET is very fast (please see section 1.B.4.D for details) and so considerable research efforts need yet to be poured in so that such anchoring units are made useful for practical applications.[94]

1.B.3.A.4. Peripheral groups

Long chain peripheral groups can lead to a considerable diminution in the tendency of the dye to aggregate or stack in solution or on the surface. This has also significance in regard to the previously discussed aqueous instability of the carboxylate mode of binding to TiO_2. Bulky alkyl substituents serve as a hydrophobic barrier and thus prevent water from hydrolyzing the dye-TiO_2 linkage. Such an effect can be seen in the dye **Z907** (Figure 5) and its high cell efficiency of 6.1% with excellent stability to both prolonged thermal stress and light soaking, attributed to the hydrophobic nature of the dye which enhances stability towards water-induced desorption.[96]

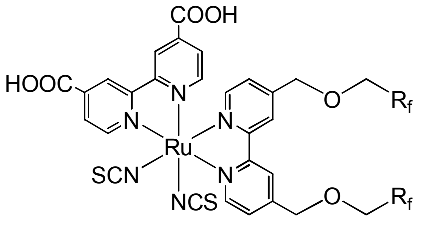

R_f = $-CF_2CF_2H$ (**CT4**)
= $-CF_2CF_2CF_3$ (**CT7**)
= $-CF_2CF_2CF_2CF_2H$ (**CT8**)

Figure 10: Molecular structures of dyes **CT4**, **CT7** and **CT8.**

The hydrophobic network also hinders the interaction between I_3^- and the TiO_2 surface and minimizes loss of the effective electron concentration at the TiO_2 conduction band.[84] Dyes with attached hydrophobic chains also enhance the wettability of mesoporous TiO_2 by the organic hole-conductor thus enhancing interaction with the dye and making dye regeneration faster.

Recently, Lu *et al.* synthesized a new set of amphiphilic dyes **CT4**, **CT7** and **CT8** (Figure 10) with a fluorous bis-ponytailed bipyridine ancillary ligand.[97] The efficiencies were observed to be comparable to that of **N719**. The increased efficiencies were assigned to be due to the fluorous chains which increased the dye density on TiO_2 and also helped suppress dye desorption.

1.B.3.A.5. Selected examples of ruthenium complex based sensitizers

The number of ruthenium complex based sensitizers is huge and a complete review is certainly beyond the present scope. A few representative examples are discussed.

The development of dyes with thiocyanate ancillary ligands is already discussed in the previous section. Further efforts, in order to increase the molar extinction coefficient led to the development of the dye **Z910** (Figure 11).[98] This dye exhibited 10.2% solar

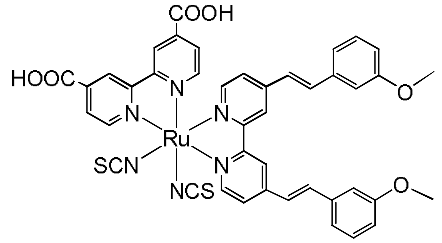

Z910

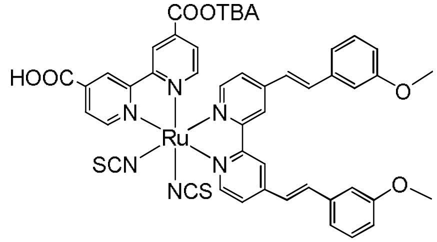

1

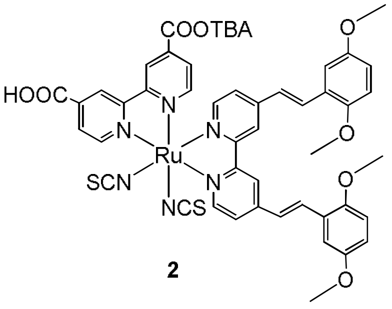

2

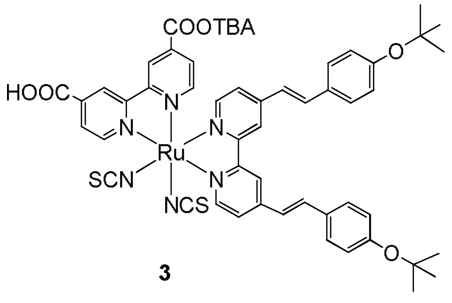

3

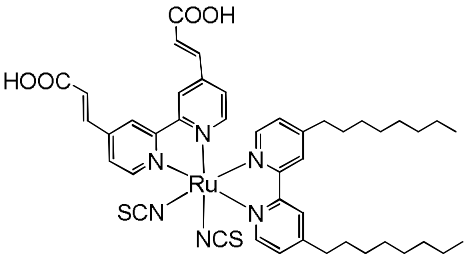

4

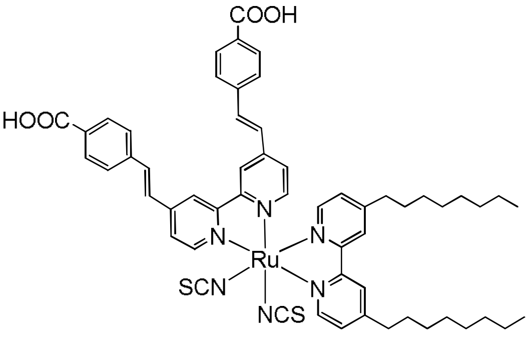

5

Figure 11: Molecular structures of dyes **1-5** and **Z910.**

conversion efficiency along with good thermal stability. Thus, the fact that increased molar extinction coefficient led to increased photoconversion efficiency led to the development of the dyes **1-3** and **K19** (Figure 5 and 11).[99-104] Nazeeruddin and co-workers reported a Ru^{II} dye, **4** (Figure 11),[105] in which by tuning of the HOMO and the LUMO levels, the spectral response and the molar extinction coefficient could be increased so as to yield an efficiency of 8.7%. This system was developed to further produce the photosensitizer **5**.[106] Recently, Liang and co-workers reported two ruthenium complexes **XS48** and **XS49** having butyloxy-substituted benzene ring and 9,9-dipropyl-9H-fluorene on the ancillary bipyridine ligand, respectively (Figure 12).[107]

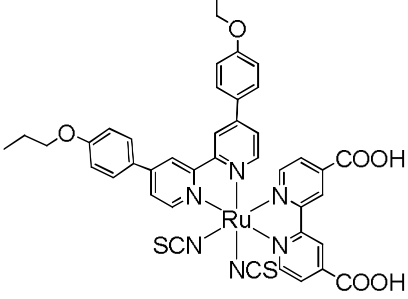

XS48

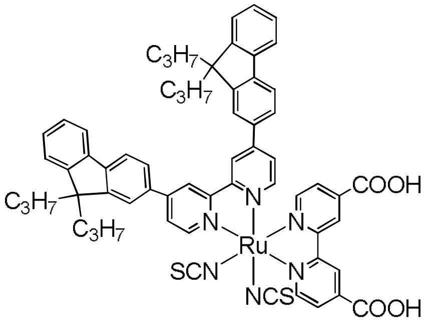

XS49

Figure 12: Molecular structures of **XS48** and **XS49.**

Both these complexes were shown to have higher photon-to-current conversion efficiencies than **N3** under analogous conditions. The enhanced extinction coefficient due to the introduction of the extended π-conjugation in the butyloxy-substituted benzene ring and 9,9-dipropyl-9H-fluorene unit, respectively, enhancing the local dipolar character of the ligand was suggested to be the reason.

The tri(ethylene oxide) methyl ether group was introduced by Grätzel and co-workers into the 2,2′-bipyridine ligand to give a novel ion coordinating sensitizer, **K51** (Figure 13).[108] The ion trapping unit in this dye inhibited the ions from reaching the TiO_2 surface. Hence, there occurred little reduction in the open-circuit voltage in a liquid electrolyte device, and for the solid state device there was a significant increase in the open-circuit voltage when Li^+ was added. The same group developed another sensitizer, **K60** (Figure 13),[109] incorporating such ion-coordinating side chains or crown ethers on

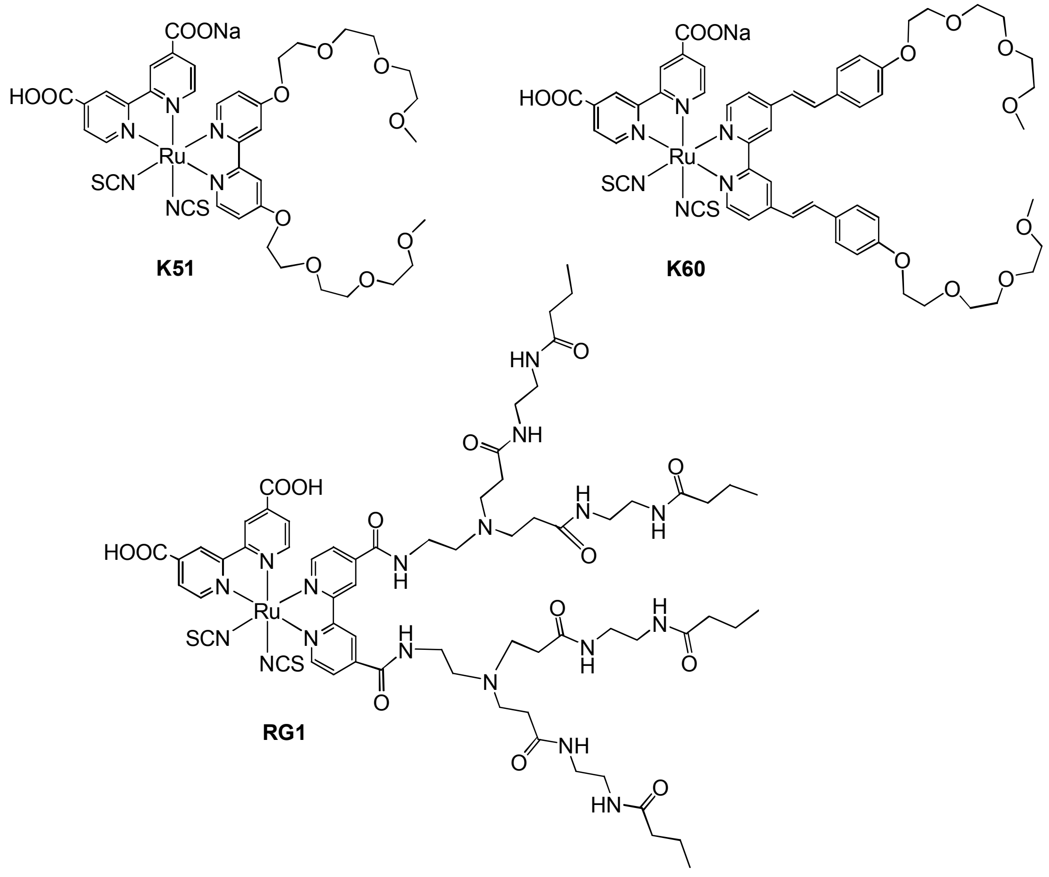

K51

K60

RG1

Figure 13: Molecular structures of the dyes **K51, K60** and **RG1.**

molecules with larger *π*-conjugated systems. A power conversion efficiency value of 8.4% was obtained with this dye. As a result of an apparent decrease in solubility, dye desorption was also lessened. Jia and co-workers reported a new dye (Figure 13), **RG1**, by incorporating poly(amido)amine dendron in their ligand.[110] They observed that **RG1** also acted as an additive in the electrolyte and resulted in high open circuit voltages. They justified the said role of the dye by arguing that the large size and the formation of densely packed structures increased the spatial separation of the $TiO_2(e^-)$ and the acceptors in the electrolyte thus reducing electron recombination. They also argued that the interaction of the dendrons with Li^+ in the electrolyte prevented the access of the said cations to TiO_2. This interaction of the dendronic moieties with the electrolyte was also argued to be assisting dye regeneration. A combination of all these factors and the N-containing nature of the dendrons were thought to increase the open circuit voltage.

Substituting one of the bipyridyl ligands with alkyl thiophene, EDOT or carbazole, Wu and co-workers developed a series of ruthenium complexes (**7-13**, Figure 14).[111-114] With incorporation of thiophene ligands, the energy levels of the metal center and the LUMO from the ligands were raised as a result of which the MLCT band was red-shifted. Under identical cell fabrication and measuring procedures, **7** gave an efficiency of 8.5%, **8**, 9.0% and dye **9**, 7.4% (**N3**, 7.7%). The noteworthy improvement in efficiency for the **8**-based cell compared with **9** demonstrates the imperative role played by the EDOT

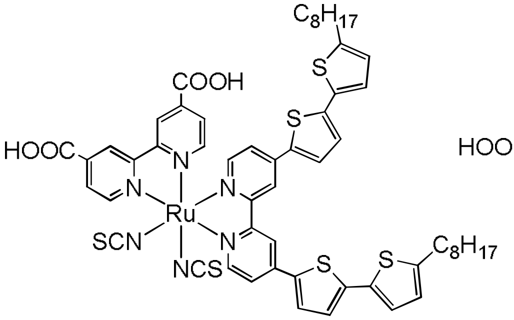

7

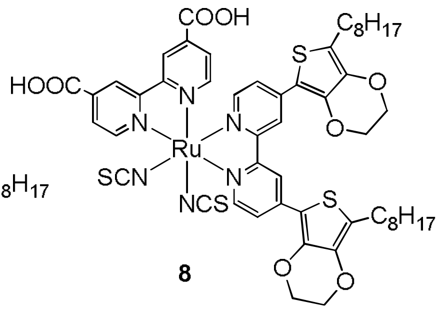

8

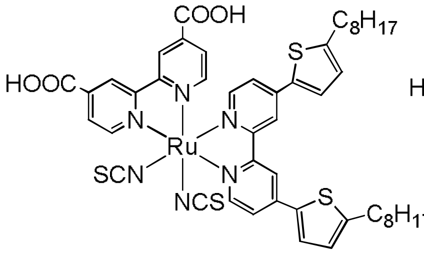

9

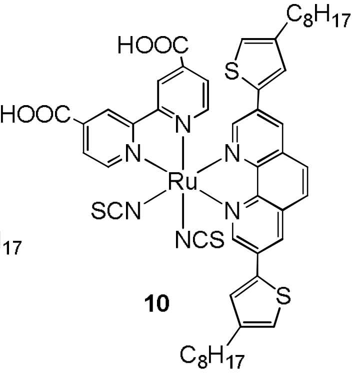

10

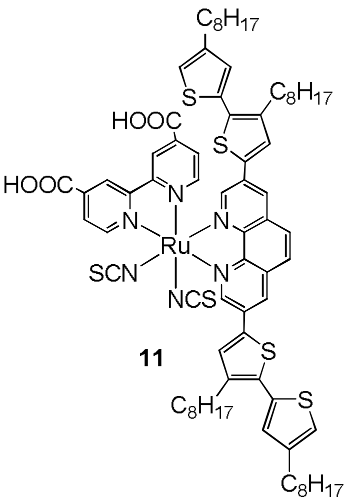

11

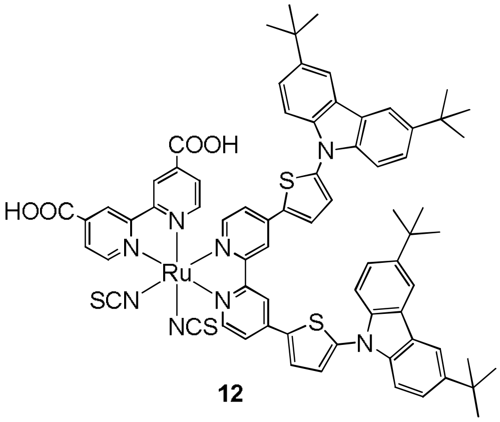

12

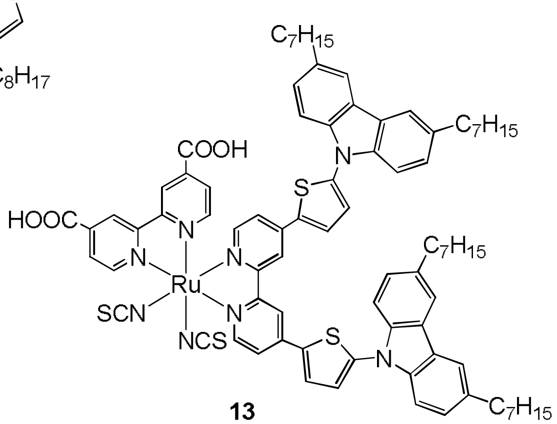

13

Figure 14: Molecular structures of dyes **7-13.**

moiety in the ancillary ligand which increases the conjugation length without increasing the size of the complex.[113] The strongly electron-donating ether group on EDOT was also cited as one of the reasons for this effect. The same group functionalized the thiophene-derived ruthenium complexes with an alkyl-substituted carbazole, a hole-transport moiety, to obtain **12** and **13**.[114] The liquid state dye solar cell based on **12** showed an efficiency of 9.7% (**N3**, 8.5%). Wang and co- co-workers prepared a series of

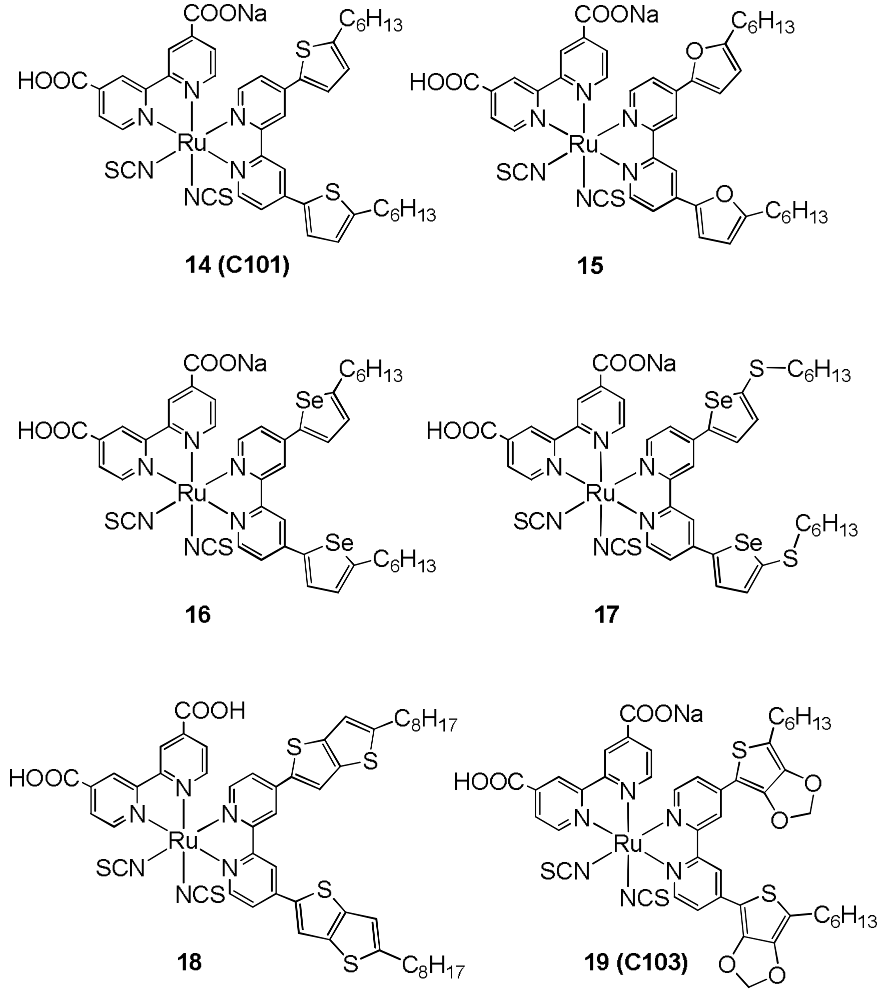

14 (C101) **15** **16** **17** **18** **19 (C103)**

Figure 15: Molecular structures of dyes **14-19.**

polypyridyl ruthenium sensitizers (**14-19**) (Figure 15) derivatized with conjugated electron rich units like alkyl thiophene, alkyl furan, alkyl selenophene, or alkyl thieno[3,2-*b*]thiophene for obtaining high molar extinction coefficients.[115-118] **14** (coded as **C101**) gave 11.0% efficiency under AM 1.5 G illumination with an acetonitrile based electrolyte. It also gave a long-term stable efficiency of > 9% using a low volatility electrolyte and ~ 7.4% using an ionic liquid electrolyte. It was also found that because of a high extinction coefficient of the sensitizer, the thickness of the TiO_2 film could be reduced thus favouring the charge collection efficiency.[115] Dye **19** (coded **C103**) showed 9.6-10.0% and 8.5-9.1% efficiencies under AM 1.5 G illumination with low-volatility and solvent-free electrolytes, respectively. In addition, solar cells based on these dyes retained more than 90% of the initial performance after sunlight soaking of full 1000 h at 60 °C.[119] Yanagida and co-workers prepared the dye **20** by introducing 2-thiophene-2-yl-vinyl into ruthenium complexes (Figure 16).[120] This dye showed a 30% increase in molar extinction coefficient and a 10 nm red shift in its absorption spectrum as compared to **N719**. An efficiency of 9.5% was achieved for this dye (**N719**, 8.9%). Recently, Ko *et al*. reported the dye **JK-142** containing an ancillary bipyridyl ligand substituted by a 3-carbazole-2-thiophenyl moiety (Figure 16).[121] The dye showed enhanced red absorption but as a result of inefficient percolation into TiO_2, the efficiency observed was somewhat less. The authors, however, obtained efficiencies upto 10.2% (**N719**, 8.68%) upon co-sensitization with another small sized triarylamine based organic dye. Diau and co-workers developed a series of heteroleptic ruthenium complexes **RD16-RD18** containing fluoro-substituted and thiophene-based benzimidazole ligands (Figure 16).[122] Because of the increased light-harvesting ability

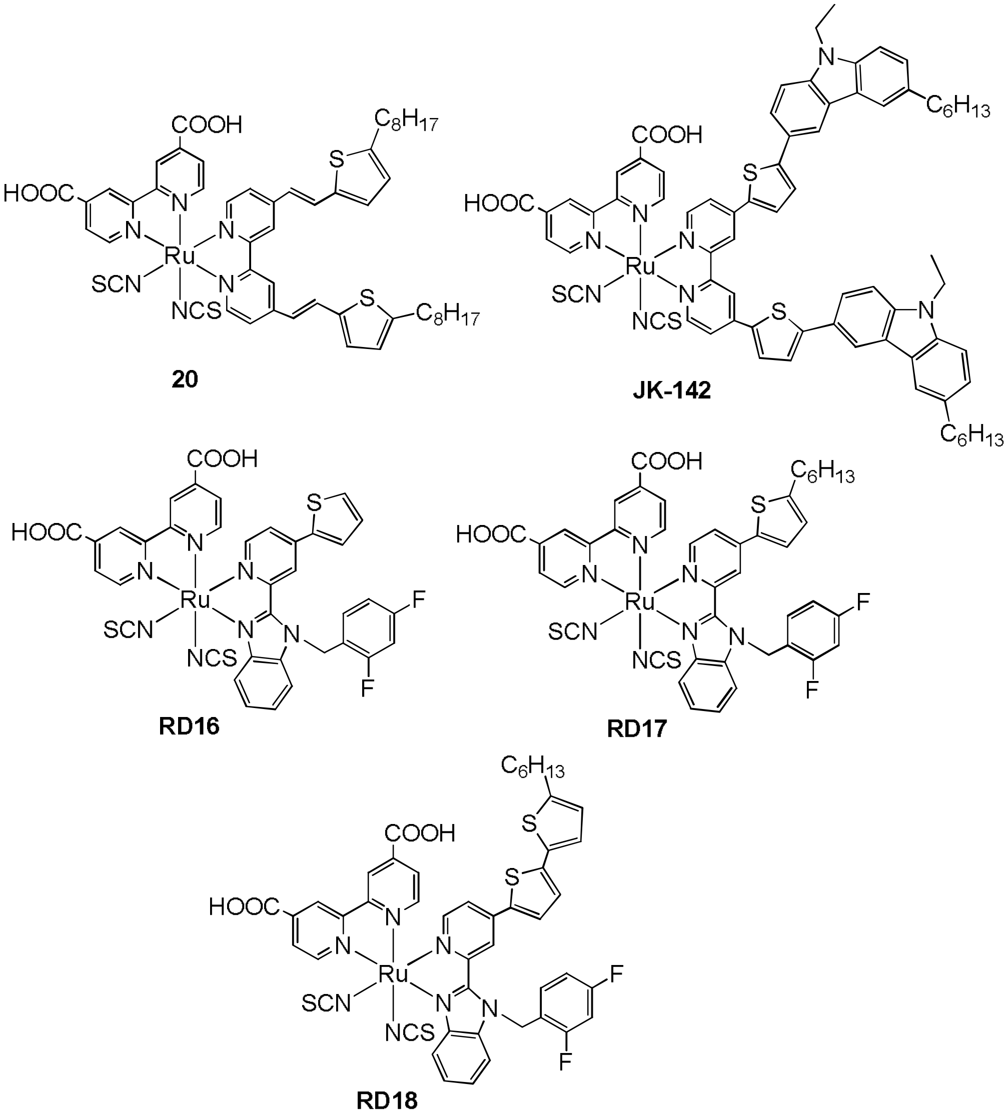
20
JK-142
RD16
RD17
RD18

Figure 16: Molecular structures of the dyes **20**, **JK-142** and **RD16-18.**

and the broadened spectral features with thiophene-based ligands, all the dyes exhibited high efficiencies. The highest efficiency was reported for the dye **RD18**, 10.0% (**N719**, 8.8%). The authors also performed a duration test of device performance and found only ~ 2% degradation of cell performance for the devices of **RD18** over 2000 h. Under the same conditions, there was a 10% decrease in overall efficiency for the **N719** device.

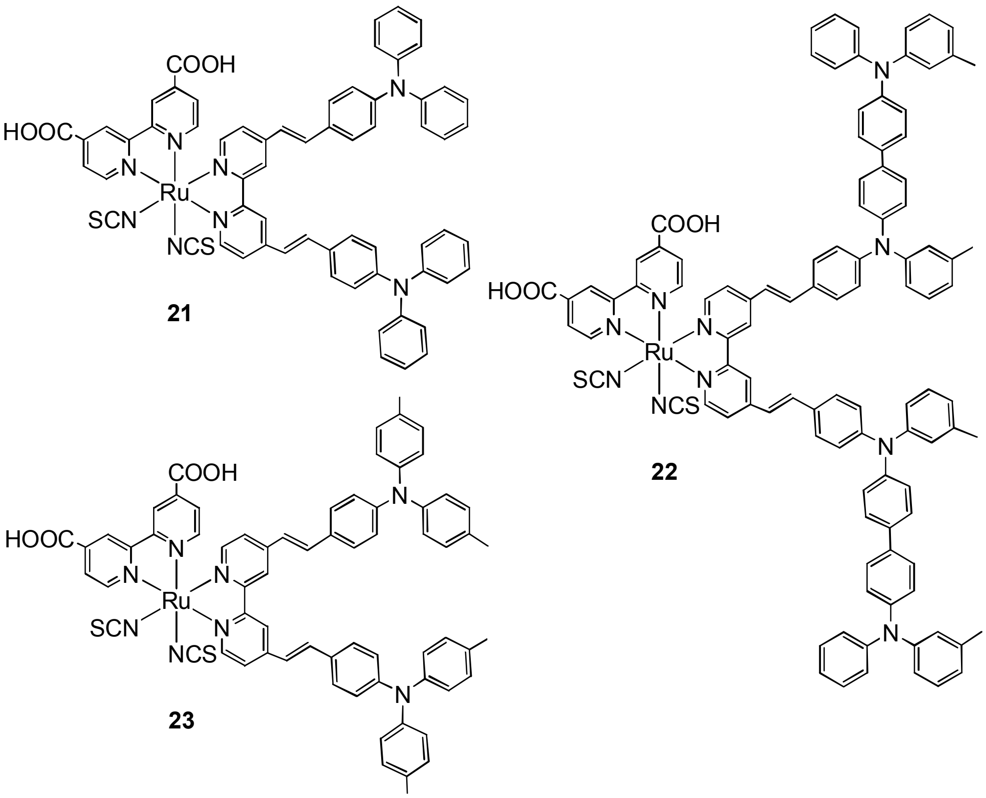

21

22

23

Figure 17: Molecular structures of dyes **21**-**23**.

Thelakkat, Durrant and co-workers developed ruthenium polypyridyl dyes based on electron donating triarylamine ancillary groups.[123-125] The extinction coefficient was found to increase substantially when the triarylamine moiety was connected with a conjugated linker. The recombination of the injected electron with the dye was found to be substantially slower and this was attributed to the location of the cationic charge largely on the triarylamine moieties of the dye and the consequently larger physical separation of the cationic charge from the TiO_2 surface (*vide infra*). Dyes **21** and **22** (Figure 17) gave efficiencies of 1.5% and 3.4%, respectively in solid state devices. Under similar conditions, **N719** dye showed a much lower value of 0.7%.[125] A very similar dye, **23**, gave an overall efficiency of 10.3% in a liquid electrolyte cell (Figure 17).[126]

In order to assist dye/redox couple interaction and hence dye regeneration, dye **24** was synthesized by Falaras and co-workers by incorporation of a CD unit into the ruthenium complex (Figure 18).[127] In comparison to the dye without this CD unit, **24** resulted in a higher efficiency. The authors justified their results by considering binding of the iodide/triiodide redox couple to the CD moiety which perhaps facilitated dye regeneration.

From a stability point of view, the monodentate thiocyanate is perhaps the weakest part of the complex. Many attempts have thus been made to replace the thiocyanate donor ligands. Cyclometalated ruthenium complexes of the type [Ru(C^N^N)(N^N^N)], were used for the first time by Koten and co-workers.[128] Dye **25**, in spite of an absence of the thiocyantate ligands (Figure 18), has a closely resembling absorption spectrum as **N719**. Grätzel and co-workers developed dye **26** (Figure 18), which exhibited an IPCE value of 83% and an extremely good conversion efficiency of 10.1% at AM 1.5 G.[129] Singh and co-workers from Indian Institute of Chemical Technology, Hyderabad recently reported a thiocyanate free Ru^{II}-polypyridyl complex, **SPS-01**, with two trifluoromethyl carbazolyl pyridine ligands along with a phenylethenyl moiety into the anchoring bipyridine ligand (Figure 18).[130] They obtained an efficiency of 7.96% which was higher than that of **N719** (7.30%) under identical experimental conditions.

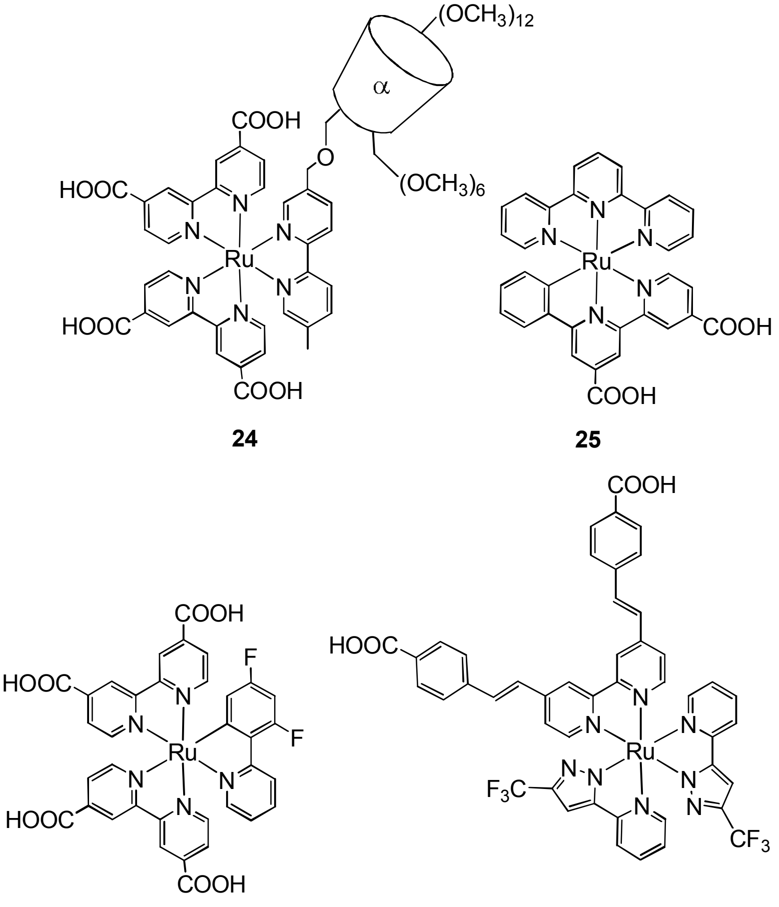

24 **25**

26 **SPS-01**

Figure 18: Molecular structures of dyes **24-26** and **SPS-01.**

1.B.3.B. Examples of other metal complex based sensitizers

Many metal complexes other than those of ruthenium have been explored. However, such metal complexes seldom give as good efficiencies as the ruthenium ones.

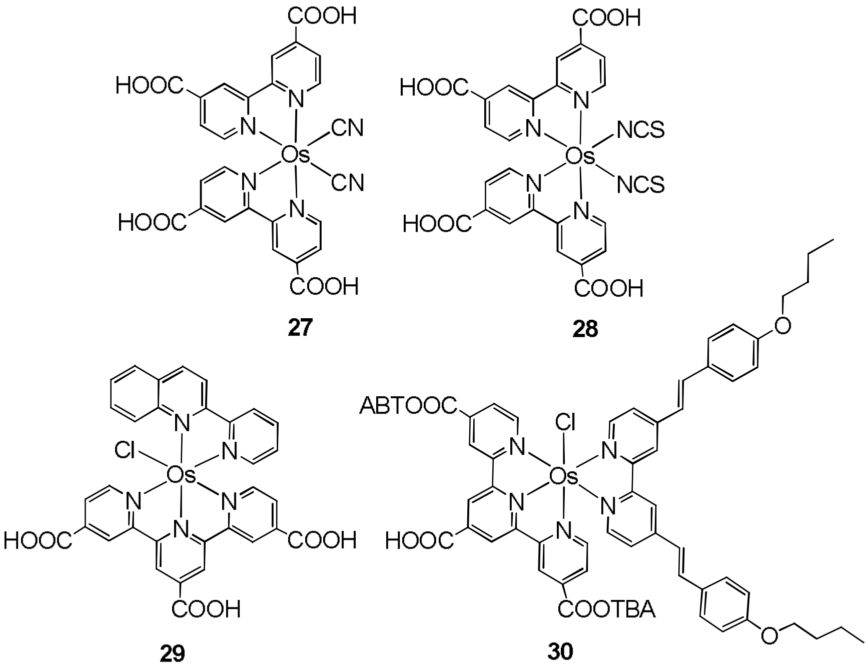

Figure 19: Molecular structures of dyes **27-30.**

Os^{II} complexes (Figure 19) have been found to be promising photosensitizers for DSSCs due to the prominent ^{3}MLCT absorption band that extends the absorption of such complexes over almost the entire visible range. Lewis and co-workers obtained dyes **27** and **28**,[131-133] and thus extended the light response without surrendering a good photovoltaic performance in DSSCs. Bignozzi and co-workers reported dye **29** which showed an IPCE spectrum up to 1100 nm.[134] The same group also demonstrated that lower photocurrent efficiency of osmium complexes was probably due to a slower electron transfer from the iodide electrolyte to the osmium dye cation.[135] Segawa and colleagues have however achieved 6.1% efficiency very recently for one of their newly synthesized near-infrared absorbing osmium terpyridyl complex, **30**, with 4,4'-bis(p-butoxystyryl)-2,2'-bipyridine as the chromophoric ligand which enhances both the spin-allowed and forbidden transitions.[136]

Re^{I} complexes (*e.g.* **31**, Figure 20) were developed mainly to study the interfacial charge injection and recombination processes.[137] The facial geometry for Re^{I} tricarbonyl complexes is said to provide a better molecular control of the orientation of the dye.[138] Lower IPCE values for these complexes in comparison to analogous Ru^{II} complexes are due to the major fraction of light transmitted, although the absorbed photon-to-current efficiency (APCE) is unity within the limit of experimental errors.[138]

On the other hand, Ferrere and co-workers developed Fe^{II} complexes (*e.g.* **32**, Figure 20) which showed a lower efficiency with IPCE values only around 10-11%.[139]

Square-planar Pt^{II} diimine dithiolate complexes have been explored as prospective dyes for DSSCs because of the highly solvatochromic nature of its CT absorption. Substituents on the diimine and the dithiolate ligands could tune the electronic and photophysical

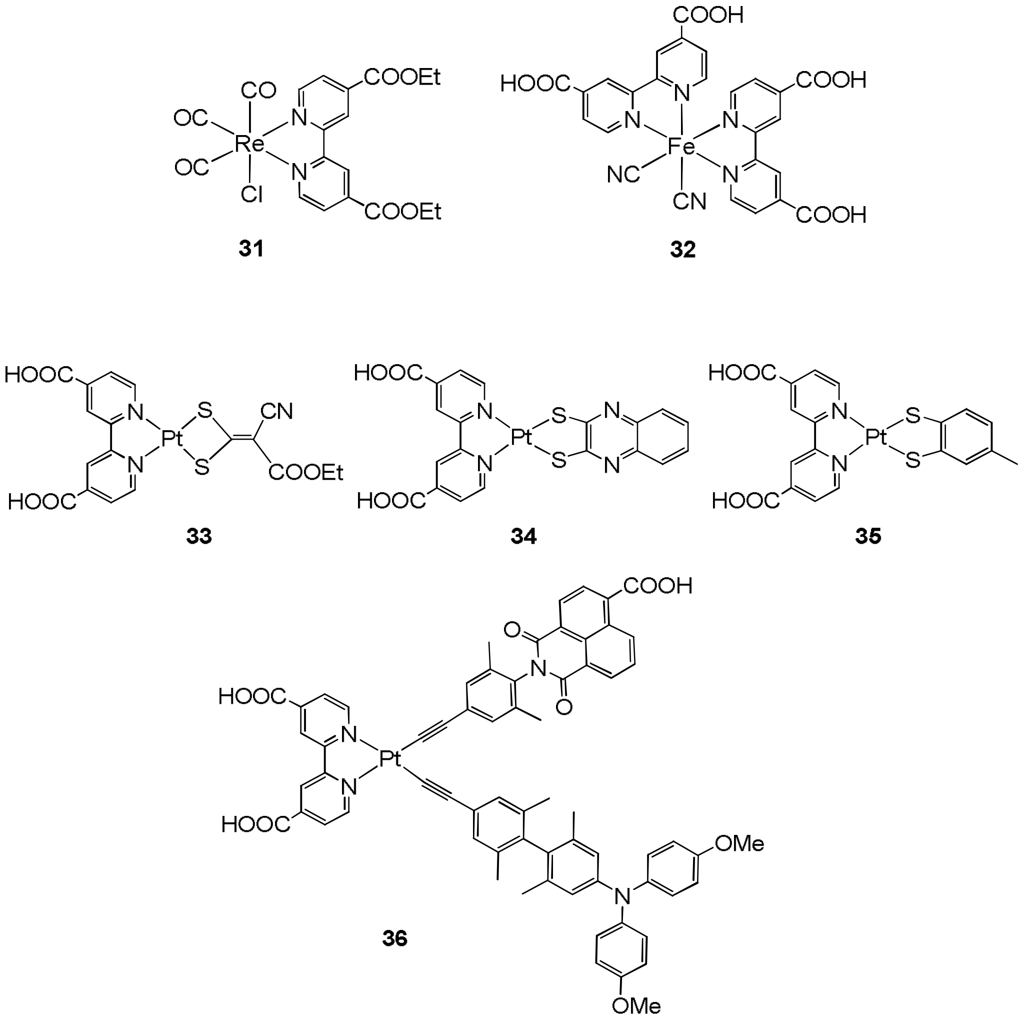
31 32 33 34 35 36

Figure 20: Molecular structures of dyes **31-36.**

properties respectively, of the LUMO and HOMO. Sugihara and co-workers developed dyes **33-35** (Figure 20)**.** Out of these, the most efficient was dye **34**, which, at 500 nm, showed a high IPCE value of 47%.[140] However, its light-harvesting capacity at wavelengths longer than 650 nm was found to be very poor. This dye exhibited an overall efficiency of 3.0%. Okada and co-workers recently published an excellent effort towards the development of novel platinum based sensitizer dyes.[141] They synthesized the molecule, **36**, having a donor triarylamine unit and an acceptor naphthaleneimide linked to the central Pt^{II} complex (Figure 20). The charge separated state, D^+-A^- was expected to inject an electron into the TiO_2 conduction band. However, the complex exhibited a poor energy conversion efficiency of 0.2%. The authors suggested that the bent molecular shape of the dye might be causing a short circuit thus leading to the observed low efficiency. Insufficient driving force for the electron injection process was also suggested as one of the probable reasons.

Because of their similar photophysical properties to ruthenium complexes, Cu^I complexes were introduced as sensitizers by Sauvage and co-workers.[142] Constable and

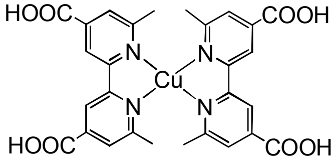
HOOC
COOH
HOOC
COOH
N
N
Cu
N
N

37

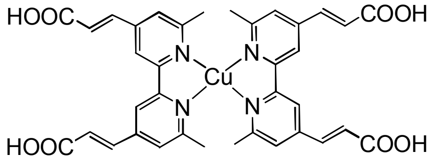
HOOC
COOH
HOOC
COOH
N
N
Cu
N
N

38

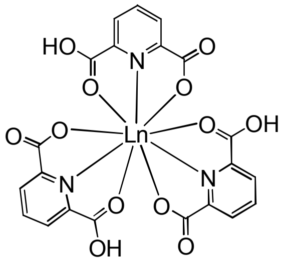
HO
O
N
O
O
O
Ln
O
OH
N
N
O
O
OH
O

Ln = Tb, **39**
= Dy, **40**

Figure 21: Molecular structures of dyes **37-40.**

co-workers reported dyes **37** and **38** recently (Figure 21).[143] As a result of a large π-conjugation and high molar extinction coefficient, dye **38** yielded an efficiency of 2.3% with liquid electrolyte.

Recently, Yang and co-workers studied terbium and dysprosium complexes, **39** and **40**, respectively, of pyridine-2,6-dicarboxylic acid ligands as co-sensitizers with **N719** to obtain appreciable efficiencies (Figure 21).[144]

1.B.3.C. Other sensitizers

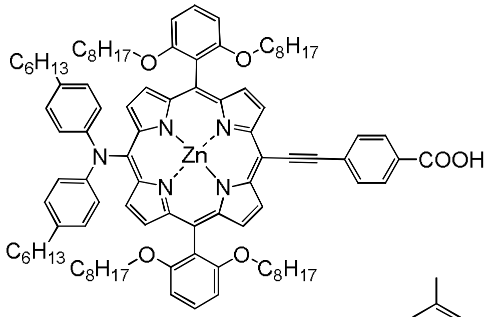
C6H13
C8H17
O
O
C8H17
N
N
N
Zn
N
N
COOH
C6H13
C8H17
O
O
C8H17

41 (YD2-*o*-C8)

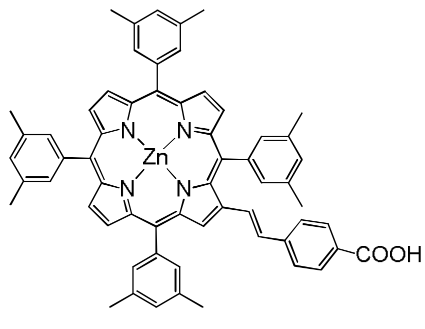
N
N
Zn
N
N
COOH

42

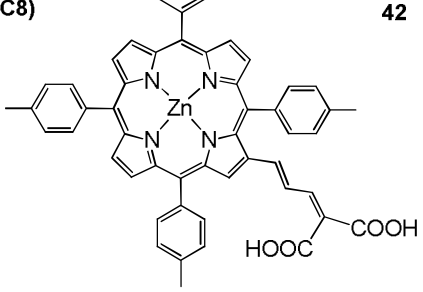
N
N
Zn
N
N
COOH
HOOC

43

Figure 22: Molecular structures of some porphyrin-based sensitizer dyes.

An overabundant number of different classes of molecules have been explored for their dye sensitization properties in the last two decades. Porphyrins and phthalocyanins remain a major category of such compounds.[28] One of the major drawbacks of ruthenium complexes discussed thus far is their limited absorption in the near-infrared region of the solar spectrum. Porphyrins and phthalocyanines exhibit intense spectral bands in the near-infrared region and possess good chemical, photo-, and thermal stability. Very recently, Grätzel and co-workers reported a donor-π-bridge-acceptor zinc porphyrin dye, **41** (coded **YD2-*o*-C8**) as sensitizer which, in conjugation with Co$^{(II/III)}$ tris(bipyridyl)–based redox electrolyte and with another organic dye as the co-sensitizer, exhibited a record 12.3% efficiency under AM 1.5 G.[145] Figure 22 shows the structures of some other porphyrin based sensitizer dyes known to have high efficiencies in regenerative solar cells. Phthalocyanines have intense Q-band absorption around 700 nm and have promising thermal, photochemical and electrochemical properties and thus possess immense prospects as near-infrared sensitizers.[28] However, such dyes have a strong tendency to aggregate on the semiconductor surface and thus require a co-adsorber dye to suppress aggregation. A large number of phthalocyanine dyes, including Zn^{II} phthalocyanines, have been studied (Figure 23).

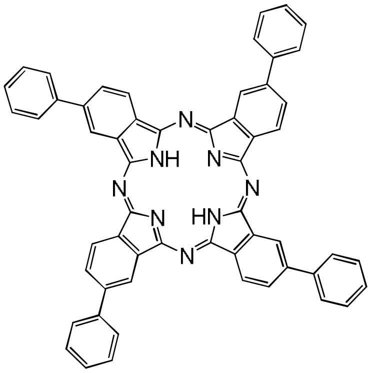

44

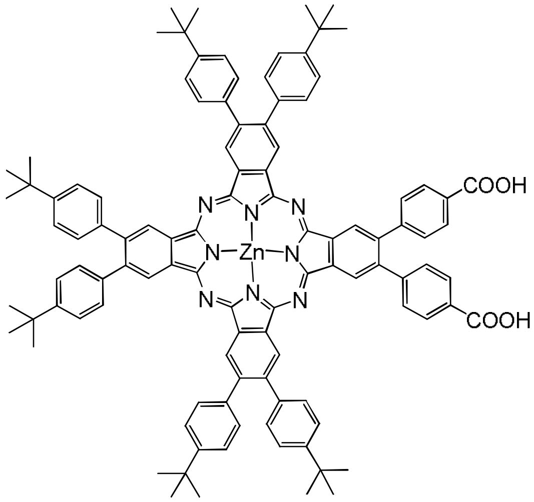

45

Figure 23: Molecular structures of some phthalocyanin-based sensitizer dyes.

Besides porphyrins and phthalocyanins, literature search reveals innumerable number of organic dyes as alternatives to the noble ruthenium complex based sensitizers. Such organic dyes are advantageous in their superiority over cost and environmental issues. Also, the molar extinction coefficients of such dyes are generally higher than those of ruthenium complexes which make them an attractive choice for thin film and solid-state DSSCs. In fact, in p-type DSSCs, organic dyes have higher efficiencies compared with that of ruthenium complexes. n-type organic dyes include coumarin dyes, indoline dyes, tetrahydroquinoline dyes, triarylamine dyes, heteroanthracene dyes, carbazole dyes, *N*,*N*-dialkylaniline dyes, hemicyanine dyes, merocyanine dyes, squaraine dyes, perylene dyes, anthraquinone dyes, BODIPY dyes, oligothiophene dyes, polymeric dyes and natural dyes.[28]

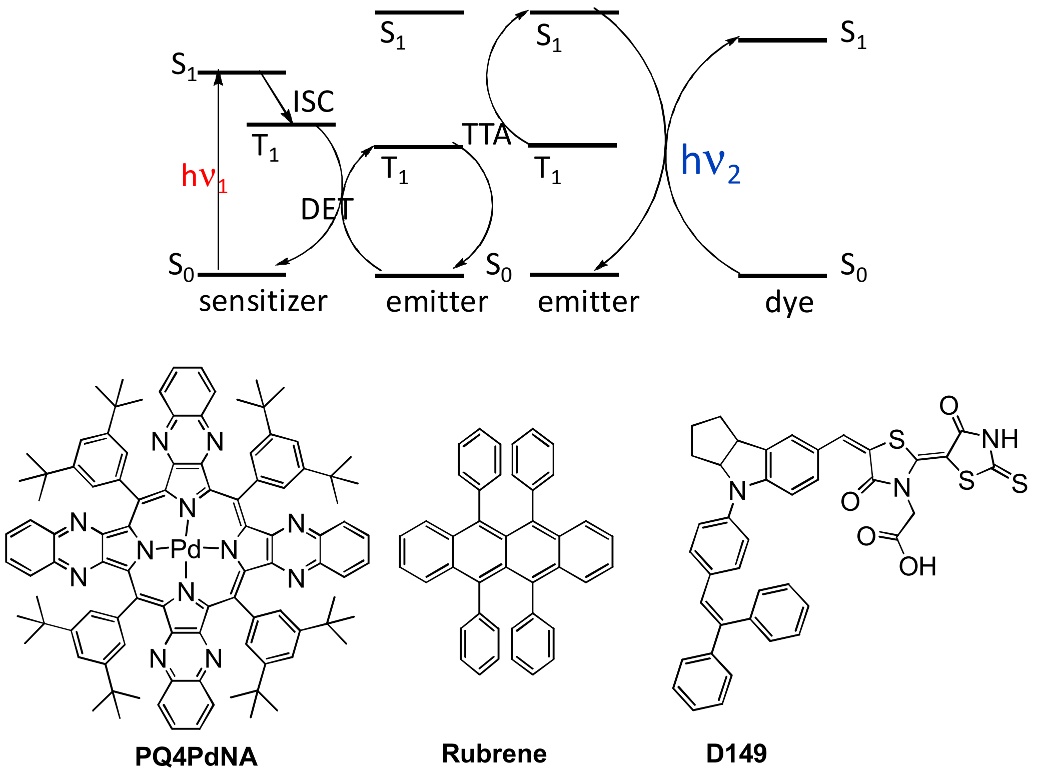

Figure 24: Illustration of triplet–triplet annihilation based photon upconversion in DSSC.

A novel example of photon upconversion by triplet–triplet annihilation (TTA) was recently employed in order to enhance the response of TiO_2 dye solar cells to sub-bandgap light (Figure 24).[146] In their system, a ground-state PQ_4PdNA sensitizer molecule absorbed a low energy photon ($h\nu_1$), then underwent ISC to its first triplet state. This triplet energy was then transferred *via* Dexter energy transfer (DET) to a rubrene emitter molecule in its ground state, which got transferred to a triplet state. TTA now occurred between two such excited emitters *via* a collisional complex to yield one emitter in the first singlet excited state and the other one in the ground state. This excited singlet emitter returned to the ground state *via* emission of a much higher energy upconverted photon ($h\nu_2$) which was captured by the **D149** dye and underwent the usual processes as in a conventional DSSC. Because this photon UC process allows for the utilization of photons with quite less energy, the concerned solar cells are expected to have a higher efficiency limit than set by the Shockley–Queisser limit for single junction devices and thus present immense future prospects.

1.B.3.D. Perovskite based sensitizers

Organic-inorganic hybrid perovskites like $CH_3NH_3PbX_3$ (X = Cl, Br, I) are attracting enormous research attention as sensitizer materials presently. For high efficiencies to be obtained from thin PV films, efficient light harvesting is very necessary. This means that the sensitizer must have high extinction coefficient bands throughout the visible and the near-infrared region and it must be possible to collect the charges at high voltages. However, typical DSSCs involve severe voltage losses since even the best dyes have limitations in their absorption properties discussed and also due to inherent losses during charge injection into the semiconductor and dye regeneration by the electrolyte. Snaith and co-workers further assigned such energy losses to the expensive exciton separation and free carrier extraction in highly disordered low-mobilty networks.[147] Typical organic-inorganic hybrid perovskites have intense absorptions in the visible and the near-infrared regions and have been demonstrated to overcome such voltage losses unusually well particularly because of high dielectric constants which makes excitonic separation easier.[148,149] Such organic-inorganic hybrid perovskites were first reported as sensitizers by Miyasaka and co-workers who obtained an efficiency of 3.8% on a $CH_3NH_3PbI_3$-TiO_2 based cell.[148] Snaith and co-workers obtained 10.9% efficiency by removing the TiO_2 and coating a mixed-halide perovskite $CH_3NH_3PbI_{3-x}Cl_x$ on an insulating mesoporous Al_2O_3 film which structured the absorber and forced the electrons to remain in and be transported through the perovskite network.[147] Very recently, Grätzel and co-workers obtained ~ 15% efficiency when they formed the perovskite pigment within the porous TiO_2 by a sequential deposition method thus controlling loss of photovoltaic performance due to large morphological variations during uncontrolled precipitation.[20]

Such architectures have been said to define a new class of hybrid semiconductor PV cells (HSPC) with ultrahigh light power conversion efficiencies and recent studies carried out by Bisquert and co-workers into the mechanism of operation of such cells substantiates this definition.[150]

1.B.4. Dynamics of interfacial electron transfer

1.B.4.A. The excited state time scales

Before discussion on the dynamics of the interfacial charge separation and recombination, an idea about the time scale of the different excited processes of Ru^{II} and Os^{II} polypyridyl complexes is necessary. For Ru^{II} and Os^{II} polypyridyl complexes, the radiative rates are orders of magnitude smaller than the non-radiative rates.[151] The excited state lifetimes are therefore controlled by these non-radiative rates. Following Energy gap law formulated by Jortner, smaller energy gap between the ground and the excited states manifests itself in an exponential increase in the non-radiative rates.[64] As a consequence, it is very difficult to have far emitting dyes with high excited state lifetimes. The additional presence of low lying LF states discussed before further adds to the decreased lifetimes.

The excited state dynamics of $[Ru(bpy)_3]^{2+}$ was studied extensively by McCusker and co-workers and they found, using transient absorption anisotropy measurements, that the initial FC state of D_3 symmetry converted to the C_2-symmetrical excited state and this charge localizing decoherence, coupled to inertial solvent dynamics, occurred with a lifetime of 59 fs in acetonitrile.[152] Their experiments disproved the contradictory conclusion that the C_2-symmetrical excited state formed immediately upon light excitation.[153] By femtosecond fluorescence upconversion, it was shown by Bhasikuttan *et al.* that the lifetime of singlet to triplet ISC in the MLCT excited state of $Ru(bpy)_3^{2+}$ was 45 ± 15 fs.[154] The measurement of this ISC time was further refined by Chergui and co-workers who, employing femtosecond broadband fluorescence observed this time to be 15 ± 10 fs.[155]

McCusker, by femtosecond magic-angle transient absorption spectroscopy, again observed spectral features lasting ~ 300 fs and these were assigned to relaxation of the ^{1}MLCT excited state to the ^{3}MLCT state with the reported half time, $t_{1/2}$ ~ 100 fs representing an upper limit to the true ISC time (Figure 25).[156] Hammarstrom and co-workers did similar experiments and they observed a higher energy (360 nm) longer lifetime (~ 5 ps) feature and this was assigned to vibrational relaxation to form the *thexi* state.[157] Various other studies showed that this vibrational relaxation time varied from ~ 0.6 to 5.0 ps.[158,159] McGarvey and co-workers, using picosecond Kerr-gated time resolved resonance Raman spectroscopy showed this relaxation time to be ~ 20 ps for homoleptic and heteroleptic $Ru(bpy)_3^{2+}$-based molecules of varying charges and isotopic compositions and in a variety of solvents.[160] For **N3**, the ISC time is reported to be ~ 30 fs and vibrational relaxation within its ^{3}MLCT state is found to occur with a ~ 80 fs half-time when bound to TiO_2.[161]

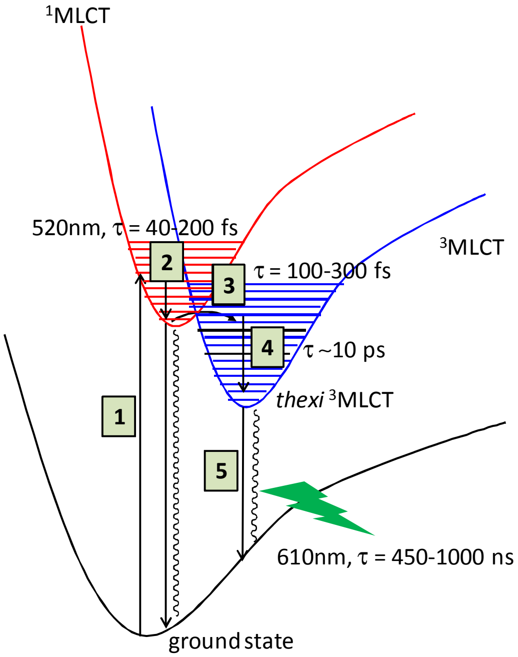

Figure 25: An overview of the processes following excitation of $[Ru(bpy)_3]^{2+}$ to the FC state.

1.B.4.B. Electron injection

Interfacial charge injection can occur by the following three mechanisms:[64] (a) injection from the excited state, *i.e.* $[Ru^{III}(bpy)_2(dcb^-)]^{2+*}$, (b) injection from the reduced state, *i.e.*

$[Ru^{II}(bpy)_2(dcb^-)]^+$, or (c) injection *via* a molecule-to-particle CT event. All of these processes require appreciable overlap of the donor states in the molecule with the accepting states in the semocinductor. Of these three mechanisms, the first one will be discussed in more detail.

1.B.4.B.1. Injection from the excited state

Electron transfer between dyes and bulk semiconductors involves electron transfer between distinct molecular states and a dense manifold of highly delocalized electronic levels in the semiconductor.[162-164] For photoinduced electron injection from the excited state of the dye to the semiconductor, the reactant-state corresponds to electron in the excited state of the dye while the product state consists of electron in the conduction band of the semiconductor. So a distinct reactant state connects to a continuum of product states, each corresponding to electrons injected at different electronic level of the semiconductor (Figure 26). The electron transfer rate to a particular electronic state in the semiconductor depends on the overlap of the donor state of the dye with the molecular Franck–Condon overlap weighted density of states. So, in the weak coupling regime, *i.e.* in the nonadiabatic limit, the total electron transfer rate can be expressed as the sum of all electron transfer rates to the different accepting states and is expressed by the following equation:[165-167]

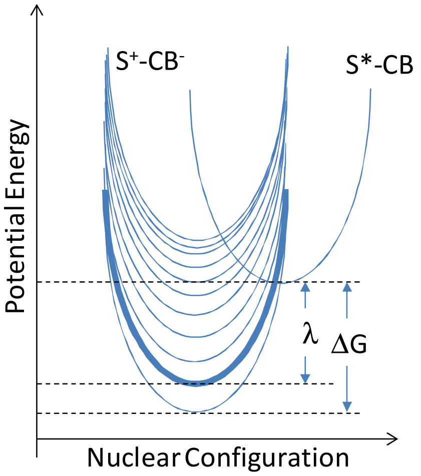

Figure 26: Marcus picture for electron transfer from a reactant state (S^*-CB) to a continuous manifold of product states (S^+-CB^-) corresponding to different **k** states in the semiconductor. Barrierless electron transfer (*thick line*) occurs to states λ below the sensitizer potential.

$$K_{ET} = \frac{2\pi}{\hbar}\int_0^{\infty} dE\rho(E)\left(1 - f(E, E_F)\right)|\bar{H}(E)|^2 \frac{1}{\sqrt{4\pi\lambda k_B T}}\, e^{\left[-\frac{(\lambda + \Delta G_0 - E)^2}{4\lambda k_B T}\right]}$$

In this equation, $\Delta G_0 = E_{cb} - E_{ox}$, *i.e.* the difference in energy between the conduction band edge and the oxidation potential of dye excited state; $\rho(E)$ the density of states at energy E relative to the conduction band edge and this can include both bulk states and surface states. $\bar{H}(E)$ is the average electronic coupling between the dye excited state and the different k states in the semiconductor at the same energy E; and λ is the total reorganization energy. $f(E, E_F)$ is the Fermi occupancy factor and it ensures that electron injection occurs only to unfilled states. However, for wide band gap semiconductors like TiO_2, under no external bias voltage, conduction band has almost negligible electron population before injection and so this factor might be omitted. For nanocrystalline semiconductor materials which are not in the quantum confined size regime, though the electronic structure of the bulk material applies, there is an appreciable contribution from the surface states and the defect states. For defect-free semiconductors, the density of states close to the band edge is given by the following equation:[168]

$$\rho_0(E)dE = \frac{(2m^*)^{3/2}}{2\pi^2\hbar^3}\sqrt{E}\,dE$$

where m^* is the effective mass of electrons in the conduction band. Defects introduce states below the conduction band edge and for metal oxide nanocrystalline thin films, the density of the defect states decays exponentially below the band edge.[169,170] If the effective electronic coupling is assumed to be independent of energy, then the injection rate, k_{ET}, can be plotted as a function of the driving force as shown in Figure 27.[162] Figure 27 shows that when the dye excited state lies high above the conduction band edge, *i.e.* for large negative values of the driving force, the change in the electron transfer rate is small. The change is however exponential when the negative value of the driving force is not so large thus reflecting the change in the conduction band density of states. However, the situation might not be this simple. The electron transfer rate does not depend on the total density of states but it depends only on those which are coupled to the dye electron donating orbital.[164] The coupling strength also varies for different band states. To add to this fact is the inhomogenous distribution of adsorbate/semiconductor interactions (crystal surfaces, adsorption site, adsorption geometry, *etc*.) which give rise to a distribution of electronic coupling elements and hence different injection rates.

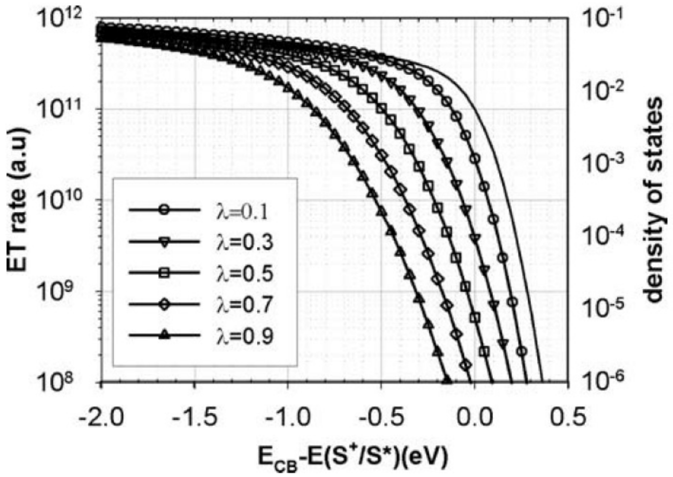

Figure 27: Calculated density of states (*thin line*) and electron transfer rates (*symbols*) to a semiconductor as a function of the driving force at different reorganization energies (Taken from Figure 1 of reference 162).

Therefore, it is only obvious that the electron injection rates will be non-exponential.[164] In the adiabatic limit, the dependence shown in Figure 27 is no longer valid. In such a case where electronic coupling is strong enough that barrierless electron transfer is possible, the injection rate is then limited by the fastest nuclear motion in the system and it no longer depends on the energy of the injecting state.[171] In this limit, injection on a < 100 fs time scale can be expected. Since this time scale is faster than the vibrational relaxation time of the adsorbate, a competition occurs between dye relaxation and electron injection pathways.

Thus, based on this discussion, the wide distribution in the reported electron injection times can be understood. The following section deals with some of such reports for the indisputably most explored **N3** dye (and other dyes as well) with most versatility in its injection rates.

Willig and co-workers reported excited-state electron injection from **N3** into TiO_2 to be occurring in ~ 25 fs in ultrahigh vacuum.[172] The process therefore did not involve redistribution of vibrational excitation energy. The finite injection time ruled out direct excitation of electrons from the Ru^{II}-center into the semiconductor, yet the < 100 fs rise-time told of vibrational wave packet motion-induced electron transfer. The same group further strengthened this conclusion by using a perylene sensitizer where they observed electron transfer from the excited singlet state of the perylene chromophore, with a time constant of 75 fs.[173] The vibrational wave packet generated in the donor state continued its motion for several hundred femtoseconds in the product state of the reaction, the ionized chromophore and this acted as a direct confirmation for electron transfer occurring from a nonrelaxed vibrational populace created by the short laser pulse in the donor. However, the situation was found to be entirely different when sensitized thin films in solvent and/or electrolyte were studied. Under such conditions, electron injection was non-exponential and occurred on the femtosecond to hundreds-of-picoseconds time scale as was observed by Durrant and co-workers for **N3** and porphyrin based sensitizers. For **N3** they found that a sum of three exponentials was required to fit the data and one of these three components was an ultrafast < 100 fs component.[174,175] The same group later found a 30 fold slower charge injection rate for **N719**, *i.e.* the dianion salt of **N3**.[177] The authors washed the sensitized TiO_2 films repeatedly with ethanol and eventually found injection rates similar to that observed for **N3** dye and they suggested that the protons from the carboxylic acid groups of the **N3** dye lowered the conduction band potential and thus faster electron injection rates were observed for **N3** than **N719**. Interestingly, the injection kinetics of **N719** was found to be slower in a full DSSC than in an inert electrolyte by not less than 20 times again.[177,178] This complete DSSC still showed excellent photovoltaic performance.[179] This effect shows that for MLCT excited states having lifetimes of the order of tens to hundreds of nanoseconds, a quantitative injection yield can still be expected even if the injection rate is slowed down drastically. Thus, for this case of **N719** dye, the kinetic redundancy is also less as the injection time is sufficiently less than the excited-state lifetime but not by an unnecessary amount.

Lian and co-workers pre-treated the **N3** sensitized TiO_2 films with aqueous buffer solutions at pH 2, 4, 6, or 8 and after subsequent removal of the weakly bound and desorbed senstitizers, the biphasic kinetics and the injection yields were found to be pH dependent.[180] As the pH was raised from 2 to 8, there was a decrease in the ratio of the faster-to-slower components and the injection yield also decreased in accordance with a Nernstian shift of the conduction band as the pH increased. Grätzel and co-workers argued that the observed heterogeneity in the electron transfer rates could be a result of aggregation of dye molecules on the surface.[181,182] By employing a very low concentration or a lower surface-coverage thin film they obtained a monophasic injection shorter than 20 fs. Piotrowiak and co-workers dialysed a solution of sensitized TiO_2 colloids and they found, using time correlated single photon counting studies, that the excited state lifetime, though multiexponential, was significantly shorter.[183] In a very recent and most interesting study,[184] O'Regan and co-workers studied **N3** and **N719** sensitized mesoporous TiO_2 films immersed in neat solvent or in I^-/I_3^- electrolyte and they observed multiple exponential injection dynamics, ranging from < 300 fs to 0.5 ns. By consecutive but immediate experiments on the **N3** dye, once in neat acetonitrile and once in I^-/I_3^- electrolyte in methoxy propionitrile, they came to the conclusion that no aggregates are ever responsible for any slow injections observed. They also argued that if indeed the slow component was due to injection from aggregate states, then it was an intrinsic characteristic of functional DSSCs. By experiments on **N719** dye, they concluded that the discrepancies in the electron injection times were reflections of conduction band changes mediated by the contribution of protons by the dyes to TiO_2 which in turn was dictated by the choice of solvent – neat, or redox electrolyte in suitable solvent. Subsequently, Grätzel and co-workers reported the interfacial electron injection dynamics of **N3** under photovoltaic operating conditions and have concluded that this component is indeed arising from the ^{3}MLCT states of aggregates or loosely bound forms of the sensitizer molecules.[185] McCusker, Lewis and co-workers studied the dynamics of dyes **N3**, *cis*-$Ru(dcb)_2(CN)_2$ and their osmium analogues on TiO_2 and observed excitation wavelength dependent electron injection dynamics on both the femtosecond and picosecond time scales that they assigned to electron injection from the ^{1}MLCT and the ^{3}MLCT states, respectively.[131] On the picosecond-time scale, ^{3}MLCT components were more pronounced for osmium analogues having larger spin–orbit coupling. For all the compounds discussed, the rate of the slower picosecond component was found to be directly related to the reduction potential of the dye excited state. In another set of study, Sundstrom and co-workers observed a time constant of 30 fs as the sum of two processes taking place simultaneously, namely, nonergodic electron transfer from the initially excited singlet state to the conduction band of TiO_2 and ISC and they obtained rate constants of 1/50 fs^{-1} for electron transfer and 1/75 fs^{-1} for ISC.[161,186] Goodenough and co-workers, on the other hand, ascribed both the components of biphasic injection kinetics to the degree of TiO_2 crystallinity.[187]

Asbury *et al.*, using transient infrared techniques, studied the interfacial electron transfer dynamics of $Ru(dcb)_2(X)_2$ (where $(X)_2$ = $2NCS^-$, $2CN^-$ or dcb).[180] They found that the excited state electron injection was biphasic for all of these. Furthermore, while the rate of the fast component showed no prominent variations within the 200 fs resolution, the rate of the slow component decreased in accordance with the trend in the energies of the dye excited states.

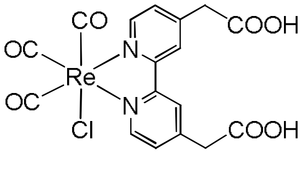

46

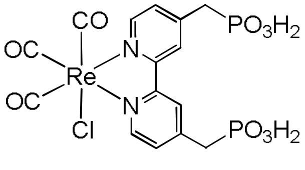

47

Figure 28: Molecular structures of dyes **46** and **47.**

They proposed a two state injection model where the fast (< 100 fs) component was assigned to injection from a nonthermalized excited state and the slow component to injection from the thermalized excited state. The same group studied a series of Re^{I}-polypyridyl complexes. For Re(dcb)CO_3Cl/TiO_2 they observed an ultrafast < 50 fs electron injection that they assigned to that from a vibrationally hot state.[164,188-189] Similar to the earlier discussed example from the same group of chemists, solvent dependent electron injection rates for Re(dcb)CO_3Cl on TiO_2 was also observed which was again explained by considering a proton induced shifting of the conduction band potential.[190] For the same class of molecules they also studied effects of changing the binding group. For such rhenium complexes bound through phosphonic acid linkers (**47**, Figure 28), they found that the injection rate was faster than the corresponding carboxylic acid bound dye **46**.[191]

Contrarily, for organic sensitizers, well-defined singlet and triplet states have been shown to be involved in injection processes since the problem of spin mixing is not as big a problem as for the metal polypyridyl sensitizers discussed above.[64]

1.B.4.B.2. Distance dependence of electron injection

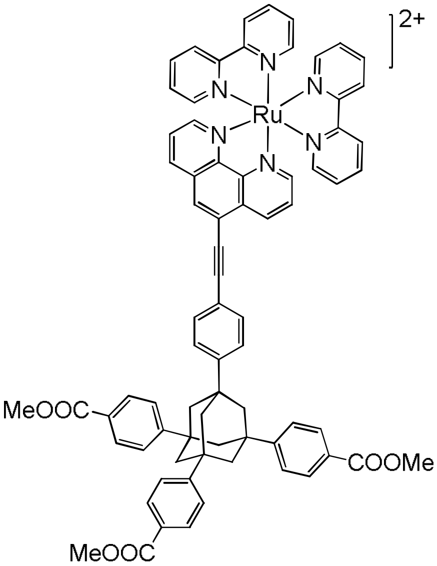

48

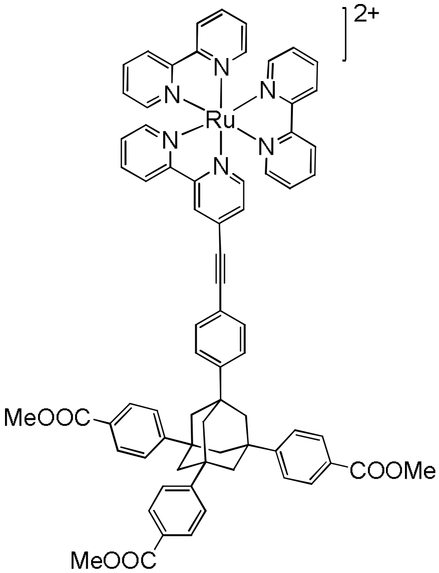

49

Figure 29: Molecular structures of the **48** and **49** studied by Galoppini and co-workers.

For many sensitizers the room temperature injection rates are known to show an exponential dependence on distance following the equation:

$$k = k_o\exp[-\beta x]$$

where β is the dampening factor and k_0 is the extrapolated rate constant for $r = 0$. A dampening factor ~1.0 Å^{-1} often indicates saturated-hydrocarbon, through-bond superexchange tunnelling behaviour.[192-194] Larger values imply at least partial through-space character while smaller ones are associated with tunnelling through conjugated π systems.[195] Such distance dependence of electron injection rate on distance has been demonstrated in dye-sensitized systems by numerous researchers.[196] Meyer and co-workers observed efficient electron injection from Ru^{II}-polypyridyl complexes where the binding carboxylic acid group remained separated from the chromophoric core by saturated methylene linkers.[93] In yet another set of studies by Galoppini and co-workers, it was found that even for Ru^{II}-polypyridyl unit separated from the TiO_2 surface by a 24 Å long linker (Figure 29), sub-picosecond injection rates could be obtained.[197,198] A most systematic study was carried out by Lian and co-workers who studied a series of Re^{I}-

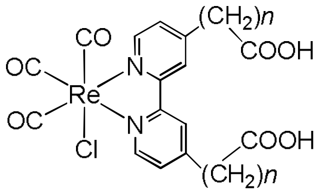

n = 0, 1, 3

Figure 30: Molecular structures of the dyes discussed by Lian and co-workers to study distance dependence of electron injection.

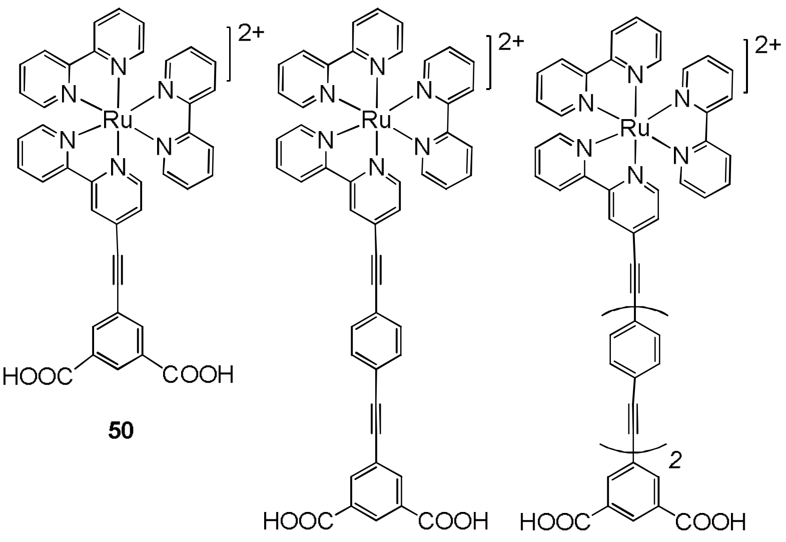

50 **51** **52**

Figure 31: Molecular structures of the rigid-rod Ru-bpy sensitizers **50**, **51** and **52** studied by Galoppini and co-workers.

polypyridyl complexes bound to TiO_2 by carboxylic acid linkers which were separated from the Re^I core unit by saturated methylene linkers of different lengths (Figure 30).[188] They found that in the nonadiabatic limit, the electron injection rate exactly followed the aforesaid exponential dependence on bridge length. However, most interesting was the fact that on introduction of a single methylene spacer between the carboxy and the chromophore unit, the electron transfer rate decreased by > 200 times and they attributed this observation to a transition from the adiabatic limit to a nonadiabatic one. The distance-dependence was investigated by Moser and colleagues who, using the dye $Ru(4'\text{-}PO_3^{2-}\text{-tpy})(NCS)_3$ on TiO_2 coated with alumina of varying thickness, observed dampening factors of $\beta = 0.11$ Å^{-1} and 0.04 Å^{-1} for the fast and slow components, respectively.[200-202] Rigid-rod Ru-bpy sensitizers with linkers made of anoligo(phenyleneethynylene) bridge varying in length were reported by Galoppini and co-workers (Figure 31) who studied the excited state electron injection dynamics to find that a monotonic decrease in injection rate (with $\beta = 0.04$ Å^{-1}) occurred as the number of linkers were increased.[203]

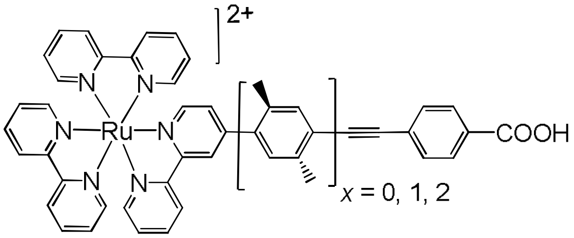

Figure 32: Molecular structures of the dyes studied by Gray and co-workers.

Gray and co-workers studied complexes of the type $Ru^{II}(bpy)_2(bpy\text{-}4\text{-}(xylyl)_x\text{-}\equiv\text{-phenyl-}COOH)(PF_6)_2$ where x = 0, 1 or 2 (Figure 32) and found that the electron injection rates for x = 1 or 2 was only two times slower than that for x = 0 and they argued it to be due

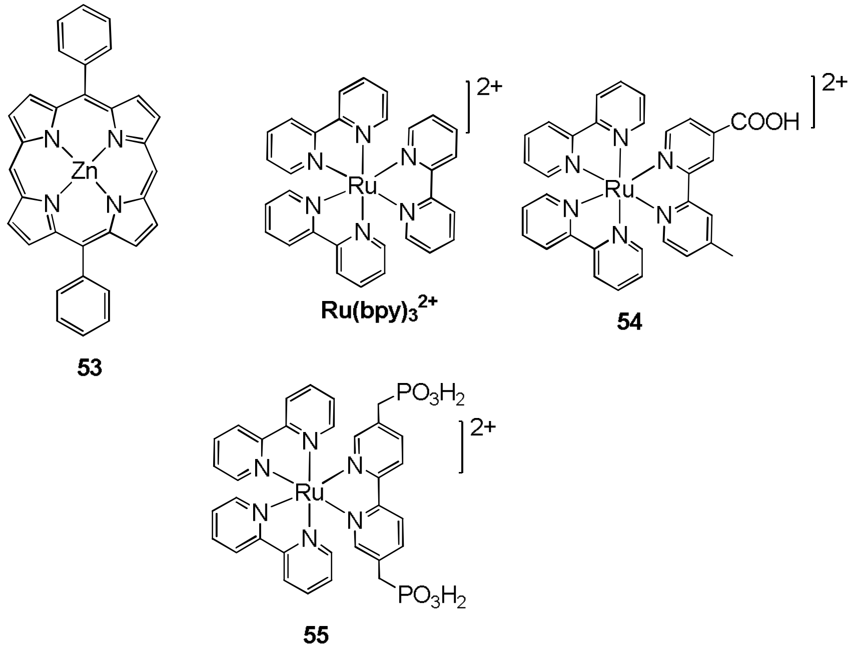

Figure 33: Molecular structures of dyes **53**-**55.**

to the flexible one-carboxyl attachment to the surface resulting in a very similar Ru-TiO_2electron-tunneling distance.[204] Diau and co-workers studied the femtosecond fluorescence dynamics of zinc biphenylporphine dye, **53** (Figure 33) and observed electron injection through space.[205] The same group studied two Ru^{II}-dyes ($Ru(bpy)_3^{2+}$ and **54**, Figure 33) and concluded that in DSSC applications, through space electron transfer processes are also significant and not only the through bond processes.[206] Meyer and co-workers postulated through space electron transfer to explain their observed comparable injection yields for two Ru^{II}-polypyridyl complexes where the binding phosphonate groups are separated from the Ru^{II}-polypyridyl unit by a -CH_2-linker in one of the dyes, **55** (Figure 33).[207] An interesting study in this regard was carried out by Sundström and co-workers where it was seen that in spite of a longer distance of the zinc-porphyrin core from the binding carboxylic unit, the electron injection was faster in **BP** than in **2,4,6-Me** (Figure 34).[208] They argued that a tilted orientation of the porphyrin moiety in **BP**, when bound to TiO_2, was the reason which decreased the edge-to-edge distance on the surface thus facilitating through space electron injection. TEM images of the sensitized and the bare nanoparticles provided good evidence of a tilted mode of binding.

For some sensitizers, efficient electron injection has also been seen to take place from the *thexi* state containing an electron localized on a ligand that was not bound to the TiO_2 surface, a phenomenon referred to as '*remote injection*'. Such remote injection has been demonstrated with surface bound 4-carboxypyridine ligands for Ru^{II}-, Re^{I}-polypyridyl complexes and with 3,4-dicarboxypyridine ligands for porphyrinic sensitizers.[209-211] An excellent example is the molecule **56** studied (Figure 35) by Argazzi *et al.*[212] The transient absorption difference spectra for this sensitizer on TiO_2 showed a broad bleach in the 400 to 600 nm region, expected for the formation of $TiO_2(e^-)$–Re^I–Ru^{III} state. In all probability, the prompt formation of this state indicated that remote electron injection into TiO_2 took place. An extremely high light-to-electrical energy conversion was reported even though the sensitizer was remote to the semiconductor-bound ligand.

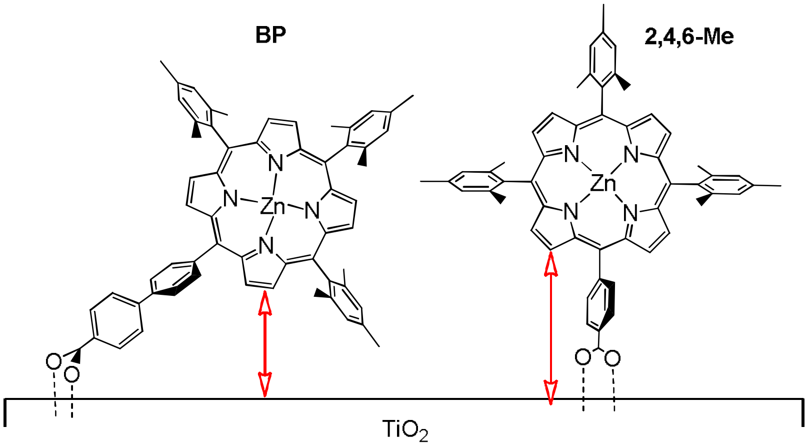

Figure 34: Binding orientations of **BP** and **2,4,6-Me** dyes on TiO_2.

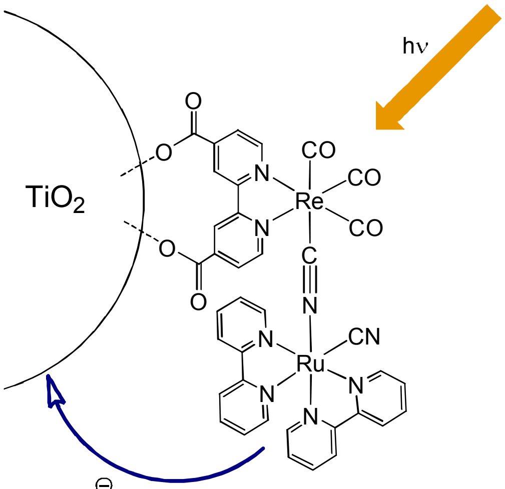

56

Figure 35: An example of *remote injection.*

1.B.4.B.3. Can '*hot*' injection be harvested?

Considering the well established fact that interfacial electron injection from the excited states of surface bound sensitizers can occur faster than the dye relaxation times raises the obvious question that whether this '*hot*' injection is indeed of any use or not. There are enough evidences to show that the electrons injected into the TiO_2 nanoparticles are trapped within picoseconds.[213] Hot injection can be useful only if the injected electrons are collected before these trapping events. This might lead us to power conversion efficiencies exceeding the single junction Shockley–Queisser limit of 31%. However, it is as well known that the electronic wave-packet representing the hot electron expands throughout the film and that elastic and inelastic scattering events alter the momentum and the electronic and vibrational energy, a process known as wave packet dephasing.[172,173,214] This means that electron transfer to a point contact is almost impossible and it is only the cold state that reaches the semiconductor-electrode interface for collection or reactivity. So, the excess energy of the hot electrons are most likely lost to phonon creation. However, hot injection can be useful in the sense that the surplus vibronic energy of the photo-excited sensitizer molecule is dispelled quickly into the semiconductor particle, thus preventing parallel destructive side reactions which might influence the long-term stability of the system.[161] Indeed, solar energy conversion in dye-sensitized devices is reported in some cases to be more efficient when operating in this aforesaid nonergodic limit.[215] This topic, however, remains highly debatable till date.

1.B.4.B.4. MPCT and reduced sensitizer injection

For metal cyano compounds attached to TiO_2, *e.g.* $M(CN)_x^{n+}$, where M = Fe, Ru, Os, Re, Mo, W, the electron injection mechanism has been termed as metal-to-particle charge transfer (MPCT) where a new absorption band is formed that was not present in fluid solution and excitation into this CT absorption band results in immediate formation of

$TiO_2(e^-)/S^+$ such that light absorption and electron transfer to TiO_2 are one in the same process.[64,216,217] Some organic compounds *e.g.* catechol,[218] resorcinol,[219] *etc.* are also known to give rise to intense CT bands upon binding to TiO_2. Such CT interactions are also reported for Os^{II}-polypyridyl complexes[220] and a Re^{I}-polypyridyl complex[221] attached to TiO_2 by catecholate linkage (*vide infra*). However, an exact discrimination between excited state injection and CT injection, as made by many researchers, might often be erroneous and these two processes might be indeed operating simultaneously depending upon the strength of electronic coupling of the dye to TiO_2.

Another notable electron injection mechanism is what is known as '*reduced sensitizer injection*' wherein electron injection takes place after the sensitizer dye is reduced and so injection takes place from the non-excited dye. This sensitization method is called '*supersensitization*'.[64,222] DSSCs operating in this mechanism are actually regenerative galvanic cells since injection is dark and thermodynamically favourable. This mechanism is very useful for those dyes that are not stable in their oxidized forms. Also, the reduced sensitizer is a powerful reductant, by about 200 to 400 mV than the MLCT excited states and this makes them all the more useful. The work by Kleverlaan *et al.* involving the bimetallic sensitizer **57** on TiO_2 is an excellent example of reduced sensitizer injection (Figure 36).[223] The MLCT excited state of the ruthenium chromophore transferred electrons to the $Rh(dcb)_2$ group to form a $(bpy)_2Ru^{III}$–BL–$Rh^{II}(dcb)_2/TiO_2$ charge-separated state (BL = 1,2-bis[4-(4'-methylbpy)]ethane), 40% of which injected electrons into TiO_2 to form $(bpy)_2Ru^{III}$–BL–$Rh^{III}(dcb)_2/TiO_2(e^-)$, and the remaining underwent back electron transfer to form the ground-state products. One third of the excited Ru^{II} chromophore injected electrons directly into TiO_2 and the ratio of this direct injection to the electron transfer to rhodium centre was proposed to result from differences in surface orientations.

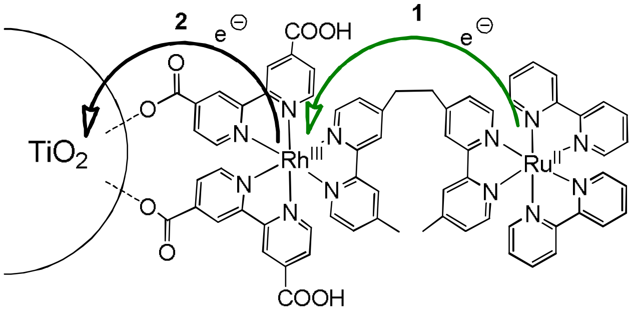

57

Figure 36: Reduced sensitizer injection in **57.**

1.B.4.C. Sensitizer regeneration and charge recombination

That the charge recombination of the $TiO_2(e^-)$ and the oxidized sensitizers occurred in tens-to hundres-of-microseconds time scale was proved in many early studies with Ru^{II}- and organic sensitizers.[224,225] Also, even with compounds having very short excited state lifetimes, *e.g.* $[cis\text{-}Ru(dcb)_2(H_2O)_2]^{2+}$, efficient sensitization could be attained.[25] This suggested extremely fast sub-nanosecond electron injection times. This orders of magnitude difference in the electron injection and the charge recombination times in metal polypyridyl complexes was attributed to the two altogether different sets of orbitals involved in these two processes. While injection occurred from the π* orbitals of the surface bound ligand which have an extensive overlap with TiO_2 density of states, recombination occurred predominantly to further contracted t_{2g} orbitals of the Ru^{III} metal centre. Thus, there is a built in rectification for compounds featuring injection through MLCT excited states.[168]

The observed slow rate of the charge recombination reaction had been a subject of debate for long. Meyer and Fitzmaurice argued that the observed slowness occurred as a result of non-geminate recombination of the $TiO_2(e^-)$ with the oxidised sensitizer.[137,226] They observed that varying the concentration of the charge separated states, *i.e.* $Ru^{III}/TiO_2(e^-)$, by over a factor of ten resulted in the same second-order rate constant. A single second-order rate constant could fit the first few microseconds of recombination, while a sum of two rate constants, *i.e.* a bi-second order kinetic model could fit the entire data. A possible distribution of second-order rate constants was also suggested to be possible. This observation suggested an efficient separation of the $TiO_2(e^-)$ from S^+ thus leading to isolated $TiO_2(e^-)$s and oxidized sensitizers. Further, actinometry measurements showed that every injected electron recombined by the second-order mechanism.[227] Following this, Jenny Nelson proposed a model where she said that the electrons became trapped in localized states in TiO_2 and the charge transport kinetics are dominated by the time constants for release from these states.[169,170] Rate limited by this step, the transient phenomena are called '*dispersive*'. A CTRW model developed initially by Scher and Montroll for diffusive movement of charge carriers on a lattice, was thus developed.[228,229] Tachiya and co-workers later extended this model to propose '*random flight multiple trapping model*' which included an equal possibility of trapping of the detrapped electron by any empty surface trap site within the nanoparticle, unlike the previous CTRW model where the destination site is one of the randomly chosen unoccupied nearest neighbour.[230] Bisquert proposed a hopping model where electron transport instead occurred by direct transfer between localized states lying just below the conduction band edge.[231]

The multiple-trapping, nearest-neighbour CTRW model proposed by Nelson remains the one that models most of the charge recombination data reported best.

The charge recombination reaction is seen to lie in the inverted Marcus region, in the majority of cases, as initially proved by Moser and Grätzel.[225] However, this observation is not unanimous.

Meyer and co-workers found the charge recombination kinetics for a family of MLCT sensitizers based on osmium, ruthenium and rhenium, to be insensitive to ~ 960 mV change in the apparent driving force, the molecular geometry, the nature of the metal center employed, *i.e.* Re, Ru, or Os and the number of carboxylic acid groups present, *i.e.* two or four and explained their observation by suggesting diffusion limited encounters of $TiO_2(e^-)$ with the oxidized sensitizer or to be due to lack of change in the apparent driving force for the recombination reaction due to concerted E_{cb} and ground-state E^o

shifts.[137] On the other hand, Lewis and co-workers could fit the charge recombination kinetics of five Ru^{III}/Os^{III} compounds to the same equal-concentration, bi-second-order recombination model and using the weighted average of the second-order rate constants together with semiclassical Marcus theory, charge recombination to the oxidized sensitizers, including $\mathbf{N3}^+/TiO_2$, was seen to fall in the Marcus inverted region with a total reorganization energy, $\lambda \sim 1.0$ eV.[227] The authors argued that nuclear tunnelling was negligible and that solvent reorganization and low-frequency, metal–ligand vibrational modes assisted the recombination reaction, rather than high-frequency, ligand-based vibrational modes. Durrant and co-workers studied a set of eight different sensitizers whose ground state redox potentials varied by 500 mV and they could fit their data to a multiple-trapping, nearest neighbour CTRW kinetic model by using the Kohlrausch-William-Watts (KWW) function (*vide supra*).[232] The driving-force dependence was quantified based on $t_{1/2}$ and it was seen that the data was insensitive to variations in $E^o(Ru^{III/II})$ indicating the charge recombination reaction to be lying near the peak of the Marcus free energy curve, $\Delta G^o \sim \lambda$, and with $\lambda \sim 0.8$ eV. The authors came to the conclusion that charge recombination to $\mathbf{N3}^+$, and other similar sensitizers, was nearly activationless. Hupp and co-workers investigated a series of phosphonated ruthenium bipyridyl complexes having different ground state redox potentials.[233] The recombination kinetics was consistent with Marcus normal region behaviour, *i.e.* thermally activated electron transfer with rate constants increasing with increasing driving force. The authors attributed this behaviour to a sequential electron and proton transfer process. It was proposed that the rate-limiting step, the BET, did not release all of the free energy in the overall reaction, and thus the variation in driving force for this step was dependent only on the changes in $E^o(Ru^{III/II})$. Since this E^o differed only slightly with pH, only a small deviation in driving force was actually observed.

The apparent contradictory conclusion of driving force independent charge recombination rates in the inverted region and as well close to the top of the curve was described by Meyer and co-workers to be arising perhaps due to differences in "details of the preparation of the TiO_2 thin films, surface chemistry such as $TiCl_4$ pre-treatments and species present in the electrolyte".[64]

Contrarily, the observations in aqueous colloidal solutions are much clearer. Hupp and co-workers monitored charge recombination in a set of $Fe(CN)_5(L)^{n-}$ sensitizers bound to colloidal TiO_2 at pH 2.[234] The recombination kinetics was seen to be biphasic; a fast first-order component was observed which varied with $E^o(Fe^{III/II})$ as expected in the Marcus inverted region.

1.B.4.C.1. Intramolecular sensitizer regeneration

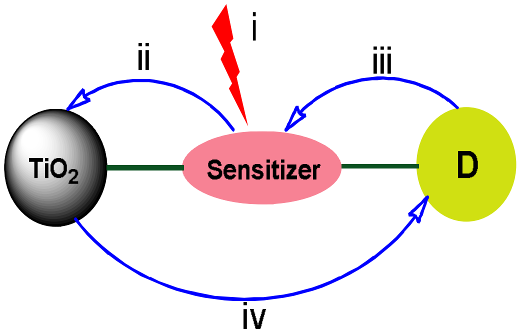

Figure 37: Steps in intramolecular sensitizer regeneration - (i) Visible light excitation, (ii) Electron injection following excitation, (iii) Secondary electron transfer from the electron donor group (D) appended and (iv) Charge recombination.

Such intramolecular regeneration reactions translate the hole created at the dye upon charge injection away from the sensitizer core and thus away from the TiO_2 surface (Figure 37). As a result of an increased charge separation, the charge recombination reaction is expected to be slowed down.

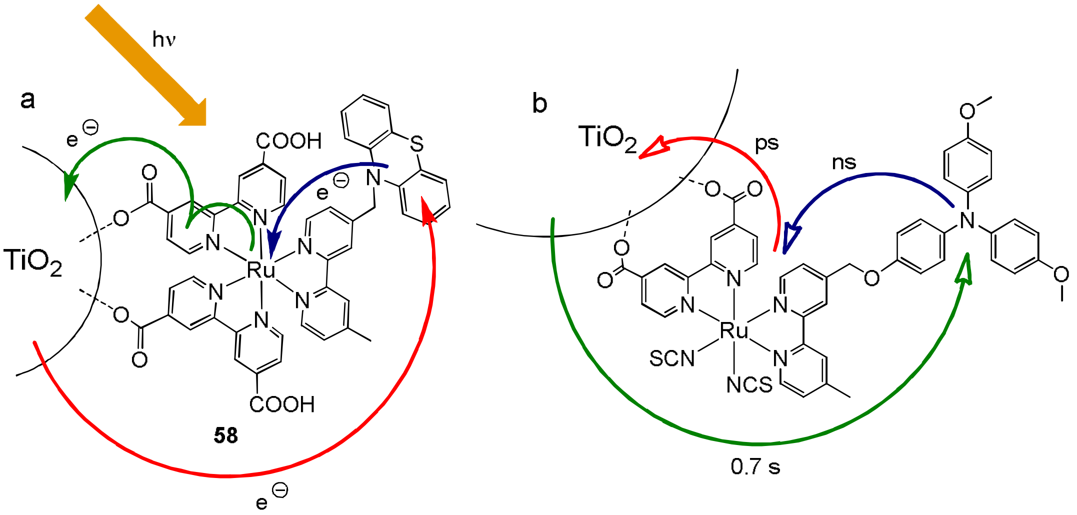

Figure 38: Secondary electron donation to Ru^{III} centre formed after electron injection into TiO_2 in (a) **58** and (b) **N845.**

Meyer and Bignozzi studied the dyad $[\mathrm{Ru(4\text{-}CH_3,4'\text{-}CH_2\text{-}PTZbpy)(dcb)_2}]^{2+}$, **58**, and observed that MLCT excitation resulted in a charge-separated state with an electron in TiO_2 and an oxidized PTZ, abbreviated $\mathrm{PTZ^{+}\text{-}Ru^{II}/TiO_2(e^{-})}$ (Figure 38).[235,236] The charge recombination was observed to be three orders of magnitude slower for the aforesaid case as compared to the molecule where no phenothiazine donors were present.

Triarylamine moiety perhaps remains the most widely studied secondary electron donor moiety. Nazeeruddin and colleagues covalently attached ether-NAr_3 donor group to a dimethyl bipyridine ligand in the ruthenium complex to result in the dye coded **N845** shown in Figure 38b and they observed the half life of the charge separated state to be over half a second.[237] In further extension of this study, Haque, Durrant and colleagues prepared ruthenium complexes having one triphenylamine group (NPh_3) (**59**), two NPh_3 groups (**60**) or a poly(vinyl-NPh_3) group of about 100 units (**61**) (Figure 39).[123] They observed that introduction of 100 triarylamine units increased the half life

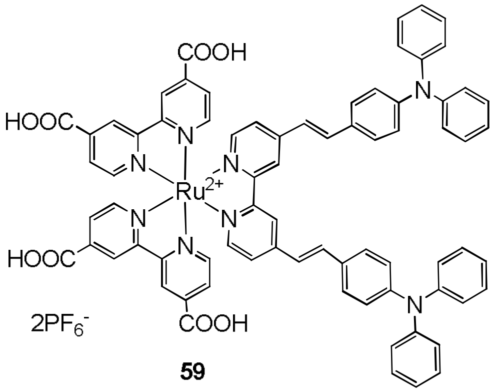
COOH
HOOC
HOOC
COOH
Ru2+
2PF6-

59

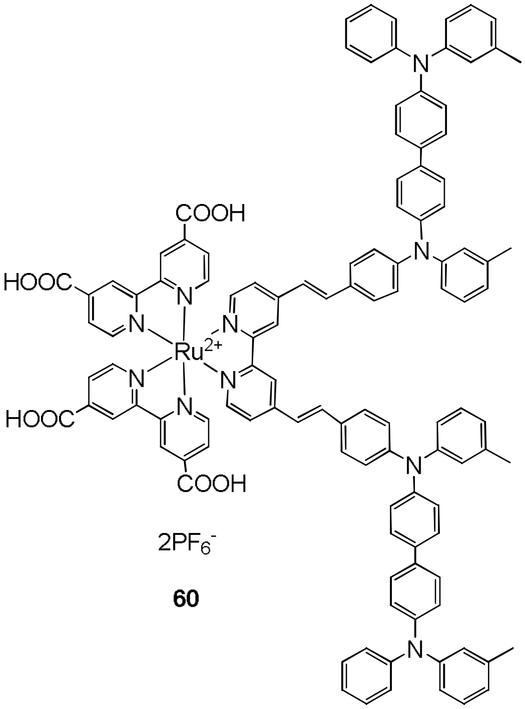
COOH
HOOC
HOOC
COOH
Ru2+
2PF6-

60

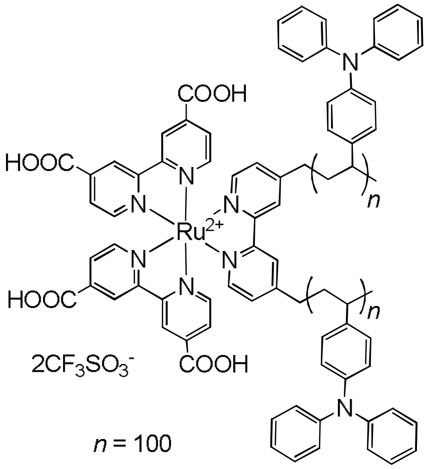
COOH
HOOC
HOOC
COOH
Ru2+
n
n
2CF3SO3-
n = 100

61

Figure 39: Molecular structures of dyes **59**, **60** and **61** synthesized by Haque, Durrant and colleagues.

of the charge separated state to 4 seconds as compared to 350 ms and 5 ms half life for the complexes with one and two NPh_3 groups, respectively.

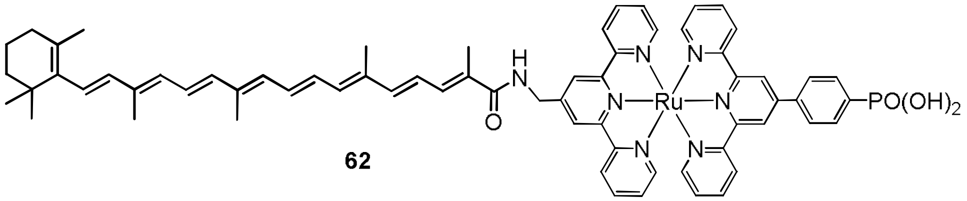
H
N
O
Ru
PO(OH)2

62

Figure 40: Chemical structure of dye **62.**

Wolpher *et al.* studied sensitizer **62** where they attached an all-trans-8′-apo-β-carotenoid secondary electron donor moiety to the ruthenium terpyridyl sensitizer unit (Figure 40) and they observed increased charge separation because of intramolecular sensitizer regeneration.[238]

Transition metal complex donors have also been used for such intramolecular regeneration reactions. An example is the work done by Meyer and colleagues where they synthesized the dyad **63.**[239] Excitation of **63**/TiO_2 thin film resulted in electron injection ($Ru^{II}* + TiO_2 \rightarrow Ru^{III} + TiO_2(e^-)$) and intramolecular hole transfer (Os^{II}–bpa–

Ru^{III} → Os^{III}–bpa–Ru^{II} , bpa = 1,2-bis(4-pyridyl)ethane) to ultimately form a charge separated state (Os^{III}–bpa–Ru/$TiO_2(e^-)$) (Figure 41).

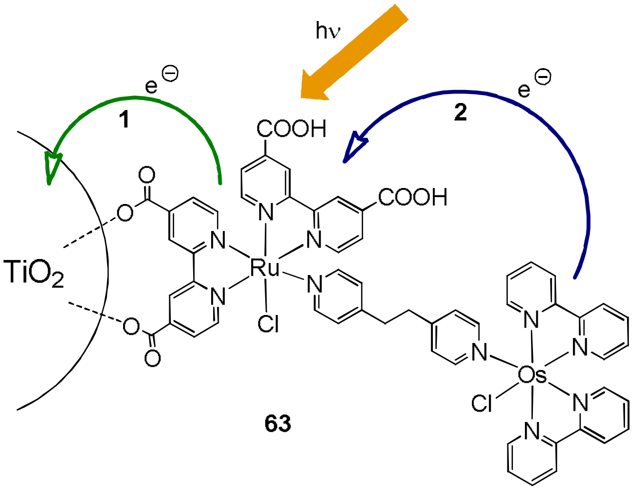

Figure 41: Intramolecular regeneration in dye **63** containing an osmium polypyridyl unit as the secondary electron donor.

In this regard it should be pointed out that **N3** dye is also reported to exhibit such intramolecular charge regeneration effects on TiO_2.[240] This is based on the facts that DFT calculations for **N3**$^+$ show appreciable hole density on the isothiocyanate ligands. Therefore, there is probably some hole transfer from Ru^{III} to the isothiocyanate ligands in **N3** sensitized TiO_2 systems. Electrochemical measurements where two close oxidations are seen, corresponding to the metal centre and to the isothiocyanate ligands, seem to corroborate this hypothesis.

1.B.4.C.2. Distance dependence of charge recombination

Similar to the dependence of the charge injection rates, the charge recombination rates have been reported to be distance dependent as well. For the dyes shown in Figure 39, studied by Durrant and colleagues, the BET rate constants were seen to have an exponential dependence on distance with dampening factor, $\beta = 0.95 \pm 0.2$ Å^{-1}.[64,123] There are numerous other examples of this effect in the literature.[64]

The $Ru^{II}(bpy)_2(bpy\text{-}4\text{-}(xylyl)_x\text{-}\equiv\text{-phenyl-COOH})(PF_6)_2$ complexes shown in Figure 32, however, stand out different.[204] As was observed with electron injection, the BET rates were also observed to be within experimental error of one another for x = 0, 1 or 2 and again variable Ru–TiO_2 distances arising because of the flexibility of the linker groups was argued to be the reason.

1.B.4.D. The interfacial electron transfer dynamics of catechol bound metal polypyridyl dyes

A major portion of this thesis discusses enediol bound systems and so a review of the most widely studied catechol based metal polypyridyl sensitizers is essential. As discussed before, catechol as an anchoring group came to be explored because of the pH lability of the carboxylate linkage.[29,95] Though there are a few reports from other groups as well on the use of such binding moieties for binding of such sensitizers to TiO_2,[138] the interfacial electron transfer dynamics have almost exclusively been studied by the group of Ghosh, Das and co-workers.

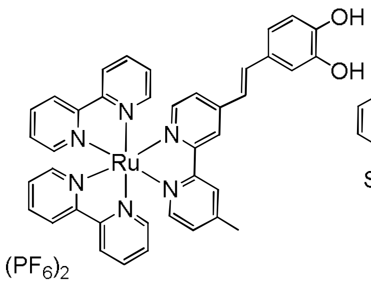

64

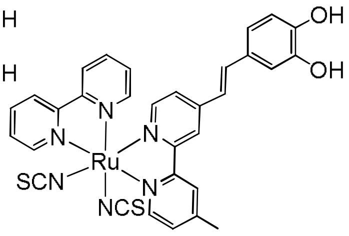

65

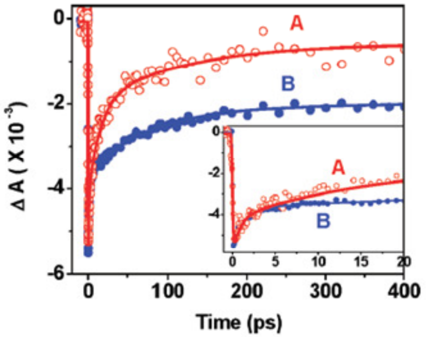

Figure 42: Molecular structures of dyes **64** and **65**. Also shown is the recovery of the ground state bleach (Taken from Figure 5, reference 241) monitored at 480 nm for (A) **65**-TiO_2 and (B) **64**-TiO_2 systems.

Using femtosecond transient absorption spectroscopy, the interfacial electron transfer dynamics of **64** was studied on TiO_2 and monophasic < 100 fs electron injection time was observed which was argued to be associated with hot ^{1}MLCT and/or ^{3}MLCT states.[94] BET was however observed to be very fast with only 37% residuals after 400 ps (Figure 42). Ward and co-workers had studied two catechol based Ru^{II}-terpyridine dyes and had observed very less photon to current conversion efficiencies.[95] They hypothesized probable aggregation of the dye on TiO_2 surface to be one of the probable reasons. The aforesaid study by Ghosh, Das and co-workers suggested fast BET of such catecholate bound dyes instead to be the reason for this observed low efficiency.

They further extended their studies and prepared a compound (**65**, Figure 42) analogous to the classical **N3** dye.[241] Though they observed a much broader absorption spectrum compared to the parent complex **64**, the potential of the S_0 state shifted by 300 mV towards negative. As a result of this, the deleterious BET reaction, which lies in the Marcus inverted region, became faster instead.

The group also studied compounds **66** and **67** and observed a distinct CT emission band for **67** on TiO_2 and assigned the observed photoluminescence to radiative CT recombination (Figure 43).[220] They further employed time correlated single photon counting techniques to determine the BET rates.

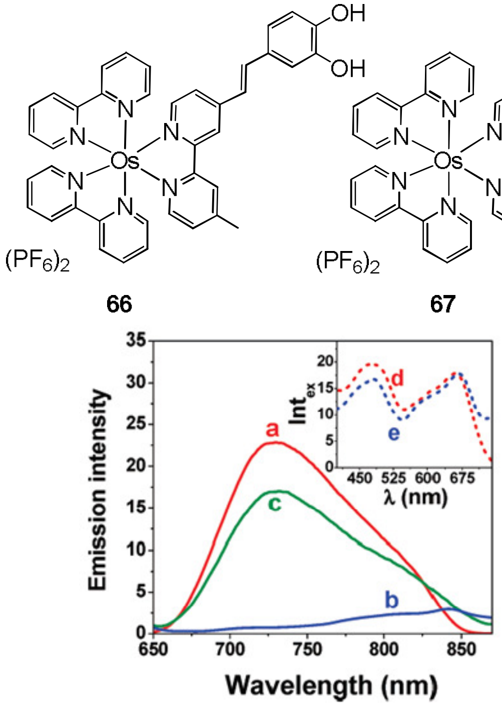

Figure 43: Molecular structures of dyes **66** and **67** and the recombination luminescence at 844 nm (spectrum b) for **67** on TiO_2. (a – **67** in water, c – **67**-ZrO_2; Inset – Excitation spectra for **67** in water at λ_{mon} = 730 nm (d) and **67**-TiO_2 in water at λ_{mon} = 844 nm (Taken from Figure 4, reference 220).

A distinct CT absorption band was observed for the dye **68** on TiO_2.[221] The recombination was found to be multiexponential and fitted with τ_1 = 0.5 ps (-30.8%), τ_2 = 4 ps (-19.7%), τ_3 = 100 (-26.5%) and τ_4 > 1 ns (-22.8%) at 900 nm. The ultrafast 500 fs

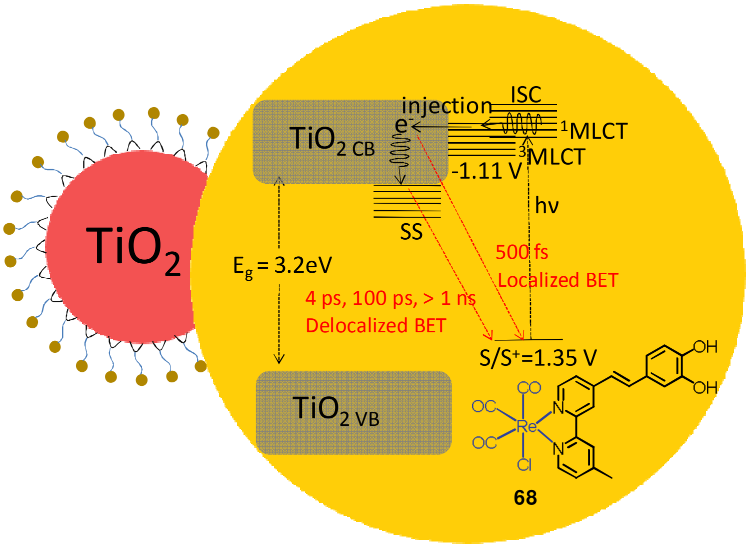
TiO2
TiO2 CB
TiO2 VB
injection
ISC
e⁻
¹MLCT
³MLCT
-1.11 V
hν
SS
Eg = 3.2eV
500 fs
Localized BET
4 ps, 100 ps, > 1 ns
Delocalized BET
S/S⁺=1.35 V
OH
OH
OC
OC
CO
Re
Cl
N
N
68

Figure 44: A Jablonski type diagram for the different electron transfer processes occurring in **68**-TiO_2 system.

component was assigned to electron recombination before delocalization into TiO_2 (Figure 44). The remaining components were argued to be arising due to recombination after this aforesaid delocalization of the injected electrons into the TiO_2 nanocrystal.

In yet another study, a new tetracyanato ruthenium(II)- polypyridyl complex, **69**, with pendant catechol moiety was synthesized and strong luminescence quenching was observed on TiO_2.[242] DFT calculations revealed that the excited state was localized selectively on the catechol based ligand and not on the cyano groups (Figure 45). Electron injection time was again observed to be pulse width limited (< 100 fs). The molecule showed solvatochromic behaviour in solution. However, the electron transfer dynamics were found not to be dependent on the solvent. Binding through the catechol linker was argued to be the probable reason for this observation.

In an effort to probe whether strong coupling, as mediated by catecholate mode of binding, always leads to ultrafast injection or not, femtosecond transient absorption spectroscopic studies of dyes and **67** and **70** were carried out and electron injection for the osmium dye **67** was found to be biphasic with time constants of τ_1 < 100 fs (42%) and τ_2 = 1.7 ps (58%) (Figure 46).[243] The pulse width limited component was attributed to injection from the hot ^{1}MLCT/^{3}MLCT states while the slower component was assigned to injection from the thermalized ^{3}MLCT states. The higher spin-orbit coupling in case of the osmium complex was argued to be the reason for the observed absence of the slower component in case of the corresponding ruthenium complex **70**.

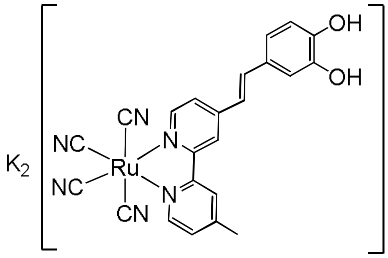

69

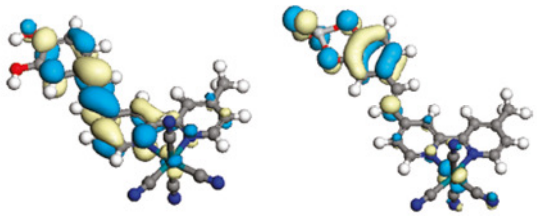

LUMO (**69**)   LUMO (**69**-TiO_2)

Figure 45: Molecular structure of dye **69** and GGA/PW91/DND calculated LUMO coefficients (Taken from Figure 4, reference 242).

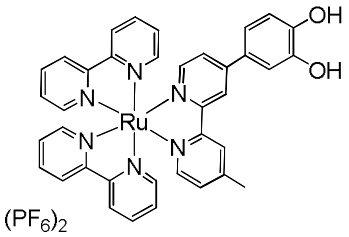

70

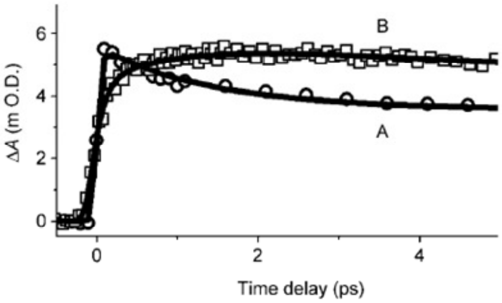

Figure 46: Molecular structure of dye **70** and biphasic electron injection (monitored at 1000 nm) observed for **67**-TiO_2 (B) but not for **70**-TiO_2 (A). (Taken from Figure 6, reference 243).

In all of the examples discussed so far, the BET rate remained appreciable and was justifiably foreseen to be the biggest hurdle towards practical development

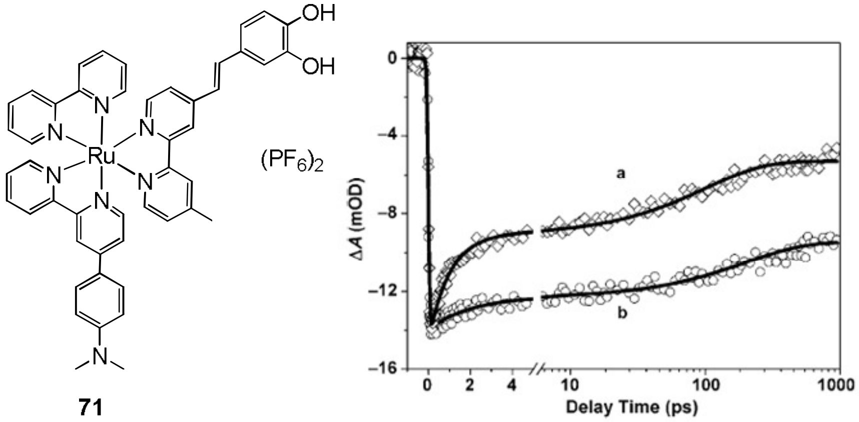

Figure 47: Molecular structure of dye **71**. Also shown is a comparison of the recovery of the ground state bleach for **64**- (a) and **71**-TiO_2 (b) systems at 480 nm. (Taken from Figure 6, reference 244).

and usage of such catecholate bound dyes. In an effort to supersede this deleterious process, dye **71** was designed.[244] Again a pulse-width-limited (< 100 fs) electron injection was observed to be occurring from the LLCT and the MLCT states. Interestingly, after electron injection, the hole was transferred to the electron-donor ligand which resulted in an increased spatial charge separation between the hole residing at the electron-donor ligand and the electrons in the TiO_2 nanoparticles. A slower BET was observed to be the effect (Figure 47).

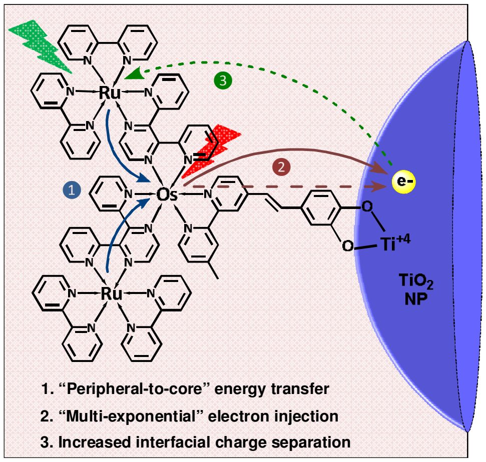
Ru
Os
Ru
N
③
②
①
e-
O
O
Ti+4
TiO2
NP
1. "Peripheral-to-core" energy transfer
2. "Multi-exponential" electron injection
3. Increased interfacial charge separation

Figure 48: Sequential energy transfer and hole delocalization in molecule **72** on TiO_2 surface. (Figure taken from reference 245).

In another report, the group discussed the development of a trinuclear Ru_2Os complex, **68**, and observed an efficient excitation energy transfer from the terminal (Ru^{II} complex) to the core (Os^{II} complex) region in an ultrafast time domain (Figure 48). This excitation energy transfer resulted in a multiexponential electron injection into TiO_2.[245] In addition, the BET rate was found to be slower and delocalization of the hole in the trinuclear complex radical cation was argued to be the reason.

1.C. Scope of the present thesis: An afterword

It is this deleterious BET reaction in such ene-diol bound TiO_2 systems that acts as a major pathway for the loss of conduction band electrons. Thus, this BET of catecholate bound dye-TiO_2 systems has to be retarded by suitable means. Also, alternative anchoring groups need to be explored that would desist surface de-chelation till significantly higher pH and at the same time elicit optimal interfacial electron transfer rates.

This review on the different aspects of dye-sensitized solar cells is an effort expected to justify the need to compel a molecular-level understanding of the underlying mechanisms for charge separation and recombination at sensitized semiconductor interfaces without which optimal light-to-electrical power conversion will be difficult to obtain. The presentiment of Hagfeldt and co-workers when they said, “A challenging but realizable goal for the present DSSC technology is to achieve efficiencies above 15%” bore fruits when Grätzel and co-workers obtained 15% efficiency in a perovskite based solar cell architecture. So, while it is true that there are enough fundamental questions yet to be answered, namely, what is the injection time required for high injection yields?, what is the exact mechanism of electron transport?, *etc*.; these apparent encumbrances should not deter us from putting our best efforts.

The present thesis is a small addition in this direction.

1.D. References

1. *International Energy Outlook 2008*, Energy Information Administration, **2008**, http://www.eia.doe.gov/oiaf/ieo/index.html.

2. Hoffmann, W. *Sol. Energy Mater. Sol. Cells*, **2006**, *90*, 3285.

3. Goncalves, L. M.; Bermudez, V. de Z.; Ribeiroa, H. A.; Mendes, A. M. *Energy Environ. Sci.*, **2008**, *1*, 655.

4. Smil, V. *Energy: A Beginner's Guide*, One World Publishers, Oxford, **2006**.

5. http://gcep.stanford.edu/research/exergycharts.html

6. Chapin, D.; Fuller, C.; Pearson, G. *J. Appl. Phys.*, **1954**, *25*, 676.

7. Goetzberger, A.; Luther, J.; Willeke, G. *Sol. Energy Mater. Sol. Cells*, **2002**, *74*, 1.

8. Zhao, J.; Wang, A.; Green, M.; Ferrazza, F. *Appl. Phys. Lett.*, **1998**, *73*, 1991.

9. Carlson, D.; Wronski, C. *Appl. Phys. Lett.*, **1976**, *28*, 671.

10. Staebler, D.; Wronski, C. *Appl. Phys. Lett.*, **1977**, *31*, 292.

11. Cusano, D. *Solid-State Electron.*, **1963**, *6*, 217.

12. Green, M.; Emery, K.; Hishikawa, Y.; Warta, W. *Prog. Photovoltaics Res. Appl.*, **2008**, *16*, 435.

13. Dimmler, B.; Schock, H. *Prog. Photovoltaics Res. Appl.*, **1996**, *4*, 425.

14. Shockley, W.; Queisser, H. J. *J. Appl. Phys.*, **1961**, *32*, 510.

15. Ma, W.; Yang, C.; Gong, X.; Lee, K.; Heeger, A. *Adv. Funct. Mater.,* **2005**, *15*, 1617.

16. Kim, J.; Lee, K.; Coates, N.; Moses, D.; Nguyen, T.; Dante, M.; Heeger, A. *Science*, **2007**, *317*, 222.

17. Ip, A. H.; Thon, S. M.; Hoogland, S.; Voznyy, O.; Zhitomirsky, D.; Debnath, R.; Levina, L.; Rollny, L. R.; Carey, G. H.; Fischer, A.; Kemp, K. I.; Kramer, J.; Ning, Z.; Labelle, A. J.; Chou, K. W.; Amassian, A.; Sargent, E. H. *Nature Nanotech.,* **2012***, 7,* 577.

18. Nazeeruddin, M. K.; De Angelis, F.; Fantacci, S.; Selloni, A.; Viscardi, G.; Liska, P.; Ito, S.; Takeru, B.; Grätzel, M. *J. Am. Chem. Soc.,* **2005**, *127*, 16835.

19. Yella, A.; Lee, H.-W.; Tsao, H. N.; Yi, C.; Chandiran, A. K.; Nazeeruddin, M. K.; Diau, E. W.-G.; Yeh, C.-Y.; Zakeeruddin, S. M.; Grätzel, M. *Science*,**2011**, *334*, 629.

20. Burschka, J.; Pellet, N.; Moon, S.-J.; Humphry-Baker, R.; Gao, P.; Nazeeruddin, M. K.; Grätzel, M. *Nature,* **2013**, doi:10.1038/nature12340.

21. Tributsch, H. *Photochem. Photobiol.*, **1972**, *16*, 261.

22. Fujishima, A.; Honda, K. *Nature,* **1972**, *238*, 37.

23. Tsubomura, H.; Matsumura, M.; Nomura, Y.; Amamiya, T. *Nature*, **1976**, *261*, 402.

24. Desilvestro, J.; Grätzel, M.; Kavan, L.; Moser, J.; Augustynski, J. *J. Am. Chem. Soc.*, **1985**, *107*, 2988.

25. Liska, P.; Vlachopoulos, N.; Nazeeruddin, M.; Comte, P.; Grätzel, M. *J. Am. Chem. Soc.*, **1988**, *110*, 3686.

26. Vlachopoulos, N.; Liska, P.; Augustynski, J.; Gr ätzel, M. *J. Am. Chem. Soc.*, **1988**, *110*, 1216.

27. O'Regan, B.; Gra¨tzel, M. *Nature*, **1991**, *353*, 737.

28. Hagfeldt, A.; Boschloo, G.; Sun, L.; Kloo, L.; Pettersson, H. *Chem. Rev.,* **2010,** *110,* 6595.

29. Kalyanasundaram, K.; Grätzel M. *Coord. Chem. Rev.,* **1998**, *77*, 347.

30. Park, N.; Lagemaat, J.; Frank, A. *J. Phys. Chem. B*, **2000**, *104*, 8989.

31. Jose, R.; Thavasi, V.; Ramakrishna, S. *J. Am. Ceram. Soc.*, **2009**, *92*, 289.

32. Bisquert, J. *Phys. Chem. Chem. Phys.*, **2008**, *10*, 49.

33. Jose, R.; Zhanpeisov, N. U.; Fukumura, H.; Baba, Y.; Ishikawa, M. *J. Am. Ceram. Soc.*, **2006**, *128*, 629.

34. Benkstein, K. D.; Kopidakis, N.; van de Lagemaat, J.; Frank, A. J. *J. Phys. Chem. B*, **2003**, *107*, 7759.

35. Schwarzburg, K.; Wiliig, F. *Appl. Phys. Lett.*, **1991**, *58*, 2520.

36. Konenkamp, R.; Henninger, R.; Hoyer, P. *J. Phys. Chem.*, **1993**, *97*, 7328.

37. Solbrand, A.; Keis, K.; Sodergren, S.; Lindstrom, H.; Lindquist, S. E.; Hagfeldt, A. *Sol. Energy Mater. Sol. Cells*, **2000**, *60*,181.

38. Saito, M.; Fujihara, S. *Energy Environ. Sci.,* **2008**, *1*, 280.

39. Chou, T. P.; Zhang, Q.; Cao, G. *J. Phys. Chem. C,* **2007**, *111*, 18804.

40. Keis, K.; Lindgren, J.; Lindquist, S.-E.; Hagfeldt, A. Langmuir, **2000**, *15*, 4688.

41. Ou, J.; Rani, Z. R. A.; Ham, M.-H.; Field, M. R.; Zhang, Y.; Zheng, H.; Reece, P.; Zhuiykov, S.; Sriram, S.; Bhaskaran, M.; Kaner, R. B.; Kalantar-zadeh, K. *ACS Nano*, **2012**, *6*, 4045.

42. Le Viet, A.; Jose, R.; Reddy, M. V.; Chowdari, B. V. R.; Ramakrishna, S. *J. Phys. Chem. C,* **2010**, *114*, 21795.

43. Sayama, K.; Sugihara, H.; Arakawa, H. *Chem. Mater.* **1998**, *10*, 3825.

44. Lenzmann, F.; Krueger, J.; Burnside, S.; Brooks, K.; Grätzel, M.; Gal, D.; Ruehle, S.; Cahen, D. *J. Phys. Chem. B*, **2001**, *105*,6347.

45. Burnside, S.; Moser, J. E.; Brooks, K.; Grätzel, M.; Cahen, D. *J. Phys. Chem. B*, **1999**, *103*, 9328.

46. Tan, B.; Toman, E.; Li, Y.; Wu, Y. *J. Am. Ceram. Soc.*, **2007**, *129*, 4162.

47. Lana-Villarreal, T.; Boschloo, G.; Hagfeldt, A. *J. Phys. Chem. B*, **2007**, *111*, 5549.

48. Tatay, S.; Haque, S. A.; O'Regan, B.; Durrant, J. R.; Verhees, W. J. H.; Kroon, J. M.; Vidal-Ferran, A.; Gavina, P.; Palomares, E. *J. Mater. Chem.,* **2007**, *17*, 3037.

49. Reynal, A.; Palomares, E. *Eur. J. Inorg. Chem.,* **2011**, 4509.

50. a) Wang, Z.-S.; Sayama, K.; Sugihara, H. *J. Phys. Chem. B,* **2005**, *109*, 22449; b) Teng, C.; Yang, X.; Li, S.; Cheng, M.; Hagfeldt, A.; Wu, L.-z.; Sun, L. *Chem. Eur. J.,* **2010**, *16*, 13127.

51. a) Oskam, G.; Bergeron, B. V.; Meyer, G. J.; Searson, P. C.; *J. Phys. Chem. B,* **2001**, *105*, 6867; b) Bergeron, B. V.; Marton, A.; Oskam, G.; Meyer, G. J. *J. Phys. Chem. B,* **2004**, *109*, 937.

52. Wang, P.; Zakeeruddin, S. M.; Moser, J.-E.; Humphry-Baker, R.; Grätzel, M. *J. Am. Chem. Soc.,* **2004**, *126*, 7164.

53. a) Gregg, B. A.; Pichot, F.; Ferrere, S.; Fields, C. L. *J. Phys. Chem. B,* **2001**, *105*, 1422; b) Daeneke, T.; Kwon, T.-H.; Holmes, A. B.; Duffy, N. W.; Bach, U.; Spiccia, L. *Nat. Chem.,* **2011**, *3*, 213.

54. Hattori, S.; Wada, Y.; Yanagida, S.; Fukuzumi, S. *J. Am. Chem. Soc.,* **2005**, *127*, 9648.

55. Li, T. C.; Spokoyny, A. M.; She, C.; Farha, O. K.; Mirkin, C. A.; Marks, T. J.; Hupp, J. T. *J. Am. Chem. Soc.,* **2010**, *132*, 4580.

56. Sapp, S. A.; Elliott, C. M.; Contado, C.; Caramori, S.; Bignozzi, C. A.; *J. Am. Chem. Soc.,* **2002**, *124*, 11215.

57. Cameron, P.; Peter, L.; Zakeeruddin, S.; Grätzel, M. *Coord. Chem. Rev.*, **2004**, *248*, 1447.

58. Ma, T.; Fang, X.; Akiyama, M.; Inoue, K.; Noma, H.; Abe, E. *J. Electroanal. Chem.*, **2004**, *574*, 77.

59. Kay, A.; Grätzel, M. *Sol. Energy Mater. Sol. Cells*, **1996**, *44*, 99.

60. Figgemeier, E.; Hagfeldt, A. *Int. J. Photoenergy*, **2004**, *6*, 127.

61. Stanley, A.; Verity, B.; Matthews, D. *J. Photochem. Photobiol., C,* **1998**, *52*, 141.

62. Gorlov, M.; Kloo, L. *Dalton Trans.*, **2008**, 2655.

63. Wang, P.; Zakeeruddin, S.; Moser, J.; Grätzel, M. *J. Phys. Chem. B*, **2003**, *107*, 13280.

64. Ardo, S.; Meyer, G. J. *Chem. Soc. Rev.,* **2009**, *38*, 115.

65. Crosby, G. A.; Hipps, K. W.; Elfring, W. H. *J. Am. Chem. Soc.*, **1974**, *96*, 629.

66. Kober, E. M.; Meyer, T. J. *Inorg. Chem.*, **1982**, *21*, 3967.

67. Condon, E. U. *Phys. Rev.*, **1928**, *32*, 858.

68. Condon, E. *Phys. Rev.*, **1926**, *28*, 1182.

69. Franck, J.; Dymond, E. G. *Trans. Faraday Soc.*, **1926**, *21*, 536.

70. Kober, E. M.; Sullivan, B. P.; Meyer, T. J. *Inorg. Chem.*, **1984**, *23*, 2098.

71. R. F. Dallinger and W. H. Woodruff, *J. Am. Chem. Soc.*, **1979**, *101*, 4391.

72. Yersin, H.; Gallhuber, E. *J. Am. Chem. Soc.*, **1984**, *106*, 6582.

73. Yersin, H.; Gallhuber, E.; Vogler, A.; Kunkely, H. *J. Am. Chem. Soc.*, **1983**, *105*, 4155.

74. Qu, P.; Thompson, D. W.; Meyer, G. J. *Langmuir*, **2000**, *16*, 4662.

75. Kalyanasundaram, K. *Photochemistry of Polypyridine and Porphyrin Complexes*; Academic Press: London, **1992**.

76. Nazeeruddin, M. K.; Kay, A.; Rodicio, I.; Humphry-Baker, R.; Mueller, E.; Liska, P.; Vlachopoulos, N.; Grätzel, M. *J. Am. Chem. Soc.*, **1993**, *115*, 6382.

77. Nazeeruddin, M. K.; Pechy, P.; Grätzel, M. *Chem. Commun.,* **1997**, 1705.

78. Chen, P.; Meyer, T. J. *Chem. Rev.*, **1998**, *98*, 1439.

79. Argazzi, R.; Bignozzi, C. A.; Yang, M.; Hasselmann, G. M.; Meyer, G. J. *Nano Lett.*, **2002**, *2*, 625.

80. Snaith, H. J.; Karthikeyan, C. S.; Petrozza, A.; Teuscher, J.; Moser, J. E.; Nazeeruddin, M. K.; Thelakkat, M.; Grätzel, M. *J. Phys. Chem. C*, **2008**, *112*, 7562.

81. Wang, P.; Zakeeruddin, S. M.; Moser, J. E.; Humphry-Baker, R.; Comte, P.; Aranyos, V.; Hagfeldt, A.; Nazeeruddin, M. K., Grätzel, M. *Adv. Mater.*, **2004**, *16*, 1806.

82. Gao, F.; Wang, Y.; Zhang, J.; Shi, D.; Wang, M.; Humphry-

Baker, R.; Wang, P.; Zakeeruddin, S. M.; Grätzel, M. *Chem. Commun.*, **2008**, 2635.

83. Amadelli, R.; Argazzi, R.; Bignozzi, C. A.; Scandola, F. *J. Am. Chem. Soc.*, **1990**, *112*, 7099.

84. Robertson, N. *Angew. Chem., Int. Ed.* **2006**, *45*, 2338.

85. Galoppini, E. *Coord. Chem. Rev.* **2004**, *248*,1283.

86. Piotrowiak, P. *Chem. Soc. Rev.* **1999**, *28*, 143.

87. Wasielewski, M. R. *Chem. Rev.* **1992**, *92*, 435.

88. Oevering, H.; Paddon-Row, M. N.; Heppener, M.; Oliver, A. M.; Cotsaris, E.; Verhoeven, J. W.; Hush, N. S. *J. Am. Chem. Soc.* **1987**, *109*, 3258.

89. Ghosh, P. K.; Spiro, T. G. *J. Am. Chem. Soc.* **1980**, *102*, 5543.

90. Wang, P.; Klein, C.; Moser, J. E.; Humphrey-Baker, R.; Cevey-Ha, N.-L.; Charvet, R.; Comte, P.; Zakeeruddin, S. M.; Grätzel, M. *J. Phys. Chem. B* **2004**, *108*, 17553.

91. Nazeeruddin, M. K.; Zakeeruddin, S. M.; Humphrey-Baker, R.; Jirousek, M.; Liska, P.; Vlachopoulos, N.; Shklover, V.; Fischer, C.-H.; Grätzel, M. *Inorg. Chem.* **1999**, *38*, 6298.

92. McNamara, W. R.; Snoeberger III, R. C.; Li, G.; Richter, C.; Allen, L. J.; Milot, R. L.; Schmuttenmaer, C. A.; Crabtree, R. H.; Brudvig, G. W.; Batista, V. S. *Energy Environ. Sci.*, **2009**, *2*, 1173.

93. Heimer, T. A.; D'Arcangelis, S. T.; Farzad, F.; Stipkala, J. M.; Meyer, G. J. *Inorg. Chem.* **1996**, *35*, 5319.

94. Ramakrishna, G.; Jose, D. A.; Krishna Kumar, D.; Das, A.; Palit, D. K.; Ghosh, H. N. *J. Phys. Chem. B* **2005**, *109*, 15445.

95. Rice, C. R.; Ward, M. D.; Nazeeruddin, M. K.; Grätzel, M. *New J. Chem.* **2000**, *24*, 651.

96. Wang, P.; Zakeeruddin, S. M.; Moser, J. E.; Nazeeruddin, M. K.; Sekiguchi, T.; Grätzel, M. *Nat. Mater.* **2003**, *2*, 402.

97. Lu, N.; Shing, J.-S.; Tu, W.-H.; Hsu, Y.-C.; Lin, J. T. *Inorg. Chem.* **2011**, *50*, 4289.

98. Wang, P.; Zakeeruddin, S. M.; Moser, J. E.; Humphry-Baker, R.; Comte, P.; Aranyos, V.; Hagfeldt, A.; Nazeeruddin, M. K.; Grätzel, M. *Adv. Mater.* **2004**, *16*, 1806.

99. Kuang, D.; Ito, S.; Wenger, B.; Klein, C.; Moser, J.-E.; Humphry-Baker, R.; Zakeeruddin, S. M.; Grätzel, M. *J. Am. Chem. Soc.* **2006**, *128*, 4146.

100. Wang, P.; Klein, C.; Humphry-Baker, R.; Zakeeruddin, S. M.; Grätzel, M. *J. Am. Chem. Soc.* **2005**, *127*, 808.

101. Nazeeruddin, M. K.; Wang, Q.; Cevey, L.; Aranyos, V.; Liska, P.; Figgemeier, E.; Klein, C.; Hirata, N.; Koops, S.; Haque, S. A.; Durrant, J. R.; Hagfeldt, A.; Lever, A. B. P.; Grätzel, M. *Inorg. Chem.* **2006**, *45*, 787.

102. Kuang, D.; Klein, C.; Ito, S.; Moser, J.-E.; Humphry-Baker, R.; Evans, N.; Duriaux, F.; Grätzel, C.; Zakeeruddin, S. M.; Grätzel, M. *Adv. Mater.* **2007**, *19*, 1133.

103. Klein, C.; Nazeeruddin, K.; Di Censo, D.; Liska, P.; Grätzel, M. *Inorg.Chem.* **2004**, *43*, 4216.

104. Kuang, D.; Klein, C.; Snaith, H. J.; Humphry-Baker, R.; Zakeeruddin, S. M.; Grätzel, M. *Inorg. Chim. Acta* **2008**, *361*, 699.

105. Klein, C.; Nazeeruddin, M. K.; Liska, P.; Di Censo, D.; Hirata, N.; Palomares, E.; Durrant, J. R.; Grätzel, M. *Inorg. Chem.* **2005**, *44*, 178.

106. Jang, S. R.; Yum, J. H.; Klein, C.; Kim, K. J.; Wagner, P.; Officer, D.; Grätzel, M.; Nazeeruddin, M. K. *J. Phys. Chem. C* **2009**, *113*, 1998.

107. Shi, Y.; Liang, M.; Wang, L.; Han, H.; You, L.; Sun, Z.; Xue, S. *ACS Appl. Mater. Interfaces* **2013**, *5*, 144.

108. Kuang, D. B.; Klein, C.; Snaith, H. J.; Moser, J. E.; Humphry-Baker, R.; Comte, P.; Zakeeruddin, S. M.; Grätzel, M. *Nano Lett.* **2006**, *6*, 769.

109. Kuang, D.; Klein, C.; Ito, S.; Moser, J.; Humphry-Baker, R.; Zakeeruddin, S. M.; Grätzel, M. *Adv. Funct. Mater.* **2007**, *17*, 154.

110. Xu, J.; Wu, H.; Jia, X.; Zou, D. *Chem. Commun.*, **2012**, *48*, 7793.

111. Chen, C.-Y.; Wu, C.-G.; Chen, J.-G.;, Ho, K.-C. *Angew. Chem., Int. Ed.* **2006**, *45*, 5822.

112. Chen, C.-Y.; Lu, H.-C.; Wu, C.-G.; Chen, J.-G.; Ho, K.-C. *Adv. Funct. Mater.* **2007**, *17*, 29.

113. Chen, C.-Y.; Wu, S.-J.; Li, J.-Y.; Wu, C.-G.; Chen, J.-G.; Ho, K.-C. *Adv. Mater. (Weinheim, Ger.)* **2007**, *19*, 3888.

114. Chen, C.-Y.; Chen, J.-G.; Wu, S.-J.; Li, J.-Y.; Wu, C.-G.; Ho, K.-C. *Angew. Chem., Int. Ed.* **2008**, *47*, 7342.

115. Gao, F.; Wang, Y.; Shi, D.; Zhang, J.; Wang, M.; Jing, X.; Humphry-Baker, R.; Wang, P.; Zakeeruddin, S. M.; Grätzel, M. *J. Am. Chem. Soc.* **2008**, *130*, 10720.

116. Gao, F.; Wang, Y.; Zhang, J.; Shi, D.; Wang, M.; Humphry-Baker, R.; Wang, P.; Zakeeruddin, S. M.; Grätzel, M. *Chem. Commun.* **2008**, 2635.

117. Cao, Y. M.; Bai, Y.; Yu, Q. J.; Cheng, Y. M.; Liu, S.; Shi, D.; Gao, F. F.; Wang, P. *J. Phys. Chem. C* **2009**, *113*, 6290.

118. Gao, F. F.; Cheng, Y. M.; Yu, Q. J.; Liu, S.; Shi, D.; Li, Y. H.; Wang, P. *Inorg. Chem.* **2009**, *48*, 2664.

119. Arakawa, H.; Yamaguchi, T.; Agatsuma, S.; Takanori, S.; Koishi, Y. *Proceedings of the 23rd European Photovoltaic Solar Energy Conference, Valencia, Spain*; **2008**.

120. Jiang, K. J.; Masaki, N.; Xia, J. B.; Noda, S.; Yanagida, S. *Chem. Commun.* **2006**, 2460.

121. Fan, S.-Q.; Kim, C.; Fang, B.; Liao, K.-X.; Yang, G.-J.; Li, C.-J.; Kim, J.-J.; Ko, J. *J. Phys. Chem. C* **2011**, *115*, 7747.

122. Huang, W.-K.; Wu, H.-P.; Lin, P.-L.; Diau, E. W.-G. *J. Phys. Chem. C* **2013**, *117*, 2059.

123. Haque, S. A.; Handa, S.; Peter, K.; Palomares, E.; Thelakkat, M.; Durrant, J. R. *Angew. Chem., Int. Ed.* **2005**, *44*, 5740.

124. Handa, S.; Wietasch, H.; Thelakkat, M.; Durrant, J. R.; Haque, S. A. *Chem. Commun.* **2007**, 1725.

125. Karthikeyan, C. S.; Wietasch, H.; Thelakkat, M. *Adv. Mater. (Weinheim, Ger.)* **2007**, *19*, 1091.

126. Yum, J. H.; Jung, I.; Baik, C.; Ko, J.; Nazeeruddin, M. K.; Grätzel, M. *Energy Environ. Sci.* **2009**, *2*, 100.

127. Faiz, J.; Philippopoulos, A. I.; Kontos, A. G.; Falaras, P.; Pikramenou, Z. *Adv. Funct. Mater.* **2007**, *17*, 54.

128. Wadman, S. H.; Kroon, J. M.; Bakker, K.; Lutz, M.; Spek, A. L.; van Klink, G. P. M.; van Koten, G. *Chem. Commun.* **2007**, 1907.

129. Bessho, T.; Yoneda, E.; Yum, J. H.; Guglielmi, M.; Tavernelli, I.; Imai, H.; Rothlisberger, U.; Nazeeruddin, M. K.; Grätzel, M. *J. Am. Chem. Soc.* **2009**, *131*, 5930.

130. Singh, S. P.; Gupta, K. S. V.; Sharma, G. D.; Islam, A.; Han, L. *Dalton Trans.*, **2012**, *41*, 7604.

131. Kuciauskas, D.; Monat, J. E.; Villahermosa, R.; Gray, H. B.; Lewis, N. S.; McCusker, J. K. *J. Phys. Chem. B* **2002**, *106*, 9347.

132. Sauve, G.; Cass, M. E.; Coia, G.; Doig, S. J.; Lauermann, I.; Pomykal, K. E.; Lewis, N. S. *J. Phys. Chem. B* **2000**, *104*, 6821.

133. Sauve, G.; Cass, M. E.; Doig, S. J.; Lauermann, I.; Pomykal, K.; Lewis, N. S. *J. Phys. Chem. B* **2000**, *104*, 3488.

134. Altobello, S.; Argazzi, R.; Caramori, S.; Contado, C.; Da Fre, S.; Rubino, P.; Chone, C.; Larramona, G.; Bignozzi, C. A. *J. Am. Chem. Soc.* **2005**, *127*, 15342.

135. Alebbi, M.; Bignozzi, C. A.; Heimer, T. A.; Hasselmann, G. M.; Meyer, G. J. *J. Phys. Chem. B* **1998**, *102*, 7577.

136. Kinoshita, T.; Fujisawa, J.; Nakazaki, J.; Uchida, S.; Kubo, T.; Segawa, H. *J. Phys. Chem. Lett.* **2012**, *3*, 394.

137. Hasselmann, G. M.; Meyer, G. J. *J. Phys. Chem. B* **1999**, *103*, 7671.

138. Polo, A. S.; Itokazu, M. K.; Iha, N. Y. M. *Coord. Chem. Rev.* **2004**, *248*, 1343.

139. Ferrere, S.; Gregg, B. A. *J. Am. Chem. Soc.* **1998**, *120*, 843.

140. Islam, A.; Sugihara, H.; Hara, K.; Singh, L. P.; Katoh, R.; Yanagida, M.; Takahashi, Y.; Murata, S.; Arakawa, H.; Fujihashi, G. *Inorg. Chem.* **2001**, *40*, 5371.

141. Suzuki, S.; Matsumoto, Y.; Tsubamoto, M.; Sugimura, R.; Kozaki, M.; Kimoto, K.; Iwamura, M.; Nozaki, K.; Senju, N.; Uragami, C.; Hashimoto, H.; Muramatsu, Y.; Konnoe, A.; Okada, K. *Phys. Chem. Chem. Phys.,* 2013, **15**, 8088.

142. Alonso-Vante, N.; Nierengarten, J.-F.; Sauvage, J.-P. *J. Chem. Soc. Dalton Trans.* **1994**, 1649.

143. Bessho, T.; Constable Edwin, C.; Gätzel, M.; Hernandez Redondo, A.; Housecroft Catherine, E.; Kylberg, W.; Nazeeruddin Md, K.; Neuburger, M.; Schaffner, S. *Chem. Commun.* **2008**, 3717.

144. Wang, X.; Yang, Y.-L.; Wang, P.; Li, L.; Fan, R.-Q.; Cao, W.-W.; Yang, B.; Wangd, H.; Liud, J.-Y. *Dalton Trans.*, **2012**, *41*, 10619.

145. Yella, A.; Lee, H.-W.; Tsao, H. N.; Yi, C.; Chandiran, A. K.; Nazeeruddin, M. K.; Diau, E. W.-G.; Yeh, C.-Y.; Zakeeruddin, S. M.; Grätzel, M. *Science* **2011**, *334*, 629.

146. Nattestad, A.; Cheng, Y. Y.; MacQueen, R. W.; Schulze, T. F.; Thompso, F. W.; Mozer, A. J.; Fückel, B.; Khoury, T.; Crossley, M. J.; Lips, K.; Wallace, G. G.; Schmidt, T. W. *J. Phys. Chem. Lett.* **2013**, *4*, 2073.

147. Lee, M. M.; Teuscher, J.; Miyasaka, T.; Murakami, T. N.; Snaith, H. J. *Science* **2012**, *338*, 643.

148. Kojima, A.; Teshima, K.; Shirai, Y.; Miyasaka, T. *J. Am. Chem. Soc.* **2009**, *131*, 6050.

149. Zhang, W.; Saliba, M.; Stranks, S. D.; Sun, Y.; Shi, X.; Wiesner, U.; Snaith, H. J. *Nano Lett*, dx.doi.org/10.1021/nl4024287.

150. Kim, H.-S.; Mora-Sero, I.; Gonzalez-Pedro, V.; Fabregat-Santiago, F.; Juarez-Perez, E. J.; Park , N.-G.; Bisquert, J. *Nature Comm.* DOI: 10.1038/ncomms3242.

151. Van Houten, J.; Watts, R. J.; *J. Am. Chem. Soc.*, **1976**, *98*, 4853.

152. Yeh, A. T.; Shank, C. V.; McCusker, J. K. *Science*, **2000**, *289*, 935.

153. Webb, M. A.; Knorr, F. J.; McHale, J. L. *J. Raman Spectrosc.,* **2001**, *32*, 481.

154. Bhasikuttan, A. C.; Suzuki, M.; Nakashima, S.; Okada, T. *J. Am. Chem. Soc.*, **2002**, *124*, 8398.

155. Cannizo, A.; Mourik, F. V.; Gawelda, W.; Zgrablic, G.; Bressler, C.; Chergui, M. *Angew. Chem.* **2006**, *118*, 3246; *Angew. Chem., Int. Ed.* **2006**, *45*, 3174–3176.

156. Damrauer, N. H.; Cerullo, G.; Yeh, A.; Boussie, T. R.; Shank, C. V.; McCusker, J. K. *Science*, **1997**, *275*, 54.

157. Wallin, S.; Davidsson, J.; Modin, J.; Hammarstrom, L. *J. Phys. Chem. A*, **2005**, *109*, 4697.

158. Damrauer, N. H.; McCusker, J. K. *J. Phys. Chem. A*, **1999**, *103*, 8440.

159. Tarnovsky, A. N.; Gawelda, W.; Johnson, M.; Bressler, C.; Chergui, M. *J. Phys. Chem. B*, **2006**, *110*, 26497.

160. Henry, W.; Coates, C. G.; Brady, C.; Ronayne, K. L.; Matousek, P.; Towrie, M.; Botchway, S. W.; Parker, A. W.; Vos, J. G.; Browne, W. R.; McGarvey, J. J. *J. Phys. Chem. A*, **2008**, *112*, 4537.

161. Benko, G.; Kallioinen, J.; Korppi-Tommola, J. E. I.; Yartsev, A. P.; Sundstrom, V. *J. Am. Chem. Soc.*, **2002**, *124*, 489.

162. Anderson, N. A.; Lian, T. *Annu. Rev. Phys. Chem.* **2005**, *56*, 491.

163. Anderson, N. A.; Lian, T. *Coord. Chem. Rev.* 2004, *248*, 1231.

164. Asbury, J. B.; Hao, E.; Wang, Y.; Ghosh, H. N.; Lian, T. *J. Phys. Chem. B* **2001**, *105*, 4545.

165. Marcus, R. A. *J. Chem. Phys.* **1965**, *43*, 679.

166. Gao, Y. Q.; Georgievskii, Y.; Marcus, R. A. *J. Chem. Phys.* **2000**, *112*, 3358.

167. Gosavi, S.; Marcus, R. A.; *J. Phys. Chem. B,* **2000**, *104*, 2067.

168. Pankove, J. I. *Optical Processes in Semiconductors*, Dover, New York, **1975**.

169. Nelson, J. ; Haque, S. A.; Klug, D. R.; Durrant, J. R. *Phys. Rev. B: Condens. Matter Mater. Phys*. **2001**, *63*, 205321.

170. Nelson, J. *Phys. Rev. B: Condens. Matter Mater. Phys.* **1999**, *59*, 15374.

171. Lanzafame, J. M.; Palese, S.; Wang, D.; Miller, R. J. D.; Muenter, A. A. *J. Phys. Chem.* **1994**, *98*, 11020.

172. Hannappel, T.; Burfeindt, B.; Storck, W.; Willig, F. *J. Phys. Chem. B*, **1997**, *101*, 6799.

173. Zimmermann, C.; Willig, F.; Ramakrishna, S.; Burfeindt, B.; Pettinger, B.; Eichberger, R.; Storck, W. *J. Phys. Chem. B*, **2001**, *105*, 9245.

174. Tachibana, Y.; Haque, S. A.; Mercer, I. P.; Durrant, J. R.; Klug, D. R. *J. Phys. Chem. B*, **2000**, *104*, 1198.

175. Tachibana, Y.; Moser, J. E.; Grätzel, M.; Klug, D. R.; Durrant, J. R. *J. Phys. Chem.*, **1996**, *100*, 20056.

176. Tachibana, Y.; Nazeeruddin, M. K.; Grätzel, M.; Klug, D. R.; Durrant, J. R. *Chem. Phys.*, **2002**, *285*, 127.

177. Durrant, J. R. *J. Photochem. Photobiol. A: Chem.*, **2002**, *148*, 5.

178. Tachibana, Y.; Rubtsov, I. V.; Montanari, I.; Yoshihara, K.; Klug, D. R.; Durrant, J. R. *J. Photochem. Photobiol. A: Chem*., **2001**, *142*, 215.

179. Haque, S. A.; Palomares, E.; Cho, B. M.; Green, A. N. M.; Hirata, N.; Klug, D. R.; Durrant, J. R. *J. Am. Chem. Soc*., **2005**, *127*, 3456.

180. Asbury, J. B.; Anderson, N. A.; Hao, E.; Ai, X.; Lian, T. *J. Phys. Chem. B*, **2003**, *107*, 7376.

181. Wenger, B.; Grätzel, M.; Moser, J.-E. *Chimia*, **2005**, *59*, 123.

182. Wenger, B.; Grätzel, M.; Moser, J. E. *J. Am. Chem. Soc.*, **2005**, *127*, 12150.

183. Bell, T. D. M.; Pagba, C.; Myahkostupov, M.; Hofkens, J.; Piotrowiak, P. *J. Phys. Chem. B*, **2006**, *110*, 25314.

184. Juozapavicius, M.; Kaucikas, M.; van Thor, J. J.; O'Regan, B. C. *J. Phys. Chem. C* **2013**, *117*, 116.

185. Teuscher, J.; Decoppet, J.-D.; Punzi, A.; Zakeeruddin, S. M.; Moser, J.-E.; Grätzel, M. *J. Phys. Chem. Lett.* **2012**, *3*, 3786–3790.

186. Kallioinen, J.; Benko , G.; Sundstrom, V.; Korppi-Tommola, J. E. I.; Yartsev, A. P. *J. Phys. Chem. B*, **2002**, *106*, 4396.

187. Kallioinen, J.; Benko, G.; Myllyperkio, P.; Khriachtchev, L.; Skarman, B.; Wallenberg, R.; Tuomikoski, M.; Korppi-Tommola, J.; Sundstrom, V.; Yartsev, A. P. *J. Phys. Chem. B*, **2004**, *108*, 6365.

188. Asbury, J. B.; Hao, E.; Wang, Y.; Lian, T. *J. Phys. Chem. B*, **2000**, *104*, 11957.

189. J. B. Asbury, Y.-Q. Wang, E. Hao, H. N. Ghosh and T. Lian, Res. Chem. Intermed., 2001, 27, 393–406.

190. She, C.; Guo, J.; Lian, T. *J. Phys. Chem. B*, **2007**, *111*, 6903.

191. She, C.; Guo, J.; Irle, S.; Morokuma, K.; Mohler, D. L.; Zabri, H.; Odobel, F.; Youm, K. T.; Liu, F.; Hupp, J. T.; Lian, T. *J. Phys. Chem. A*, **2007**, *111*, 6832.

192. Closs, G. L.; Miller, J. R.; *Science*, **1988**, *240*, 440.

193. Smalley, J. F.; Finklea, H. O.; Chidsey, C. E. D.; Linford, M. R.; Creager, S. E.; Ferraris, J. P.; Chalfant, K.; Zawodzinsk, T.; Feldberg, S. W.; Newton, M. D. *J. Am. Chem. Soc.*, **2003**, *125*, 2004.

194. Smalley, J. F.; Feldberg, S. W.; Chidsey, C. E. D.; Linford, M. R.; Newton, M. D.; Liu, Y.-P. *J. Phys. Chem*., **1995**, *99*, 13141.

195. Gray, H. B.; Winkler, J. R. *Proc. Natl. Acad. Sci. U. S. A.*, **2005**, *102*, 3534.

196. References 72, 104, 105, 267-279 of reference 64.

197. Galoppini, E.; Guo, W.; Qu, P.; Meyer, G. J. *J. Am. Chem. Soc.,* **2001**, *123*, 4342.

198. Piotrowiak, P.; Galoppini, E.; Wei, Q.; Meyer, G. J.; Wiewior, P. *J. Am. Chem. Soc*., **2003**, *125*, 5278.

199. Palomares, E.; Clifford, J. N.; Haque, S. A.; Lutz, T.; Durrant, J. R. *J. Am. Chem. Soc.*, **2003**, *125*, 475.

200. Kortan, A. R.; Hull, R.; Opila, R. L.; Bawendi, M. G.; Steigerwald, M. L.; Carroll, P. J.; Brus, L. E. *J. Am. Chem. Soc*., **1990**, *112*, 1327.

201. a) Bedja, I.; Kamat, P. V. *J. Phys. Chem*., **1995**, *99*, 9182; b) Diamant, Y.; Chappel, S.; Chen, S. G.; Melamed, O.; Zaban, A. *Coord. Chem. Rev.*, **2004**, *248*, 1271.

202. Zaban, A.; Chen, S. G.; Chappel, S.; Gregg, B. A. *Chem. Commun.*, **2000**, 2231.

203. Myahkostupov, M.; Piotrowiak, P.; Wang, D.; Galoppini, E. *J. Phys. Chem. C*, **2007**, *111*, 2827.

204. Kilsa, K.; Mayo, E. I.; Kuciauskas, D.; Villahermosa, R.; Lewis, N. S.; Winkler, J. R.; Gray, H. B.; *J. Phys. Chem. A*, **2003**, *107*, 3379.

205. Luo, L.; Chang, C.-W.; Lin, C.-Y.;E. Diau, W.-G. *Chem. Phys. Lett.* **2006**, *432*, 452–456.

206. Chang, C.-W.; Chou, C. K.; Chang, I-J.; Lee, Y.-P.; Diau, E. W.-G. *J. Phys. Chem. C* **2007,** *111,* 13288-13296.

207. Gillaizeau-Gauthier, I.; Odobel, F.; Alebbi, M.; Argazzi, R.; Costa, E.; Bignozzi, C. A.; Qu, P.; Meyer, G. J. *Inorg. Chem.* **2001,** *40,* 6073.

208. Imahori, H.; Kang, S.; Hayashi, H.; Haruta, M.; Kurata, H.; Isoda, S.; Canton, S. E.; Infahsaeng, Y.; Kathiravan, A.; Pascher, T.; Chabera, P.; Yartsev, A. P.; Sundstrom, V. *J. Phys. Chem. A* **2011**, *115*, 3679.

209. Liu, F.; Meyer, G. J. *Inorg. Chem*., **2005**, *44*, 9305.

210. Hasselmann, G. M.; Meyer, G. J. *Z. Phys. Chem. (Munich)*,**1999**, *212*, 39.

211. Nazeeruddin, M. K.; Humphry-Baker, R.; Grätzel M.; Murrer, B. A. *Chem. Commun.*, **1998**, 719.

212. Argazzi, R.; Bignozzi, C. A.; Heimer, T. A.; Meyer, G. J. *Inorg. Chem*., **1997**, *36*, 2

213. Reference 291-295 of reference 64.

214. Willig, F.; Zimmermann, C.; Ramakrishna, S.; Storck, W. *Electrochim. Acta*, **2000**, *45*, 4565.

215. McFarland, S. A.; Lee, F. S.; Cheng, K. H. W. Y.; Cozens, F. L.; Schepp, N. P. *J. Am. Chem. Soc.* **2005**, *127*, 7065.

216. Vrachnou, E.; Grätzel M.; McEvoy, A. J. *J. Electroanal. Chem.*, **1989**, *258*, 193.

217. Vrachnou, E.; Vlachopoulos, N.; Grätzel, M. *J. Chem. Soc., Chem. Commun.*, **1987**, 868.

218. Moser, J.; Punchihewa, S.; Infelta, P. P.; Grätzel, M. *Langmuir*, **1991**, *7*, 3012.

219. Kaniyankandy, S.; Rawalekar, S.; Sen, A.; Ganguly, B.; Ghosh, H. N. *J. Phys. Chem. C* **2012**, *116*, 98.

220. Verma, S.; Kar, P.; Das, A.; Palit, D. K.; Ghosh, H. N. *J. Phys. Chem. C* **2008**, *112*, 2918.

221. Kar, P.; Banerjee, T.; Verma, S.; Sen, A.; Das, A.; Ganguly, B.; Ghosh, H. N. *Phys. Chem. Chem. Phys.* **2012**, *14*, 8192.

222. Ortmans, I.; Moucheron, C.; Mesmaeker, A. K.-D. *Coord. Chem. Rev.*, **1998**, *168*, 233.

223. Kleverlaan, C. J.; Indelli, M. T.; Bignozzi, C. A.; Pavanin, L.; Scandola, F.; Hasselman, G. M.; Meyer, G. J. *J. Am. Chem. Soc.*, **2000**, *122*, 2840.

224. Gerischer, H. *Photochem. Photobiol.*, **1972**, *16*, 243.

225. Moser, J. E.; Grätzel, M. *Chem. Phys.*, **1993**, *176*, 493.

226. Kelly, C. A.; Farzad, F.; Thompson, D. W.; Stipkala, J. M.; Meyer, G. J. *Langmuir*, **1999**, *15*, 7047.

227. Kuciauskas, D.; Freund, M. S.; Gray, H. B.; Winkler, J. R.; Lewis, N. S. *J. Phys. Chem. B*, **2001**, *105*, 392.

228. Pfister, G.; Scher, H. *Phys. Rev. B*, **1977**, *15*, 2062.

229. Scher, H.; Montroll, E. W. *Phys. Rev. B*, **1975**, *12*, 2455.

230. Katoh, R.; Furube, A.; Barzykin, A. V.; Arakawa, H.; Tachiya, M. *Coord. Chem. Rev.*, **2004**, *248*, 1195.

231. Bisquert, J. *J. Phys. Chem. C*, **2007**, *111*, 17163.

232. Clifford, J. N.; Palomares, E.; Nazeeruddin, M. K.; Grätzel, M.; Nelson, J.; Li, X.; Long, N. J.; Durrant, J. R. *J. Am. Chem. Soc.*, **2004**, *126*, 5225.

233. Yan, S. G.; Hupp, J. T. *J. Phys. Chem*., **1996**, *100*, 6867.

234. Lu, H.; Prieskorn, J. N.; Hupp, J. T. *J. Am. Chem. Soc*., **1993**, *115*, 4927.

235. Argazzi, R.; Bignozzi, C. A.; Heimer, T. A.; Castellano, F. N.; Meyer, G. J. *J. Am. Chem. Soc*., **1995**, *117*, 11815.

236. Argazzi, R.; Bignozzi, C. A.; Heimer, T. A.; Castellano, F. N.; Meyer, G. J. *J. Phys. Chem. B*, **1997**, *101*, 2591.

237. Hirata, N.; Lagref, J.-J.; Palomares, E. J.; Durrant, J. R.; Nazeeruddin, M. K.; Grätzel, M.; Di Censo, D. *Chem. Eur. J.*, **2004**, *10*, 595.

238. Wolpher, H.; Sinha, S.; Pan, J.; Johansson, A.; Lundqvist, M. J.; Persson, P.; Lomoth, R.; Bergquist, J.; Sun, L.; V. Sundstrom, Akermark, B.; Polivka, T. *Inorg. Chem.*, **2007**, *46*, 638.

239. Kleverlaan, C.; Alebbi, M.; Argazzi, R.; Bignozzi, C. A.; Hasselmann, G. M.; Meyer, G. J. *Inorg. Chem*., **2000**, *39*, 1342.

240. Persson, P.; Bergstrom, R.; Ojamae, L.; Lunell, S. *Quantum-Chemical Studies of Metal Oxides for Photoelectrochemical Applications*, Adv. Quantum Chem., **2002**, *41*, 203.

241. Kar, P.; Verma, S.; Das, A.; Ghosh, H. N. *J. Phys. Chem. C* **2009**, *113,* 7970.

242. Kar, P.; Verma, S.; Sen, A.; Das, A.; Ganguly, B.; Ghosh, H. N. *Inorg. Chem.* **2010**, *49*, 4167.

243. Verma, S.; Kar, P.; Das, A.; Palit, D. K.; Ghosh, H. N. *Chem. Eur. J.* **2010**, *16*, 611.

244. Verma, S.; Kar, P.; Das, A.; Ghosh, H. N. *Chem. Eur. J.* **2011**, *17*, 1561.

245. Verma, S.; Kar, P.; Banerjee, T.; Das, A.; Ghosh, H. N. *J. Phys. Chem. Lett.* **2012**, *3*, 1543.

Chapter 2

Effect of Electron Donating Groups on the Interfacial Electron Transfer Dynamics of Catecholate Bound Ru(II) Polypyridyl Based Sensitizers on TiO_2 Nanoparticle Surface

European Journal of Inorganic Chemistry **2011**, 4187–4197

2.A. Foreword

One of the major factors controlling the overall light to current conversion yield in light harvesting devices is the effective charge separation at the sensitizer-semiconductor interface and a long lived charge separated state is imperative in order to obtain a good photocurrent response. Longer lived charge separated states may be achieved by making the positive charge move away from the photo-oxidised sensitizer core which is in turn possible by covalently attaching an electron donor to the sensitizer. By connecting phenothiazine or triarylamine to Ru^{II}-polypyridine based complexes long lived charge separation has been obtained (See Chapter 1, Section 1.B.4.C.1.).[1-11] Much work has also been done on systems where a secondary redox couple based on phenols have been used to re-reduce the Ru^{III} that had been created by excited state electron transfer to nanoparticulate TiO_2 in a way analogous to electron transfer from Tyr_z to P 680 in photosystem II.[12,13]

In order to explore the possibility of retarding the deleterious BET of the catechol bound systems with such electron donating moieties, two new Ru^{II}-polypyridyl-catechol based sensitizer molecules, **5** and **6** (Scheme 1), with two different but analogous secondary electron donating groups having different electron donating abilities (covalently attached tyrosine and phenol), have been synthesized. The effect of these electron donating groups on the interfacial electron transfer dynamics of **5**/**6** sensitized TiO_2 has been studied using femtosecond transient absorption spectroscopy and the results have been compared with our previously reported results for **7** sensitized TiO_2.[14]

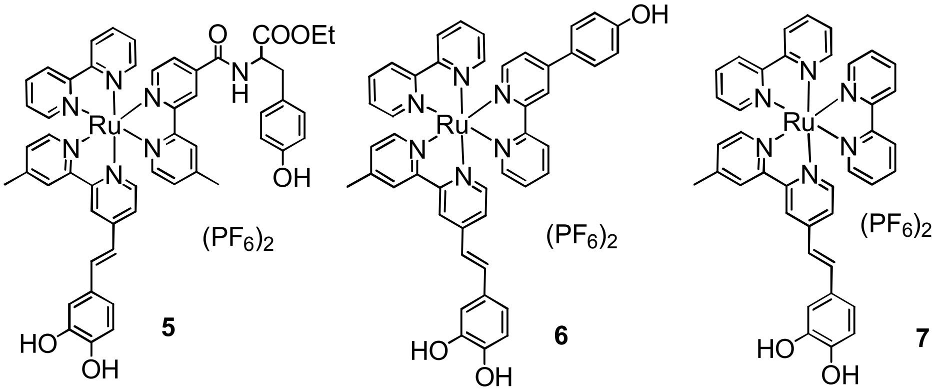

Scheme 1: Molecular structures of **5**, **6** and **7**.

2.B. Experimental Section (please see Appendix A for details)

2.B.1. Synthesis

2.B.1.A. 4'-Methyl-[2,2']bipyridinyl-4-carboxylic acid (1): This compound is prepared following a slightly modified reported procedure.[15] 4,4′-Dimethyl-[2,2′]bipyridine (3 g, 16.3 mmol) and SeO_2 (2.2 g, 19.8 mmol) are taken in 1,4-dioxane (120 ml) and this suspension is heated to reflux for a period of 30 hours with continuous stirring. After this period the solution is filtered hot through a bed of celite. The filtrate is evaporated to dyness and a suspension of it is made in ethanol. To this suspension aq. $AgNO_3$ (3.04 g, 17.9 mmol) is added and is stirred rapidly when a 1 M NaOH solution (75 ml) is added dropwise over half an hour. The reaction mixture is then stirred for 24 hours. Ethanol is removed by evaporation and the residue is filtered in grade 4 sintered glass crucible and is washed with dilute aqueous NaOH solution and then with water. The filtrate is extracted thrice with dichloromethane and the pH of the aqueous part is adjusted to 3.5 by addition of 6 N hydrochloric acid to precipitate a white solid. The solution along with the precipitate is kept in refrigerator for 6 hours and then filtered and dried. Pure **1** is obtained after continuously extracting this solid with acetone in a Soxhlet apparatus for 7 days. Yield - 2.69 g, 77%. ESI-MS (*m/z*): Calculated for $C_{12}H_{10}N_2O_2$ - 214.22, Observed - 215.15 $[M + H]^+$; ^1H NMR (500 MHz, d_6-DMSO): δ (ppm) 8.87 (1H, d, J = 4.5 Hz, H^6 (bpy)); 8.82 (1H, s, H^3 (bpy)); 8.58 (1H, d, J = 4.5 Hz, $H^{6'}$ (bpy)); 8.27 (1H, s, $H^{3'}$ (bpy)); 7.87 (1H, d, J = 4.5 Hz, H^5 (bpy)); 7.34 (1H, d, J = 4 Hz, $H^{5'}$ (bpy)); 2.44 (3H, s, $-CH_3$). IR (KBr pellet, ν (cm^{-1})): 3427 (OH), 1710 (C=O). Elemental Analysis: Calculated for $C_{12}H_{12}N_2O_2$: C, 67.28; H, 4.71; N, 13.08; Found: C, 67.0; H, 4.97; N, 13.1.

2.B.1.B. 3-(4-Hydroxy-phenyl)-2-[(4'-methyl-[2,2']bipyridinyl-4-carbonyl)-amino]-propionic acid ethyl ester (2): Synthesis of this compound is done following a modified literature procedure.[16] **1** (500 mg, 2.336 mmol) is put in 25 ml of thionyl chloride and the solution is heated to reflux for 6 hours. After this time the excess thionyl chloride is first removed by downward distillation and then under reduced pressure. In another round bottomed flask L-tyrosine ethyl ester hydrochloride (636.7 mg, 2.562 mmol) is taken in 30 ml of predried and distilled acetonitrile and to this 1 ml of dry triethylamine is added. The acid chloride is dissolved in dry acetonitrile and this is added in a dropwise manner to the L-tyrosine ethyl ester hydrochloride solution over a period of one hour. When the addition is complete, the solution is stirred for a period of half an hour at room temperature and then it is refluxed for 12 hours under nitrogen. The solution is then allowed to attain room temperature and is filtered. The filtrate is evaporated to dryness, dissolved in dichloromethane (~ 30 ml) and washed three times with water to remove the excess triethylamine. The organic phase is dried over anhydrous sodium sulphate and evaporated to dryness. The crude product so obtained is purified by gravity chromatography using silica as the stationary phase and ethyl acetate/hexane as the eluent. Yield- 476.35 mg, 50%. ESI-MS (*m/z*): Calculated for $C_{23}H_{23}N_3O_4$ - 405.45, Observed - 406.38 $[M + H]^+$; ^1H NMR (200 MHz, $CDCl_3$): δ (ppm) 8.71 (1H, d, J = 5 Hz, H^6 (bpy)); 8.55 (1H, s, H^3 (bpy)); 8.48 (1H, d, J = 4.8 Hz, $H^{6'}$ (bpy)); 8.12 (1H, s, $H^{3'}$ (bpy)); 7.64 (1H, d, J = 4.8 Hz, H^5 (bpy)); 7.25 (1H, d, J = 4.2 Hz, $H^{5'}$ (bpy)); 7.1 (2H, d, J = 8.4 Hz, H^3 (phenyl) and H^5 (phenyl)); 6.72 (2H, d, J = 8.2 Hz, H^2 (phenyl) and H^6 (phenyl)); 4.86-4.78 (1H, m, C**H**(COOEt)); 4.18 (2H, q, J = 7.2 Hz, $-COOC\mathbf{H}_2CH_3$); 3.26-2.98 (2H, m, $-CH_2$-ph); 2.43 (3H, s, bpy-CH_3); 1.23 (3H, t, J = 7.2 Hz, $-COOCH_2C\mathbf{H}_3$); IR (KBr pellet, ν (cm^{-1})): 3320 (OH), 1728 $(C=O)_{ester}$, 1656 $(C=O)_{amide}$. Elemental Analysis: Calculated for $C_{23}H_{23}N_3O_4$: C, 68.13; H, 5.72; N, 10.36; Found: C, 68.1; H, 5.8; N, 10.5.

2.B.1.C. 4-[2,2']Bipyridinyl-4-yl-phenol (3): This compound is prepared following a reported procedure.[17] ESI-MS (*m/z*): Calculated for $C_{16}H_{12}N_2O$ - 248.28, Observed - 249.16 $[M + H]^+$, 271.15 $[M + Na]^+$; ^1H NMR (200 MHz, d_6-DMSO): δ (ppm) 9.91 (1H, s, H (hydroxyl); 8.73 (1H, m, $H^{6'}$ (bpy)); 8.68 (1H, d, *J* = 5.2 Hz, H^6(bpy)); 8.62 (1H, d, *J* = 1.2 Hz, H^3 (bpy)); 8.44 (1H, d, *J* = 7.8 Hz, $H^{3'}$ (bpy)); 7.98 (1H, td, *J* = 7.7 Hz and 2 Hz, $H^{4'}$ (bpy)); 7.73-7.70 (3H, m, H^5 (bpy), H^2 (phenyl) and H^6 (phenyl)); 7.53-7.46 (1H, m, $H^{5'}$ (bpy)); 6.94 (2H, d, *J* = 8.6 Hz, H^3 (phenyl) and H^5 (phenyl)). IR (KBr pellet, ν (cm^{-1})): 3397 (OH). Elemental Analysis: Calculated for $C_{16}H_{12}N_2O$: C, 77.40; H, 4.87; N, 11.28; Found: C, 77.2; H, 5.0; N, 11.5.

2.B.1.D. 4-[2-(4'-Methyl-[2,2']bipyridinyl-4-yl)-vinyl]-benzene-1,2-diol (4): This compound is again prepared following a literature procedure.[18] ESI-MS (*m/z*): Calculated for $C_{19}H_{16}N_2O_2$ - 304.34, Observed - 305.22 $[M + H]^+$; ^1H NMR (500 MHz, CD_3OD): δ (ppm) 8.54 (1H, d, *J* = 5.5 Hz, $H^{6'}$ (bpy)); 8.52 (1H, d, *J* = 5 Hz, H^6 (bpy)); 8.34 (1H, s, $H^{3'}$ (bpy)); 8.13 (1H, s, H^3 (bpy)); 7.53 (1H, dd, *J* = 4 Hz, 1 Hz, $H^{5'}$ (bpy)); 7.43 (1H, d, *J* = 16 Hz, H (ethenyl)); 7.32 (1H, dd, *J* = 4 Hz, 1 Hz, H^5 (bpy)); 7.11 (1H, d, *J* = 1.5 Hz, H^2 (phenyl)); 7.02-6.98 (2H, m, H (ethenyl) and H^6 (phenyl)); 6.79 (1H, d, *J* = 8 Hz, H^5 (phenyl)); 2.49 (3H, s, bpy-CH_3). IR (KBr pellet, ν (cm^{-1})): 3238 (OH), 1590 (C=C). Elemental Analysis: Calculated for $C_{19}H_{16}N_2O_2$: C, 74.98; H, 5.30; N, 9.20; Found: C, 74.5; H, 5.3; N, 9.7.

2.B.1.E. {(2,2'-Bipyridine)-(3-(4-Hydroxy-phenyl)-2-[(4'-methyl-[2,2']bipyridinyl-4-carbonyl)-amino]-propionic acid ethyl ester)-(4-[2-(4'-Methyl-[2,2']bipyridinyl-4-yl)-vinyl]-benzene-1,2-diol)} ruthenium(II) hexafluorophosphate (5): $RuCl_3.xH_2O$ (51.2 mg, 0.247 mmol) and 2,2'-bipyridine (39 mg, 0.247 mmol) are taken in 30 ml dimethylformamide solvent and heated at 80 ^{0}C for 4 hours. To the resulting solution **2** is added and the reaction mixture is again heated at 110 ^{0}C for 4 hours. After 4 hours, **4** is finally added and the reaction mixture is heated at 135 ^{0}C for 8 hours. The reaction mixture is then allowed to cool to room temperature. The solvent is evaporated and the residue is dissolved in acetonitrile and is stirred in the presence of ten equivalents of potassium hexafluorophosphate for 24 hours. After 24 hours, acetonitrile is evaporated and the residue so obtained is washed repeatedly with large volumes of water to remove the excess KPF_6. The crude product obtained is purified by column chromatography by using silica as the stationary phase and acetonitrile/water/saturated aqueous KPF_6 as the eluent. The first fraction is collected and evaporated to dryness. It is redissolved in dichloromethane and two drops of acetonitrile and solvent extraction is done to remove the excess KPF_6 used in the eluent. The organic phase is dried over anhydrous sodium sulphate and is evaporated to dryness to give the desired product. The compound is further purified by using vapour diffusion method of recrystallization. The compound is dissolved in a minimum volume of acetonitrile and this sample tube is kept inside another larger sample tube that contains diethyl ether in it. The whole system is closed thoroughly to avoid any solvent loss by evaporation. Though no single crystals are obtained, the pure ruthenium complex gets deposited on the walls of the sample container and this is characterized fully and used for further studies. Yield - 85 mg, 27.4%. ESI-MS (*m/z*): Calculated for $C_{52}H_{47}F_{12}N_7O_6P_2Ru$ – 1256.97, Observed – 1112.5 [M - PF_6^-]$^+$, 966.3 [M - 2PF_6^- - H^+]$^+$; ^{1}H NMR (200 MHz, CD_3CN): δ (ppm) 8.68 (1H, s, H^6 (bpy-tyr)); 8.49 (5H, m, H^6 and $H^{6'}$ (bpy), H^6 and $H^{6'}$ (bpy-cat), $H^{6'}$ (bpy-tyr)); 8.05 (3H, m, H^3 and $H^{3'}$ (bpy), H^3 (bpy-tyr)); 7.81 (2H, m, $H^{3'}$ (bpy-tyr), $H^{3'}$ (bpy-cat)); 7.73-7.71 (3H, m, H^4 and $H^{4'}$ (bpy), H^3 (bpy-cat)); 7.62-7.54 (4H, m, H (ethenyl), H^5 (bpy-tyr), H^5 and $H^{5'}$ (bpy)); 7.4 (3H, s, $H^{5'}$ (bpy-tyr), $H^{5'}$ (bpy-cat), H^6 (catechol)); 7.28-7.25 (2H, m, H^2 and H^5 (catechol)); 7.15-7.04 (4H, m, H (ethenyl), H^5 (bpy-cat), H^2 and H^6 (phenol)); 6.72 (2H, d, *J* = 6.8 Hz, H^3 and H^5 (phenol)); 4.85-4.74 (1H, m, C**H**(COOEt)); 4.15 (2H, q, *J* = 7 Hz, -COOC**H**$_2$CH$_3$); 3.17-3.03 (2H, m, -C**H**$_2$-phenol); 2.56 (6H, s, -CH$_3$ (bpy-tyr), -CH$_3$ (bpy-cat)); 1.12 (3H, t, *J* = 7.2 Hz, -COOCH$_2$C**H**$_3$). IR (KBr pellet, ν (cm^{-1})): 3419 (OH), 1734 (C=O)$_{ester}$, 1605 (C=C), 841 (PF_6^-). Elemental Analysis: Calculated for $C_{52}H_{47}F_{12}N_7O_6P_2Ru$: C, 49.69; H, 3.77; N, 7.80; Found: C, 50.01; H, 3.85; N, 7.69.

2.B.1.F. {(2,2'-Bipyridine)-(4-[2,2']Bipyridinyl-4-yl-phenol)-(4-[2-(4'-Methyl-[2,2']bipyridinyl-4-yl)-vinyl]-benzene-1,2-diol)} ruthenium(II) hexafluorophosphate (6): 6 is synthesized in an analogous manner. $RuCl_3.xH_2O$ (51.2 mg, 0.247 mmol) and 2,2'-bipyridine (39 mg, 0.247 mmol) are taken in 30 ml dimethylformamide solvent and heated at 80 °C for 4 hours. To the resulting solution **3** is added and the reaction mixture is again heated at 110 °C for 5 hours. The addition of **4**, however, requires a longer time. After 4 hours of addition of **3**, **4** is finally added and the reaction mixture is heated at 140 °C for 15 hours. Rest of the procedure is the same as for the synthesis of complex **5**. Yield - 90 mg, 33%. ESI-MS (*m/z*): Calculated for $C_{45}H_{36}F_{12}N_6O_3P_2Ru$ – 1099.8, Observed – 808.24 [M - 2PF_6^- - H^+]$^+$; ^{1}H NMR (200 MHz, CD_3CN): δ (ppm) 8.70 (4H, s, H_3, H^6 and $H^{6'}$ (bpy-ph), H^6 or $H^{6'}$ (bpy)); 8.53 (4H, d, *J* = 7.4 Hz, H^6 and $H^{6'}$ (bpy-cat), H^6 or $H^{6'}$ (bpy), H^5 or $H^{5'}$ (bpy)); 8.39 (1H, d, *J* = 7.6 Hz, $H^{3'}$ (bpy-ph)); 8.12-8.04 (5H, m, H^3 and $H^{3'}$ (bpy), H^3 and $H^{3'}$ (bpy-cat), $H^{4'}$ (bpy-ph)); 7.88 (2H, d, *J* = 6 Hz, H^4 and $H^{4'}$ (bpy)); 7.83-7.74 (5H, m, H^2 and H^6 (phenol), H^5 (bpy-ph), H^5 (bpy-cat), H^5 or $H^{5'}$ (bpy)); 7.62 (2H, m, H^6 (catechol), H^5 (bpy-cat)); 7.45-7.39 (3H, m, H (ethenyl), H^2 and H^5 (catechol)); 7.28 (1H, t, *J* = 6.4 Hz , $H^{5'}$ (bpy-ph)); 7.02 (3H, m, H (ethenyl), H^3 and H^5 (phenol)); 2.55 (3H, s, -CH$_3$ (bpy-cat)). IR (KBr pellet, ν (cm^{-1})): 3438 (OH), 1606 (C=C), 840 (PF_6^-). Elemental Analysis: Calculated for $C_{45}H_{36}F_{12}N_6O_3P_2Ru$: C, 49.14; H, 3.30; N, 7.64. Found: C, 49.24; H, 3.40; N, 7.60.

2.C. Results and Discussion

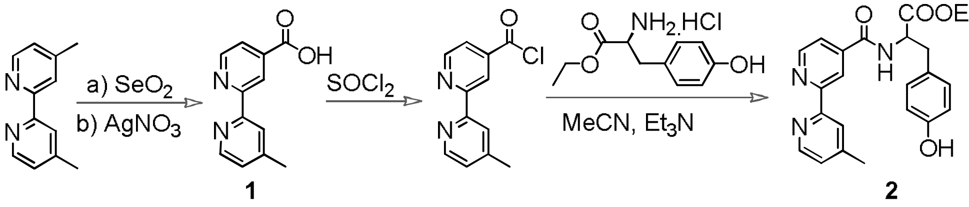

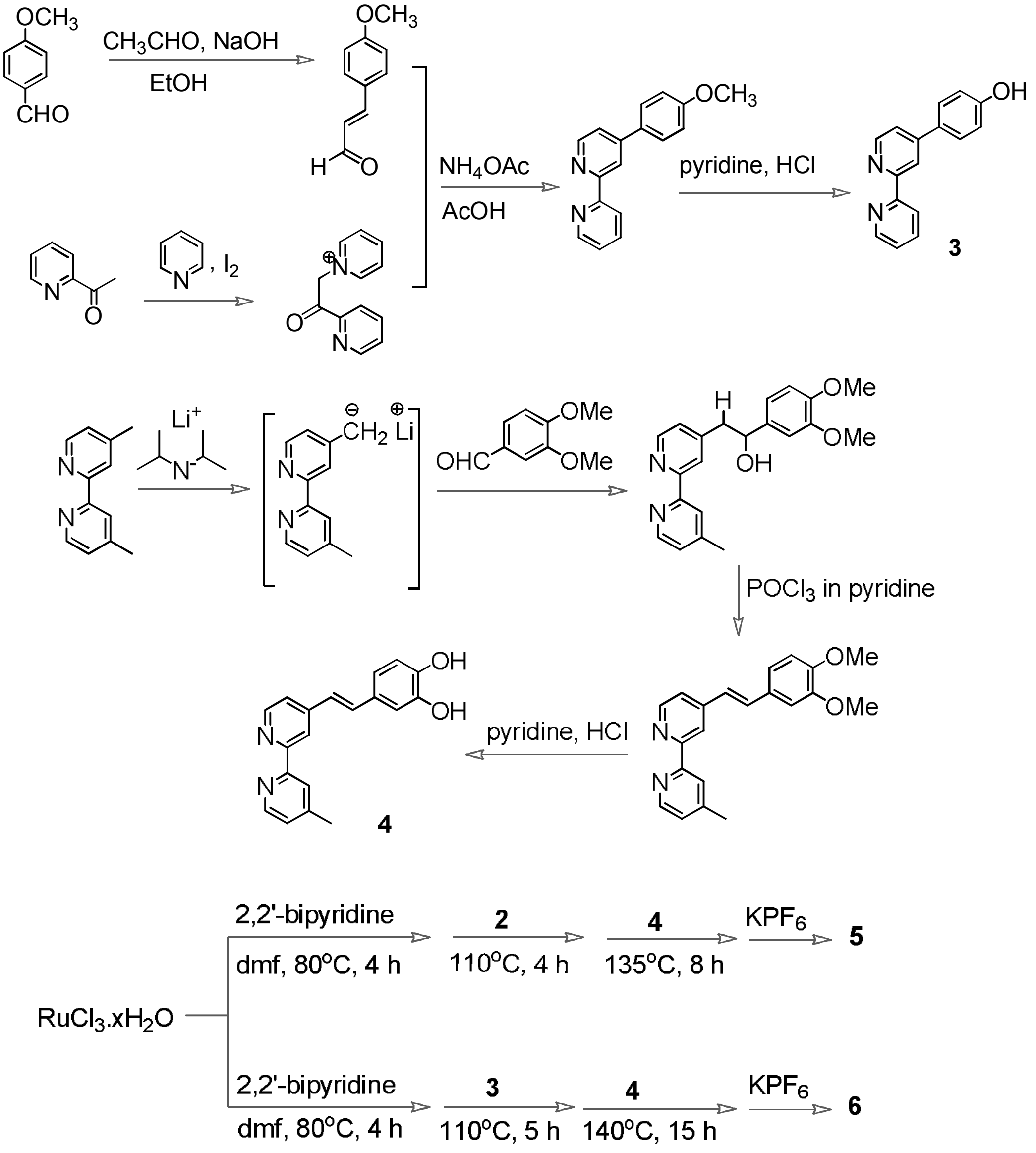
OCH3
CH3CHO, NaOH
EtOH
CHO
OCH3
H
O
NH4OAc
AcOH
OCH3
N
N
pyridine, HCl
OH
N
N
3
N
O
N, I2
N
O
N
Li+
N
N
N
CH2 Li
N
N
OHC
OMe
OMe
H
OMe
OMe
N
OH
N
POCl3 in pyridine
OH
OH
N
N
4
pyridine, HCl
OMe
OMe
N
N
RuCl3.xH2O
2,2'-bipyridine
dmf, 80°C, 4 h
2
110°C, 4 h
4
135°C, 8 h
KPF6
5
2,2'-bipyridine
dmf, 80°C, 4 h
3
110°C, 5 h
4
140°C, 15 h
KPF6
6

Scheme 2: Synthetic route for the preparation of the complexes.

The synthetic methodology adopted in the synthesis of the bipyridine based ligands and the complexes are outlined in Scheme 2. **2** and **3** have been synthesised as per previous reports and the analytical data match well with the reported compounds. **1** is prepared by a selenium dioxide oxidation of 4,4'-Dimethyl-[2,2']bipyridine followed by further oxidation with silver oxide. Once purified by Soxhlet extraction, **1** is converted into its acid chloride and this is made to react with L-tyrosine ethyl ester hydrochloride in acetonitrile in presence of triethylamine as the base. Purification by column chromatography yields pure **2**. **5** is prepared in a one pot reaction wherein $RuCl_3.xH_2O$ is allowed to react successively with molar equivalents of 2,2'-bipyridine, **2** and **4** at different time intervals and at progressively higher temperatures. After evaporation of the solvent anion exchange is done by making the product soluble in acetonitrile and stirring it in presence of an excess amount of potassium hexafluorophosphate. Acetonitrile is used because the product is only partially soluble in water. The crude product is purified by column chromatography and is further purified by vapour diffusion method of recrystallization. **6** is prepared following a similar methodology. The purity of the complexes is checked by different analytical and spectroscopic methods and the analytical data matches well with that of the expected formulation.

Figure 1 shows the optical absorption spectra of **5** and **6** in acetonitrile. Also shown is the optical absorption spectrum of **7** for comparison. The low energy broad absorption band for **5** at 456 nm and that for **6** at 456 nm along with a shoulder at 433 nm arise due to overlapping MLCT based $d_{Ru(II)} \rightarrow \pi^*_{2,2'\text{-bpy}}$, $d_{Ru(II)} \rightarrow \pi^*_{\text{bpy-cat}}$ and $d_{Ru(II)} \rightarrow \pi^*_{\text{bpy-tyr}}$ or $d_{Ru(II)} \rightarrow \pi^*_{\text{bpy-phenol}}$ transitions. The absorptions of tyrosine ($\lambda_{max} \sim 274$ nm, $\varepsilon = 1405$)[19] in **5** and that for phenol in **6** (λ_{max} at ~270 nm, $\varepsilon = 2340$)[20] are masked due to strong intra and/or interligand π-π^* transitions at 288 nm ($\varepsilon \sim 10^5$).[21,22] The band at 245 nm along with the shoulder at 253 nm have been assigned to higher energy MLCT d-π^* transitions.[22] The absorption band at 354 nm for **5** and that at 322 nm for **6** can be attributed to interligand charge transfer transition from π_{bpy} to $\pi^*_{\text{bpy-tyr}}$ and from π_{bpy} to $\pi^*_{\text{bpy-phenol}}$, respectively.[22] This relative shift of 32 nm for **6** as compared to that of **5** is due to the higher donating ability of phenol (E_{ph} = 0.98 V) as compared to tyrosine (E_{tyr} = 1.03 V) (see below for electrochemical data).

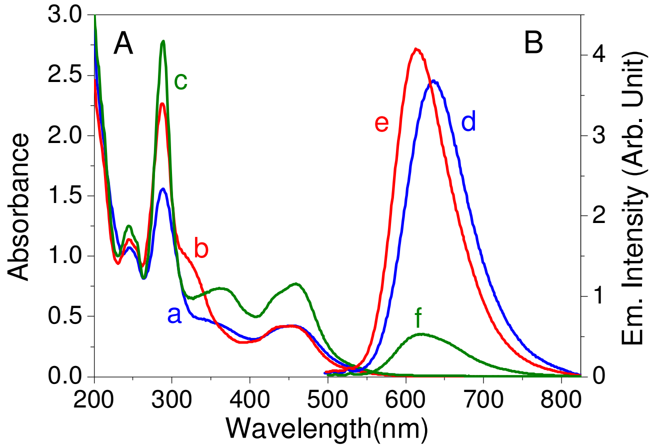

Figure 1: (A) Absorption spectra of (a) **5**, (b) **6** and (c) **7** in acetonitrile (concentration for all the three complexes is 3 × 10^{-5} M); (B) Emission spectra of (d) **5**, (e) **6** and (f) **7** in acetonitrile. Emisson spectra have been recorded for identical absorbances of the three complexes at 457 nm excitation wavelength.

The steady state emission spectra of **5**, **6** and **7** in acetonitrile recorded after exciting at 457 nm are shown in Figure 1B. Figure 1B shows that **5** emits with λ_{max} at 635 nm while **6** emits at 614 nm. The blueshift observed in the emission spectrum of **6** as compared to that of **5** is due to the presence of phenol moiety which again acts as a better donor than tyrosine and raises the π^*_{bpy} level (LUMO).

Cyclic voltammogram of the complexes in acetonitrile are very similar in nature (Figure 2). The $Ru^{II/III}$ redox potential for **5** is found to be 1.35 V while that for **6** is found to be 1.30 V in de-aerated acetonitrile**.** Both tyrosine and phenol show an irreversible oxidation peak, respectively at 1.03 V and 0.98 V. The irreversible nature of the oxidation peak is previously reported for phenols because the oxidised species have lifetimes smaller than the time scale of the instrument.[23]

In order to comprehend the feasibility of electron injection into the conduction band of the semiconductor nanoparticles, it becomes necessary to calculate the redox potential of the ^{3}MLCT state of the dye. E_{0-0} transition energy is calculated to be 2.21 eV for **5** and 2.24 eV for **6** from the respective excitation and emission spectra in acetonitrile. The redox potentials of the ^{3}MLCT state, $E(S^+/S^*)$,[24,25] are thus calculated to be -0.86 V and -0.94 V for **5** and **6**, respectively following the equation $[E(S^+/S^*)] = [E(S^+/S)] - E_{0-0}$. The excited state potentials being above the conduction band level, electron injection from the excited state of the sensitizers into the conduction band of TiO_2 becomes feasible. As is evident from the cyclic voltammograms, the potential of the tyrosine and the phenolic moieties in compounds **5** and **6** are quite lower than that of the ruthenium centre. So electron transfer from tyrosine or phenol to ruthenium(II)-centre is thermodynamically possible.

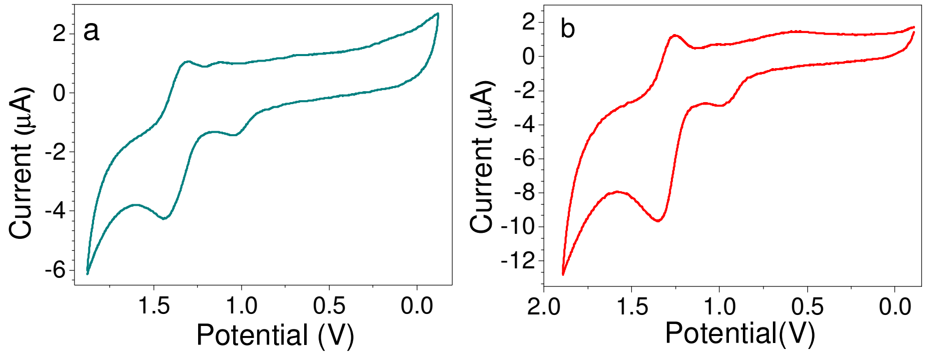

Figure 2: Cyclic Voltammogram of (a) **5** and (b) **6** in acetonitrile. SCE has been used as the reference electrode. Scan rate for both the scans shown above is 100 mV/s.

Figure 3 shows the optical absorption and emission spectrum of **5** and **6** in aqueous solution in absence and in the presence of TiO_2 nanoparticles. The observed spectral features of **5** and **6** in water are very similar to that in acetonitrile (Figure 3). The absorption spectra for both the complexes show a prominent increase in absorbance and broadening, along with a slight red shift, of the MLCT band at 456 nm in the presence of TiO_2 nanoparticles, which can be explained on the basis of strong interaction of the sensitizer molecules with TiO_2 nanoparticles through the formation of a five membered ring.[26,27] This observation is in accordance with the results reported earlier where we have shown that dyes bound to TiO_2 surface *via* catecholate anchoring groups interact very strongly with them.[28-35] The strong interaction of the sensitizers with the semiconductor nanoparticles is further supported by the fact that the luminescence spectra of both the complexes are quenched considerably in presence of TiO_2 nanoparticles due to electron injection (Figure 3). Thus, steady state studies confirm strong binding of the sensitizer molecules with the nanoparticles and permit further studies into their effectiveness as efficient sensitizers and the possible effects of the electron donating groups attached.

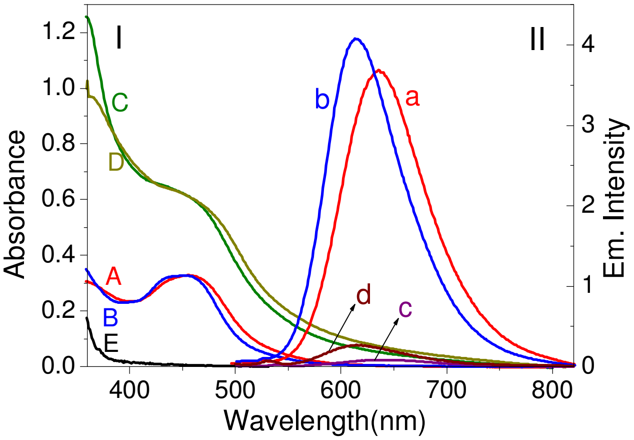

Figure 3: (I) A: Absorption spectrum of **5**, B: absorption spectrum of **6**, C: absorption spectrum of **5** in the presence of TiO_2 nanoparticles, D: Absorption spectrum of **6** in the presence of TiO_2 nanoparticles and E: Absorption spectrum of TiO_2 nanoparticles. (II) a: Emission spectrum of **5**, b: emission spectrum of **6,** c: emission spectrum of **5** in the presence of TiO_2 nanoparticles and d: emission spectrum of **6** in the presence of TiO_2 nanoparticles. Dye concentration for all the UV measurements is 2.5×10^{-5} M while for the fluorescence measurements the dye concentration is 3×10^{-5} M. TiO_2 concentration is 15 g/L for all measurements.

To develop a comprehensive understanding of the dynamics of electron injection into the semiconductor nanoparticles, it is essential to study in detail the excited state

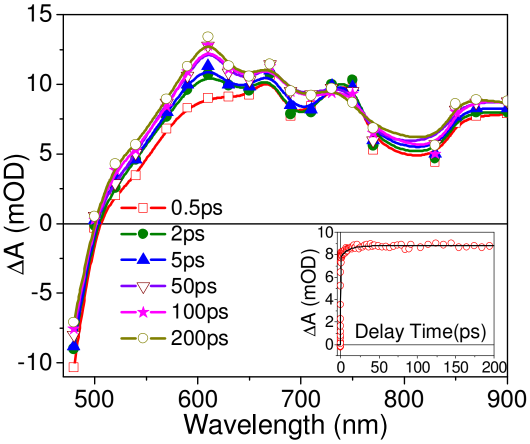

Figure 4: Transient absorption spectra of **5** in acetonitrile at different delay times following excitation at 400 nm. Inset: Kinetic trace of the excited triplet state (^{3}MLCT) of **5** at 650 nm in acetonitrile after excitation at 400 nm.

dynamics of the free sensitizer molecules. With this aim we have carried out transient absorption studies (in femtosecond time domain), in the visible and in the near infrared region, of **5** and **6** in acetonitrile. Figure 4 and Figure 5 show the transient absorption spectrum of **5** and **6** in acetonitrile. Both the spectra show two broad absorption features, one ranging from 510-780 nm and another in the near infrared region ranging from 830-1000 nm along with a bleach before 500 nm due to ground state MLCT absorption discussed before. The aforementioned transient absorption bands are assigned to excited triplet state absorption,[14,28,29,31] because ISC in ruthenium(II)-polypyridyl complexes is known to be very fast and is completed in 15 ± 10 fs.[36] Thus, the singlet to triplet conversion is expected to have occurred within the pulse width of the instrument (< 100 fs). We have monitored excited state dynamics of **5** and **6** by monitoring the kinetics at 650 nm shown as insets of Figure 4 and Figure 5 respectively.

The kinetic trace for **5** at 650 nm is found to be having two growth components with time constants of < 100 fs (85%) and 10 ps (15%). The first growth component is pulse width limited (< 100 fs), which can be attributed to the formation of singlet and/or triplet state. The origin of the second component is debatable. Interligand electron transfer can be a possibility since the kinetic data has been recorded by excitation with a very high energy 400 nm light. However, keeping in mind the structural complexity which might arbitrate numerous relaxation pathways, this assignment can be said to be only a tentative one.[14, 37-39] Also, the kinetic trace does not decay in 1 ns time scale

because of the >> 1 ns lifetime of such Ru^{II}-polypyridyl complexes.[40] The kinetic decay trace of **6** monitored at 650 nm shows single exponential growth (< 100 fs) followed by

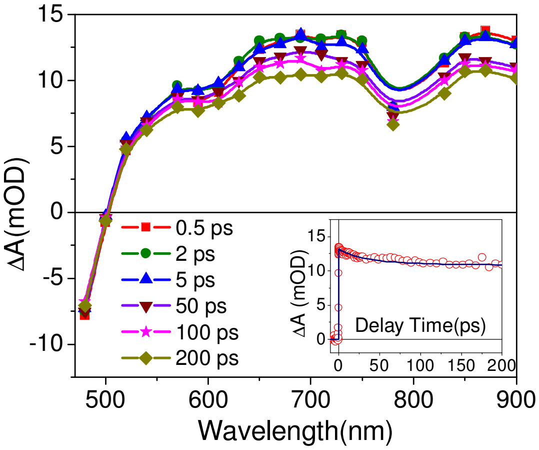

Figure 5: Transient absorption spectra of **6** in acetonitrile at different delay times following excitation at 400 nm. Inset: Kinetic trace of the excited triplet state (^{3}MLCT) of **6** at 650 nm in acetonitrile after excitation at 400 nm.

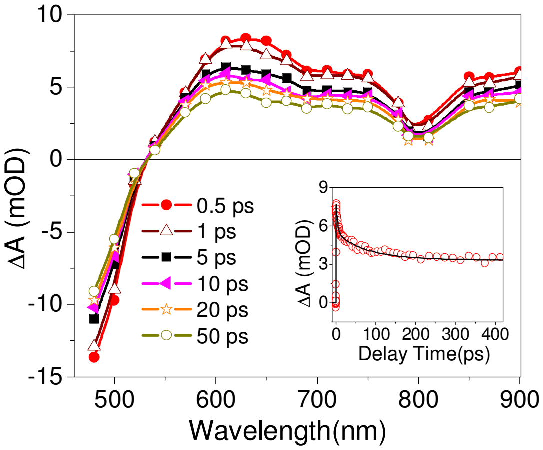

Figure 6: Transient absorption spectra of **5**-TiO$_2$ in water at different time delays after excitation at 400 nm. Typical concentration for **5** is ~ 200 μM, while that for TiO$_2$ nanoparticles is ~ 15 g/L. Inset: Kinetic trace of the cation radical of **5** at 590 nm.

bi-exponential decay with time constants 30 ps (-15.4%) and > 1 ns (-84.6%). It is interesting to see that **6** has an additional decay time constant of 30 ps in addition to the > 1ns component (Figure 5 inset) as compared to **5** which has only one decay component of > 1 ns. The hydroxyl group of the bpy-phenol moiety in **6** can form H-bonds with the solvent molecules and the excited state can get relaxed resulting in the 30 ps decay component. The phenolic hydroxyl group is in direct conjugation with the chromophoric centre in **6**, unlike in **5** where it is linked *via* a non conjugated amide spacer. This could be the reason why the aforesaid decay component is absent in **5**. A similar observation was noted for $Ru(CN)_4(\mathbf{4})^{2-}$ which had an extra decay component of 10 ps assigned to an extra decay channel associated with the excited states because of the cyano groups forming H- bonds with the surrounding solvent molecules.[29]

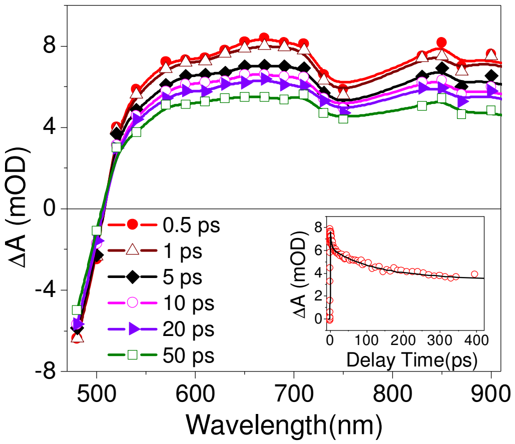

Figure 7: Transient absorption spectra of **6**-TiO_2 nanoparticle in water at different time delay after excitation at 400 nm. Typical concentration for **6** is ~ 200 µM while that for TiO_2 nanoparticles is ~ 15 g/L. Inset: Kinetic trace of the cation radical of **6** at 610 nm.

Figure 6 and Figure 7 show the transient absorption spectrum of **5**-TiO_2 and **6**-TiO_2 systems in water. Both the transient spectra show two broad absorption bands, one ranging from 540-750 nm and the other in the region 800-1000 nm. The first absorption feature can be assigned to the formation of the cation radical ($\mathbf{5}^{\cdot+}$ or $\mathbf{6}^{\cdot+}$) based upon the previous results from our group.[14,28,31] The lower energy absorption band in the 800-1000 nm region can be assigned to electrons in the conduction band of TiO_2 nanoparticles. This assignment corroborates with the results of different groups where it has been shown that electrons in the conduction band can be detected by visible,[41-43] near IR[44] and mid IR[45,46] absorption.

The electron injection time can be predicted by monitoring the time of appearance of the electron signal and it is found to be pulse width limited (< 100 fs) and monoexponential at all the wavelengths monitored and for both the compounds. That the electron is injected in majority from the nonthermalized states and not from the thermalized states is confirmed by the fact that no associated growth for either the cation radical signal or the electron signal is observed and that the kinetic traces (evolve and) decay with almost similar time constants from 540-900 nm. Had there been injection from the thermalized triplet states, one would have observed a growth of the cation radical signal in the early time scale along with a decay of the triplet state.[47] Also, our previous studies confirm that the transients obtained at different wavelengths is due to the charge separated species and that any contribution due to excited states is negligible.[28,29,31]

The non-thermalized excited states involved in the interfacial electron transfer process are presumably both the hot singlet and the triplet states because ISC is known to be very fast in Ru^{II}-polypyridyl complexes and this competes with electron injection into TiO_2. **5** and **6** being anchored to TiO_2 surface *via* catecholate functionality result in a very strong electronic coupling and this is responsible for electron injection from the nonthermalized states and hence a single exponential and ultrafast electron injection.

The primary aim of this investigation is to monitor the effect of electron donating groups on the electron transfer dynamics of catecholate bound dyes. Provided the charge separation at the dye-semiconductor interface is maintained efficiently, the dye sensitized solar cell can be made to work resourcefully. Charge recombination, *i.e.,* BET dynamics therefore becomes necessary to be studied for it is one of the major pathways of loss of the effective electron concentration in the conduction band. The injected electron has to escape the reaction distance of recombination and reach the bulk of the electrode *via* downhill migration for it to contribute to the photocurrent response of the cell.[48]

The dynamics of the BET can be determined by monitoring the recovery of the ground state bleach. Figure 8 shows the bleach recovery kinetics of **5**-, **6**- and **7**-TiO_2 systems. The kinetic trace of **5**-TiO_2 at 480 nm can be fitted multi-exponentially with time constants $\tau_1 = 2.7$ ps (+39.5%), $\tau_2 = 70$ ps (+16%), and $\tau_3 >$ 1ns (+44.5%), and the kinetic trace for **6**-TiO_2 system can be fitted multi-exponentially with time constants $\tau_1 = 3.3$ ps (+19%), $\tau_2 = 110$ ps (+32%), and $\tau_3 >$ 1ns (+49%). On the other hand, the bleach recovery for **7**-TiO_2 system can be fitted with $\tau_1 = 1.5$ ps (+37.6%), $\tau_2 = 70$ ps (+19.4%), $\tau_3 >$ 1 ns (+43%).

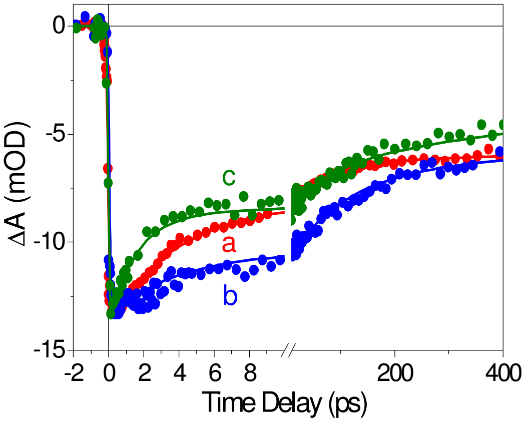

Figure 8: Bleach recovery kinetics at 480 nm for (a) **5**–TiO_2, (b) **6**–TiO_2 and (c) **7**–TiO_2 systems after excitation at 400 nm.

It can be seen that the bleach recovery is slowest in case of **6**-TiO_2 as compared to the other systems. The decay of the conduction band electron signal at 900 nm for the three aforesaid systems follows a similar trend (Figure 9).

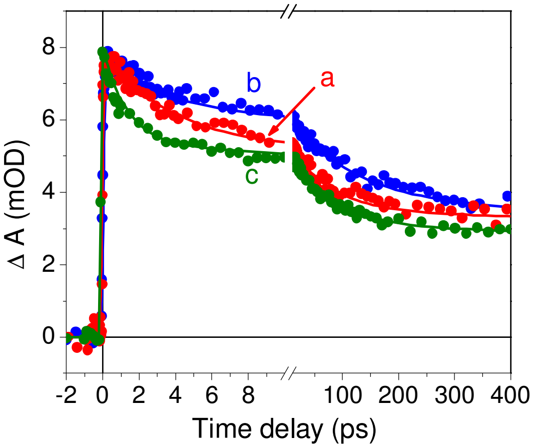

Figure 9: Transient decay kinetics of the injected electron at 900 nm in (a) **5**-TiO_2, (b) **6**-TiO_2 and (c) **7**-TiO_2 systems after excitation at 400 nm.

The kinetic trace of the injected electron signal for **5**-TiO_2 system can be fitted multi-exponentially with time constants τ_1 = 3.5 ps (-28%), τ_2 = 70 ps (-28%) and τ_3 > 1ns (-44%), while that for **6**-TiO_2 system can be fitted with time constants τ_1 = 3.3 ps (-25.8%), τ_2 = 110 ps (-29%) and τ_3 > 1ns (-45.2%). On the other hand, the signal for **7**-TiO_2 system at 900 nm is reported to be fitting with time constants τ_1 = 1.5 ps (-34.8%), τ_2 = 70 ps (-26.8%), τ_3 > 1 ns (-38.4%). As is evident from the above time constants, BET is always faster compared to dyes with carboxylate anchoring groups.[49,50] Stronger binding of the catechol functionality is responsible for such fast BET in all the above systems.

As told before, the aim of this work is to monitor the effect of electron donating groups on the electron transfer dynamics. Following previous reports as discussed in section 2.A., it is expected that the laser pulse of 400 nm would populate the MLCT states which will inject electrons into the conduction band of TiO_2. Immediately after electron injection, the hole is expected to be transferred to the electron donating groups thus causing an increase in spatial charge separation and the BET dynamics is thus expected to be slower.

It is evident from Figure 8 that the charge recombination reaction is fastest in **7**-TiO_2 system (where there are no secondary electron donating groups). Similar trend is observed for the electron signal as well (Figure 9). The charge recombination reaction is therefore indeed slower in the systems having secondary electron donating groups. Phenol is a better electron donor as compared to tyrosine (as observed from electrochemical studies) and so very likely, in the early time scale, bleach recovery of **6**-TiO_2 system is the slowest, followed by that of **5**-TiO_2, and the recovery of **7**-TiO_2 is the fastest where there are no electron donating groups (Scheme 3). However, in order to confirm that the electron donating groups are indeed participating, it is important to monitor the oxidized donor moiety (tyrosyl and phenoxy cation radical moiety in **5** and **6**, respectively) in the transient spectra. Unfortunately, these radicals absorb below 450

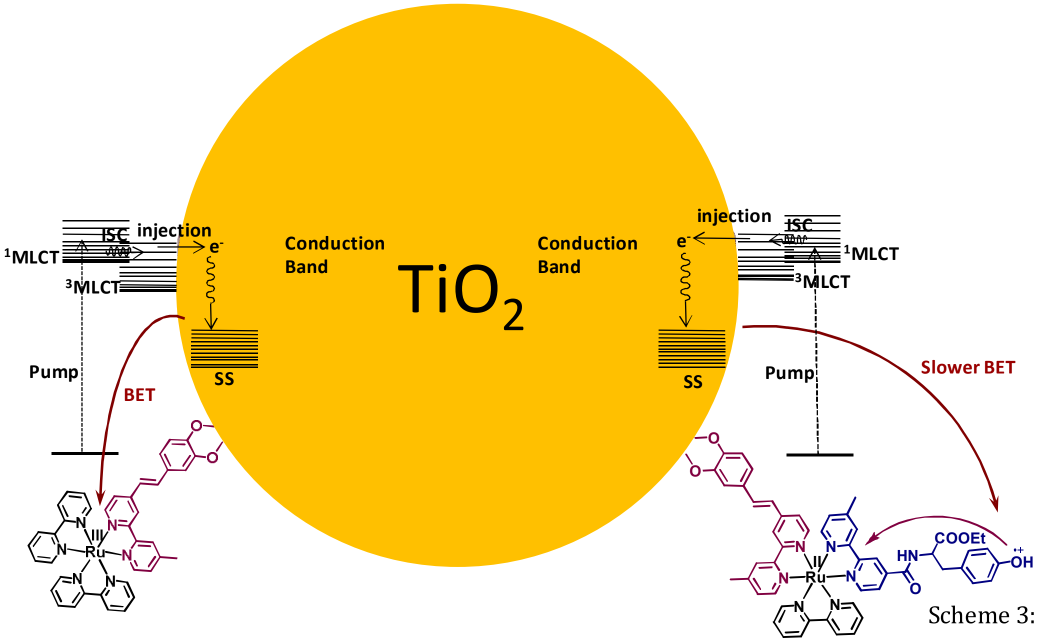
TiO$_2$
Conduction Band
Conduction Band
^{1}MLCT
^{3}MLCT
ISC
injection
e$^-$
SS
Pump
BET
^{1}MLCT
^{3}MLCT
ISC
injection
e$^-$
SS
Pump
Slower BET
Ru
III
II
COOEt
HN
OH
O
N
Scheme 3:

Scheme 3: Schematic representation of the interfacial electron transfer processes in **7**-TiO$_2$ and **5**-TiO$_2$ systems.

nm in the transient spectra[16,51] which is beyond the detection range of our femtosecond transient spectrometer (450 – 1000 nm) and thus our argument cannot be validated by concomitant observation of the formation of the respective radical cation species.

2.D. Conclusions

Two new ruthenium(II) polypyridyl complexes, **5** and **6**, having pendant catechol moiety along with tyrosine or phenol as the electron donating groups have been synthesized and characterized by various analytical and spectroscopic techniques. The catechol functionality allows strong coupling of these sensitizer molecules to TiO$_2$. Electron injection is found to be single exponential and pulse width limited (< 100 fs) indicating electron injection from non-thermalized singlet state (^{1}MLCT), and/or triplet states (^{3}MLCT). BET dynamics is studied by monitoring the recovery of the ground state bleach and the decay kinetics of the injected electron in the conduction band of TiO$_2$. In an early time scale BET dynamics is found to follow the exact order of the electron donating abilities of the secondary electron donating groups and is the slowest in **6**-TiO$_2$ system followed by that of **5**-TiO$_2$ system and is the fastest in **7**-TiO$_2$ system because of the absence of any electron donating groups.

2.E. References

1. Argazzi, R.; Bignozzi, C. A. *J. Am. Chem. Soc.* **1995**, *117,* 11815.
2. Agrazzi, R.; Bignozzi, C. A.; Heimer, T. A.; Castellano, F. N.; Meyer, G. J. *J. Phys. Chem. B* **1997**, *101,* 2591.
3. Bonhote, P.; Moser, J. E.; Vlachopoulos, N.; Walder, L.; Zakeeruddin, S. M.; Humphrey-Baker, R.; Pechy, P.; Grätzel, M. *Chem. Commun.* **1996**, 1163.
4. Bonhote, P.; Moser, J. E.; Humphrey-Baker, R.; Vlachopoulos, N.; Zakeeruddin, S. M.; Walder, L.; Grätzel, M. *J. Am. Chem. Soc.* **1999**, *121,* 1324.
5. Handa, S.; Wietasch, H.; Thelakkat, M.; Durrant, J. R.; Haque, S. A. *Chem. Commun.* **2007**, 1725.
6. Karthikeyan, C. S.; Wietasch, H.; Thelakkat, M. *Adv. Mater.* **2007**, *19*, 1091.
7. Hirata, N.; Lagref, J. J.; Palomares, E. J.; Durrant, J. R.; Nazeeruddin, M. K.; Grätzel, M.; Censo, D. D. *Chem. Eur. J*. **2004**, *10*, 595.
8. Snaith, H. J.; Karthikeyan, C. S.; Petrozza, A.; Teuscher, J.; Moser, J. E.; Nazeeruddin, M. K.; Thelakkat, M.; Grätzel, M. *J. Phys. Chem. C* **2008**, *112,* 7562-7566.
9. Haque, S. A.; Handa, S.; Peter, K., Palomares, E.; Thelakkat, M.; Durrant, J. R. *Angew. Chem. Int. Ed.* **2005***, 44,* 5740.
10. Willinger, K.; Fischer, K.; Kisselev, R.; Thelakkat, M. *J. Mater. Chem.* **2009**, *19*, 5364.
11. Li, J. Y.; Chen, C. Y.; Chen, J. G.; Tan, C. J.; Lee, K. M.; Wu, S. J.; Tung, Y. L.; Tsai, H. H.; Ho, K. C.; Wu, C. G. *J. Mater. Chem.* **2010**, *20*, 7158.
12. Wolpher, H.; Sinha, S.; Pan, J.; Johansson, A.; Lundqvist, M. J.; Persson, P.; Lomoth, R.; Bergquist, J.; Sun, L.; Sundstrom, V.; Akermark, B.; Polivka, T. *Inorg. Chem.* **2007***, 46,* 638.
13. Pan, J.; Xu, Y.; Benko, G.; Feyziyev, Y.; Styring, S.; Sun, L.; Akermark, B.; Polivka, T.; Sundstrom, V. *J. Phys. Chem. B* **2004***, 108,* 12904.
14. Ramakrishna, G.; Jose, D. A.; Krishna Kumar, D.; Das, A.; Palit, D. K.; Ghosh, H. N. *J. Phys. Chem. B* **2005**, *109*, 15445.
15. McCafferty, D. G.; Bishop, B. M.; Wall, C. G.; Hughes, S. G.; Mecklenberg, S. L.; Meyer, T. J.; Erickson, B. W. *Tetrahedron* **1995**, *51*, 1093.
16. Ghanem, R.; Xu, Y.; Pan, J.; Hoffmann, T.; Andersson, J.; Polivka, T.; Pascher, T.; Styring, S.; Sun, L.; Sundstrom, V. *Inorg. Chem.* **2002**, *41*, 6258.
17. Hayes, M. A.; Meckel, C.; Schatz, E.; Ward, M. D. *J. Chem. Soc., Dalton Trans.* **1992**, 703.

18. Shukla, A. D.; Whittle, B.; Bajaj, H. C.; Das, A.; Ward, M. D. *Inorg. Chim. Acta* **1999**, *285*, 89.
19. Fasman, G. D. *Handbook of Biochemistry and Molecular Biology, Proteins, I,* CRC Press, **1976**.
20. Berlman, I. B. *Handbook of Fluorescence Spectra of Aromatic Molecules*, Academic Press, **1971**.
21. Jose, D. A.; Kar, P.; Koley, D.; Ganguly, B.; Thiel, W.; Ghosh, H. N.; Das, A. *Inorg. Chem.* **2007**, *46*, 5576.
22. Kalyanasundaram, K. *Photochemistry of Polypyridine and Porphyrin Complexes*, Academic Press, London, **1992**, Chapter 6.
23. Tommos, C.; Skalicky, J. J.; Pilloud, D. L.; Wand, J.; Dutton, P. L. *Biochemistry* **1999**, *38*, 9495.
24. S here stands for Sensitizer. It therefore denotes complex **5** and **6**.
25. Kuang, D.; Wenger, B.; Klein, C.; Moser, J. E.; Baker, R. H.; Zakeeruddin, S. M.; Grätzel, M. *J. Am. Chem. Soc.* **2006**, *128*, 4146.
26. Moser, J.; Punchihewa, S.; Infelta, P. P.; Grätzel, M. *Langmuir* **1991**, *7*, 3012.
27. Rajh, T.; Chen, L. X.; Lukas, K.; Liu, T.; Thurnauer, M. C.; Teide, D. M. *J. Phys. Chem. B* **2002**, *106*, 10543.
28. Kar, P.; Verma, S.; Das, A.; Ghosh, H. N. *J. Phys. Chem. C* **2009**, *113,* 7970.
29. Kar, P.; Verma, S.; Sen, A.; Das, A.; Ganguly, B.; Ghosh, H. N. *Inorg. Chem.* **2010**, *49*, 4167.
30. Verma, S.; Kar, P.; Das, A.; Palit, D. K.; Ghosh, H. N. *J. Phys. Chem. C* **2008**, *112*, 2918.
31. Verma, S.; Kar, P.; Das, A.; Palit, D. K.; Ghosh, H. N. *Chem. Eur. J.* **2010**, *16*, 611.
32. Ramakrishna, G.; Singh, A. K.; Palit, D. K.; Ghosh, H. N. *J. Phys. Chem. B* **2004**, *108*, 1701.
33. Kaniyankandy, S.; Verma, S.; Mondal, J. A.; Palit, D. K.; Ghosh, H. N. *J. Phys. Chem. C* **2009**, *113*, 3593.
34. Ramakrishna, G.; Ghosh, H. N.; Singh, A. K.; Palit, D. K.; Mittal, J. P.; *J. Phys. Chem. B* **2001**, *105*, 12786.
35. a) Ramakrishna, G.; Verma, S.; Jose, D. A.; Krishna Kumar, D.; Das, A.; Palit, D. K.; Ghosh, H. N. *J. Phys. Chem. B* **2006**, *110*, 9012; b) Verma, S.; Kar, P.; Das, A.; Ghosh, H. N. *Chem. Eur. J.* **2011**, *17*, 1561.
36. Cannizo, A.; Mourik, F. V.; Gawelda, W.; Zgrablic, G.; Bressler, C.; Chergui, M. *Angew. Chem. Int. Ed.* **2006***, 45,* 3174.

37. Kuciauskas, D.; Monat, J. E.; Villahermosa, R.; Gray, H. B.; Lewis, N. S.; McCusker, J. K. *J. Phys. Chem. B* **2002**, *106*, 9347.

38. McCusker, J. *Acc. Chem. Res*. **2003**, *36*, 876.

39. Henry, W.; Coates, C. G.; Brady, C.; Ronayne, K. L.; Matousek, P.; Towrie, M.; Botchway, S. W.; Parker, A. W.; Vos, J. G.; Browne, W. R.; McGarvey, J. J. *J. Phys. Chem. A*, **2008**, *112*, 4537.

40. Vlcek Jr., A. *Coord. Chem. Rev*. **2000**, *200*, 933.

41. Zhang, J. Z. *Acc. Chem. Res*. **1997**, *30*, 423.

42. Colombo Jr, D. P.; Bowman, R. M. *J. Phys. Chem*, **1996**, *100*, 18445.

43. Ghosh, H. N. *J. Phys. Chem. B* **1999**, *103*, 10382.

44. Hannapel, T.; Burfeindt, B.; Storck, W.; Willig, F. *J. Phys. Chem B*, **1997**, *101*, 6799

45. Asbury, J. B.; Hao, E.; Wang, Y.; Ghosh, H. N.; Lian, T. *J. Phys. Chem. B* **2001**, *105*, 4545.

46. Asbury, J. B.; Ellingson, R. J.; Ghosh, H. N.; Ferrere, S.; Nozik, A.; Lian, T. *J. Phys. Chem. B* **1999**, *103*, 3110.

47. Benko, G.; Kallioinen, J.; Korppi-Tommola, J. E. I.; Yartsev, A. P.; Sundstrom, V. *J. Am. Chem. Soc.*, **2002**, *124*, 489.

48. Miller, R. J. D.; McLendon, G. L.; Nozik, A. J.; Schmickler, W.; Willig, F. *Surface Electron Transfer Processes*, VCH Publisher, Inc., Chapter 5.

49. She, C.; Guo, J.; Lian, T. *J. Phys. Chem. B*, **2007**, *111*, 6903.

50. She, C.; Guo, J.; Irle, S.; Morokuma, K.; Mohler, D. L.; Zabri, H.; Odobel, F.; Youm, K. T.; Liu, F.; Hupp, J. T.; Lian, T. *J. Phys. Chem. A*, **2007**, *111*, 6832.

51. Sjodin, M.; Styring, S.; Wolpher, H.; Xu, Y.; Sun, L.; Hammarstrom, L. *J. Am. Chem. Soc.* **2005**, *127*, 3855.

Chapter 3

Studies of *Resorcinol* Bound Ruthenium(II), Osmium(II), Rhenium(I)-polypyridyl Complexes on Nano-TiO_2 Surface

Inorganic Chemistry **2013**, *52*, 5366-5377

Journal of Physical Chemistry C **2013**, *117*, 3084-3092

New Journal of Chemistry **2013**, *37*, 3100-3108

3.A. Synthesis, steady state and femtosecond transient absorption studies of ruthenium(II) and osmium(II)-polypyridyl complexes on nano-TiO_2 surface in water

3.A.1. Foreword

This problem of fast BET because of the very strong binding in such catecholate bound systems is presumably because of the hydroxyl groups binding to TiO_2 in a very localized manner *i.e.* to a single Ti^{4+} atom forming a five-membered chelate ring.[1-5] If the binding of the enediol dye is made to involve multiple Ti^{4+} centres then the overlap of the dye LUMO with the Ti 3*d* orbital network would not be that localized and one can expect the effective binding to become weaker. Binding of the dye to multiple Ti^{4+} centres is also expected to enhance the electron delocalization in the TiO_2 nanocrystal after initial electron injection which in turn is expected to decrease the BET rate.

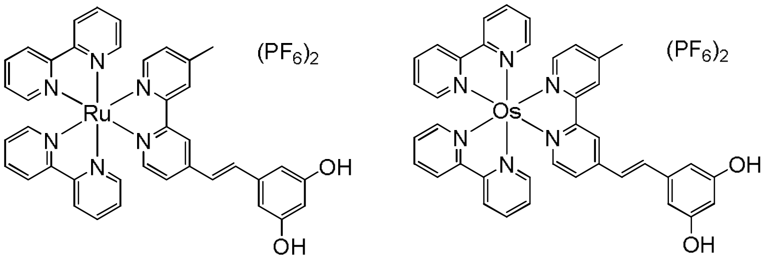

3

4

Scheme 1: Molecular structures of **3** and **4.**

To explore this hypothesis, an innovative ruthenium(II), osmium(II), rhenium(I)-polypyridyl based sensitizer system containing resorcinol instead of catechol, as the enediol anchor has been developed. This section of the chapter studies the effect of the alteration in the anchoring moiety as discussed above, on the interfacial electron transfer dynamics of the ruthenium(II), osmium(II)-polypyridyl complex, **3** and **4**, respectively (Scheme 1), in aqueous environment, as probed by femtosecond transient absorption spectroscopic study. The present work is expected to add significantly to the ongoing research efforts towards the development of aqueous dye sensitized photoelectrochemical fuel cells.[6-8]

3.A.2. Experimental Section (please see Appendix A for details)

3.A.2.A. Synthesis of TiO_2 nanoparticles

TiO_2 nanoparticles have been prepared by controlled hydrolysis of titanium (IV) tetraisopropoxide as discussed in Appendix A. TiO_2 nanoparticles at neutral pH are obtained by following the procedure reported by Wachtveitl and co-workers.[9] To a 15 g/L solution of such nanoparticles, the stabilizing agent PVA (0.1% solution) is added. The pH is then raised to about 6 by removing the protons *via* treatment with Dowex

MR-3 mixed bed ion-exchange resin. The final adjustment to neutral pH is done by adding aqueous NaOH dropwise.

3.A.2.B. Synthesis

3.A.2.B.1. 4-(3,5-dimethoxystyryl)-4'-methyl-2,2'-bipyridine (1): To a solution of 4,4′-dimethyl-2,2′-bipyridine (1.84 g, 10 mmol) in ice-cold THF (30 ml) under N_2, a solution of lithium diisopropylamide (10 mmol; freshly prepared by mixing 6.65 ml of 1.6 M *n*-BuLi in hexanes and 1.325 ml of dry di-isopropylamine at room temperature under N_2) is added dropwise over 15 minutes. The deep chocolate brown solution is stirred at 0 ^{0}C for 1 hour, after which a solution of 3,5-dimethoxybenzaldehyde (1.66 g, 10 mmol) in THF (20 ml) is added dropwise while maintaining the temperature at - 30 ^{0}C. The mixture is allowed to warm to room temperature and stirred overnight. After quenching the reaction with water and evaporation to dryness in vacuum an oily mass is obtained. This is dissolved in chloroform and solvent extraction is done to remove the ionic impurities. The organic layer is dried with anhydrous sodium sulphate and evaporated to give a crude oily residue (the crude intermediate alcohol) which is used without purification for the subsequent dehydration. The oil is dissolved in dry pyridine (50 ml) and a solution of $POCl_3$ (1.16 ml, 12.5 mmol) in dry pyridine (50 ml) is added dropwise under N_2 at room temperature with vigorous stirring. After 1 hour the pyridine is evaporated in vacuum and crushed ice is added; the mixture is left for 30 minutes to ensure that all residual $POCl_3$ is destroyed. The pH of the aqueous solution is adjusted to between 3 and 4, and unwanted organic materials are extracted with CH_2Cl_2. The aqueous solution is then made just alkaline (pH~8) and the crude products are extracted into CH_2Cl_2 which is subsequently dried with anhydrous sodium sulphate and evaporated to give a yellowish brown solid. This is purified by column chromatography over silica using chloroform/methanol as the eluent to give the desired product in pure form. Yield: 1.66 g, 50%. ESI-MS (*m/z*): Calculated for $C_{21}H_{20}N_2O_2$ – 332.15, Observed – 333.27 $[M + 1]^+$; ^{1}H NMR (200 MHz, $CDCl_3$): δ (ppm) 8.39 (1H, d, *J* = 5 Hz, $H^{6'}$ (bpy)); 8.35 (1H, d, *J* = 5 Hz, $H^{5'}$ (bpy)); 8.30 (1H, s, $H^{3'}$ (bpy)); 8.06 (1H, s, H^3 (bpy)); 7.09 (1H, d, *J* = 13.2 Hz, $H^{ethenyl}$); 7.05 – 7.02 (1H, m, H^6 (bpy)); 6.87 (1H, d, *J* = 5 Hz, H^5 (bpy)); 6.80 (1H, d, *J* = 16.4 Hz, $H^{ethenyl}$); 6.47 (2H, d, *J* = 2 Hz, H^2(phenyl)); 6.24 - 6.21 (1H, m, H^4(phenyl)); 3.57 (6H, s, $-OCH_3$); 2.17 (3H, s, $-CH_3$) IR (KBr pellet, cm^{-1}) 1591 (ν(C=C)), 1056 (ν(C-O)). Elemental Analysis: Calculated for $C_{21}H_{20}N_2O_2$: C, 75.88; H, 6.06; N, 8.43. Found: C, 75.5; H, 6.26; N, 8.47.

3.A.2.B.2. 5-(2-(4'-methyl-2,2'-bipyridin-4-yl)vinyl)benzene-1,3-diol (2): 32 ml analytical grade pyridine is taken in a round bottomed flask equipped for distillation and 35.2 ml concentrated hydrochloric acid is added to it with continuous stirring. This mixture is then heated for two hours at 220 ^{0}C to distil off the water from the mixture. After cooling to 140 ^{0}C, **1** (1 g, 3.01 mmol) is added as a solid and the reaction mixture is stirred and heated at 200 ^{0}C for 4 hours. The reaction mixture is then cooled down and 30 ml of water is added to dissolve the crude mixture. The pH of the resulting solution is then raised to 6 - 6.5 by slowly adding a dilute solution of caustic soda to precipitate the desired compound. This precipitate is then filtered through a grade 4 sintered glass crucible, washed with large volumes of water and dried overnight in a vacuum desiccator to give compound **2** in pure form. Yield: 870 mg, 95%. ESI-MS (*m/z*): Calculated for $C_{19}H_{16}N_2O_2$ – 304.12, Observed – 305.4 $[M + 1]^+$; ^1H NMR (200 MHz, CD_3CN): δ (ppm) 8.58 (1H, d, *J* = 5.2 Hz, $H^{6'}$ (bpy)); 8.53 (1H, d, *J* = 5 Hz, $H^{5'}$ (bpy)); 8.38 (1H, s, $H^{3'}$ (bpy)); 8.16 (1H, s, H^3 (bpy)); 7.57 (1H, d, *J* = 5 Hz, H^6 (bpy)); 7.42 (1H, d, *J* = 16.2 Hz, $H^{ethenyl}$);7.33 (1H, d, *J* = 4.6 Hz, H^5 (bpy)); 7.13 (1H, d, *J* = 16.4 Hz, $H^{ethenyl}$); 6.59 - 6.58 (2H, m, H^2(phenyl)); 6.28 - 6.26 (1H, m, H^4(phenyl)); 2.49 (3H, s, $-CH_3$) IR (KBr pellet, cm^{-1}) 3430 (ν(OH)), 1589 (ν(C=C)). Elemental Analysis: Calculated for $C_{19}H_{16}N_2O_2$: C, 74.98; H, 5.3; N, 9.2. Found: C, 75.2; H, 5.15; N, 9.1.

3.A.2.B.3. {bis-(2,2′-bpy)-(5-[2-(4'-methyl-2,2'-bipyridin-4-yl)vinyl]benzene-1,3-diol)} ruthenium(II) hexafluorophosphate (**3**): $Ru(bpy)_2Cl_2.2H_2O$ (86 mg, 0.165 mmol) and **2** (50.2 mg, 0.165 mmol) are refluxed in ethanol for 8 hours with continuous stirring. The solvent is then evaporated and the product is made soluble in a minimum volume of water. Saturated aqueous NH_4PF_6 (10 mole equivalents) is added to the resulting solution to precipitate the desired Ru^{II}-polypyridyl complex as the hexafluorophosphate salt. This is kept as such for 4-5 hours in a refrigerator to ensure complete precipitation after which it is filtered, washed with large volumes of cold water and dried in a vacuum desiccator. The crude compound so obtained is purified by column chromatography over silica using acetonitrile/water/saturated aqueous KPF_6 as the eluent. The second fraction is collected and the solvent is removed to isolate a red solid which is redissolved in dichloromethane and two drops of acetonitrile and solvent extraction is done to remove the excess KPF_6 used in the eluent. The organic phase is dried over anhydrous sodium sulphate and is evaporated to dryness to give the desired product in pure form. Yield: 58.3 mg (35%). ESI-MS (*m/z*): Calculated for $C_{39}H_{32}N_6O_2PF_6Ru$ 863.09 $[M - PF_6^-]^+$, Observed 863.43 $[M - PF_6^-]^+$; ^1H NMR (200 MHz, CD_3CN): δ (ppm) 8.62 – 8.58 (1H, m, $H^{6'}$ (bpy-res)); 8.53 – 8.50 (2H, m, H^6 (bpy) and/or $H^{6'}$ (bpy); 8.49 – 8.46 (2H, m, H^6 (bpy) and/or $H^{6'}$ (bpy)); 8.09 - 8.01 (4H, m, H^3 (bpy) and $H^{3'}$ (bpy)); 7.81 (1H, d, *J* = 5.6 Hz, H^4 (bpy) or $H^{4'}$ (bpy)); 7.75 – 7.68 (3H, m, H^4 (bpy) and $H^{4'}$ (bpy)); 7.60 (1H, d, *J* = 4.6 Hz, $H^{5'}$ (bpy-res)); 7.55 – 7.49 (2H, m, $H^{3'}$ (bpy-res) and $H^{ethenyl}$); 7.43 – 7.36 (5H, m, H^5 (bpy) and $H^{5'}$ (bpy), H^3 (bpy-res)); 7.29 – 7.22 (3H, m, H^5 (bpy-res) and H^6 (bpy-res), $H^{ethenyl}$); 6.62 (2H, d, *J* = 2 Hz, H^2(phenyl)); 6.34 (1H, t, *J* = 2 Hz, H^4(phenyl)); 2.56 (3H, s, $-CH_3$(bpy-res)). IR (KBr pellet, cm^{-1}) 3432 (ν(OH)), 1606 (ν(C=C)), 840 (ν(PF_6)). Elemental Analysis: Calculated for $C_{39}H_{32}N_6O_2P_2F_{12}Ru$: C, 46.48; H, 3.20; N, 8.34; Found: C, 46.47; H, 3.18; N, 8.38.

3.A.2.B.4. {bis-(2,2′-bpy)-(5-[2-(4'-methyl-2,2'-bipyridin-4-yl)vinyl]benzene-1,3-diol)} osmium(II) hexafluorophosphate (**4**): This is prepared by a similar procedure as adopted for the synthesis of **3**. $Os(bpy)_2Cl_2.2H_2O$ (100 mg, 0.165 mmol) and **2** (50.2 mg, 0.165 mmol) are refluxed in ethanol for 8 hours with continuous stirring. Then the solvent is evaporated and the product is made soluble in a minimum volume of water.

Saturated aqueous KPF_6 (10 mole equivalents) is added to the resulting solution to precipitate the desired Os^{II}-polypyridyl complex as the hexafluorophosphate salt. This is kept as such for 4-5 hours in a refrigerator to ensure complete precipitation after which it is filtered, washed with cold water and dried in a vacuum desiccator. The crude compound so obtained is purified by column chromatography over alumina using acetonitrile/water/saturated aqueous KPF_6 as the eluent. The last fraction is collected and the solvent is removed to isolate a greenish-black solid which is redissolved in dichloromethane and two drops of acetonitrile and solvent extraction is done to remove the excess KPF_6 used in the eluent. The organic phase is dried over anhydrous sodium sulphate and is evaporated to dryness to give the desired product. Yield: 57.6 mg (32%). ESI-MS (*m/z*): Calculated for $C_{39}H_{32}N_6O_2PF_6Os$ 953.15 $[M - PF_6^-]^+$, Observed 953.53 $[M - PF_6^-]^+$, 404.21 $[M - 2PF_6^-]^{2+}$; ^1H NMR (200 MHz, CD_3CN): δ (ppm) 8.57 – 8.49 (1H, m, $H^{6'}$ (bpy-res)); 8.51 – 8.47 (2H, m, H^6 (bpy) and/or $H^{6'}$ (bpy); 8.47 – 8.43 (2H, m, H^6 (bpy) and/or $H^{6'}$ (bpy)); 7.89 – 7.81 (4H, m, H^3 (bpy) and $H^{3'}$ (bpy)); 7.71 (1H, d, *J* = 5.6 Hz, H^4 (bpy) or $H^{4'}$ (bpy)); 7.66 – 7.62 (3H, m, H^4 (bpy) and $H^{4'}$ (bpy)); 7.54 (1H, d, *J* = 4.6 Hz, $H^{5'}$ (bpy-res)); 7.50 – 7.42 (2H, m, $H^{3'}$ (bpy-res) and $H_{ethenyl}$); 7.34 – 7.25 (5H, m, H^5 (bpy) and $H^{5'}$ (bpy), H^3 (bpy-res)); 7.21 – 7.13 (3H, m, H^5 (bpy-res) and H^6 (bpy-res), $H^{ethenyl}$); 6.61 (2H, d, *J* = 2 Hz, H^2(phenyl)); 6.32 (1H, t, *J* = 2 Hz, H^4(phenyl)); 2.64 (3H, s, $-CH_3$(bpy-res)). IR (KBr pellet, cm^{-1}) 3433 (ν(OH)), 1608 (ν(C=C)), 838 (ν(PF_6)) Elemental Analysis: Calculated for $C_{39}H_{32}N_6O_2P_2F_{12}Os$: C, 42.7; H, 2.94; N, 7.66; Found: C, 42.6; H, 2.9; N, 7.8.

3.A.3. Results and Discussion

The synthetic methodology adopted for the synthesis of **3** and **4** is shown in Scheme 2. Synthesis of **1** is done *via* a lithium diisopropyl amide mediated C-C bond formation reaction to give the precursor alcohol which is dehydrated to **1** using $POCl_3$ in pyridine

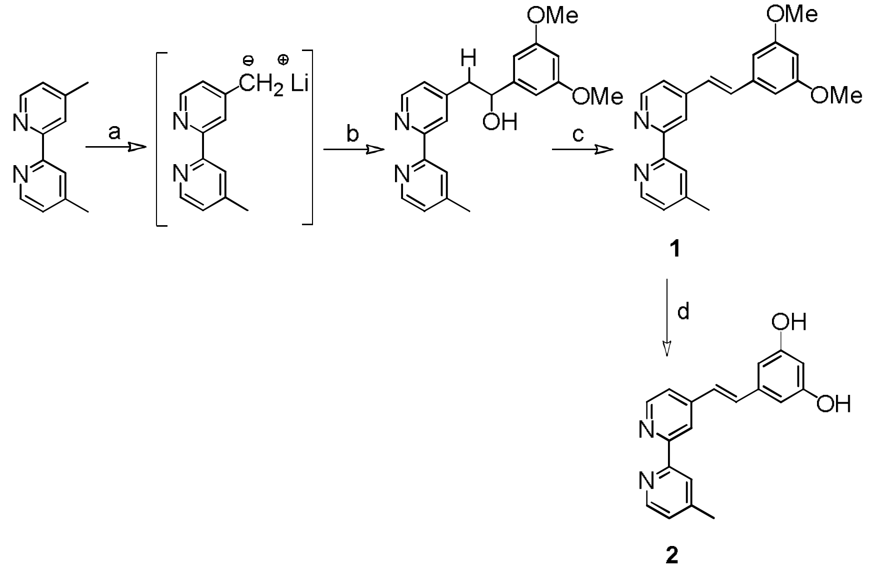

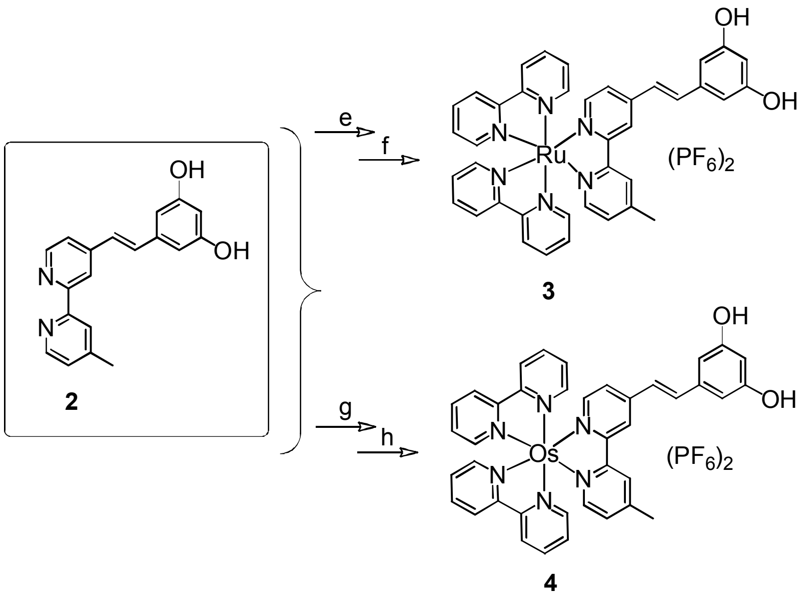

a = LDA, THF, 0 °C; b = 3,5-dimethoxybenzaldehyde, THF, - 30 °C;
c = $POCl_3$, pyridine, RT; d = pyridine, HCl, 200 °C; e= $Ru(bpy)_2Cl_2.2H_2O$, EtOH, reflux;
f = satd. aq. NH_4PF_6; g= $Os(bpy)_2Cl_2$, EtOH, reflux; h = satd. aq. NH_4PF_6

Scheme 2: Reaction scheme for the synthesis of **3** and **4.**

solvent that itself acts as the base. Removal of the methyl group in **1** is done with molten pyridinium hydrochloride to give **2**. The final ruthenium- and osmium- complexes, **3** and **4**, are prepared by reactions of **2** respectively with $Ru(bpy)_2Cl_2$ and $Os(bpy)_2Cl_2$ in ethanol. The purity of the complexes is checked by different analytical and spectroscopic methods and the analytical data matches well with that of the expected formulation. 2,2′-bipyridine (bpy) ligands are employed to make sure that the MLCT excited state has electrons localized on the surface-bound ligand for all the sensitizers. This is because the surface bound ligand *i.e.* the bipyridine ligand with appended resorcinol moiety, because of its extended conjugated structure, is energetically low lying as compared to the unsubstituted bipyridine ligands (*vide infra*). As a result of the low lying nature of the surface bound bipyridine-resorcinol ligand in **3** and **4**, upon excitation, population of the corresponding MLCT state is expected to dominate over that constituted by the other unsubstituted ligands. Moreover, the unsubstituted 2,2’-bpy ligands being at higher energies, electron density from these ligands is expected to get transferred to the surface bound bipyridine-resorcinol ligand with time.

Absorption and emission spectra, recorded for **3** and **4** in water are shown in Figure 1. The absorption spectrum is characterised by strong ligand centered π-π* transitions at 288 nm and 296 nm for **3** and **4**, respectively; while the band at 330 nm can be assigned either to delocalized interligand charge transfer or MC transitions.[10-11] The familiar metal to ligand charge transfer comprising of overlapping ^{1}MLCT based $d_{M(II)} \rightarrow \pi^*_{bpy}$ [M = Ru^{II}/Os^{II}] manifests in the low energy broad absorption band peaking at 460 nm for **3** ($\varepsilon = 1.58 \times 10^4$ M^{-1} cm^{-1}) and at 488 nm for **4** ($\varepsilon = 1.44 \times 10^4$ M^{-1} cm^{-1}).[10-11] The Os^{II} centre, as compared to the Ru^{II} centre, is characterised by a significantly higher spin orbit coupling and this is responsible for the allowedness of the spin forbidden ^{3}MLCT based $d_{Os(II)} \rightarrow \pi^*_{bpy}$ transition,[11,12] resulting in another broad absorption between 550-710 nm for **4** (ε_{500} = 1.437 × 10^4 M^{-1} cm^{-1}, ε_{630} = 3730 M^{-1} cm^{-1}). The emission spectrum of **3** consists of a broad ^{3}MLCT based emission with λ_{max} at 640 nm when excited at 460 nm. For **4**, this emission peaks at λ_{max} = 750 nm when excited at either 488 nm or at 630 nm.

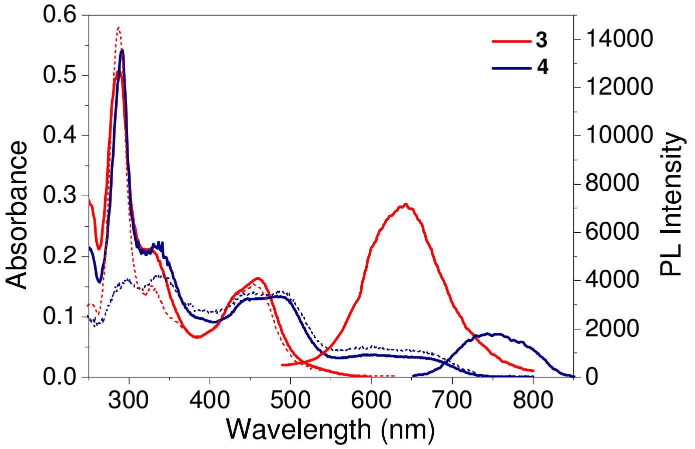

Figure 1: Absorption and emission spectra of **3** (red) and **4** (blue) in water. The concentrations of both **3** and **4** are 1 × 10^{-5} M. The dotted lines show the normalised excitation spectra.

Excitation spectra of **3** and **4** (Figure 1) agree well with their respective absorption and spectra indicating that the observed photoluminescence is from the sensitizers.[13]

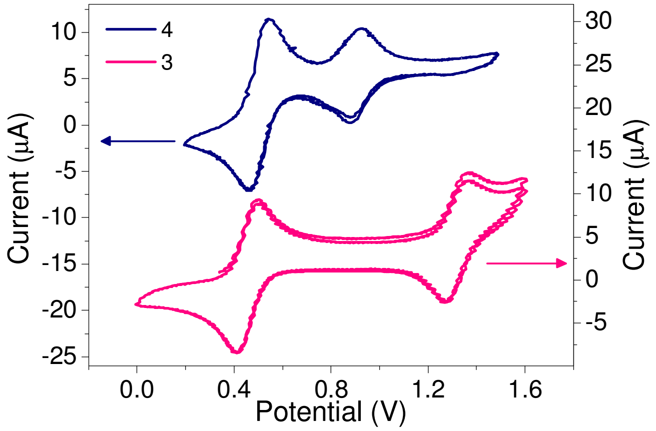

Figure 2: Cyclic Voltammogram of **3** (pink, right hand side layer in figure) and **4** (navy blue, left hand side layer in figure) in acetonitrile. Ag/AgCl (saturated KCl) has been used as the reference electrode. Scan rate for both the scans shown above is 100 mV/s. Ligand based reductions are omitted since only the metal based redox potentials have been used in the interpretation of data throughout the chapter. The peak on the left side in both the voltammograms is due to the ferrocene/ferrocenium couple which has been added as an internal standard. A difference in the concentrations of potassium chloride solutions in the reference electrodes presumably causes the difference in the $E_{1/2}$ $^{Fc/Fc+}$ values in the two voltammograms.

Electrochemical studies of **3** (Figure 2) reveals a reversible Ru^{2+}/Ru^{3+} redox couple at 1.25 V (ΔE = 69 mV) and only two bipyridyl centered reductions can be observed at -1.39 V and -1.52 V in the + 2V to -2V potential window available. For **4**, the Os^{2+}/Os^{3+}

reversible redox couple appears at 0.8 V (ΔE = 58 mV) (Figure 2) and bipyridyl centered reductions can be seen at -1.37 V and -1.58 V. An important point to note is that the metal centered redox potential values in these resorcinol dyes are significantly more negative than the respective catechol dyes, **5** and **6** (Scheme 3).

For **5**, the Ru^{2+}/Ru^{3+} redox couple appears at 1.32 V while the Os^{2+}/Os^{3+} redox couple appears at 1.14 V in **6**.[14,15] Intra- and/or intermolecular hydrogen bonding is expected to be more prominent for the catechol moiety in **5** and **6** than in the resorcinol counterpart in **3** and **4**. Probably a greater participation of the catechol moiety in this aforesaid hydrogen bonding curtails the electron density from active involvement in +R resonance effects towards the sensitizer core in **5** and **6**.[16-18] This effect, being most likely less dominant for the resorcinol moiety in **3** and **4**, is presumably being reflected in lower values of the metal centered redox potentials. Also, this effect is most likely more prominent in case of the Os^{II}- based dyes and hence, a greater difference in the potential values is seen.

.

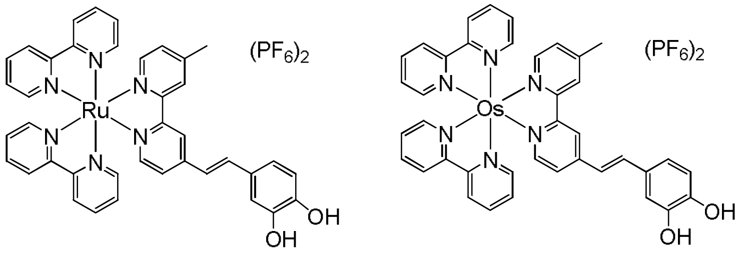

5 6

Scheme 3: Molecular structures of **5** and **6**.

Knowledge about the position of the excited state of the dye with respect to the conduction band of TiO_2 is essential in order to comprehend the feasibility of electron injection from the dye to the semiconductor nanoparticles. E_{0-0} transition energy for the ^{3}MLCT states of **3** and **4** are calculated to be 2.16 eV and 1.78 eV, respectively, from the respective excitation and emission spectra. The excited state potentials $E(S^+/S^*)$ are thus -0.91 V and -0.98 V for **3** and **4** respectively following the equation $[E(S^+/S^*)] = [E(S^+/S)] - E_{0-0}$.[19,20] The E_{0-0} values for the ^{1}MLCT states are approximated to be 2.41 eV and 2.21 eV for **3** and **4**, respectively, from the onset of optical absorption (unlike the estimation of E_{0-0} for ^{3}MLCT states which have been done as stated above). The corresponding excited state potentials are thus -1.16 V and -1.41 V for **3** and **4**, respectively. The excited state potentials being above the conduction band level, electron injection from the excited state of the sensitizers into the conduction band of TiO_2 becomes thermodynamically feasible.[21,22]

The absorption spectrum becomes broad with simultaneous increase in absorbance on steady addition of an aqueous solution of TiO_2 nanoparticles to the aforesaid complexes (Figures 3a and b) which indicates significant interaction of the dye molecules with the

TiO_2 nanoparticles. Unlike many dyes with pendant catechol groups for binding to TiO_2, no new CT band appears.[23-25] This suggests weaker electronic coupling of the resorcinol dyes, **3** and **4**, to TiO_2 than the catechol dyes **5** and **6.**

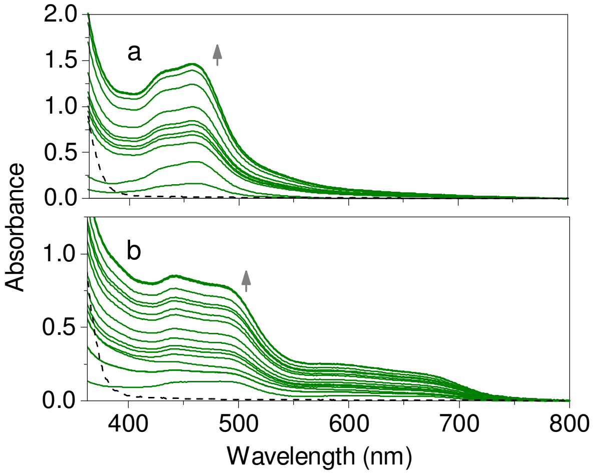

Figure 3: Changes in absorbance of (a) **3** (1.034×10^{-5} M) on TiO_2 (0 – 4.06 g/L) and (b) **4** (0.9266×10^{-5} M) on TiO_2 (0 – 3.52 g/L) in water. Shown in dashed line is the spectral profile of TiO_2 (15 g/L) in water.

This conclusion is further supported by the fact that the emission spectrum of **3** and **4** in solution are identical to that on TiO_2. However, the MLCT absorption of the dyes become broad and the OD increases upon binding to TiO_2.[14,15,19,26-30]

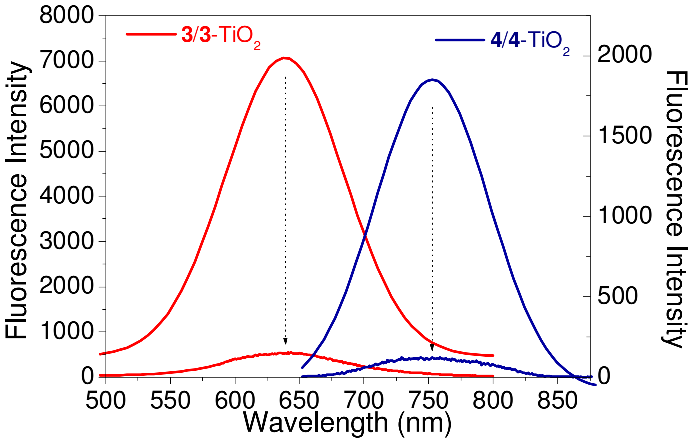

Figure 4: Fluorescence quenching of **3** (1×10^{-5} M) (left layer, red) and **4** (1×10^{-5} M) (right layer, blue) on TiO_2 (5 g/L) water.

The emission intensity is radically diminished on TiO_2 surface (Figure 4) suggesting substantial quenching of the excited state by electron injection[15,19,27,28,31] and hence negligible contribution of excited state features in the transient absorption data on TiO_2 (*vide infra*).

For a comprehensive understanding of the electron transfer dynamics of **3** and **4** on TiO_2 nanoparticle surface, a detailed study of the excited state dynamics of the free sensitizer molecules is essential. Transient absorption spectrum has been recorded both in acetonitrile and in water and the kinetic data are very similar in the two solvents.

Figure 5 shows the transient absorption spectrum of **3** in water. The transient absorption spectrum of **3** shows a broad absorption ranging from 500 to 1000 nm. Recent work by Chergui *et al.* employing broadband fluorescence spectroscopy has revealed that ISC in ruthenium polypyridyl complexes occurs in 15 ± 10 fs.[32] The absorption feature, therefore, in the transient absorption spectrum can be assigned to excited *triplet* state absorption.[14,23,26,27,29] This is accompanied by a simultaneous negative absorption due to the ground state bleach below 500 nm. [14,23,26,29]

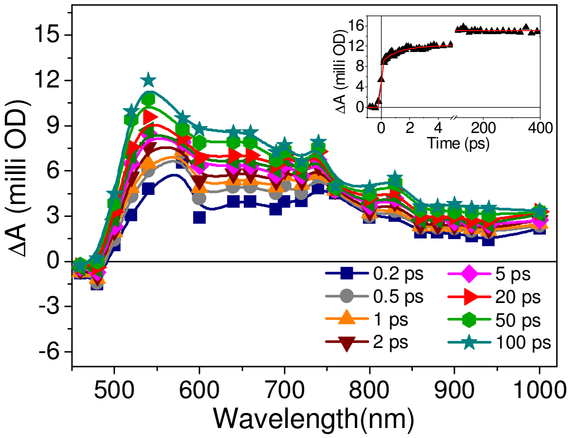

Figure 5: Transient absorption spectrum of **3** at different delay times in water measured after 400 nm (fwhm < 120 fs) excitation. Concentration of **3** is ~ 200 μM. Shown in inset is the kinetic trace for **3** monitored at 900 nm

The kinetic trace of **3** at 900 nm (Figure 5 inset) shows a 1 ps (19.2%) and a 25 ps (23.2%) increase in oscillator strength after the initial excited state population occurring in pulse width limited time (< 120 fs, +57.6%). McCusker *et al*. studied the ultrafast dynamics of the excited state evolution of a series of ruthenium polypyridyl complexes pumping at 400 nm and could observe a 5 ps component in the pump-probe difference absorption kinetics monitored at 532 nm that they assigned as the vibrational cooling dynamics in the ^{3}MLCT excited state.[33] Their assignment was corroborated by the fact that similar dynamics could again be observed for a comparable complex when excited with a 400 nm pump and probed at 510 nm; while with 480 nm pump at the same probe wavelength the complex did not show any dynamics beyond 200 fs.[34] Interestingly, in the complex with appended phenyl rings, the component due to vibrational cooling decreased to 2 ps because of the phenyl ring rotation that acted as an easy pathway for dispelling the excess vibrational energy. Therefore, considering the non rigid structure and also the appended hydroxyl groups that might arbitrate additional relaxation pathways - more so in solvent water, it would not be injudicious to assign the 1 ps component to vibrational relaxation in the ^{3}MLCT manifolds. In addition, the average solvation relaxation time, $<\tau_s>$, in water and in acetonitrile is reported to be ~ 500-600 fs.[35] This and the fact that on TiO_2 surface we have a similar 1.5 ps injection component whose amplitude is probe wavelength dependent (*vide infra*) rules out the possibility of this component in the free dye arising due to solvation.

As told before, the average solvation relaxation time, $<\tau_s>$, in water and in acetonitrile is reported to be ~ 500-600 fs. This eliminates the possibility of the 25 ps component arising due to solvation. The transient studies have been carried out by excitation at the blue edge of the MLCT band. This necessitates simultaneous electron localization in all the three bipyridine ligands after initial photoexcitation. The 25 ps component is therefore tentatively assigned to interligand electron redistribution along the ^{3}MLCT potential energy surface.[36] The lifetime of the MLCT state of Ru^{II}-polypyridyl complexes are known to be > 100 ns[37] so we can safely assume that it is the long lifetime of this state that is mirrored in the decay trace for **3** that does not decay until 400 ps.

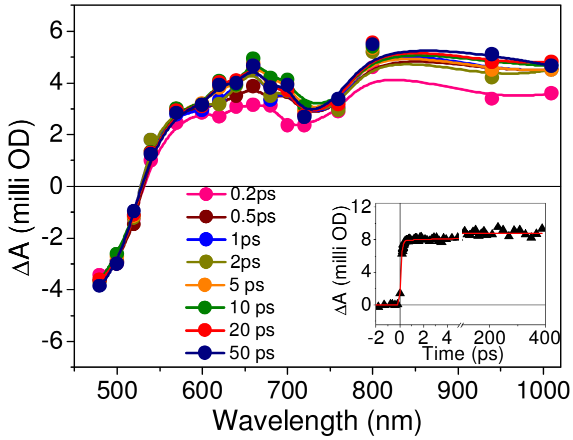

Figure 6: Transient absorption spectrum of **4** at different delay times in water measured after 400 nm (fwhm < 120 fs) excitation. Concentration of **4** is ~ 200 μM. Shown in inset is the kinetic trace for **4** monitored at 900 nm.

The transient absorption spectrum of **4** (Figure 6) shows two bands at 540-720 nm and 760-1000 nm in addition to a negative absorption below 520 nm due to ground state bleach. Following a similar argument as in the case of **3**, these bands are assigned to excited triplet state absorption.[26] An important point to note in the transient absorption spectrum is the absence of any bleach band in the 560-750 nm region, corresponding to the ground state ^{3}MLCT absorption. This is probably due to the higher molar extinction coefficient of the excited state relative to the aforesaid ground state absorption so that the former dominates the transient absorption spectrum.

The kinetic trace monitored for **4** at 900 nm (Figure 6 inset) shows a 13 ps rise (10.2%) after initial population of the excited state (< 120 fs, 89.8%). This 13 ps component is again assigned tentatively to interligand electron redistribution along the ^{3}MLCT potential energy surface.[38]

The redox potential values could be obtained only for two bipyridine ligands in **3** and **4** from the electrochemical studies (*vide supra*). The most positive of these, i.e. -1.39 V for **3** and -1.37 V for **4**, indisputably corresponds to the reduction of the coordinated ligand

2.[14] The other redox potential value is -1.52 V for **3**, *i.e.* 0.13 V more cathodic. On the other hand, this difference is 0.21 V for **4** for which the second reduction appears at -1.58 V. This implies the fact that, compared to **3**, for **4**, the ^{3}MLCT potential energy surface corresponding to the ligand **2** is energetically more distantly placed than the other 2,2′-bipyridine ligands. Considering Marcus normal region behaviour of interligand electron redistribution,[39] this presumably is the reason for which the aforesaid interligand electron redistribution occurs at a faster rate in **4** than in **3**.

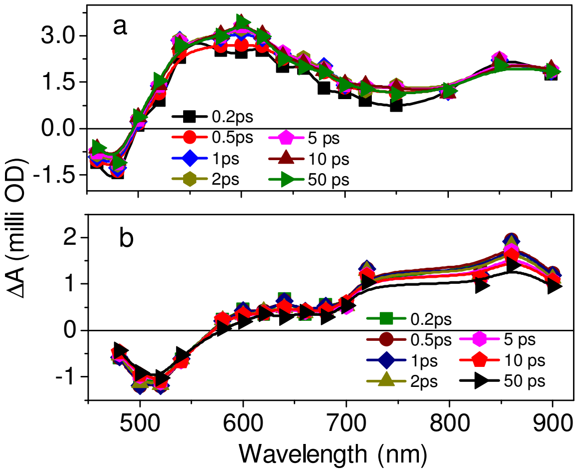

Figure 7: Transient absorption spectrum of (a) **3** and (b) **4** on TiO$_2$ (15 g/L) in water at different delay times measured after 400 nm (fwhm < 120 fs) excitation. Concentrations of **3** and **4** are ~ 100 μM.

Transient absorption spectrum of **3** on TiO$_2$ nanoparticle surface is shown in Figure 7a. The spectrum shows two major absorption bands in the regions 500-700 nm and 760-900 nm. The former band can be irrefutably assigned to the formation of the cation radical (**3**$^{\cdot+}$). Assignment of this band has been made on the basis of the results obtained in a complementary pulse radiolysis experiment where **3**$^{\cdot+}$ has been generated selectively by the reaction of N$_3$ radical with **3** in N$_2$O-saturated aqueous solution (5% acetonitrile + 95% water) (Figure 8a). This assignment is also corroborated by the

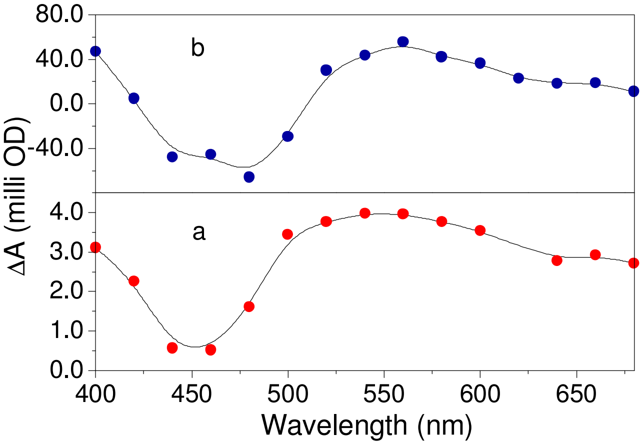

Figure 8: Uncorrected transient absorption spectrum of the cation radical of (a) **3** and (b) **4** obtained from one-electron oxidation in pulse radiolysis.

previously reported transient absorption spectrum of **5** where the cation radical appears in the 500-670 nm region with the absorption peak at 590 nm.[14] Numerous other studies on similar ruthenium polypyridyl complexes corroborate this assignment.[19,23,26] The lower energy absorption band in the 760-900 nm region can be assigned to electrons in the conduction band of TiO_2 nanoparticles. Again, this assignment is corroborated by previous literature reports where it has been shown that electrons in the conduction band can be detected by visible, near IR and mid IR absorption.[40-42] In addition to these bands, a negative absorption can be seen below 500 nm due to the ground state bleach. [14,23,26,29] The transient absorption spectrum of **4** (Figure 7b) again presents two absorption bands between 560-680 nm and 720-900 nm. The first absorption band can again be assigned to the formation of cation radical (**4**$^{\cdot+}$) based on our complementary pulse radiolysis experiment to generate **4**$^{\cdot+}$ selectively as described above and also by previous results from our group on a similar osmium complex (Figure 8b).[26] The cation radical appears at 520-660 nm in this reported complex where there is no double bond between bipyridine and catechol. Apparently, the enhanced conjugation because of the presence of the double bond in **4** shifts the absorption band of the cation radical to higher wavelengths.

In order to slow down the inherently fast BET of catechol bound complexes, several approaches have been adopted by the group of Das and Ghosh (see Chapter 1, Section 1.B.4.D. for details), unfortunately not to much effect. Moreover, for practical applications, such bulky molecules as discussed in Figure 48 might present serious shortcomings in terms of not only synthetic viability but also photocurrent yields because of their lower surface coverage and probable tendency to aggregate. Based on this knowledge we set out on the task of lowering the BET rates by a modification of the molecular skeleton itself, thus avoiding any cumbersome synthesis and exclusive of making the molecule any bulkier and have developed a ruthenium(II), osmium(II), rhenium(I)-polypyridyl based sensitizer system containing resorcinol instead of catechol as the enediol anchor.

Table 1: Lifetimes of the transients for **3**- and **5**-TiO_2 systems at different wavelengths

System	Monitoring Wavelength (nm)	Lifetimes
3-TiO_2	480	< 120 fs (-100%), 1.2 ps (+29%), 33 ps(+1.3%), > 400 ps (+69.7%)
	640	< 120 fs (+89.5%), 1.5 ps (+10.5%), 33 ps (-3.1%), > 400 ps (-96%)
	900	< 120 fs (+92.5%), 1.5 ps (+7.5%), 33 ps(-6.5%), > 400 ps (-92%)
5-TiO_2	480	< 120 fs (-100%), 1.5 ps (+37.6%), 70 ps (+19.4%), > 400 ps (+43%)
	900	< 120 fs (+100%), 1.5 ps (- 34.8%), 70 ps (-26.8%), > 400 ps (-38.4%)

An analysis of the kinetic traces of **3**-TiO_2 at various wavelengths presents the most striking results. Lower panel of figure 9 shows a comparison of the normalized kinetic traces for the ground state bleach recovery of **3**-TiO_2 and **5**-TiO_2 systems both monitored at 480 nm.

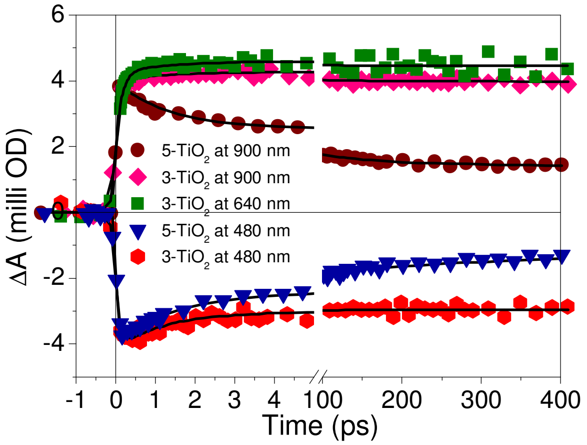

Figure 9: Comparison of the kinetic traces of **3** and **5** adsorbed on TiO_2 at 480 nm (lower panel) and comparison of the electron injection dynamics of **3**-TiO_2 system with that of **5**-TiO_2 system with the kinetic traces normalized with respect to the ultrafast growth component (upper panel).

The kinetic trace of **3**-TiO_2 at 480 nm can be fitted multiexponentially with $\tau_1 < 120$ fs (-100%), $\tau_2 = 1.2$ ps (+ 29%), $\tau_3 = 33$ ps (+ 1.3%) and $\tau_4 > 400$ ps (+ 69.7%) in contrast to $\tau_1 < 120$ fs (- 100%), $\tau_2 = 1.5$ ps (+ 37.6%), $\tau_3 = 70$ ps (+ 19.4%), $\tau_4 > 400$ ps (+ 43%) fit of the kinetic trace for **5**-TiO_2 (Table 1). The ground state bleach recovery represents the true recombination dynamics and a look at the residuals at 400 ps suggests a not less than 30% slowdown in this primary charge recombination rate; such phenomenal effect having been brought about just by changing the position of the hydroxyl groups with respect to each other.

The electron injection time in **3**-TiO_2 system is monitored by the time of appearance of the electron signal at 900 nm. Electron injection is found to be fitting with $\tau_1 < 120$ fs (+ 92.5%) and $\tau_2 = 1.5$ ps (+ 7.5%) at 900 nm followed by a decay with time constants $\tau_3 = 33$ ps (- 6.5%) and $\tau_4 > 400$ ps (- 92%) (Figure 9, upper panel). This is in stark contrast to a < 120 fs only electron injection from the hot ^{1}MLCT and/or ^{3}MLCT states observed in case of **5**-TiO_2 system which decays with $\tau_1 = 1.5$ ps (- 34.8 %), $\tau_2 = 70$ ps (- 26.8%) and $\tau_3 > 400$ ps (- 38.4%) time constants (Table 1). It may be noted that injection component in addition to the pulse width limited < 120 fs component is a very rare observation for ruthenium polypyridyl enediol complexes as sensitizers.

In order to comprehend the true origin of the 1.5 ps injection component in the kinetic trace of the electron signal, we recorded the kinetic trace for the decay of the cation radical signal at 640 nm (Figure 9, upper panel) and it is found to be fitting with $\tau_1 < 120$ fs (+ 89.5%), $\tau_2 = 1.5$ ps (+ 10.5%), $\tau_3 = 33$ ps (- 3.1%) and $\tau_4 > 400$ ps (- 96%). Again, two injection times are observed; however, the amplitude of the 1.5 ps component is greater than observed in case of electron signal. The concerned difference though small, represents genuine difference in amplitudes and, keeping in mind the extremely small noise (< 0.1%) at these wavelengths, any fitting errors can be safely ruled out. While discussing the kinetic data for the free dye we came across a 1 ps component that we assigned to a thermal electron relaxation to the *thexi* state. Thus, we can see that the 1.5 ps component observed in the kinetic traces of the conduction band electron signal and the cation radical signal corresponds to the component due to vibrational relaxation in the free dye dynamics and is therefore attributed to electron injection from the thermally relaxed ^{3}MLCT states. That this component is indeed due to electron injection from the thermally relaxed states is proved by the fact that the relative amplitude of the component is greater in case of the cation radical signal where the probe pulse (at 640 nm) is of higher energy than that when the electron signal is being monitored (at 900 nm). The pulse width limited component, on the other hand, is attributed to electron injection from hot singlet/triplet FC states as in the case for **5**-TiO_2. An interesting point to note is that the residuals at 400 ps for the cation radical in **3**-TiO_2 system at 640 nm is no less than 96% as compared to a mere 38% for **5**-TiO_2 system at the same time.

The electron injection rate from the dye to the semiconductor is determined by many factors, an important one of which is the potential energy difference between the dye excited state and conduction band edge.[42c,43] A higher excited state of the dye results in injection in a higher density of states thus resulting in a very fast injection. For **5**, the ^{3}MLCT state lies at -0.68 V; while for **3**, the same state lies at -0.91 V. With the TiO_2 conduction band edge at -0.5 V,[21,22] it is evident that in **3**-TiO_2 system the electron injection rate should be faster. Instead we observe a slower component. This clearly suggests that some other factor is being operational.

One of the other factors affecting the electron injection rate is the electronic coupling between the electron-donating orbital of the adsorbate and the electron-accepting orbital of the semiconductor.[41,42c] Apparently, in both **3** and **5**, the π* orbital of the almost similarly substituted bipyridine is the electron donating ligand overlapping with the π symmetry t_{2g} d orbital of Ti^{4+} in TiO_2. However, the situation is somewhat more intricate.

Catechol is long known to interact with TiO_2 with the formation of a stable five membered ring involving only one Ti atom of the whole nanocluster.[1-5] This is certainly much improbable an interaction to occur in case of resorcinol where the hydroxyl groups are disposed further away from each other. Any reasonable interaction is therefore expected to involve at least more than one Ti atom. This proposition is proved by one of the recent works from our group where theoretical calculations have proved that the energy minimised structure for the molecule resorcinol binding to TiO_2 on the {101} anatase plane of a titanium dioxide cluster [Ti_8O_{32}] involves multiple non-adjacent Ti atoms.[44] This suggests a probably weaker overlap of the bipyridine π* orbital with the d orbital network of TiO_2 compared to that in case of catechol. Formation constants have also been calculated to show that binding of resorcinol on TiO_2 is relatively weaker as compared to the binding of catechol.[44] We therefore believe that this comparatively weaker resorcinolate binding serves as the cause for the slower injection component in case of **3**-TiO_2 as compared to that in **5**-TiO_2 system.

Furthermore, transient absorption studies carried out on the aforesaid resorcinol-TiO_2 system showed long time offset which persisted with significant amplitudes upto > 200 ps as compared to almost complete recombination for the molecule catechol binding to TiO_2.[44]

These observations tend to suggest that, as a result of increasing the number of Ti atoms and the Ti-Ti distance involved in the binding, not only is the electronic coupling (H_{AB}) reduced but there is also a significant change in the electronic structure of the excited state involving the π* orbital of the bipyridine ligand and the π symmetry t_{2g} d orbital of Ti^{4+} in TiO_2 as one moves from catechol to resorcinol. This change in the electronic structure of the excited state implies a much greater degree of charge delocalization as we move from catechol to resorcinol. In other words, as we move from catechol to resorcinol, because of the reduced electronic coupling and because of this enhanced charge diffusion along different directions into the bulk TiO_2, a significantly slower charge recombination rate in the kinetic traces of **3** on TiO_2 is observed.

Following Marcus semi-classical electron transfer theory, the BET rate can be expressed as a function of the driving force, reorganization energy and the coupling element in the following way (Equation 1): [45]

$$k_{BET} = \left(\frac{2\pi}{\hbar}\right)\left[H_{AB}\right]^2 \frac{1}{\sqrt{4\pi\Lambda kT}} \exp\left\{-\frac{(\Delta G^0 + \Lambda)^2}{4\Lambda kT}\right\}$$

Now, the charge recombination dynamics in a ruthenium polypyridyl dye-TiO_2 system generally lies in the Marcus inverted regime where with an increase in the thermodynamic driving force ($-\Delta G^0$), the BET rate decreases provided the coupling element remains the same (Equation 1).[23,25,29,46,47] For the sake of argument, let us suppose that the coupling elements for **3**-TiO_2 and **5**-TiO_2 systems are indeed the same. Reorganization energy values are generally very small compared to the driving force in the inverted region ($-\Delta G^0 >> \lambda$, respective values for the classical **N719** dye being 1.5 and 0.3 eV);[44,47-49] the changes in the reorganization energy values, if any, will therefore be insignificant with respect to the changes in the driving force values. Now, ΔG^0 is $E_C - E_{S/S+}$,[19,23,50] where E_C is the potential of the conduction band edge (- 0.5 V)[21,22] and $E_{S/S+}$ is the ground state redox potential of the dye which is 1.25 V for **3** and 1.32 V for **5**. Using the above equation the ($-\Delta G^0$) values for **3**-TiO_2 and **5**-TiO_2 systems are respectively calculated to be 1.75 eV and 1.82 eV. The recombination should therefore be faster for the **3**-TiO_2 system which is contrary to what we observe. Thus we see that the electron recombination rate cannot be explained on the basis of changes in free energy alone and that coupling plays a significant role.

Logically, a similar reasoning, as thought of for explaining the injection dynamics of **3** on TiO_2, should apply in case of **4**-TiO_2 system as well. To our surprise this is not the case.

Electron injection in both **4**-TiO_2 and **6**-TiO_2 system is pulse width limited and is found to be fitting to < 120 fs only, as monitored by the time of appearance of the conduction band electron signal. The kinetic trace for the decay of the signal in **4**-TiO_2 system recorded at 620 nm can be fitted with 0.9 ps (- 29.4%), 22 ps (- 9.4%) and > 400 ps (- 61.2%) time constants (Figure 10) while the decay of the conduction band electron signal at 900 nm can be fitted with 0.9 ps (- 20.9%), 22 ps (- 10.4%) and > 400 ps (- 68.7%) time constants (Figure 11 and Table 2). On the other hand, the decay of the conduction band electron signal for the **6**-TiO_2 system at 900 nm can be fitted with 1.2 ps (- 22.5%), 10 ps (- 3.5%) and > 400 ps (- 74%) time constants.

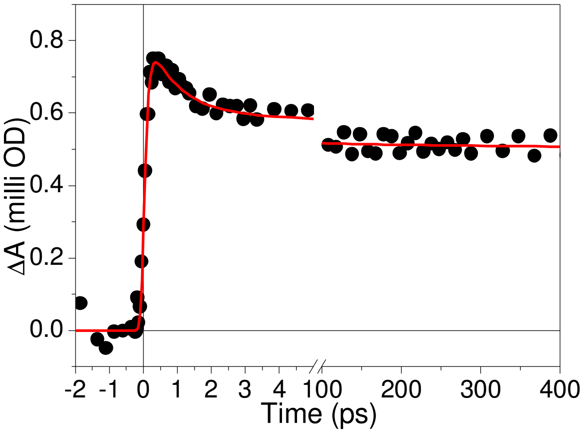

Figure 10: Kinetic trace for the decay of the 620 nm signal in **4**-TiO_2 system.

Table 2: Lifetimes of the transients at different wavelengths for **4**- and **6**-TiO_2 systems

System	Monitoring Wavelength (nm)	Lifetimes
4-TiO_2	480	< 120 fs (-100%), 0.9 ps (+28.5%), 22 ps(+10.3%), > 400 ps (+61.2%)
	620	< 120 fs (+100%), 0.9 ps (-29.4%), 22 ps (-9.4%), > 400 ps (-61.2%)
	900	< 120 fs (+100%), 0.9 ps (-20.9%), 22 ps(-10.4%), > 400 ps (-68.7%)
6-TiO_2	480	< 120 fs (-100%), 1.2 ps (+16.5%), 10 ps (+3.5%), > 400 ps (+80%)
	900	< 120 fs (+100%), 1.2 ps (-22.5%), 10 ps (-3.5%), > 400 ps (-74%)

Lian and co-workers studied a series of ruthenium polypyridyl complexes and they proved that in the nonadiabatic limit, provided coupling and reorganization energy parameters are the same, with an increase in the excited state energies the electron injection rates become faster.[42c,51] They explained their observation by considering electron injection in successively higher density of states with successive increase in the excited state energies of the sensitizer dyes. In our case we observe that the ^{3}MLCT excited state of **4** lies higher at -0.98 V as compared to that of **3** at -0.91 V (Scheme 4).

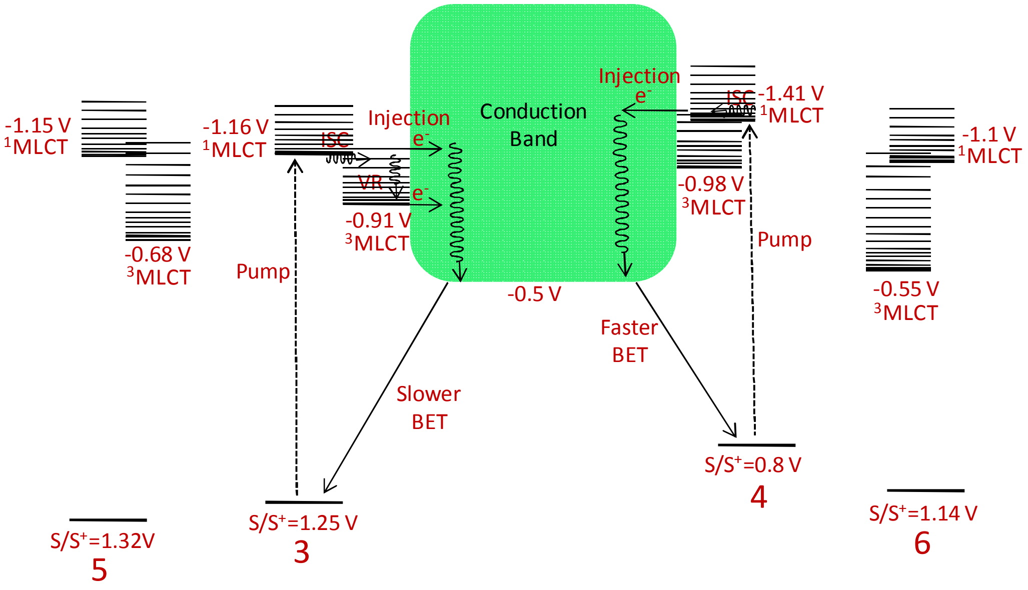
-1.15 V
^{1}MLCT
-0.68 V
^{3}MLCT
S/S$^+$=1.32V
5
-1.16 V
^{1}MLCT
ISC
VR
Injection
e$^-$
e$^-$
-0.91 V
^{3}MLCT
Pump
S/S$^+$=1.25 V
3
Slower
BET
Conduction
Band
-0.5 V
Injection
e$^-$
ISC
-1.41 V
^{1}MLCT
-0.98 V
^{3}MLCT
Pump
Faster
BET
S/S$^+$=0.8 V
4
-1.1 V
^{1}MLCT
-0.55 V
^{3}MLCT
S/S$^+$=1.14 V
6

Scheme 4: Mechanistic scheme showing the different electron transfer processes in **3**, **4**, **5** and **6** adsorbed on TiO_2.

Following a similar analogy as Lian and colleagues, this means that for **4**-TiO_2 system electron injection takes place in a relatively higher density of states as compared to that in the case of **3**-TiO_2 system.

This, therefore, might be the reason for the absence of any slow component in the electron injection parameters which supersedes the effects of weaker coupling of resorcinolate binding.

Lower panel of Figure 11 compares the BET dynamics of **4**-TiO_2 and **6**-TiO_2 systems based on the recovery of the ground state bleach monitored at 480 nm. The recovery in the **4**-TiO_2 system can be fitted with 0.9 ps (+ 28.5%), 22 ps (+ 10.3%) and > 400 ps (+ 61.2%) while that in **6**-TiO_2 system can be fitted with 1.2 ps (+ 16.5%), 10 ps (+ 3.5%) and > 400 ps (+ 80%) (Table 2). The recombination dynamics in the **4**-TiO_2 system is therefore ~ 20% *faster* than in the **6**-TiO_2 system. This also is wholly contrary to that observed in case of the corresponding ruthenium complex **3** on TiO_2. The aforesaid trend is visible in the electron signal at 900 nm as well but is not prominent because of possible electron trapping at various trap sites of different trap energies and distances from the adsorbed dye.[52]

This faster recombination observed in case of **4**-TiO_2 system can be explained again on the basis of Marcus theory. We have mentioned before that the charge recombination dynamics in such systems falls in the Marcus inverted regime where with an increase in the thermodynamic driving force ($-\Delta G^0$), the BET rate (given by equation 1) decreases provided coupling parameters are the same. Electron recombination in the case of **3**-TiO_2 system is seen to be governed by the nature of electronic coupling of the dye to

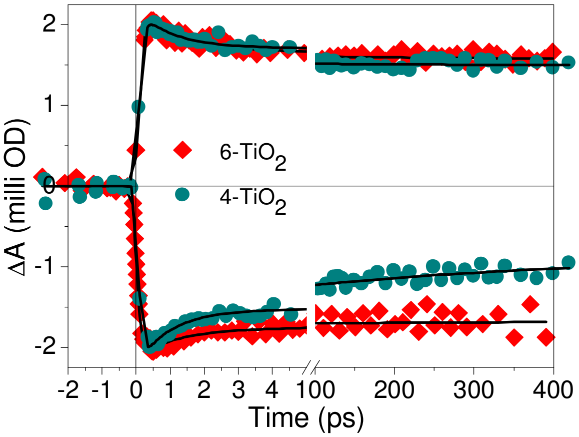

Figure 11: Comparison of the kinetic traces of **4** and **6** adsorbed on TiO_2 at 480 nm (lower panel) and 900 nm (upper panel).

TiO_2 (*vide supra*). This factor therefore must apply in case of **4**-TiO_2 system as well and this would have governed the recombination rate provided the other factors were maintained same and this is not the case for the osmium complexes. The ($-\Delta G^0$) values for the **4**-TiO_2 and **6**-TiO_2 systems are calculated to be 1.3 eV and 1.64 eV, respectively. A significantly lower ($-\Delta G^0$) value (0.34 eV) in the **4**-TiO_2 system, which again presides over the electronic coupling effects, presumably results in the faster recombination observed. In case of the ruthenium complexes, this difference in the ($-\Delta G^0$) values between the catecholate and resorcinolate binding analogues is only 0.07 eV which, we believe, is not enough to outdo the effects of resorcinolate binding.

3.B. Ru(II)- and Re(I)- polypyridyl complexes on oleic acid capped TiO_2 in non-aqueous solvent: prolonged charge separation and substantial thermalized ^{3}MLCT injection

3.B.1. Foreword

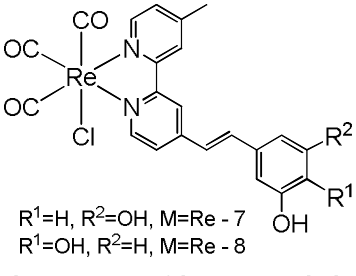

Scheme 5: Molecular structures of the compounds discussed in the text.

Surface modification of TiO_2 semiconductor nanoparticles by adsorption of monolayer of adsorbate may enhance its photostability and, compared to that on unmodified surface, may improve the efficiency of light-induced reactions occurring on the surface by affecting the rates of the different interfacial electron transfer processes.[53] This is because the performance of most semiconductor-containing devices depends critically on the electronic properties of the semiconductor surface band bending (V_s) and the surface recombination velocity. These properties in turn depend on the density and energy distribution of surface states whose properties are controlled by the chemistry of the surface. The use of suitable organic or organometallic molecules as capping agents holds great promise for fine-tuning the desired surface electronic properties.[50] Oleic acid capped TiO_2 nanoparticles have been much explored in this regard.[51] The interfacial electron transfer dynamics of the newly synthesized sensitizer dyes, **3** and the corresponding rhenium(I) polypyridyl complex **7**, have therefore been studied on such nanoparticles (Scheme 5).

3.B.2. Experimental Section (please see Appendix A for details)

3.B.2.A. Analytical methods

All potentials in section 3.B have been quoted with respect to NHE in chloroform.[55]

3.B.2.B. Preparation of sample solution

The complexes discussed are insoluble in chloroform and so sensitization has been done by dissolving the complexes in least possible volume of methanol (this volume is less than 1% of the total volume) and then adding the dissolved dye into the chloroform solution of the nanoparticles. Spectroscopic grade chloroform has been used for making all solutions. The complexes discussed are insoluble in chloroform and so sensitization has been done by dissolving the complex in least possible volume of methanol (this volume is less than 1% of the total volume) and then adding the dissolved dye into the chloroform solution of the nanoparticles. Throughout the chapter, therefore, chloroform:methanol (99:1, *v/v*) is abbreviated as chloroform.

3.B.2.C. Synthesis of oleic acid capped TiO_2 nanoparticles

Synthesis is carried out by following a previously reported procedure.[44] Briefly, 0.3 g of titanium isopropoxide is added to a 5 mL ethylene glycol and 4 mL oleic acid mixture at room temperature. The above mixture is stirred for 30 minutes after which 20 mL of water is added under vigorous stirring. The above solution is heated to 100 ^{o}C under reflux conditions. TiO_2 is precipitated by the addition of acetone. The precipitate is later cleaned by dissolving it in toluene and again precipitating with 10% acetone (in methanol) at least 3 times. The powder is dried in ambient conditions and used for further studies.

3.B.2.D. Synthesis

3.B.2.D.1.Tricarbonyl[5-(2-(4'-methyl-2,2'-bipyridin-4-yl)vinyl)benzene-1,3-diol]chlororhenium(I) (7): $[Re(CO)_5Cl]$ (100 mg, 0.276 mmol) and **2** (83.9 mg, 0.276 mmol) are dissolved in 25 mL of dry THF and refluxed for 6 hours with continuous stirring in an inert atmosphere. The solvent is then reduced to 2 mL and 20 mL of diethyl ether is added to it which precipitated a yellow solid. This is filtered off using a grade 4 sintered glass crucible, washed with ether and then air dried. The solid so obtained is further purified by column chromatography using silica as the stationary phase and acetonitrile as the eluent. Yield: 100 mg (60%). ESI-MS (*m/z*): calculated for $C_{22}H_{16}ClN_2O_5Re$ 610.03, observed 575.27 $[M - Cl]^+$; ^1H NMR (500 MHz, d_6-DMSO): δ (ppm) 9.52 (2H, br, – OH); 8.89 (1H, s, $H^{3'}$ (bpy)); 8.88 (1H, d, *J* = 5.5 Hz, $H^{6'}$ (bpy)); 8.85 (1H, d, *J* = 5.5 Hz, H^6 (bpy)); 8.74 (1H, s, H^3 (bpy)); 7.82 (1H, dd, *J* = 5 Hz, 0.8 Hz, $H^{5'}$ (bpy)); 7.74 (1H, d, *J* = 16.5 Hz, $H^{ethenyl}$); 7.60 (1H, d, *J* = 5.5 Hz, H^5 (bpy)); 7.24 (1H, d, *J* = 16 Hz, $H^{ethenyl}$); 6.59 (2H, d, *J* = 2 Hz, H^2 (phenyl)); 6.30 (1H, m, H^4 (phenyl)); 2.60 (3H, s, bpy-CH_3). IR (KBr pellet, cm^{-1}): 3260 (ν(O–H)), 1913, 1884 (ν(C=O)). Elemental analysis: Calculated for $C_{22}H_{16}ClN_2O_5Re$: C, 43.31; H, 2.64; N, 4.59; found: C, 43.30; H, 2.66; N, 4.59.

3.B.3. Results and Discussion

3.B.3.A. Synthesis

TEM images (Figure 12) show the particle size of oleic acid capped TiO_2 nanoparticles to be ~3 nm with a fairly good size distribution.

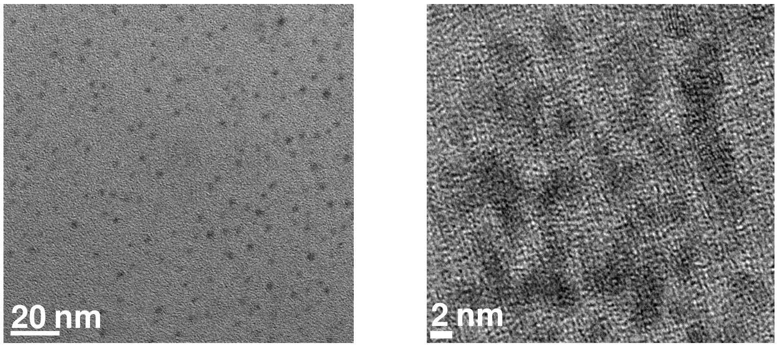

Figure 12: TEM images of oleic acid capped TiO_2 nanoparticles. Average particle size is ~3 nm.

7 is prepared by a simple reaction of $Re(CO)_5Cl$ with **2** in THF and is well characterized by standard analytical methods (Scheme 6).

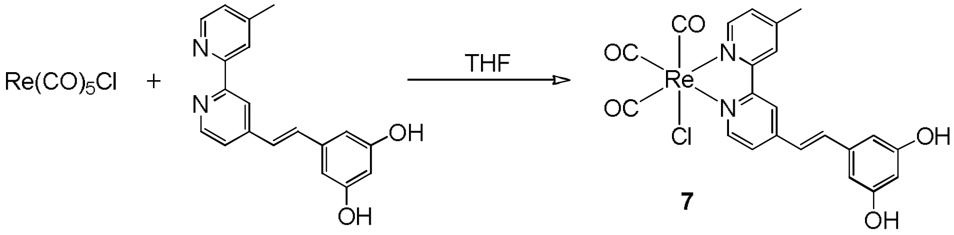

Scheme 6: Reaction scheme for the synthesis of **7**.

3.B.3.B. Electrochemical studies

E(S$^+$/S) value of **7** is found to be 1.14 V with respect to the NHE in chloroform (Figure 13). **7** being non-emissive, the redox potential value of the ^{3}MLCT state could not be calculated. The E_{0-0} value for the ^{1}MLCT state is approximated to be 2.69 eV for **7**, from the onset of optical absorption of the ^{1}MLCT state. The corresponding excited state potential is thus -1.55 V (*vide supra*). The excited state potential being above the conduction band level, electron injection from the excited state of the sensitizer into the conduction band of TiO_2 becomes thermodynamically feasible. E(S$^+$/S) value of **3** is calculated to be 1.12 V while the redox potential values of the ^{1}MLCT and the ^{3}MLCT states are estimated to be -1.29 V and -1.04 V.

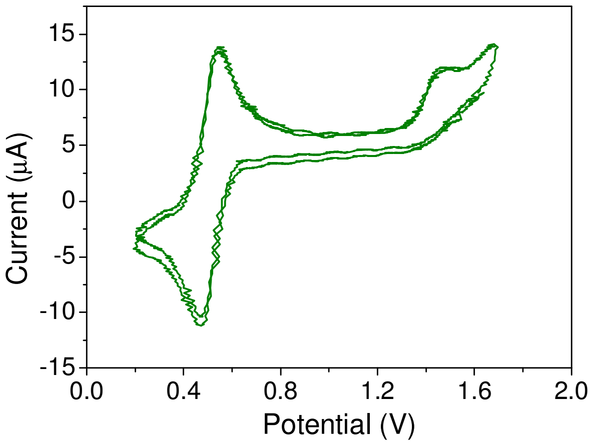

Figure 13: Cyclic Voltammogram of **7** in acetonitrile. Ag/AgCl (saturated KCl) has been used as the reference electrode. Scan rate is 100 mV/s. Ferrocene has been added as an internal standard.

3.B.3.C. Steady state and transient spectral characterization

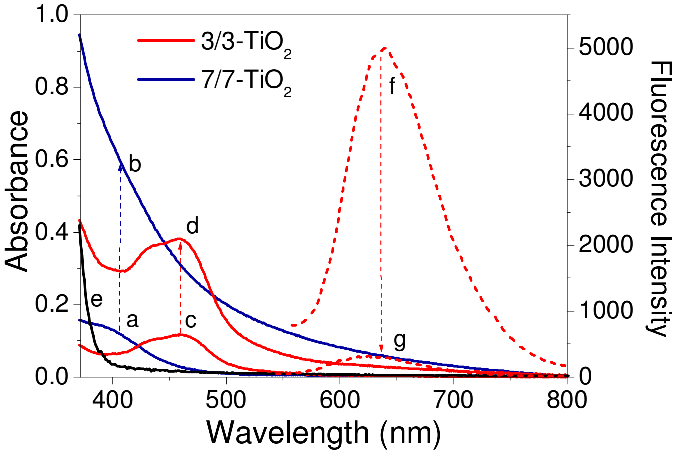

Figure 14: Changes in absorbance of **3** (0.7×10^{-5} M) (c → d) and **7** (0.895×10^{-5} M) (a → b) on addition of 2.34 g/L TiO_2 to both in chloroform. The black line (e) shows the absorption spectrum of oleic acid capped TiO_2 in chloroform (15 g/L). Also shown is the fluorescence quenching of **3** in the same solvent in dotted lines (f → g). The respective concentration of the dye and TiO_2 are the same. Compound **7** is non-emissive.

The steady state absorption spectrum of **3** and **7** show considerable broadening and increased absorbance on steady addition of increasing concentrations of TiO_2 nanoparticles in chloroform (Figure 14 and 15) indicating significant interaction of the dye molecules with TiO_2.

A weaker electronic coupling of the resorcinol bound dyes to TiO_2, than the catechol analogs, is again evident from the non-appearance of new CT bands as was the case with many dyes with pendant catechol groups for binding to TiO_2.[23-25] Also, the emission intensity is highly diminished on TiO_2 surface (Figure 14) indicating substantial quenching of the excited state by electron injection and hence negligible contribution of excited state features in the transient absorption data on TiO_2 (*vide infra*). [15,19,27,56]

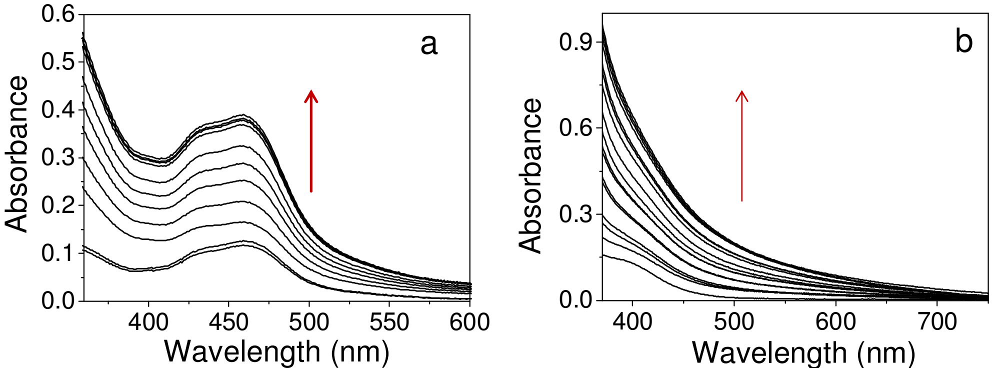

Figure 15: Changes in absorbance of (a) **3** (0.7×10^{-5} M) on TiO_2 (0 – 2.34 g/L) and **7** (0.895×10^{-5} M) on TiO_2 (0 – 2.34 g/L) in chloroform.

The transient absorption spectrum of the free complexes in chloroform is shown in Figure 16. The broad band ranging from 500-1000 nm for **3** is attributed to excited triplet state absorption (*vide supra*).[14,23,26,27,29]

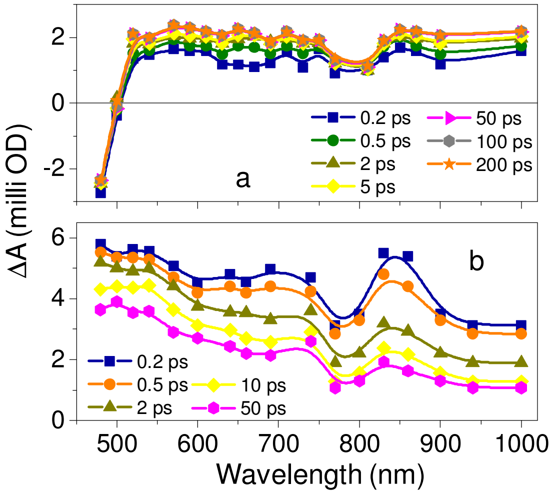

Figure 16: Transient absorption spectrum of (a) **3** and (b) **7** at different delay times in chloroform measured after 400 nm (fwhm < 120 fs) excitation. Concentration of **3** and **7** is ~ 200 µM and ~300 µM, respectively.

Due to a higher spin–orbit coupling corresponding to the Re^I centre in **7** as compared to that of Ru^{II} in the analogous Ru^{II}-complex **3**, one would expect a more efficient and faster

ISC in **7** than in **3**. Recent studies by Vlcek Jr. *et al.* revealed that ISC for an analogous Re^{I}-complex happens within 85 fs.[57] This, therefore, necessitates the absorption feature in the transient absorption spectrum of **7** again to be assigned as that to the absorption of the excited triplet state. This assignment is also corroborated by our previous studies of the excited state dynamics of **8**.[24] The negative absorption in the spectrum of **3** before 500 nm arises due to simultaneous ground state absorption as is evident from an analysis of the corresponding UV-Vis spectrum (Figure 14).

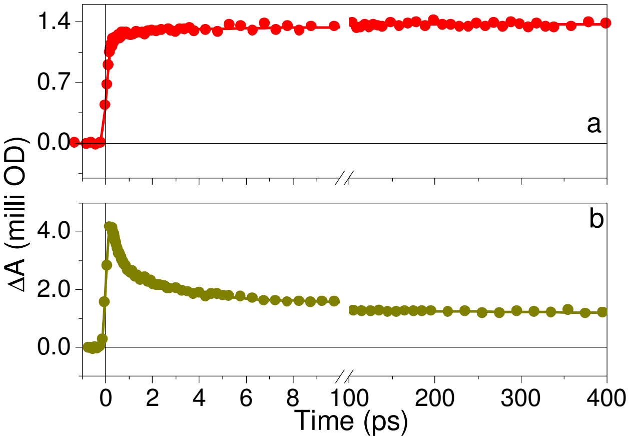

Figure 17: Kinetic trace of (a) **3** and (b) **7** in chloroform measured after 400 nm (fwhm < 120 fs) excitation. The monitoring wavelength is 900 nm for **3** and 600 nm for **7.**

The kinetic trace of the free dye **3** recorded at 900 nm after excitation at 400 nm (Figure 17a) can be fitted with < 120 fs (+82.5%), 0.6 ps (+11%) and 10 ps (+5.8%) time constants. The pulse width limited component corresponds to the population of the hot MLCT excited states. [14,23,26,27,29] The average solvation relaxation time, $<\tau_s>$, in methanol is reported to be ~ 3-4 ps; while that in chloroform is reported to be of the order of 100-150 fs.[35,58] Thus the 600 fs component apparently does not arise due to solvation. Following similar analogy as that followed for interpreting the dynamics of **3** and **5** on PVA capped TiO_2 in water, the 600 fs component is assigned to the same thermalization of the hot electrons inside the ^{3}MLCT manifolds. Also, considering the fact that the transient absorption kinetics have been recorded by excitation with a very high energy of 400 nm light, the 10 ps component is tentatively assigned to inerligand electron redistribution in the ^{3}MLCT manifolds.[59] Because of the significantly longer lifetime (*i.e.* >> 1 ns) of the associated Ru^{II}-polypyridyl unit, the kinetic trace of **3** does not decay till 400 ps.[14,15,26,37] The kinetic trace of the excited state of the free dye **7** at 600 nm (Figure 17b) can be fitted with < 120 fs (+100%), 300 fs (-59.7%), 2 ps (-18.1%), 20 ps (-5.4%), > 400 ps (-16.8%). While the < 120 fs component again corresponds to the population of the hot excited states, the > 400 ps component reflects the long lifetime of the ^{3}MLCT state.[24,60] The radiative and non-radiative decay pathways of the excited states of $(d\pi)^6$ rhenium-polypyridyl complexes are mechanistically complex because of the associated triplet CT excited states- such as metal-to-ligand (^{3}MLCT), ligand-to-ligand (^{3}LLCT), and σ-to-ligand ($^3\sigma$-π^*) states.[61] Additionally, triplet ligand-centered (^{3}LC) excited states and triplet ligand-field (^{3}LF) states are also present. The 300 fs, 2 ps and 20 ps components therefore correspond to various intra- and/or intermolecular relaxation pathways.

The transient absorption spectrum of **3** (Figure 18a) on TiO$_2$ surface shows two absorption bands. The first band in the 560-740 nm region is due to the formation of the cation radical because of photoinduced electron injection from the dye molecule into the conduction band of TiO$_2$ while the lower energy absorption band in the 800-1000 nm region can be assigned to electrons in the conduction band of TiO$_2$ nanoparticles (*vide supra*). In addition to these bands, a negative absorption can be seen below 540 nm due to the ground state bleach.[14,23,26,29]

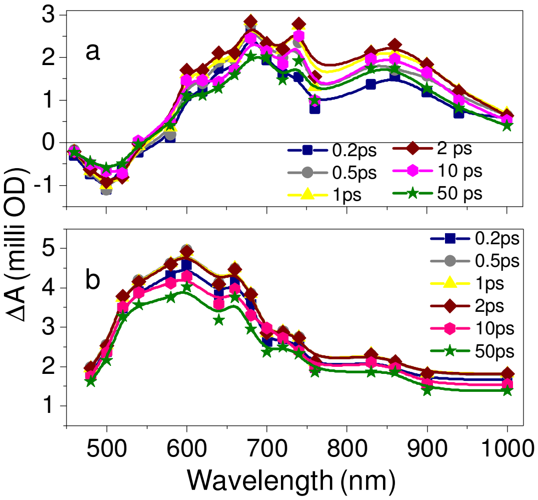

Figure 18: Transient absorption spectrum of (a) **3** and (b) **7** on oleic acid capped TiO$_2$ at different delay times in chloroform measured after 400 nm (fwhm < 120 fs) excitation. Concentration of **3** and **7** is ~ 200 μM and 250 μM, respectively.

The transient absorption spectrum of **7** on TiO$_2$ surface again exhibits similar absorption features. Absorption due to the cation radical of **7** on TiO$_2$ surface appears in the 480-700 nm region while that due to the electrons in the conduction band appears in the 800-1000 nm region. Assignment of the former band to the cation radical (**7**$^{\cdot+}$) is based on our complementary pulse radiolysis experiment to generate **7**$^{\cdot+}$ selectively as described before (Figure 19). All these assignments are well validated by several literature reports.[14,24,26]

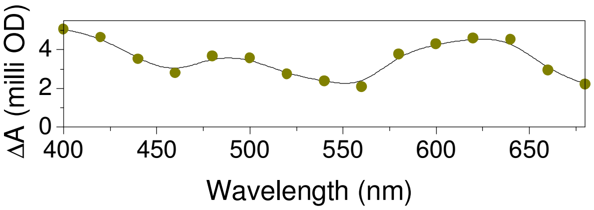

Figure 19: Uncorrected transient absorption spectrum of the cation radical of **7** obtained from one-electron oxidation in pulse radiolysis.

3.B.3.D. Electron injection

Electron injection time in the dye-TiO_2 systems can be deduced from the time of appearance of either the conduction band electron signal or that of the cation radical signal. Figure 20 presents a comparison of the kinetic traces for the decay of the conduction band electrons at 900 nm for **3**-TiO_2 and **7**-TiO_2 systems which can be fitted respectively with < 120 fs (+64.5%), 0.7 ps (+35.45%), 2.5 ps (-20%), 100 ps (-17.3%) and > 400 ps (-62.7%); and < 120 fs (+100%), 6 ps (-12.72%), 45 ps (-23%) and > 400 ps (-64.28%). Similar to that discussed for the dynamics of **3** on PVA capped TiO_2 in water, electron injection in **3**-TiO_2 system in chloroform is therefore found to be biexponential with one major pulse width limited ultrafast component and a 700 fs slower component. The kinetic traces for this system at 640 nm and at 740 nm have also been recorded and they have been found to be fitting with < 120 fs (+30%), 0.7 ps (+70%), 2.5 ps (-16.14%), 100 ps (-26.14%), > 400 ps (- 57.72%) and < 120 fs (+43%), 0.7 ps (+57%), 2.5 ps (-18.3%), 100 ps (-21.5%), > 400 ps (-60.2%), respectively. Interestingly, the amplitude of the 700 fs component increases as one moves towards lower wavelengths. On the other hand, the kinetic trace for the decay of the cation radical at 640 nm for the **5**-TiO_2 system can be fitted with < 120 fs (+100%), 6 ps (-21.5%), 45 ps (-23%) and > 400 ps (55.5%) and no biphasic injection could be observed again (Figure 20). The slower component of 700 fs in the appearance time of the cation radical signal of **3**-TiO_2 system, therefore, becomes the major one of the two components as one moves towards lower wavelengths. This 700 fs component in the appearance of the electron and the cation radical signal can be clearly seen to be corresponding with the 600 fs component in the dynamics of the free dye (*vide supra*) and is therefore accredited to electron injection from the thermally relaxed ^{3}MLCT state or the *thexi* state.[63] That it is indeed so is proved by the fact that the amplitude of this component increases when the energy of the probe pulse is increased; at 900 nm it is 35.45%, at 740 nm it is 57% and at 640 nm it is 70%. The pulse width limited

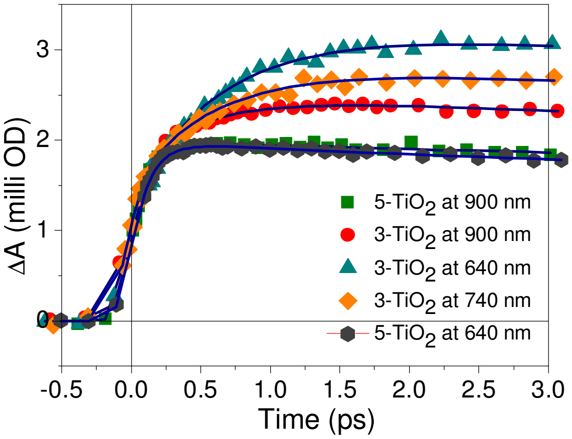

Figure 20: Comparison of the electron injection dynamics of **3**-TiO_2 system with that of **5**-TiO_2 system in chloroform. The kinetic traces have been normalized with respect to the ultrafast growth component.

component, on the other hand, is attributed to electron injection from hot singlet/triplet MLCT states as is the case for **5**-TiO_2 system.

The observations can be explained following similar arguments as that for the dye-TiO_2 systems in water. For the localized one point binding of the catechol moiety with TiO_2, highly localized and therefore very efficient overlap of the donor bipyridine π^* orbital with the Ti^{4+} 3d orbital of a single Ti^{4+} atom of the whole TiO_2 nanocluster takes place. As a result of this localized and therefore strong binding, the forward electron transfer process proceeds prior to all possible dye relaxation pathways like hot electron thermalization *etc. i.e.,* ultrafast pulse-width limited electron injection is observed for the dye-TiO_2 systems like **5**-TiO_2 which have pendant catechol groups for binding to TiO_2.[14,19,23,24,26,27,29]

Upon widening the distance of the hydroxyl groups with respect to each other, the donor bipyridine π^* orbital no longer interacts with only one Ti^{4+} 3d orbital; the hydroxyl groups now bind themselves with multiple Ti^{4+} atoms leading to a much poorer overlap of the donor and the acceptor states - the binding therefore becomes weaker. FT-IR spectroscopic studies on **3**- and **5**-TiO_2 systems also support weaker binding of **3** to TiO_2 surface (Figure 21). It can be seen that the spectra for **3**- and **5**-TiO_2 systems are fairly similar to that of OA capped TiO_2 absorptions. This is reasonable since to achieve efficient sensitization, OA-capped TiO_2 is used in excess of the sensitizer. An analysis of Figure 21a reveals peaks at 1027 cm^{-1} and 1004 cm^{-1} for **5**- and **3**-TiO_2 systems, respectively. An important point to note is that no such peaks are present in this region in the spectrum of the OA capped TiO_2 nanoparticles only. Interestingly, for **3** and **5** also, peaks at 1020 cm^{-1} can be seen (Figure 21b). However, the peaks for **3**- and **5**-TiO_2 at 1004 cm^{-1} and 1027 cm^{-1}, respectively, cannot be said to be coming from the sensitizers. This is because of the following two reasons. As told previously, spectra for **3**- and **5**-TiO_2 are dominated by absorptions due to OA capped TiO_2. For the sensitizers, therefore, absorptions that don't coincide with absorptions of OA capped TiO_2 cannot be seen. This includes strong absorption due to the PF_6^- anion at 841 nm which is absent in case of **3**- and **5**-TiO_2. Secondly, had the concerned absorptions been appearing from the

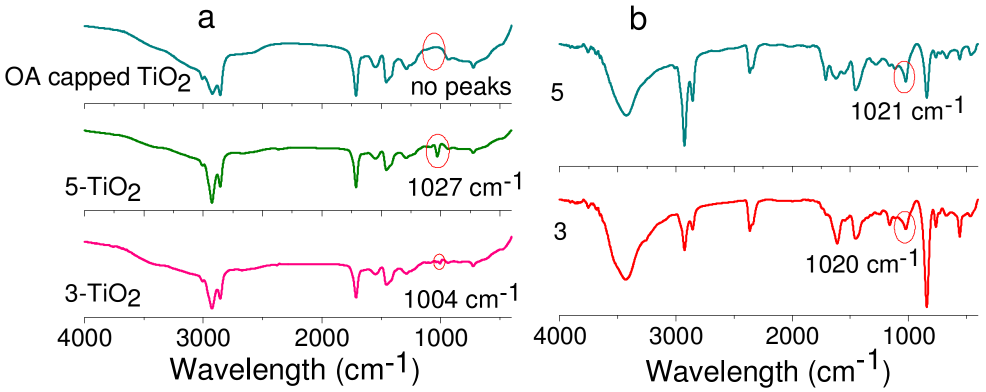

Figure 21: FT-IR spectra of (a) bare OA-capped TiO_2 and the sensitized TiO_2 samples, (b) **3** and **5.**

sensitizers itself, sensitization would have resulted in either a bathochromic or a hypsochromic shift of the peak at 1020 cm^{-1}. However, there is no such trend in the peak values with that for **5**-TiO$_2$ in that range appearing at 1027 cm^{-1} and that for **3**-TiO$_2$ appearing at 1004 cm^{-1}. This clearly suggests a different origin of the aforesaid peaks in the IR spectrum of **3**- and **5**-TiO$_2$. Instead, the aforesaid peaks in the spectrum of the sensitized samples are attributed to ν(Ti-OC) based on an analysis of the available literature. For **5**-TiO$_2$, catechol mode of binding leads to stronger Ti-O bonds because of the formation of a stable 5-membered chelate ring and the Ti-OC stretch appears at 1027 cm^{-1}. For **3**-TiO$_2$, this peak appears at 1004 cm^{-1} indicating weaker Ti-OC bond and hence supports binding of resorcinol to multiple Ti centres. The peak at 1020 cm^{-1} for **3** and **5**, on the other hand, represents presumably the alcohol C-O stretch.

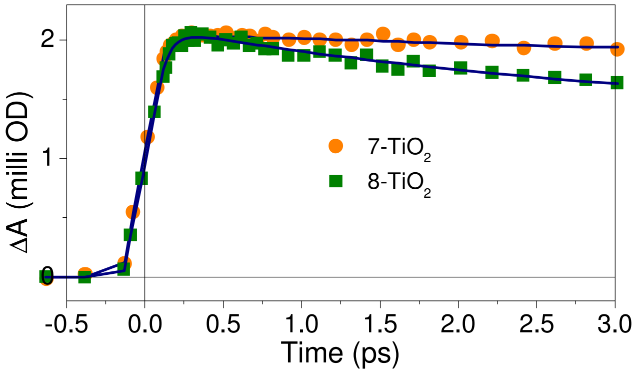

Figure 22: Single exponential ultrafast injection in rhenium(I)-complex (**7**) sensitized system. The monitoring wavelength is 900 nm for both the kinetic traces.

The slower component in the injection dynamics of **3**-TiO$_2$ system therefore arises as a result of this weaker resorcinolate binding and is absent in the injection dynamics of **5**-TiO$_2$ system. This aforementioned biexponential electron injection is an exclusive observation for any ruthenium(II)-polypyridyl enediol sensitizer. However, electron injection from thermalized ^{3}MLCT state is not a ubiquitous feature of resorcinolate type of binding. Following similar analogy as discussed above, injection dynamics in **7**-TiO$_2$ system is expected to be biexponential. But this is not the case. Similar to the catechol analogue, electron injection is strictly single exponential and occurs in < 120 fs in this system (Figure 22). The ^{1}MLCT state of **7** lies not less than 260 mV above that of **3**. In nanostructured TiO$_2$, there is an exponential distribution of the localized states in the band gap, as described by the expression (Equation 2)

$$g(E) = \frac{N_L}{k_B T_0} \exp\left[\frac{E - E_C}{k_B T_0}\right]$$

Here, N_L is the total density of the localized states and T_0 is a parameter with temperature units that determines the depth of the distribution below the lower edge of the conduction band, E_C.[31] Considering this fact that the TiO$_2$ density of states increases exponentially with increase in energy, because of this higher donor state potential, presumably, electron injection in **7**-TiO$_2$ system takes place in a higher density of states

(Scheme 7);[42,51] this effect presides over the effects of weak binding of resorcinol so that injection proceeds at a faster rate in a single exponential ultrafast manner.

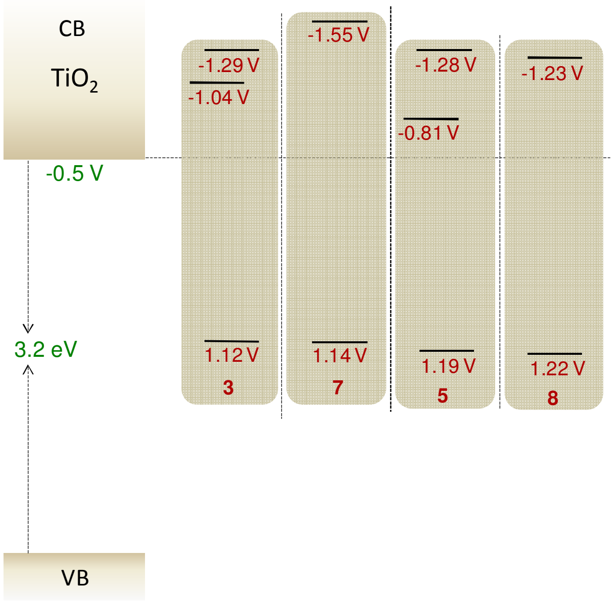

Scheme 7: Relative energetics of sensitizer excited states and TiO_2. Redox potentials of the reference dyes have been obtained from reference 14 and 24.

3.B.3.E. Charge Recombination

Figure 23 compares the ground state bleach recovery dynamics of **3**-TiO_2 and **5**-TiO_2 systems at 480 nm. While this recombination can be fitted with 6 ps (+22.5%), 45 ps (+22%) and > 400 ps (+55.5%) for the **5**-TiO_2 system, it can be fitted with 2.5 ps (+16.3%), 100 ps (+17.3%) and > 400 ps (+66.4%) for the **3**-TiO_2 system (Table 3). A comparison of the residual offset after 400 ps indicates a remarkably slower BET rate for the resorcinolate bound system. This indicates that, as a consequence of increasing the number of Ti atoms and the Ti-Ti distance involved in binding, not only is the electronic coupling (H_{AB}) reduced but there is also a major change in the electronic

Table 3: Recombination lifetimes at different wavelengths for the dye-TiO_2 systems

System	Monitoring Wavelength (nm)	Lifetimes
3-TiO_2	480	2.5 ps (16.3%), 100 ps (17.3%), > 400 ps (66.4%)
5-TiO_2	480	6 ps (22.5%), 45 ps (22%), > 400 ps (55.5%)
7-TiO_2	600	8 ps (15.2%), 60 ps (8.3%), > 400 ps (76.5%)
8-TiO_2	600	3 ps (34%), 15.5 ps (13%), 95 ps (23.8%), > 400 ps (29.2%)

structure of the excited state (which involves π* orbital of the bipyridine ligand and the π symmetry t_{2g} d orbital of Ti^{4+} in TiO_2) and this results in a much greater degree of charge delocalization as one moves from catechol to resorcinol *i.e.* there is an enhanced charge diffusion along different directions into the bulk TiO_2 (Scheme 8).

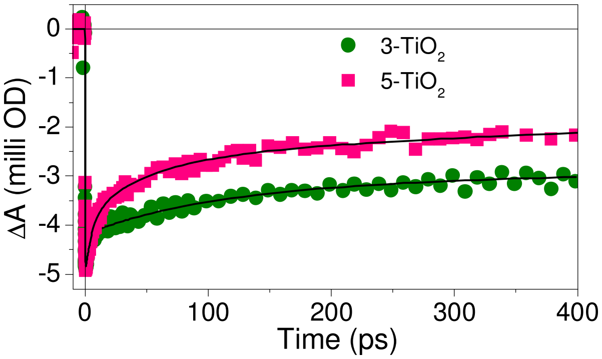

Figure 23: Comparison of the recovery of the ground state bleach of **3**- and **5**-TiO_2 systems at 480 nm.

As a result of this effect and due to reduced electronic coupling, charge recombination rate in **3**-TiO_2 system is considerably slower. That this effect is indeed due to a change in the electronic coupling parameters is again proved by an analysis of the $-\Delta G^0$ value estimates of the charge recombination reaction. Taking into account the ground state redox values of 1.12 V for **3** and 1.19 V for **5**, and the TiO_2 conduction band edge at – 0.5 V,[21,63] this free energy for charge recombination comes to 1.62 eV and 1.69 eV, respectively for **3**-TiO_2 and **5**-TiO_2 systems.[19,23] Assuming Marcus inverted region behaviour,[23,29,44,46,47,48,49,64] charge recombination rate should have been faster for **3**-TiO_2 system. That this is not the case proves the fact that electronic coupling parameters indeed play a significant role.

The BET dynamics of the rhenium dyes follow a similar trend as that for the ruthenium analogues. The charge recombination reaction could not be monitored at the bleach wavelength due to instrumental limitations. However, a comparison of the decay of the cation radical signal for **7**-TiO_2 and **8**-TiO_2 systems at 600 nm has been made.

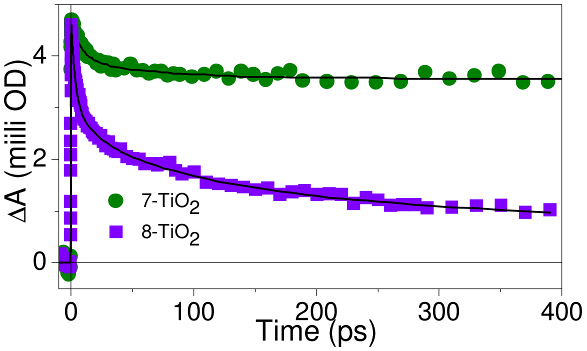

Figure 24: Dynamics of the decay of the cation radical at 600 nm for **7**-TiO_2 and **8**-TiO_2 systems.

The decay of the corresponding signal for **7**-TiO_2 system can be fitted with 8 ps (-15.2%), 60 ps (-8.3%) and > 400 ps (-76.5%) while that for the **8**-TiO_2 system can be fitted with

3 ps (-34%), 15.5 ps (-13%), 95 ps (-23.8%) and > 400 ps (-29.2%) (Figure 24 and Table 3). The charge recombination is therefore about 50% slower in the resorcinol bound system. This is a remarkably large value in view of the nominal changes in the molecular structures of the sensitizers.

As told previously, the kinetic trace of the excited state of the free dye **7** at 600 nm (Figure 17b) can be fitted with < 100 fs (+100%), 300 fs (-59.7%), 2 ps (-18.1%), 20 ps (-5.4%), > 400 ps (-16.8%). The important point to note is that the excited state is evidently very short lived with only ~ 17% residuals after 400 ps. It might consequently seem that the excited state relaxation pathways might compete with electron injection thus resulting in very less charge injection yields.[23,65] However, the results are entirely contrary to this belief. A comparison of the BET dynamics for **7**-TiO_2 system with the excited state decay dynamics of the free dye **7** reveals that on TiO_2 surface the decay is massively slower with 76.5% residuals after 400 ps as compared to only 17% for the free dye. The dynamics being entirely different, one can easily surmise that the fast excited state relaxation of the free dye does not interfere with the electron transfer processes at the interface and the dynamics observed for **7**-TiO_2 system is that due to the charge separated species only and that there are no contributions from the excited states. This, we believe, is a virtue of resorcinolate binding which, on one hand, mediates ultrafast charge injection in < 120 fs in this system, *i.e.* prior to all dye relaxation pathways, and on the other hand, because of larger diffusion of the injected electrons into TiO_2, renders the geminate charge recombination very slow and effectively stabilizes the hole created at the dye after initial photoexcitation.

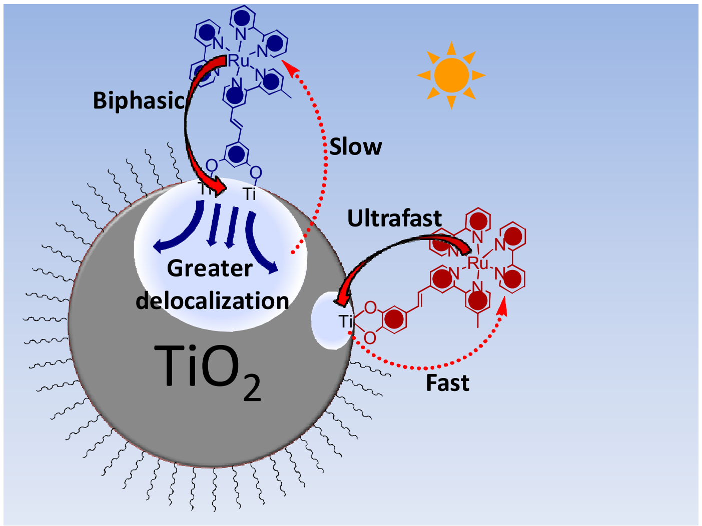

Scheme 8: An illustration of the effects of changing the disposition of the hydroxyl groups on the interfacial electron transfer dynamics for the ruthenium polypyridyl complexes discussed.

3.C. Regulating interfacial charge recombination of Os(II)-polypyridyl-resorcinol complex on TiO_2 surface by controlling density of semiconductor surface traps

3.C.1. Foreword

The interfacial electron transfer parameters are the cumulative imprint of an array of factors of which the relative energetics of the dye and the semiconductor nanoparticles is an extremely important one.[62,66] Regulating the dye-semiconductor interaction by tuning the energy levels of the sensitizer moiety (which in turn is done by suitable ligand modification) is relatively a cumbersome process. On the other hand, by a not so tedious process, the energy levels of the semiconductor nanoparticles can be modulated in an extraordinarily controlled manner. This assertion is proved by the vast number of contemporary literature reports on the modulation of the bandgap and the conduction band level position of TiO_2 (E_{CB}).[67] However, of particular importance is the role of pH, alkali metal ions and nitrogen containing heterocycles as potential determinants for the practical development of high-performance DSSCs.[67a,b,d-h] In measurements of the performance of such DSSC devices, the effects of protons, alkali metal ions and 4-*tert*-Butylpyridine on electron injection efficiency have been explained in terms of a *conduction band shift*.[67b,e]

The other alternative might be the modification of the TiO_2 surface by appropriate capping agents. This is because on surface modification the energy levels of the semiconductor *i.e.* the conduction band edge, the Fermi level and the shallow and the deep trap states are driven up in energy, a process known as Fermi level pinning.[53,68] Moreover, surface modification of semiconductor nanoparticles can significantly change their optical and chemical properties as a result of many possible effects namely, enhanced excitonic and defect emission upon blocking of nonradiative electron/hole recombination at the trap sites on the surface, increased photostability of the nanoparticles, creation of new traps on the surface of the nanoparticles *etc.*[69] Moreover, surface band bending and surface recombination velocity are critical in defining the performance of most semiconductor-containing devices.[70] On the other hand, these properties depend on the density and energy distribution of surface states.[71] Since the chemistry of the surface controls the surface state properties, exorbitant efforts have been devoted to amend and fine tune the surface states and their electronic properties by chemical methods.[72] Thus, an astutely chosen group can provide shrewd control over dipole moments, frontier orbital energy levels, light sensitization properties, hydrophilic/ hydrophobic character, *etc.*

Keeping these in mind, a comparative study of the interfacial electron transfer dynamics of **4** on PVA and OA capped TiO_2 has been made.

3.C.2. Experimental Section (please see Appendix A for details)

3.C.2.A. Computational methodology

All the geometries have been optimized at B3LYP/6-31G(d) level of theory.[73] The solvent calculations have been performed with PCM in water and chloroform.[74] The calculations have been performed in Gaussian 03 suite of program.[75] Energy calculations using DFT cannot be called very accurate. However, this uncertainity, we believe, is not of much consequence in the present study. This is because in the present study, the relative positions of the HOMO levels of OA and PVA is important and not their absolute energy values. While the individual positions of these levels might change if calculated in some higher level of theory, we believe, keeping in mind the 7.5 kcal difference between the two levels, that the relative positions would not change.

3.C.3. Results and Discussion

3.C.3.A. Steady state and transient spectral characterization

Figure 25 shows the absorption and the emission spectrum of **4** in water and chloroform in the presence and in the absence of TiO_2 nanoparticles. The absorption spectrum of **4** in chloroform is characterised by high energy MLCT transitions at 255 nm and strong ligand centered π-π* transitions at 290 nm. The familiar metal to ligand charge transfer comprising of overlapping ^{1}MLCT based $d_{Os(II)} \rightarrow \pi^*_{bpy}$ manifests in the low energy broad absorption band peaking at 486 nm. Os^{II} centre is characterised by a significantly higher spin orbit coupling and this is responsible for the allowedness of the spin forbidden ^{3}MLCT based $d_{Os(II)} \rightarrow \pi^*_{bpy}$ transition, resulting in another broad absorption between 550-710 nm. Prevailing literature reports suggest the absorption band arising at *ca.* 350 nm to be a combination of bipyridine-based delocalized interligand charge transfer and/or MC transitions.[11,23] MC transitions are, however, insensitive to solvent environment because the *d* electrons of osmium are shielded by the π electron cloud of the attached bipyridine moieties. CT transitions are, on the other

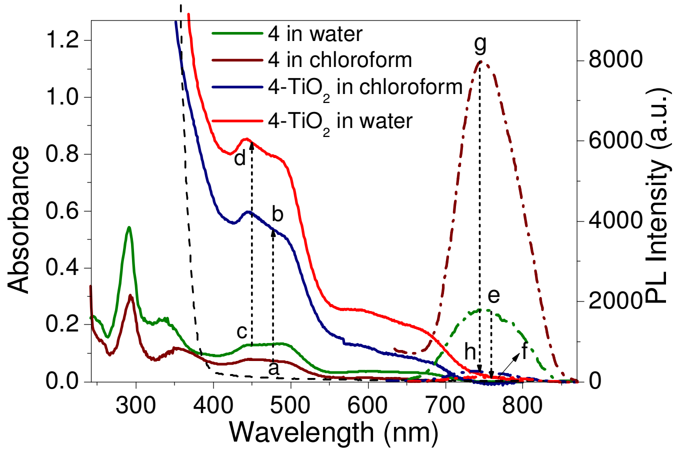

Figure 25: Changes in absorbance of **4** (1×10^{-5} M) on addition of 2.35 g/L TiO_2 in chloroform (a → b) and 3.52 g/L TiO_2 in water (c → d). Also shown is the fluorescence quenching of **4** in the same solvent in dotted lines (e → f and g → h). The respective concentration of the dye and TiO_2 are the same. The dotted line shows the absorption spectrum of 15 g/L TiO_2 in chloroform.

hand, generally characterised by a bathochromic shift with an increase in the polarity of the solvent because of a better stabilization of the polar excited state with increase in solvent polarity.[76] Thus, the appearance of the concerned band at 334 nm in water and at 355 nm in chloroform presumably represents an appreciable contribution of $n_0 \rightarrow \pi^*_{\text{bpy-res}}$ based transition since the energy of the *n* electrons would decrease significantly on formation of hydrogen bonds.[77] The emission spectrum (Figure 25) on the other hand consists of a broad ^{3}MLCT based emission with λ_{max} at 750 nm when excited at either 486 or 630 nm.

The absorption spectrum becomes broad with simultaneous increase in absorbance on steady addition of a chloroform solution of TiO_2 nanoparticles to **4** (Figure 25) which indicates significant interaction of the dye molecule with TiO_2.[19,23,24,26,28,56,78] Also, the emission intensity is radically diminished on TiO_2 surface (Figure 25) indicating substantial quenching of the excited state by electron injection [19,23,24,26,28,56,78] and hence negligible contribution of excited state features in the transient absorption data on TiO_2 (*vide infra*).

3.C.3.B. Transient spectral characterization

The transient absorption spectrum of **4** (Figure 26) in chloroform is very similar to that in water and shows two bands at 540-750 nm and 830-1000 nm assigned to excited triplet state absorption, in addition to a negative absorption below 510 nm due to ground state bleach.

The kinetic trace of **4** at 900 nm (Figure 26, inset) shows a 9.5 ps component (16%) after initial population of the hot excited states (< 120 fs, 84%).[19,23,24,26,28,56,78] The 9.5 ps component, similar to the 13 ps component observed in water, is tentatively assigned to interligand electron redistribution along the ^{3}MLCT potential energy surface.[38] However,

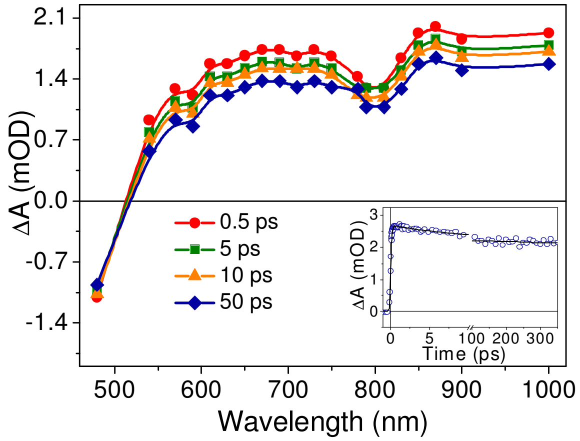

Figure 26: Transient absorption spectrum of **4** at different delay times in chloroform measured after 400 nm (fwhm < 120 fs) excitation. Concentration of **4** is ~ 100 µM. Shown in inset is the kinetic trace for **4** monitored at 900 nm.

recent studies by Hammarstrom and co-workers seem to illustrate that already after one picosecond the molecule has no memory of which bipyridine was initially photoexcited.[79a] Also, the presence of a slow 15 ps component has been observed very recently by Chergui and co-workers on [Re(L)$(CO)_3$(bpy)] complexes that cannot undergo interligand electron redistribution.[79b] This component was proposed to be originating from restructuring of solvent molecules that are very close to the metal center and inserted between the ligands. Thus, our assignment of the 9. 5 ps component (and all the free dye components in this chapter assigned as interligand electron redistribution as well) to interligand electron redistribution is only a very timorous one and much further studies need to be done in order to confirm its true origin. The > 400 ps component arises because of the significantly long lifetimes (*i.e.* >> 1 ns) of the associated Os^{II}-polypyridyl unit.[78b] The transient absorption spectrum of **4** on OA capped TiO_2 surface (Figure 27) shows two absorption bands – the first band in the 550-750 nm region is due to the formation of the cation radical because of photoinduced electron injection from the dye molecule into the conduction band of TiO_2.[14,19,23,24,26,78] The lower energy absorption band in the 800-1000 nm region can be assigned to electrons in the conduction band of TiO_2 nanoparticles. This assignment is corroborated by numerous literature reports where it has been shown that electrons in the conduction band can be detected by visible, near IR and mid IR absorption. [14,19,23,24,26,78] In addition to these bands, a negative absorption can be seen below 540 nm due to the ground state bleach.[78b]

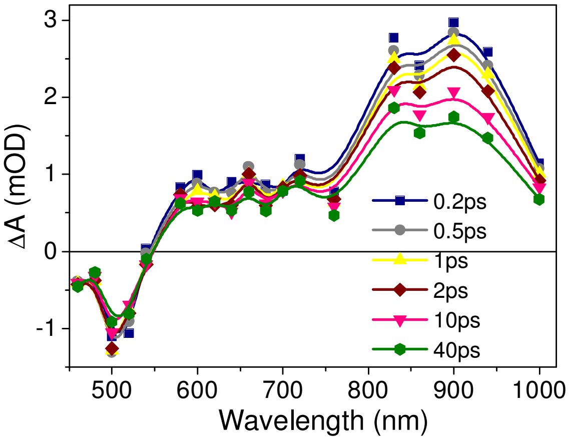

Figure 27: Transient absorption spectrum of **4** on OA capped TiO_2 at different delay times in chloroform measured after 400 nm (fwhm < 120 fs) excitation. Concentration of **4** is ~ 100 μM.

3.C.3.C. Electron injection

Interfacial electron transfer kinetics is decisive in the functioning of an efficient dye sensitized solar cell. Kinetic antagonism at the sensitised interface plays a vital role in determining the efficiency of the device. Efficient charge separation requires the electron injection kinetics to be faster than the rate of excited state decay to ground and the BET has to be as slow as possible.[66a] Of the enediol anchoring groups (which have an obvious advantage over the carboxylic/phosphonic acid based anchoring groups due to the concerned protolytic equilibrium (*vide supra*)), resorcinol has emerged as the superlative one in this regard.[44,78] This is because the deleterious interfacial charge recombination in resorcinol bound TiO_2 systems is extremely slow while exceedingly fast charge injection rates are still maintained.

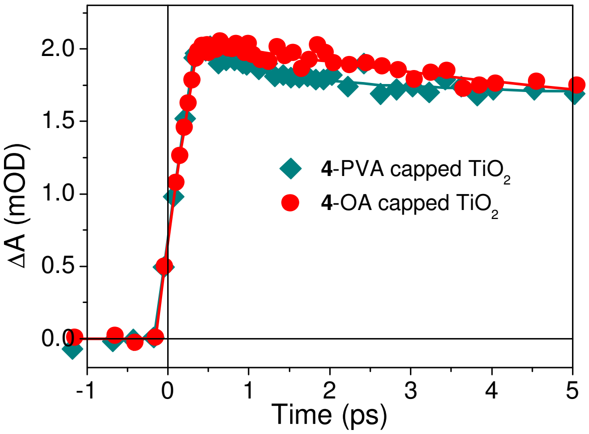

Figure 28: Kinetic traces for the conduction band electrons monitored at 900 nm showing single exponential ultrafast (< 120 fs) electron injection for **4**-PVA capped TiO_2 system in water and **4**-OA capped TiO_2 system in chloroform.

In terms of exponentiality of *electron injection*, however, resorcinol mode of binding does not always show biexponentiality like that seen in our previous studies on **3** bound to TiO_2 where electron injection from both the hot singlet/triplet MLCT states and cold triplet MLCT states could be seen.[78] The corresponding rhenium(I) complex, **7**, showed single exponential injection and injection in a higher density of states of TiO_2 was argued to be the reason.[78a]The conduction band electron signal at 900 nm for **4**-OA capped TiO_2 system in chloroform can be fitted with < 120 fs (+100%), 7 ps (-32.9%), 102 ps (-10.2%), > 400 ps (-56.9%). For the **4**-TiO_2 system involving PVA capped TiO_2 this signal can be fitted with < 120 fs (+100%), 0.9 ps (-20.9%), 22 ps (- 10.4%) and > 400 ps (-68.7%). In the present study the electron injection rate of **4**-OA capped TiO_2 system in chloroform is deduced by monitoring the time of appearance of the aforesaid conduction band electron signal (Figure 28) and, similar to that observed in water,[78b] is observed to be pulse width limited *i.e.* < 120 fs. The same trend is observed in the signal monitored at 600 nm as well, which, for the OA capped TiO_2 system, can be fitted with < 120 fs (+100%), 6 ps (-24%), 102 ps (-24%) and > 400 ps (-52%). The ^{3}MLCT excited state potential for **4** is -0.98 V while that for the ^{1}MLCT state is -1.41 V. On the other hand, the corresponding values for the ruthenium complex are -0.91 V and -1.16 V, respectively.[78b] Analogous to that for the rhenium complex discussed above, therefore, by taking into account an exponential increase in the density of states with increase in energy, this pulse width limited electron injection is accounted for by assuming electron injection in an appreciably high density of states as compared to the corresponding ruthenium complex in the same solvent.[42,51]

Also, sensitized **4**-TiO_2 system with OA capped TiO_2 and PVA capped TiO_2 in chloroform and water, respectively, are so prepared that both the solutions have the same optical density of 1.2 OD at the pump wavelength *i.e.* 400 nm. This means that both of them absorb the same number of pump photons and therefore have the potential to inject the same number of electrons into the TiO_2 conduction band. Consequently, the measured signal magnitudes, which reflect the population of injected electrons, are a direct measure of the relative injection quantum yields for the aforesaid two systems.[42] Figure 29 shows a comparison of the relative injection yields and it can be seen that the relative signal magnitudes are almost similar for the OA capped and PVA capped **4**-TiO_2 in chloroform and in water, respectively, signifying similar electron injection yields for sensitization of two differently capped TiO_2 by **4**.

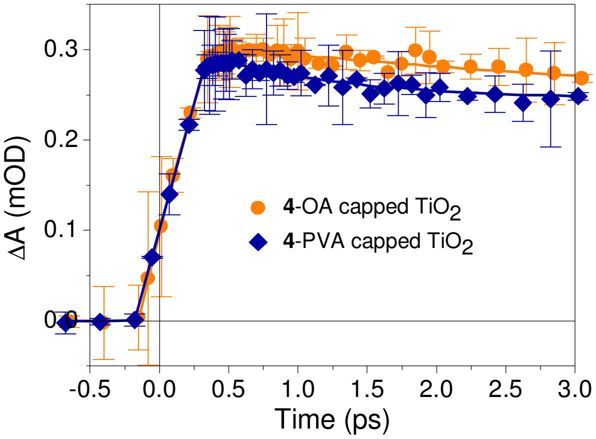

Figure 29: Comparison of electron injection kinetics in **4**-OA capped and **4**-PVA capped TiO_2 systems measured at 900 nm after 400 nm excitation. The standard deviation is plotted as *y*-axis error.

3.C.3.D. Back electron transfer

Electron transfer dynamics are known to be affected by surface modification because of many probable reasons like possible blocking of nonradiative electron/hole recombination at the traps on the surface of the semiconductor nanoparticles or creation of new trap sites *etc*.[69] A systematic study of the electron transfer dynamics on modified surfaces is thus essential in order to be able to optimise the BET rates.

BET rates for **4**-OA capped TiO_2 system in chloroform is monitored by the time of recovery of the ground state bleach at 480 nm and is found to be fitting multiexponentially with the following time constants < 120 fs (-100%), 6 ps (+34%), 102 ps (+19%) and > 400 ps (+47%) (Figure 30). On the other hand, the same transient was found to be fitting with < 120 fs (-100%), 0.9 ps (+28.5%), 22 ps (+10.3%) and > 400 ps (+61.2%) when done on PVA-capped TiO_2 in water.

One can clearly observe that in the longer time scale, dye recombination is faster on OA capped TiO_2 in chloroform than that on PVA capped TiO_2 in water. In order to understand the origin of this difference, the relative HOMO levels of OA in chloroform and PVA in water are calculated at B3LYP/6-31G(d) level of theory. An eighteen carbon $HOCH_2$-$(CH_2$-$CHOH)_8$-CH_3 moiety is used as a probable model unit in calculations of PVA. The aforesaid number of carbon atoms is chosen so as to match the carbon skeleton with that of OA. Calculations reveal that the HOMO of PVA in water lies at -0.24426 a.u. and is at a lower energy with respect to that of oleic acid in chloroform which lies at -0.23236 a.u. In this perspective, the faster recovery on OA capped TiO_2 can be explained by considering orbital interaction between the HOMO of the surface modifier molecule and the unfilled surface trap states (which consequently act as LUMO) in a way analogous to the formation of molecular orbitals from a linear combination of atomic orbitals.[50,53,68b-d,72f] Such interactions are known to influence the charge recombination dynamics of sensitized TiO_2 systems as proved by one of our previous reports on the charge transfer dynamics of dibromofluorescein on unmodified and on dodecylbenzenesulfonate modified TiO_2 nanoparticles.[50]

In our case, as a result of this interaction, the aforesaid LUMO is further destabilized and the HOMO stabilized. The energy of the surface trap states therefore increases on interaction with the surface modifier molecules. Presumably, the HOMO of OA is closer in energy to that of these surface states than the HOMO of PVA which, as per our calculations, lies at a lower energy than the HOMO of OA. As a result, with OA, there is a greater interaction and hence greater perturbation in the energy of these surface states than in the case of interaction with PVA. These states are therefore more destabilized *i.e.* the density of trap states decreases more for OA capped TiO_2 than for PVA capped TiO_2.

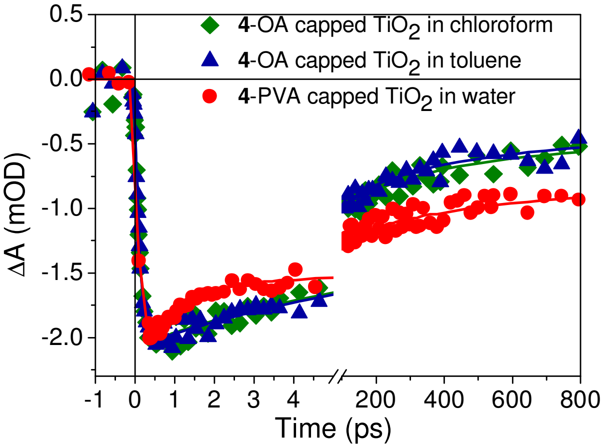

Figure 30: Comparison of the ground state bleach recovery of **4**-OA capped TiO_2 system in chloroform and toluene and **4**-PVA capped TiO_2 system in water measured at 480 nm after 400 nm excitation.

Though similar kind of interaction can be expected between both the deep and the shallow trap states with the HOMO of surface modifier molecules, the shallow trap states being higher in energy compared to the deep traps,[50] interaction between the modifier orbital and the deep trap states is presumably much more pronounced compared to that with the shallow traps and the density of the deep trap states decreases more than that of the shallow trap states.

BET is known to be much slower for electrons in trap states due to a low coupling matrix and the effect is much more pronounced for electrons in deep traps.[49a,80] Since the density of the traps decreases more for OA capped TiO_2, apparently therefore, in the longer time scale, BET for **4**-TiO_2 system is faster on OA capped TiO_2 in chloroform compared to that on PVA capped TiO_2 in water.

Studies on interfacial electron transfer processes in dye sensitized nanoparticles show that before getting trapped, the injected electrons get to diffuse some expanse and hence electrons being quite far from the cation radical at the dye, electronic coupling is extremely small and recombination through tunnelling cannot take place.[81] The trapped electrons instead move by thermal energy assistance *i.e.* by a trap and detrap process. Now, since the density of surface traps is less for OA capped TiO_2 in chloroform than that for PVA capped TiO_2 in water; the aforesaid faster recovery of **4** for the OA capped TiO_2 system can therefore also be explained by considering lesser chances of thermal energy assisted diffusion from one trap to another trap.

It might be noted in this regard that in nanoparticulate TiO_2, electron transportation is reported to be sturdily affected by trapping and detrapping events.[82] The transit time of trapping is about three orders of magnitude faster than that of detrapping. This signifies that most of the photoinjected electrons are localized in the trap states.[83] These trap-filled conditions result in an enhancement of photoconductivity, suggesting that the mechanism of trapping/detrapping controls the charge transport.[84] Therefore, it can be reasonably argued that the trapping/detrapping processes at the various trap sites of surface modified TiO_2 are reflected in the dye recombination dynamics in our system.

BET in dye sensitized systems is known to lie in the Marcus inverted region where with an increase in the driving force ($-\Delta G^0$) the rate of reaction decreases.[47a,48] Now, the redox potentials of osmium dyes are independent of the solvent. But as a result of the aforesaid orbital interactions, the conduction band potential is also expected to shift to more negative values[47e,63,85] and following a similar analogy as discussed before, this shift is expected to be more for OA than that for PVA. This means that for OA capped **4**-TiO_2 system, the $-\Delta G^0$ value would be larger than for the PVA capped **4**-TiO_2 system and hence the recombination is instead expected to be slower for the former. A similar effect has been demonstrated by a previous study from our group on the interfacial dynamics of alizarin on surface modified TiO_2.[67j] Indeed, in an early time scale the recombination of **4** on OA capped TiO_2 is slower than that on PVA capped TiO_2 (Figure 30). However, this effect is soon superseded by the role of trap sites in the longer time scale when the situation is reversed *i.e.* recombination on OA capped TiO_2 becomes faster.

Also, in order to probe any probable influence of the changes in the total reorganization energy on BET rate as a result of a change in the solvent for the two systems, BET rate for **4**-TiO_2 system with OA capped TiO_2 has been studied in toluene which has significantly lower dielectric constant ($\varepsilon = 2.38$) than chloroform ($\varepsilon = 4.81$).[86] The choice of the solvent is limited by the sensitivity of OA capping towards polar solvents. Interestingly, the BET rate, as monitored by the same recovery of the ground state bleach at 480 nm, is very similar to that in chloroform and is found to be fitting with < 120 fs (-100%), 7 ps (+36.5%), 100 ps (+19%) and > 400 ps (+44.5%) (Figure 30) and hence indicating least change of total reorganization energy with change in the solvent dielectric constant in the present case. Though the total reorganization energy parameter would depend on the nature of the surface capping agent, it would not be very erroneous to assume that the more polar the capping agent is, more would be its interaction with the solvent and hence a greater effect on the total reorganization energy should be noted. However, studies similar to this one have been previously carried out by us with dibromofluorescein on sodium dodecylbenzene sulfonate modified TiO_2 nanoparticles and almost similar transients were obtained in pyridine, chloroform and dimethylformamide.[50] It would thus be not unreasonable to assume that changes in the total reorganization energy, if any, does not affect the BET rate in *our* system.

In order to validate these explanations, BET dynamics of the corresponding catechol dye,[78b] **6**, has also been analyzed on PVA and OA capped TiO_2 in the same solvents as for **4** and the results are shown in Figure 31. BET for **6** on OA capped TiO_2 in chloroform is found to be fitting multiexponentially with < 120 fs (-100%), 2 ps (+13%), 16 ps (+15%) and > 400 ps (+72%) and is therefore 25% slower than the corresponding resorcinol dye **4** (*vide supra*). The ground state of the dyes **4** and **6** lie respectively at 0.8 V and 1.14 V, respectively.[78b] The BET of **4** on OA capped TiO_2 is therefore faster than that of **6** because of a smaller driving force for the corresponding BET reaction (1.3 eV for **4**-TiO_2 *vs.* 1.64 eV for **6**-TiO_2, assuming E_{CB} to be -0.5 V at neutral pH *vs.* NHE in water).[49a]

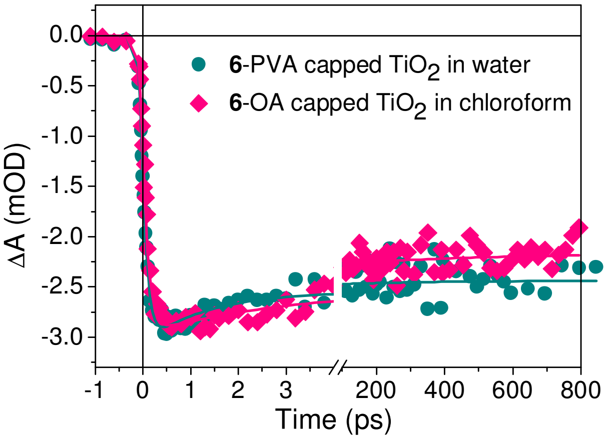

Figure 31: Comparison of the ground state bleach recovery of **6**-OA capped TiO_2 system in chloroform and **6**-PVA capped TiO_2 system in water measured at 480 nm after 400 nm excitation.

Of greater importance, however, is the fact that BET for **6** on PVA capped TiO_2 in water is found to be fitting multiexponentially with < 120 fs (-100%), 1.2 ps (+16.5%), 10 ps (+3.5%) and > 400 ps (+80%) and, similar to the case of **4** discussed above, is therefore slower than the recovery of **6** on OA capped TiO_2 in a longer time scale while it is faster than the recovery of **6** on OA capped TiO_2 in the early time scale (Figure 31). The differences in the concerned dynamics in this case is however small. Thus, the fact that the BET dynamics of **6** on OA and PVA capped TiO_2 surfaces follow a similar trend corroborate our hypothesis that effects of the inverted region and the role of surface trap states in the early and long time scale, respectively, indeed play a significant role in determining the BET dynamics of our molecule **4** on the aforesaid TiO_2 surfaces (Scheme 9).

Surface modification by OA or by PVA does not presumably remove the trap states quantitatively. Interaction of the trap states with the HOMO of the modifier molecules only raises the energy of these trap states so that some of them become surface resonances. This is apparently reflected in the significant residuals of the OA capped **4**-TiO_2 system after 800 ps (Figure 30).

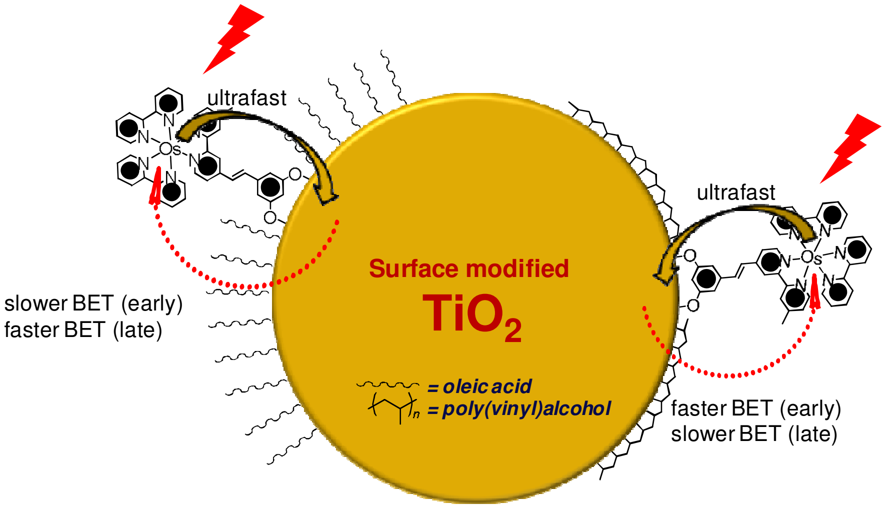

Scheme 9: Schematic representation of the electron transfer processes occurring at the interface in **4**-OA capped and **4**-PVA capped TiO_2 systems.

3.D. Conclusion

In conclusion, therefore, femtosecond transient absorption studies with our newly synthesized sensitizer dyes reinforce the fact that by replacing catechol based enediol anchoring groups with those based on resorcinol *i.e.*, by merely changing the position of the hydroxyl groups, the exceedingly deleterious charge recombination in ruthenium and rhenium polypyridyl enediol based sensitizers can be slowed down outstandingly. The ruthenium complex with this substitute anchoring group, as a result of its weak binding with TiO_2, elicits electron injection simultaneously from the thermalized ^{3}MLCT states in addition to the sub 100 fs electron injection from the hot singlet/triplet MLCT states, which is an entirely new observation for any ruthenium-polypyridyl-enediol complex reported thus far. However, exponentiality and rate of electron injection is a delicate balance of the binding strength of the dye to the semiconductor and the relative energetics of the dye excited state and the semiconductor accepting states. This is reflected in the single exponential ultrafast electron injection for the rhenium based sensitizer for which the dye excited state is too cathodic resulting in electron injection in a very high density of states of TiO_2 thus overruling the effects of weak resorcinolate binding. With the rhenium complex, it could also be shown that resorcinolate binding can mediate effective hole stabilization for dyes that have extremely fast excited state relaxation pathways. This study therefore strengthens our assertion of resorcinol being a very promising anchoring group towards the development of efficient sensitizers for use in DSSCs. The present work is also expected to add significantly to the ongoing research efforts towards the development of aqueous dye sensitized photoelectrochemical fuel cells.[1g,h,I] Studies on the efficiency and the current voltage characteristics of such dyes are currently underway in our laboratory. A point, however, to be taken care of while designing the dyes is that the ground state redox level of the dye must not be too cathodic in order to prevent possible inverted region effects presiding over effects of weak binding, as is evident from a study of the BET rate of the corresponding Os^{II}-polypyridyl dye. The direct comparison of the electron transfer dynamics on the two differently capped surfaces reveals a significant contribution of the trap states in determining the dynamics and is expected to add significantly to the present understanding of the various effects that might be modulated to optimise electron transfer rates in dye sensitized systems thus demanding further research efforts towards modification of the surface properties of TiO_2 by suitable capping agents so that the deleterious BET is slowed down significantly.

3.E. References

1. Moser, J.; Punchihewa, S.; Infelta, P. P.; Grätzel, M. *Langmuir* **1991**, *7*, 3012.

2. Redfern, P. C.; Zapol, P.; Curtiss, L. A.; Rajh, T.; Thurnauer, M. C. *J. Phys. Chem. B* **2003**, *107,* 11419.

3. Duncan, W. R.; Prezhdo, O. V. *J. Phys. Chem. B* **2005**, *109,* 365.

4. Wang, Y.; Hang, K.; Anderson, N. A.; Lian, T. *J. Phys. Chem. B* **2003**, *107,* 9434.

5. Rajh, T.; Chen, L. X.; Lukas, K.; Liu, T.; Thurnauer, M. C.; Tiede, D. M. *J. Phys. Chem. B* **2002**, *106,* 10543.

6. Brennaman, M. K.; Patrocinio, A. O. T.; Song, W.; Jurss, J. W.; Concepcion, J. J.; Hoertz, P. G.; Traub, M. C.; Iha, N. Y. M.; Meyer, T. J. *ChemSusChem*, **2010**, *4*, 216.

7. Song, W.; Brennaman, M. K.; Concepcion, J. J.; Jurss, J. W.; Hoertz, P. G.; Luo, H.; Chen, C.; Kenneth, H. G.; Meyer, T. J. *J. Phys. Chem. C*, **2011**, *115*, 7081.

8. More references of the works from the Solar Fuels EFRC centered at UNC, Chapel Hill on the use of dye-sensitized architectures for aqueous photoelectrochemical fuel-forming applications can be found at http://www.efrc.unc.edu/

9. Matylitsky, V. V.; Lenz, M. O.; J. Wachtveitl, *J. Phys. Chem. B* **2006**, *110,* 8372.

10. Jose, D. A.; Kar, P.; Koley, D.; Ganguly, B.; Thiel, W.; Ghosh, H. N.; Das, A. *Inorg. Chem.* **2007**, *46*, 5576.

11. Kalyanasundaram, K. *Photochemistry of Polypyridine and Porphyrin Complexes*, Academic Press, London, **1992**, chapter 6.

12. Kuciauskas, D.; Monat, J. E.; Villahermosa, R.; Gray, H. B.; Lewis, N. S.; McCusker, J. K. *J. Phys. Chem. B* **2002**, *106*, 9347.

13. Heimer, T. A.; D'Arcangelis, S. T.; Farzad, F.; Stipkala, J. M.; Meyer, G. J. *Inorg. Chem.* **1996**, *35*, 5319.

14. Ramakrishna, G.; Jose, D. A.; Krishna Kumar, D.; Das, A.; Palit, D. K.; Ghosh, H. N. *J. Phys. Chem. B* **2005**, *109*, 15445.

15. Verma, S.; Kar, P.; Das, A.; Palit, D. K.; Ghosh, H. N. *J. Phys. Chem. C* **2008**, *112*, 2918.

16. Estacio, S. G.; do Couto, P. C.; Cabral, B. J. C.; da Piedade, M. E. M.; Simoes, J. A. M. *J. Phys. Chem. A* **2004**, *108,* 10834.

17. -Zaleta, B. G.; –Balderas, R. G.; –Trujillo, J. H. *Phys. Chem. Chem. Phys.* **2010**, *12*, 4783.

18. Pimentel, G. C.; McClellan, A. L. *The Hydrogen Bond*, W. H. Freeman: San Francisco, **1960**.

19. Banerjee, T.; Rawalekar, S.; Das, A.; Ghosh, H. N. *Eur. J. Inorg. Chem.* **2011**, 4187.

20. Kuang, D.; Wenger, B.; Klein, C.; Moser, J. E.; Baker, R. H.; Zakeeruddin, S. M.; Grätzel, M. *J. Am. Chem. Soc.* **2006**, *128*, 4146.

21. Ramakrishna, G.; Ghosh, H. N. *J. Phys. Chem. A* **2002**, *106*, 2545.

22. Duonghong, D.; Ramsden, J.; Grätzel, M. *J. Am. Chem. Soc.* **1982**, *104,* 2917.

23. Kar, P.; Verma, S.; Das, A.; Ghosh, H. N. *J. Phys. Chem. C* **2009**, *113,* 7970.

24. Kar, P.; Banerjee, T.; Verma, S.; Sen, A.; Das, A.; Ganguly, B.; Ghosh, H. N. *Phys. Chem. Chem. Phys.* **2012**, *14*, 8192.

25. Kaniyankandy, S.; Verma, S.; Mondal, J. A.; Palit, D. K.; Ghosh, H. N. *J. Phys. Chem. C* **2009**, *113*, 3593.

26. Verma, S.; Kar, P.; Das, A.; Palit, D. K.; Ghosh, H. N. *Chem. Eur. J.* **2010**, *16*, 611.

27. Kar, P.; Verma, S.; Sen, A.; Das, A.; Ganguly, B.; Ghosh, H. N. *Inorg. Chem.* **2010**, *49*, 4167.

28. Pan, J.; Xu, Y.; Benko, G.; Feyziyev, Y.; Styring, S.; Sun, L.; Akermark, B.; Polivka, T.; Sundstrom, V. *J. Phys. Chem. B* **2004**, *108,* 12904.

29. Verma, S.; Kar, P.; Das, A.; Ghosh, H. N. *Chem. Eur. J.* **2011**, *17*, 1561.

30. Verma, S.; Kar, P.; Banerjee, T.; Das, A.; Ghosh, H. N. *J. Phys. Chem. Lett.* **2012**, *3*, 1543.

31. Handa, S.; Wietasch, H.; Thelakkat, M.; Durrant, J. R.; Haque, S. A. *Chem. Commun.* **2007**, 1725.

32. Cannizo, A.; Mourik, F. V.; Gawelda, W.; Zgrablic, G.; Bressler, C.; Chergui, M. *Angew. Chem*. **2006**, *118*, 3246; *Angew. Chem. Int. Ed.* **2006**, *45*, 3174.

33. Damrauer, N. H.; McCusker, J. K. *J. Phys. Chem. A* **1999**, *103*, 8440.

34. Damrauer, N. H.; Cerullo, G.; Yeh, A.; Boussie, T. R.; Shank, C. V.; McCusker, J. K. *Science* **1997**, *275*, 54.

35. (a) Jarzeba, W.; Walker, G. C.; Johnson, A. E.; Barbara, P. F. *Chem. Phys.* **1991**, *152*, 57. (b) Ramakrishna, G.; Jose, D. A.; Kumar, D. K.; Das, A.; Palit, D. K.; Ghosh, H. N. *J. Phys. Chem. B* **2006**, *110*, 10197

36. (a) Malone, R. A.; Kelley, D. F. *J. Chem. Phys.* **1991**, *95*, 8970. (b) Henrich, J. D.; Zhang, H.; Dutta, P. K.; Kohler, B. *J. Phys. Chem. B* **2010**, *114,* 14679 and references therein.

37. Vlcek Jr, A. *Coord. Chem. Rev.* **2000**, *200*, 933.

38. Shaw, G. B.; Brown, C. L.; Papanikolas, J. M. *J. Phys. Chem. A* **2002**, *106,*1483.

39. Liard, D. J.; Vlcek Jr, A. *Inorg. Chem.*, **2000**, *39*, 485.

40. Hannappel, T.; Burfeindt, B.; Storck, W.; Willig, F. *J. Phys. Chem. B* **1997**, *101,* 6799.

41. Asbury, J. B.; Ellingson, R. J.; Ghosh, H. N.; Ferrere, S.; Nozik, A. J.; Lian, T. *J. Phys. Chem. B* **1999**, *103*, 3110.

42. (a) Zhang, J. Z. *Acc. Chem. Res.* **1997**, *30*, 423. (b) Colombo Jr., D. P.; Bowman, R. M. *J. Phys. Chem.* **1996**, *100*, 18445. (c) Asbury, J. B.; Hao, E.; Wang, Y.; Ghosh, H. N.; Lian, T. *J. Phys. Chem. B* **2001**, *105*, 4545.

43. Gerischer, H. in: *Semiconductor Electrochemistry. In Physical Chemistry: An Advance Treatise*; Eyring, H.; Henderson, D.; Jost, W. Eds.; Academic Press, New York, **1970**, Vol. *9A*, 463.

44. Kaniyankandy, S.; Rawalekar, S.; Sen, A.; Ganguly, B.; Ghosh, H. N. *J. Phys. Chem. C* **2012**, *116*, 98.

45. (a) Marcus, R. A. *Annu. Rev. Phys. Chem*. **1964**, *15*, 155. (b) Marcus, R. A.; Sutin, N. *Biochim. Biophys. Acta* **1985**, *811*, 265.

46. Bonhote, P.; Moser, J. E.; Vlachopoulos, N.; Walder, L.; Zakeeruddin, S. M.; Humphry-Baker, R.; Pechy, P.; Grätzel, M. *Chem. Commun.* **1996**, 1163.

47. (a) Meyer, G. J. *Inorg. Chem.* **2005**, *44*, 6852. (b) Clifford, J. N.; Palomares, E.; Nazeeruddin, M. K.; Grätzel, M.; Nelson, J.; Li, X.; Long, N. J.; Durrant, J. R. *J. Am. Chem. Soc.* **2004**, 126, 5225. (c) Hagfeldt, A.; Grätzel, M. *Chem. Rev.* **1995**, *95*, 49. (d) Nakade, S.; Kanzaki, T.; Kubo, W.; Kitamura, T.; Wada, Y.; Yanagida, S. *J. Phys. Chem. B* **2005**, *109,* 3480. (e) Yan, S. G.; Hupp, J. T. *J. Phys. Chem.* **1996**, *100,* 6867.

48. Grätzel, M. *Inorg. Chem.* **2005**, *44*, 6841.

49. (a) Moser, J. E.; Grätzel, M. *Chem. Phys.* **1993**, *176*, 493. (b) Odobel, F.; Blart, E.; Lagree, M.; Villieras, M.; Boujtita, H.; Murr, N. E.; Caramoric, S.; Bignozzi, C. A. *J. Mater. Chem.* **2003**, *13*, 502. (c) Yang, M.; Thompson, D. W.; Meyer, G. J. *Inorg. Chem.* **2002**, *41*, 1254. (d) Hilgendorff, M.; Sundstrom, V. *J. Phys. Chem. B* **1998**, *102,* 10505. (e) Martini, I.; Hodak, J. H.; Hartland, G. V. *J. Phys. Chem. B* **1998**, *102,* 9508.

50. Ramakrishna, G.; Das, A.; Ghosh, H. N. *Langmuir* **2004**, *20*, 1430.

51. Asbury, J. B.; Anderson, N. A.; Hao, E.; Ai, X.; Lian, T. *J. Phys. Chem. B* **2003**, *107*, 7376.

52. (a) Ramakrishna, G.; Singh, A. K.; Palit, D. K.; Ghosh, H. N. *J. Phys. Chem. B* **2004**, *108*, 4775. (b) Takeshita, K.; Sasaki, Y.; Kobashi, M.; Tanaka, Y.; Maeda, S.; Yamakata, A.; Ishibashi, T.; Onishi, H. *J. Phys. Chem. B* **2004,** *108,* 2963 and references therein.

53. Ramakrishna, G.; Ghosh, H. N. *Langmuir* **2003**, *19*, 505.

54. (a) Huang, Y.-C.; Hsu, J.-H.; Liao, Y.-C.; Yen, W.-C. ; Li, S.-S.; Lin, S.-T.; Chen, C.-W.; Su, W.-F. *J. Mater. Chem.* **2011**, *21*, 4450. (b) Holmberg, J. P. Hydrolytic Synthesis and Physicochemical Properties of TiO_2 Nanoparticles: Fundamentals and Applications. *Ph.D. Thesis*, Department of Chemistry and Molecular Biology, University of Gothenburg, **2012**. (c) Chen, J.; Song, J. L.; Sun, X. W.; Deng, W. Q.; Jiang, C. Y.; Lei, W.; Huang, J. H.; Liu, R. S. *App. Phys. Lett.* **2009**, *94*, 153115. (d) Hikov, T.; Schroeter, M.-K.; Khodeir, L.; Chemseddine, A.; Muhler, M.; Fischer, R. A. *Phys. Chem. Chem. Phys.* **2006**, *8*, 1550. (e) Hikov, T. Photo-assisted preparation of nanocomposites. *Ph.D. Thesis*, Ruhr University, Bochum, Germany, **2009**.

55. (a) Nazeeruddin, M. K.; Zakeeruddin, S. M.; Kalyanasundaram, K. *J. Phys. Chem.* **1993**, *97*, 9607. (b) Pavlishchuk, V. V.; Addison, A. W. *Inorg. Chim. Acta* **2000**, *298*, 97. (c) Kuster, S.; Geiger, T. *Dyes and Pigments* **2012**, *95*, 657.

56. Tachibana, Y.; Moser, J. E.; Grätzel, M.; Klug, D. R.; Durrant, J. R. Subpicosecond Interfacial Charge Separation in Dye-Sensitized Nanocrystalline Titanium Dioxide Films. *J. Phys. Chem.* **1996**, *100*, 20056.

57. (a) Cannizzo, A.; Blanco-Rodriguez, A. M.; Nahhas, A. E.; Sebera, J.; Zalis, S.; Vlcek Jr A.; Chergui, M. *J. Am. Chem. Soc.* **2008**, *130*, 8967. (b) Bubsy, M.; Hartl, F.; Matousek, P.; Towrie, M.; Vlcek Jr, A. *Chem.–Eur. J.*, **2008**, *14*, 6912.

58. Toele, P.; Zhang, H.; Trieflinger, C.; Daub, J.; Glasbeek, M. *Chem. Phys. Lett.* **2003**, *368*, 66.

59. Henrich, J. D.; Zhang, H.; Dutta, P. K.; Kohler, B. *J. Phys. Chem. B* **2010**, *114,* 14679 and references therein.

60. Yam, V. W.-W.; Lau, C.-Y.; Wu, L.-X. Synthesis, photophysical, photochemical and electrochemical properties of rhenium(I) diimine complexes with photoisomerizable pyridyl-azo, -ethenyl or -ethyl ligands. *J. Chem. Soc. Dalton Trans.* **1998**, 1461.

61. Koike, K.; Okoshi, N.; Hori, H.; Takeuchi, K.; Ishitani, O.; Tsubaki, H.; Clark, I. P.; George, M. W.; Johnson, F. P. A.; Turner, J. J. *J. Am. Chem. Soc.* **2002**, *124*, 114485 and references therein.

62. Ardo, S.; Meyer, G. J. *Chem. Soc. Rev.* **2009**, *38*, 115.

63. Duonghong, D.; Ramsden, J.; Grätzel, M. *J. Am. Chem. Soc.* **1982**, *104,* 2977.

64. Hagfeldt, A.; Grätzel, M. *Chem. Rev.* **1995**, *95*, 49.

65. Robertson, N. *Angew. Chem. Int. Ed.* **2006**, *45*, 2338.

66. (a) Durrant, J. R.; Haque, S. A.; Palomares, E. *Coord. Chem. Rev.,* **2004**, *248*, 1247; (b) Hagfeldt, A.; Grätzel, M. *Acc. Chem. Res.,* **2000**, *33*, 269.

67. (a) Harima, Y.; Kawabuchi, K.; Kajihara, S.; Ishii, A.; Ooyama, Y.; Takeda, K. *Appl. Phys. Lett.* **2007**, *90*, 103517; (b) Asaduzzaman, A. M.; Schreckenbach, G. *Phys. Chem. Chem. Phys.,* **2010**, *12*, 14609; (c) Duan, Y.; Fu, N.; Liu, Q.; Fang, Y.; Zhou, X.; Zhang, J.; Lin, Y. *J. Phys. Chem. C* ***2012***, *116*, 8888; (d) Furube, A.; Katoh, R.; Hara, K.; Sato, T.; Murata, S.; Arakawa, H.; Tachiya, M. *J. Phys. Chem. B* **2005,** *109,* 16406; (e) Katoh, R.; Kasuya, M.; Kodate, S.; Furube, A.; Fuke, N.; Koide, N. *J. Phys. Chem. C* **2009**, *113,* 20738; (f) Lu, X.; Mou, X.; Wu, J.; Zhang, D.; Zhang, L.; Huang, F.; Xu, F.; Huang, S. *Adv. Funct. Mater.* **2010**, *20*, 509; (g) Watson, D. F.; Meyer, G. J. *Coord. Chem. Rev.* **2004**, *248*, 1391; (h) Rothenberger, G.; Fitzmaurice, D.; Grätzel, M. *J. Phys. Chem*. **1992**, *96*, 5983; (i) Feng, X. J.; Shankar, K.; Paulose, M.; Grimes, C. A. *Angew. Chem., Int. Ed.* **2009**, *48*, 8095; (j) Ramakrishna, G.; Singh, A. K.; Palit, D. K.; Ghosh, H. N. *J. Phys. Chem. B* **2004**, *108*, 1701.

68. (a) G. Ramakrishna, A. Das and H. N. Ghosh, *Langmuir* 2004, **20**, 1430; (b) E. F. Schubert, J. M. Kuo, R. F. Kopf, A. S. Jordan, H. S. Luftman and L. C. Hopkins, *Phys. Rev. B* 1990, **42**, 1364; (c) M. Kawakita, J. Kawakita, Y. Sakka and T. Shinohara, *J. Electrochem. Soc.* 2010, **157**, H65; (d) A. J. Bard, A. B. Bocarsly, F. R. F. Fan, E. G. Walton and M. S. Wrighton, *J. Am. Chem. Soc.*, 1980, **102**, 3671.

69. (a) Kamat, P. V. *Chem. Rev.* **1993**, *93*, 267; (b) Spanhel, L.; Haase, M.; Weller, H.; Henglein, A. *J. Am. Chem. Soc.* **1987**, *109*, 5649; (c) Spanhel, L.; Weller, H.; Fojtik, A. *Henglein. Ber. Bunsenges. Phys. Chem.* **1987**, *91*, 88.

70. (a) Sze, S. M. *Physics of Semiconductor Devices*, 2nd ed.; John Wiley & Sons: New York, **1981**; (b) Brillson, L. J. *Contacts to Semiconductors*, Noyes Publications: Park Ridge, NJ, **1993**.

71. Many, A.; Goldstein, Y.; Grover, N. B. *Semiconductor Surfaces*; North-Holland: Amsterdam, **1965**.

72. (a) Cahen, D.; Noufi, R. *Appl. Phys. Lett.* **1989**, *54*, 558; (b) Gayen, S.; Ermler, W. C.; Sandroff, C. J. *J. Phys. Chem.* **1991**, *95*, 7357; (c) Lisensky, G. C.; Penn, R. L.; Murphy, C. J.; Ellis, A. B. *Science* **1990**, *248*, 840; (d) Lorenz, J. K.; Kuech, T. F.; Ellis, A. B. *Langmuir* **1998**, *14*, 1680; (e) Sweryda-Krawiec, B.; Chandler-Henderson, R. R.; Coffer, J. L.; Rho, Y. G.; Pinizzotto, R. F. *J. Phys. Chem.* **1996**, *100*, 13776 and references therein; (f) Cohen, R.; Kronic, L.; Shanzer, A.; Cahen, D.; Liu, A.; Rosenwaks, Y.; Lorenz, J. K.; Ellis, A. B. *J. Am. Chem. Soc.* **1999**, *121*, 10545.

73. (a) Becke, A. D. *J. Chem. Phys.* **1993**, *98*, 5648; (b) Lee, C. W.; Parr, R. G. *Phys. Rev. B* **1988**, *37*, 785; (c) Beck, J. M.; Hadad, C. M. *Chem. Biol. Interact.* **2008**, *175*, 200; (d) Hehre, W. J.; Radom, L.; Schleyer P. R.; Pople, J. A. *Ab initio molecular orbital theory*, Wiley, New York, **1988**.

74. (a) Cance`s, E.; Mennucci, B.; Tomasi, J. J. *Chem. Phys.* **1997**, *107*, 3032; (b) Mennucci, B.; Tomasi, J. J. *Chem. Phys.*, **1997**, *106*, 5151; (c) Barone, V.; Cossi, M.; Tomasi, J. *J. Chem. Phys.* **1997**, *107*, 3210; (d) Barone, V.; Cossi, M.; Tomasi, J. *J. Comput. Chem.* **1998**, *19*, 404; (e) Tomasi, J.; Mennucci, B.; Cance`s, E. *J. Mol. Struct. (Theo-chem)* **1999**, *464*, 211.

75. Frisch, M. J.; Trucks, G. W.; Schlegel, H. B.; Scuseria, G. E.; Robb, M. A.; Cheeseman, J. R.; Montgomery Jr., J. A.; Vreven, T.; Kudin, K. N.; Burant, J. C.; Millam, J. M.; Iyengar, S. S.; Tomasi, J.; Barone, V.; Mennucci, B.; Cossi, M.; Scalmani, G.; Rega, N.; Petersson, G. A.; Nakatsuji, H.; Hada, M.; Ehara, M.; Toyota, K.; Fukuda, R.; Hasegawa, J.; Ishida, M.; Nakajima, T.; Honda, Y.; Kitao, O.; Nakai, H.; Klene, M.; Li, X.; Knox, J. E.; Hratchian, H. P.; Cross, J. B.; Bakken, V.; Adamo, C.; Jaramillo, J.; Gomperts, R.; Stratmann, R. E.; Yazyev, O.; Austin, A. J.; Cammi, R.; Pomelli, C.; Ochterski, J. W.; Ayala, P. Y.; Morokuma, K.; Voth, G. A.; Salvador, P.; Dannenberg, J. J.; Zakrzewski, V. G.; Dapprich, S.; Daniels, A. D.; Strain, M. C.; Farkas, O.; Malick, D. K.; Rabuck, A. D.; Raghavachari, K.; Foresman, J. B.; Ortiz, J. V.; Cui, Q.; Baboul, A. G.; Clifford, S.; Cioslowski, J.; Stefanov, B. B.; Liu, G.; Liashenko, A.; Piskorz, P.; Komaromi, I.; Martin, R. L.; Fox, D. J.; Keith, T.; Al-Laham, M. A.; Peng, C. Y.;

Nanayakkara, A.; Challacombe, M.; Gill, P. M. W.; Johnson, B.; Chen, W.; Wong, M. W.; Gonzalez, C.; Pople, J. A. *Gaussian 03, Revision E.01*, Gaussian, Inc., Wallingford CT, **2004**.

76. Valeur, B. *Molecular Fluorescence – Principles and Applications*, Wiley-VCH, **2005**, chapter 4.

77. Robinson, J. W.; Frame, E. M. S. K.; Frame II, G. M. *Undergraduate instrumental analysis*, 6th Edition, **2005**, Chapter 5.

78. (a) Banerjee, T.; Kaniyankandy, S.; Das, A.; Ghosh, H. N. *J. Phys. Chem. C* **2013,** *117*, 3084; (b) Banerjee, T.; Kaniyankandy, S.; Das, A.; Ghosh, H. N. *Inorg. Chem.* **2013,** *52***,** 5366.

79. (a) Wallin, S.; Davidsson, J.; Modin, J.; Hammarstrom, L. *J. Phys. Chem. A* **2005**, *109,* 4697; (b) El Nahhas, A.; Cannizzo, A.; van Mourik, F.; Blanco-Rodriguez, A. M.; Zalis, S.; Vlcek, Jr. A.; Chergui, M. *J. Phys. Chem. A* ***2010***, *114,* 6361.

80. Ramakrishna, G.; Ghosh, H. N.; Singh, A. K.; Palit, D. K.; Mittal, J. P. *J. Phys. Chem. B* **2001**, *105*, 12786.

81. (a) Nelson, J.; Haque, S. A.; Klug, D. R.; Durrant, J. R. *Phys. Rev. B* **2001**, *63*, 205321; (b) Barzykin, A. V.; Tachiya, M. *J. Phys. Chem. B* **2002**, *106*, 4356.

82. Shkrob, I. A.; Sauer, M. C. *J. Phys. Chem. B* **2004**, *108*, 12497.

83. Fisher, A. C.; Peter, L. M.; Wijayantha, K. G. U. *J. Phys. Chem. B* **2000**, *104*, 949.

84. Hagfeldt, A.; Grätzel, M. *J. Phys. Chem.* **1996**, *100*, 8045.

85. Dimitrijevic, N. M.; Savic, D.; Micic, O. I.; Nozik, A. J. *J. Phys. Chem.* **1984**, *88*, 4278.

86. Gokel, G. W. *Dean's Handbook of Organic Chemistry*, 2nd Ed, McGraw Hill, **2004**.

Chapter 4

Superior Grafting and state-of-the-art Interfacial Electron Transfer Rates for Newly Designed Geminal Dicarboxylate Bound Ru(II)- and Os(II)-polypyridyl Dyes on TiO_2 Nanosurface

Communicated to J. Phys. Chem. C

4.A. Foreword

The efficiency, long term stability and hence the cost-effectiveness of the devised dye sensitized solar assemblies is known to depend on a multitude of factors.[1,2f] Most obviously, of these factors, the most important is the kind, the strength and the durability of the dye-TiO_2 binding. In this regard, carboxylate binding has undoubtedly been the most promising anchoring group so far. However, sensitizers bound to metal oxide surfaces through this linkage exhibit high stability in most anhydrous organic solvents and in acidic aqueous solution only; in neutral and basic aqueous solutions the sensitizers are rapidly desorbed from the surface.[3,4] The stability of the dye-TiO_2 conjugate is extremely important not only in terms of the practical applicability of solar cell architectures but immensely so in terms of the recent research efforts towards the development of aqueous dye sensitized photoelectrochemical fuel cells.[5]

With an aim to overcome this problem, many alternative anchoring moieties have been proposed, each with its own merits and demerits. Keeping in mind the impediments to be overtaken, therefore, it seems more practical to engineer the carboxylic acid anchoring group itself so as to overcome its instability in aqueous solutions of higher pHs while still preserving the evident merits that has made this anchoring moiety the one most explored (See Chapter 1, Section 1.B.3.A.3.).

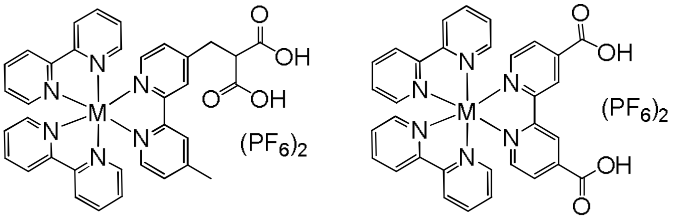

5, M = Ru^{2+}
6, M = Os^{2+}

8, M = Ru^{2+}
9, M = Os^{2+}

Scheme 1: Molecular structures of the sensitizer dyes.

With this idea the previously reported *geminal* dicarboxylic acid anchoring unit has been covalently attached to the well known Ru^{II}-/Os^{II}- polypyridyl chromophore, but in an all new and innovative arrangement of the *gem*-dicarboxy linker with respect to the chromophore, in a very simple but efficient synthetic procedure, to give two sensitizer dyes **5** and **6** (Scheme 1). The second *p*Ka of such *geminal* diacids is known to be significantly high due to the positive inductive effect of the mono-deprotonated species and thus the resulting dye-TiO_2 conjugates are expected to have high pH stability. Any possible disfigurement of the anchoring unit can change its properties drastically, most importantly at the molecular level. In order to confirm therefore that these newly synthesized dyes, **5** and **6**, indeed have potential for probable use in DSSCs, interfacial electron transfer dynamics of these dyes in aqueous environment is studied by femtosecond transient absorption spectroscopy and the results are compared with the corresponding 4,4′-dicarboxy-2,2′-bipyridine analogues of the dyes, **8** and **9** (Scheme 1).

Officer and co-workers attached malonic acid to their porphyrin cores by unsaturated conjugated spacers and obtained good photocurrent yields.[6] Hagfeldt and co-workers studied the electrochemical and photoelectrochemical properties of a lithiated malonic acid ruthenium(II)-polypyridyl dye on TiO_2.[7]

The work by Meyer and co-workers, on the other hand, involved preparation of a ruthenium(II)-polypyridyl based photosensitizer using again a malonic acid linker conjugated with the sensitizer core.[8] They argued that the sp^2 hybridization of the olefin linker in the ligand ensured a planar orientation of the binding carboxylic acid groups with the connecting pyridine rings, thus ensuring optimal injection rates. However, no ultrafast studies were carried out for a quantitative estimation of the electron transfer rates. Futhermore, a planar orientation of the malonic acid unit also locks its flexibility and might affect its binding with TiO_2.

In this viewpoint, our arrangement of the *gem*-dicarboxy linker with respect to the chromophore proves that a planar orientation of the anchoring moiety with respect to the bipyridine unit might not be necessary to optimize electron injection rates whatever be the origin of its components. This report also proves that such arrangements can be arrived at using very simple protocols as compared to the cumbersome synthetic protocols reported before. This article is also the first femtosecond pump-probe spectroscopic study of sensitizer dyes with *geminal* dicarboxylic acid based anchoring moiety and, in view of the remarkable results obtained, will add notably towards the development of novel sensitizer dyes with superior solar photovoltaic and aqueous photoelectrochemical applications.

4.B. Experimetal Section (please see Appendix A for details)

4.B.1 Computational Methodologies

All DFT calculations have been performed with the program package $DMol^3$ in Materials Studio (version 4.1) from Accelrys Inc.[9] We have used DND (double numerical with *d* polarization) and DNP (double numerical with *d* and *p* polarization) basis sets which are comparable to 6-31G* and 6-31G** Gaussian-type basis sets, respectively. The optimization of additive on the surface has been performed with LDA/PWC/DND level of theory. The single point calculations have been reported with GGA/PBE/DNP level of theory[10] while the frontier molecular orbitals have been calculated at GGA/PBE/DNP level of theory. The implicit conductor like screening model (COSMO) has been employed using the dielectric constant of water (dielectric constant = 78.54) to take into account the solvent effect in these calculations.[11] To improve the computational performance, a Fermi smearing of 0.002 hartree (1 Ha = 27.212 eV) and a global cutoff of 4.5 Å has been employed. The tolerance of the energy, gradient, and displacement convergences are 2×10^{-5} Ha, 4×10^{-3} Ha.Å^{-1} and 5×10^{-3} Å, respectively. In this study, as illustrated in Figure 13, a previously reported titanium dioxide cluster [Ti_8O_{32}] has been used for the TiO_2 anatase {101} surfaces.[12] The charge of the cluster is made neutral by adding hydrogen atoms on oxygen atoms with dangling bonds.

4.B.2. Synthesis

4.B.2.A. 4-(bromomethyl)-4'-methyl-2,2'-bipyridine (**1**)**:**[13] To 4,4′-dimethyl-2,2′-bipyridine (1.8 g, 9.78 mmol) and N-bromosuccinimide (1.8 g, 10.1 mmol) in a 100 ml round bottomed flask, 40 ml dry CCl_4 is added under an inert Ar atmosphere. The reaction mixture is then set to reflux. As soon as boiling starts, a pinch (~ 50 mg) of azobisisobutyronitrile is added. The reaction mixture is refluxed for exactly 2 hours after which it is cooled to room temperature and the precipitated succinimide is filtered through a grade III sintered glass crucible. The filtrate is evaporated to near dryness in a rotary evaporator at a temperature not more than 50 ^{0}C. The viscous liquid so obtained is purified over 230-400 mesh silica using dichloromethane/acetone as the eluent to obtain pure **1** as a white solid which is stored at low temperature under hexane. Yield: 0.772 g, 30%. ESI-MS (*m/z*): Calculated for $C_{12}H_{11}BrN_2$ – 262.01, Observed – 263.01, 265.01 $[M + 1]^+$; ^{1}H NMR (500 MHz, $CDCl_3$): δ (ppm) 8.66 (1H, d, *J* = 5 Hz, H^6 (bpy)); 8.54 (1H, d, *J* = 5 Hz, $H^{6'}$ (bpy)); 8.41 (1H, s, H^3 (bpy)); 8.24 (1H, s, $H^{3'}$ (bpy)); 7.34 – 7.33 (1H, m, H^5 (bpy)); 7.15 (1H, d, *J* = 5 Hz, $H^{5'}$ (bpy)); 4.48 (2H, s, –C**H**$_2$Br); 2.44 (3H, s, bpy–C**H**$_3$). IR (KBr pellet, cm^{-1}) 1199 (ν_{bend}(C–Br)). Elemental Analysis: Calculated for $C_{12}H_{11}BrN_2$: C, 54.77; H, 4.21; N, 10.65. Found: C, 54.75; H, 4.24; N, 10.61.

4.B.2.B. Diethyl 2-((4'-methyl-2,2'-bipyridin-4-yl)methyl)malonate (**2**)**:** NaH (60% dispersion in mineral oil, 36.5 mg, 0.9125 mmol) is washed thrice with dry hexane in a 100 ml round bottomed flask under an inert nitrogen atmosphere and 10 ml of dry THF solvent is added to it. This is followed by addition of diethyl malonate (115.4 μl, 0.7604 mmol) while maintaining the temperature at 0 ^{0}C. The reaction mixture is allowed to stir at this temperature for 15-20 minutes after which **1** (200 mg, 0.7604 mmol) in dry THF is added dropwise over a 30 minute period. The reaction mixture is then stirred for 24 hrs at room temperature. After completion of the reaction, a minimum quantity of water is added and stirred for 5 minutes. THF is then evaporated and solvent extraction is performed with chloroform; the organic layer is collected, dried with anhydrous sodium sulphate and evaporated to dryness to obtain a crude solid. This is finally purified by column chromatography over silica gel 200-400 mesh using $CHCl_3$/MeOH as the eluent to obtain pure **2** as a viscous liquid. Yield: 110 mg, 42.1%. ESI-MS (*m/z*): Calculated for $C_{19}H_{22}N_2O_4$ – 342.16, Observed – 343.07 $[M + 1]^+$; ^{1}H NMR (500 MHz, CD_2Cl_2): δ (ppm) 8.64 (1H, d, *J* = 5 Hz, H^6 or $H^{6'}$); 8.60 (1H, d, *J* = 4.5 Hz, H^6 or $H^{6'}$); 8.41 (1H, s, H^3 or $H^{3'}$); 8.36 (1H, s, H^3 or $H^{3'}$); 7.27 (1H, d, *J* = 5 Hz, H^5 or $H^{5'}$); 7.25 (1H, d, *J* = 5 Hz, H^5 or $H^{5'}$);4.30 – 4.21 (4H, m, –COOC**H**$_2$CH$_3$); 3.85 (1H, t, *J* = 7.5 Hz, –CH$_2$–C**H**–); 3.38 (2H, d, *J* = 7.5 Hz, –C**H**$_2$–CH–); 2.53 (3H, s, bpy-C**H**$_3$); 1.31 (6H, t, *J* = 7 Hz, –COOCH$_2$C**H**$_3$). IR (KBr pellet, cm^{-1}) 1743 (ν(C=O$_{ester}$)). Elemental Analysis: Calculated for $C_{19}H_{22}N_2O_4$: C, 66.65; H, 6.48; N, 8.18. Found: C, 66.8; H, 6.50; N, 8.1.

4.B.2.C. {bis-(2,2′-bpy)-(diethyl 2-((4'-methyl-2,2'-bipyridin-4-yl)methyl)malonate)} ruthenium(II) hexafluorophosphate (**3**): Ru(bpy)$_2$Cl$_2$.2H$_2$O (166 mg, 0.3198 mmol) and **2** (105 mg, 0.3198 mmol) are refluxed in ethanol for 8 hours with continuous stirring. The solvent is then evaporated and the product is made soluble in a minimum volume of water. Saturated aqueous NH$_4$PF$_6$ (10 mole equivalents) is added to the resulting solution to precipitate the desired Ru(II)-polypyridyl complex as the hexafluorophosphate salt. This is kept as such for 4-5 hours in a refrigerator to ensure complete precipitation after which it is filtered, washed with large volumes of cold water and dried in a vacuum desiccator. The crude compound so obtained is purified by column chromatography over alumina using acetonitrile/toluene as the eluent. The second fraction is collected and the solvent is removed to isolate a red solid which is redissolved in dichloromethane and two drops of acetonitrile and solvent extraction is done to remove the excess KPF$_6$ used in the eluent. The organic phase is dried over anhydrous sodium sulphate and is evaporated to dryness to give the desired product in pure form. Yield: 306 mg (91.6%). ESI-MS (*m/z*): Calculated for $C_{39}H_{38}N_6O_4PF_6Ru$ 901.0128 $[M - PF_6^-]^+$, Observed 900.45 $[M - PF_6^-]^+$; ^1H NMR (500 MHz, CD$_3$CN): δ (ppm) 8.51 (3H, d, *J* = 8 Hz, H^6 and $H^{6'}$ (bpy-ester), H^6 or $H^{6'}$ (bpy)); 8.41 (1H, s, H^3 or $H^{3'}$ (bpy-ester)); 8.38 (1H, s, H^3 or $H^{3'}$ (bpy-ester)); 8.08 – 8.05 (3H, m, H^6 and/or $H^{6'}$ (bpy)); 7.75 – 7.73 (2H, m, H^3 and/or $H^{3'}$ (bpy)); 7.68 (1H, d, *J* = 5 Hz, H^3 and/or $H^{3'}$ (bpy)); 7.61 (1H, d, *J* = 6 Hz, H^3 and/or $H^{3'}$ (bpy)); 7.55 (1H, d, *J* = 6 Hz, H^5 (bpy-ester)); 7.43 – 7.39 (3H, m, $H^{5'}$ (bpy-ester) (1 proton), H^4 and/or $H^{4'}$ (bpy)); 7.29 – 7.25 (3H, m, H^4 and/or $H^{4'}$ (bpy), H^5 and/or $H^{5'}$ (bpy) (1 proton)); 7.22 – 7.16 (3H, m, H^5 and/or $H^{5'}$ (bpy)); 4.15 – 4.08 (4H, m, –COOC**H**$_2$CH$_3$); 3.88 (1H, t, *J* = 7.5 Hz, –CH$_2$–C**H**–); 3.35 (2H, d, *J* = 8 Hz, –C**H**$_2$–CH–); 2.56 (3H, s, bpy-C**H**$_3$); 1.14 – 1.08 (6H, m, –COOCH$_2$C**H**$_3$). IR (KBr pellet, cm^{-1}) 1730 ($\nu(C{=}O_{ester})$), 839 ($\nu(PF_6)$). Elemental Analysis: Calculated for $C_{39}H_{38}N_6O_4P_2F_{12}Ru$: C, 44.79; H, 3.66; N, 8.04; Found: C, 44.90; H, 3.59; N, 8.01.

4.B.2.D. {bis-(2,2′-bpy)-(diethyl 2-((4'-methyl-2,2'-bipyridin-4-yl)methyl)malonate)} osmium(II) hexafluorophosphate (**4**): This is prepared by a similar procedure as adopted for the synthesis of **3**. Os(bpy)$_2$Cl$_2$.2H$_2$O (200 mg, 0.328 mmol) and **2** (114 mg, 0.333 mmol) are refluxed in ethanol for 8 hours withs continuous stirring. Then the solvent is evaporated and the product is made soluble in a minimum volume of water. Saturated aqueous KPF$_6$ (10 mole equivalents) is added to the resulting solution to precipitate the desired Os^{II}-polypyridyl complex as the hexafluorophosphate salt. This is kept as such for 4-5 hours in a refrigerator to ensure complete precipitation after which it is filtered, washed with cold water and dried in a vacuum desiccator. The crude compound so obtained is purified by column chromatography over alumina using acetonitrile/toluene as the eluent. The last fraction is collected and the solvent is removed to isolate a greenish-black solid which is redissolved in dichloromethane and two drops of acetonitrile and solvent extraction is done to remove the excess KPF$_6$ used in the eluent. The organic phase is dried over anhydrous sodium sulphate and is evaporated to dryness to give the desired product.

Yield: 196 mg (52.5%). ESI-MS (*m/z*): Calculated for $C_{39}H_{38}N_6O_4PF_6Os$ 991.231 [M - PF_6^-]$^+$, Observed 990.60 [M - PF_6^-]$^+$, 422.84 [M - $2PF_6^-$]$^{2+}$; ^{1}H NMR (500 MHz, CD_3CN): δ (ppm) 8.49 – 8.45 (4H, m, H^6 and $H^{6'}$ (bpy-ester) and/or H^6 and/or $H^{6'}$ (bpy)); 8.35 (1H, s, H^3 (bpy-ester)); 8.32 (1H, s, $H^{3'}$ (bpy-ester)); 7.84 (4H, m, H^6 and $H^{6'}$ (bpy-ester) and/or H^6 and/or $H^{6'}$ (bpy) (two protons), H^4 and/or $H^{4'}$ (bpy)); 7.64 – 7.58 (3H, m, H^4 and/or $H^{4'}$ (bpy) (two protons), H^3 and/or $H^{3'}$ (bpy)); 7.58 (1H, d, *J* = 5.5 Hz, H^3 and/or $H^{3'}$ (bpy)); 7.49 (1H, d, *J* = 6 Hz, H^3 and/or $H^{3'}$ (bpy)); 7.42 (1H, d, *J* = 5.5 Hz, H^3 and/or $H^{3'}$ (bpy)); 7.31 – 7.24 (4H, m, H^5 and $H^{5'}$ (bpy)); 7.20 – 7.15 (2H, m, H^5 and $H^{5'}$ (bpy-ester)); 4.12 – 4.05 (4H, m, $-COOC\mathbf{H}_2CH_3$); 3.84 (1H, t, *J* = 7.5 Hz, $-CH_2-C\mathbf{H}-$); 3.37 (2H, d, *J* = 8 Hz, $-C\mathbf{H}_2-CH-$); 2.61 (3H, s, bpy-$C\mathbf{H}_3$); 1.11 – 1.06 (6H, m, $-COOCH_2C\mathbf{H}_3$). IR (KBr pellet, cm^{-1}) 1728 (ν(C=O_{ester})), 839 (ν(PF_6)). Elemental Analysis: Calculated for $C_{39}H_{38}N_6O_4P_2F_{12}Os$: C, 41.27; H, 3.37; N, 7.40; Found: C, 41.5; H, 3.11; N, 7.42.

4.B.2.E. {bis-(2,2′-bpy)-(2-((4'-methyl-2,2'-bipyridin-4-yl)methyl)malonic acid)} ruthenium(II) hexafluorophosphate (**5**): **3** (100 mg, 0.096 mmol) is dissolved in acetone (10 mL) and aqueous NaOH (4 M, 0.1 mL, 0.4 mmol) is added to it. The reaction mixture is then refluxed in dark under N_2. The progress of the reaction is monitored by TLC over silica at every one hour interval. After 6 hours, it is observed that the starting material **3** is completely consumed to yield a single product with a much less R_f value than that of **3**. The solution is now evaporated to complete dryness and the residue is dissolved in 3-4 ml of water. 1M HPF_6 is added dropwise to this solution until complete precipitation of an orange solid which is filtered through a Whatman 42 filter paper, washed thoroughly with cold water and finally dried in a vacuum desiccator. Yield: 30 mg (31.7%). ESI-MS (*m/z*): Calculated for $C_{35}H_{30}N_6O_4P_2F_{12}Ru$ 990.0656, Observed 1031.28 [M + Na + H_2O]$^+$; ^{1}H NMR (200 MHz, CD_3CN): δ (ppm) 8.51 – 8.46 (4H, d, *J* = 8.6 Hz, H^6 and $H^{6'}$ (bpy-diCOOH) and/or H^6 and/or $H^{6'}$ (bpy)); 8.39 – 8.36 (1H, d, *J* = 5.8 Hz, H^3 (bpy-diCOOH)); 8.09 – 8.00 (4H, m, H^6 and $H^{6'}$ (bpy-diCOOH) and/or H^6 and/or $H^{6'}$ (bpy) (two protons), $H^{3'}$ (bpy-diCOOH), H^3 and/or $H^{3'}$ (bpy)); 7.81 – 7.65 (4H, m, H^3 and $H^{3'}$ (bpy), H^4 and/or $H^{4'}$ (bpy) (one proton); 7.63 – 7.46 (3H, m, H^4 and $H^{4'}$ (bpy)); 7.46 – 7.31 (4H, m, H^5 and $H^{5'}$ (bpy)); 7.29 – 7.22 (2H, m, H^5 and $H^{5'}$ (bpy-diCOOH)); 3.83 (1H, t, *J* = 7.6 Hz, $-CH_2-C\mathbf{H}-$); 3.32 – 3.27 (2H, m, $-C\mathbf{H}_2-CH-$); 2.53 (3H, s, bpy-$C\mathbf{H}_3$). IR (KBr pellet, cm^{-1}) 1723 (ν(C=O_{acid})), 842 (ν(PF_6)). Elemental Analysis: Calculated for $C_{35}H_{30}N_6O_4P_2F_{12}Ru$: C, 42.48; H, 3.06; N, 8.49; Found: C, 42.63; H, 3.09; N, 8.47.

4.B.2.F. {bis-(2,2′-bpy)-(2-((4'-methyl-2,2'-bipyridin-4-yl)methyl)malonic acid)} osmium(II) hexafluorophosphate (**6**): This is prepared by a similar procedure as adopted for the synthesis of **5**. **4** (113.6 mg, 0.1 mmol) is dissolved in acetone (10 mL) and aqueous NaOH (4 M, 0.1 mL, 0.4 mmol) is added to it. The reaction mixture is then refluxed in dark under N_2. The progress of the reaction is again monitored by TLC over silica at every one hour interval. After 8 hours, it is observed that the starting material **4** is completely consumed to yield a single product with a much less R_f value than that of **4**. The solution is now evaporated to complete dryness and the residue is dissolved in 3-4 ml of water. 1M HPF_6 is added dropwise to this solution until complete precipitation of an orange solid which is filtered through a Whatman 42 filter paper, washed thoroughly with cold water and finally dried in a vacuum desiccator. Yield: 25 mg (23.2%). ESI-MS (*m/z*): Calculated for $C_{35}H_{30}N_6O_4Os$ 394.05 $[M - 2PF_6^-]^{2+}$, Observed 394.46 $[M - 2PF_6^-]^{2+}$, 848.1 $[M - 2PF_6^- - 2H^+ + Na^+ + K^+]^{2+}$; ^1H NMR (500 MHz, CD_3CN): δ (ppm) 8.48 – 8.44 (4H, m, H^6 and $H^{6'}$ (bpy-diCOOH) and/or H^6 and/or $H^{6'}$ (bpy)); 8.34 (2H, s, H^3 and $H^{3'}$ (bpy-diCOOH)); 7.85 – 7.82 (4H, m, H^6 and $H^{6'}$ (bpy-diCOOH) and/or H^6 and/or $H^{6'}$ (bpy), H^4 and/or $H^{4'}$ (bpy) (two protons)); 7.65 – 7.61 (4H, m, H^4 and $H^{4'}$ (bpy) (two protons), H^5 and $H^{5'}$ (bpy-diCOOH)); 7.46 (1H, d, *J* = 6 Hz, H^3 and/or $H^{3'}$ (bpy)); 7.43 (1H, d, *J* = 6 Hz, H^3 and/or $H^{3'}$ (bpy)); 7.32 – 7.26 (4H, m, H^5 and $H^{5'}$ (bpy)); 7.19 (1H, d, *J* = 6 Hz, H^3 and/or $H^{3'}$ (bpy)); 7.15 (1H, d, *J* = 5.5 Hz, H^3 and/or $H^{3'}$ (bpy)); 3.11 (1H, t, *J* = 7.5 Hz, $-CH_2-C\mathbf{H}-$); 2.73 (2H, m, $-C\mathbf{H}_2-CH-$); 2.60 (3H, s, bpy-$C\mathbf{H}_3$). IR (KBr pellet, cm^{-1}) 1723 ($\nu(C{=}O_{acid})$), 842 ($\nu(PF_6)$). Elemental Analysis: Calculated for $C_{35}H_{30}N_6O_4F_{12}P_2Os$: C, 38.97; H, 2.80; N, 7.79; Found: C, 39.10; H, 2.85; N, 7.75.

4.B.2.G. 2,2'-bipyridine-4,4'-dicarboxylic acid (7):[14] 4,4′-dimethyl-2,2′-bipyridine (1g, 6.41 mmol) is dissolved in 10 ml of concentrated H_2SO_4 and the solution is cooled to 0 ^0C. To this solution, a solution of CrO_3 (3.2 g. 32 mmol) in 30 ml of concentrated H_2SO_4 is added under ice cold conditions whereupon a green colour is obtained. The mixure is then heated at 75 ^0C for two and a half hours. A perfect deep green solution is obtained which is poured into 200 ml of crushed ice. The white precipitate so obtained is filtered through a grade 4 sintered glass crucible, washed thoroughly with water and finally dried in vacuum to give pure **7**. Yield: 1.27 g (81.2%). ESI-MS (*m/z*): Calculated for $C_{12}H_8N_2O_4$: 244.05, Observed: 243.12 $[M - H^+]^-$; ^1H NMR (500 MHz, d_6-DMSO): δ (ppm) 8.92 (2H, d, *J* = 5 Hz, H^6 and $H^{6'}$); 8.85 (2H, s, H^3 and $H^{3'}$); 7.92 (2H, d, *J* = 4 Hz, H^5 and $H^{5'}$). IR (KBr pellet, cm^{-1}) 1722 ($\nu(C{=}O_{acid})$). Elemental Analysis: Calculated for $C_{12}H_8N_2O_4$: C, 59.02; H, 3.30; N, 11.47; Found: C, 59.3; H, 3.22; N, 11.35.

4.B.2.H. {bis-(2,2′-bpy)-(2,2'-bipyridine-4,4'-dicarboxylic acid)} ruthenium(II) hexafluorophosphate (8): $Ru(bpy)_2Cl_2.2H_2O$ (100 mg, 0.192 mmol) and **7** (58.6 mg, 0.24 mmol) are refluxed in ethanol:water 5:3(*v/v*) for 14 hours with continuous stirring. Ethanol is then evaporated and unreacted **7** is filtered off. To the resulting aqueous solution, saturated aqueous KPF_6 (10 mole equivalents) is added to convert the desired Ru^{II}-polypyridyl complex to its hexafluorophosphate salt. A small amount of precipitate is obtained which is filtered off. To the resulting red fitrate, 5-6 drops of concentrated HPF_6 is added. A fine crystalline precipitate is obtained which is filtered through a grade 4 sintered glass crucible, washed with cold water and then dried in vacuum to give spectroscopically pure **8**. Yield: 133 mg (35%). ESI-MS (*m/z*): Calculated for $C_{32}H_{24}N_6O_4PF_6Ru$ 803.0724 $[M - PF_6^-]^+$, Observed 802.66 $[M - PF_6^-]^+$; ^1H NMR (500 MHz, CD_3CN): δ (ppm) 9.02 (2H, s, H^3 and $H^{3'}$ (bpy-COOH)); 8.51 (2H, d, *J* = 5 Hz, H^6 and $H^{6'}$ (bpy-COOH)); 8.50 (2H, d, *J* = 4.5 Hz, H^6 and/or $H^{6'}$ (bpy)); 8.08 (4H, m, H^3 and/or $H^{3'}$ (bpy), H^6 and/or $H^{6'}$ (bpy)); 7.93 (2H, d, *J* = 6 Hz, H^3 and/or $H^{3'}$ (bpy)); 7.82 (2H, dd, *J* = 4

Hz, 1.5 Hz, H^4 and/or $H^{4'}$ (bpy)); 7.70 (2H, d, *J* = 5.5 Hz, H^5 and $H^{5'}$ (bpy-COOH)); 7.65 (2H, d, *J* = 5.5 Hz, H^5 and/or $H^{5'}$ (bpy)); 7.43 – 7.41 (2H, m, H^5 and/or $H^{5'}$ (bpy) or H^4 and/or $H^{4'}$ (bpy)); 7.39 – 7.37 (2H, m, H^5 and/or $H^{5'}$ (bpy) or H^4 and/or $H^{4'}$ (bpy)). IR (KBr pellet, cm^{-1}) 1733 ($\nu(C{=}O_{acid})$), 840 ($\nu(PF_6)$). Elemental Analysis: Calculated for $C_{32}H_{24}N_6O_4P_2F_{12}Ru$: C, 40.56; H, 2.55; N, 8.87; Found: C, 40.45; H, 2.59; N, 8.75.

4.B.2.I. {bis-(2,2′-bpy)-(2,2'-bipyridine-4,4'-dicarboxylic acid)} osmium(II) hexafluorophosphate (9): This is prepared by a similar procedure as adopted for the synthesis of **8**. $Os(bpy)_2Cl_2.2H_2O$ (200 mg, 0.33 mmol) and **7** (80 mg, 0.33 mmol) are refluxed in ethanol:water 5:3(*v/v*) for 14 hours with continuous stirring. Ethanol is then evaporated and unreacted **7** is filtered off. To the resulting aqueous solution, saturated aqueous KPF_6 (10 mole equivalents) is added to convert the desired Os^{II}-polypyridyl complex to its hexafluorophosphate salt. A small amount of precipitate is obtained which is filtered off. To the resulting red fitrate 5-6 drops of concentrated HPF_6 is added. A fine crystalline precipitate is obtained which is filtered through a grade 4 sintered glass crucible, washed with cold water and then dried in vacuum to give spectroscopically pure **9**. Yield: 170 mg (20%). ESI-MS (*m/z*): Calculated for $C_{32}H_{24}N_6O_4P_2F_{12}Os$ 1038.0757, Observed 374.07 $[M - 2PF_6^-]^{2+}$, 403.05, 808.13 $[M - 2PF_6^- - 2H^+ + Na^+ + K^+]^{2+}$; ^1H NMR (200 MHz, D_2O): δ (ppm) 8.73 (2H, s, H^3 and $H^{3'}$ (bpy-COOH)); 8.39 (4H, d, *J* = 8 Hz, $2H^6$ and $2H^{6'}$ (bpy)); 7.78 – 7.70 (6H, m, H^6 and $H^{6'}$ (bpy-COOH), $2H^3$ and $2H^{3'}$ (bpy)); 7.61 – 7.54 (4H, m, $2H^4$ and $2H^{4'}$ (bpy)); 7.42 (2H, d, *J* = 6 Hz, H^5 and $H^{5'}$ (bpy-COOH)); 7.20 – 7.11 (4H, m, $2H^5$ and $2H^{5'}$ (bpy)). IR (KBr pellet, cm^{-1}) 1733 ($\nu(C{=}O_{acid})$), 837 ($\nu(PF_6)$). Elemental Analysis: Calculated for $C_{32}H_{24}N_6O_4P_2F_{12}Os$: C, 37.07; H, 2.33; N, 8.11; Found: C, 37.19; H, 2.35; N, 8.12.

4.C. Results and Discussion

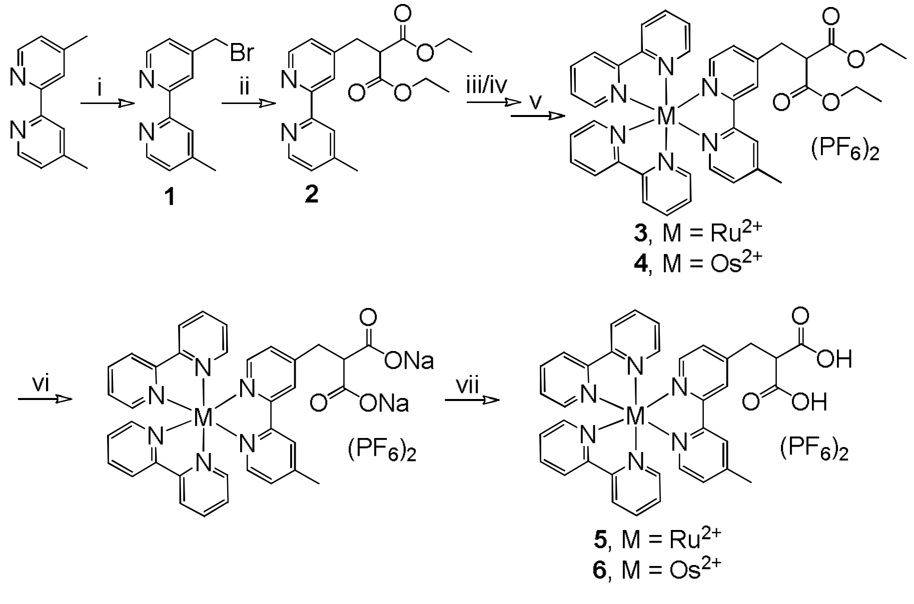

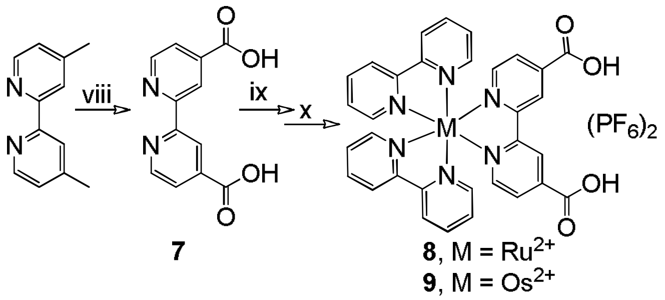

i = NBS, AIBN in CCl_4, ii = DEM, NaH in THF, iii = $Ru(bpy)_2Cl_2.2H_2O$ in EtOH,
iv = $Os(bpy)_2Cl_2$ in EtOH, v = satd. aq. KPF_6, vi = NaOH in acetone, vii = HPF_6,
viii = CrO_3, H_2SO_4, ix = $Ru(bpy)_2Cl_2.2H_2O$ in EtOH/water, x = HPF_6

Scheme 2: Methodology for the synthesis of **5** and **6** and the reference complexes **8** and **9.**

The synthetic methodology adopted for the synthesis of the respective complexes is shown in Scheme 2. 4,4′-dimethyl-2,2′-bipyridine is first monobrominated at one of the methyl groups by typical radical bromination using N-bromosuccinimide to give **1**. This is then allowed to react with diethyl malonate; a nucleophilic substitution reaction takes place in presence of sodium hydride as the base to yield **2** which is subsequently allowed to react with $Ru(bpy)_2Cl_2$ and $Os(bpy)_2Cl_2$ in ethanol, respectively, to give the respective precursor complexes, **3** and **4**. The ester groups in these complexes are then hydrolysed in alkaline conditions in refluxing acetone. Finally, protonation to carboxylic acid groups is done by addition of HPF_6 to yield **5** and **6** as the newly designed sensitizer dyes.

.

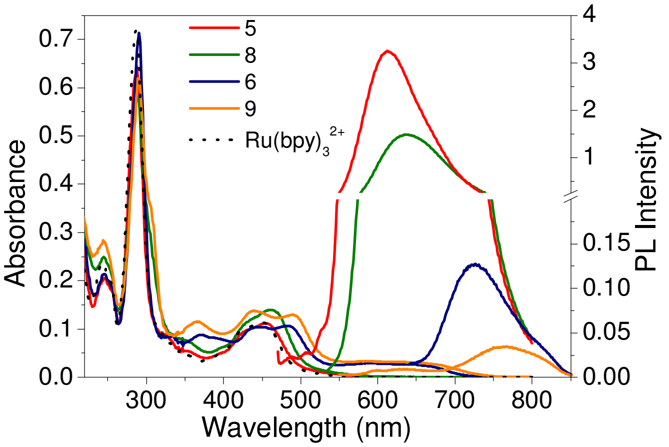

Figure 1: Absorption and emission spectra of **5** (red), **6** (blue), **8** (olive) and **9** (orange) in water. The concentration of all the dyes is 1 × 10^{-5} M. The dotted lines shows the normalized absorption spectra of Ru^{II}-tris(2,2′-bipyridine) in water.

The reference complexes, **8** and **9**, are prepared by reactions respectively of $Ru(bpy)_2Cl_2$ and $Os(bpy)_2Cl_2$ with **7** which is prepared by simple oxidation of 4,4′-dimethyl-2,2′-bipyridine. The purity of the complexes is checked by different analytical and spectroscopic methods (*vide supra*) and the analytical data matches well with that of the expected formulation.

Figure 1 shows the absorption and emission spectrum of **5** and **6** in water. The former is seen to be characterised by strong ligand centered π-π^* transitions at 289 nm for both **5** and **6**. The band at 355 nm and 370 nm, on the other hand, for **5** and **6**, respectively, arises either due to delocalized interligand charge transfer or MC transitions. The metal to ligand charge transfer (MLCT) comprising of overlapping ^{1}MLCT based $d_{M(II)} \rightarrow \pi^*_{bpy}$ [M = Ru^{II}/Os^{II}] manifests in the broad absorption band peaking at 455 nm for **5** ($\varepsilon = 1.1 \times 10^4$ M^{-1} cm^{-1}) and at 485 nm for **6** ($\varepsilon = 1.04 \times 10^4$ M^{-1} cm^{-1}). In addition, the otherwise spin forbidden ^{3}MLCT based $d_{Os(II)} \rightarrow \pi^*_{bpy}$ transition results in another broad absorption between 542-680 nm (ε_{647} = 2700 M^{-1} cm^{-1}) for **6.** A point of interest is the fact that the MLCT maxima in **5** and **6** is blueshifted with respect to that for the corresponding 4,4′-dicarboxy reference complexes, **8** and **9**. This is because the electron withdrawing carboxylic acid groups, in contrary to that in the reference complexes, are separated from the chromophoric unit by saturated spacers; the electron withdrawing resonance effects are therefore inoperative. The reduced electronic interaction between the bipyridine and the anchoring group, by the spacers between them, is further proved by the fact that the MLCT band position in the electronic absorption spectrum of ruthenium(II)-tris(2,2′-bipyridine) closely resembles to that of **5** in the same solvent. The emission spectrum of **5** consists of a broad ^{3}MLCT based emission with λ_{max} at 613 nm when excited at 455 nm. For **6**, this emission peaks at λ_{max} = 726 nm when excited at either 485 nm or at 625 nm. It can again be seen that the emission maxima for these complexes are blushifted with respect to that for the corresponding reference complexes.

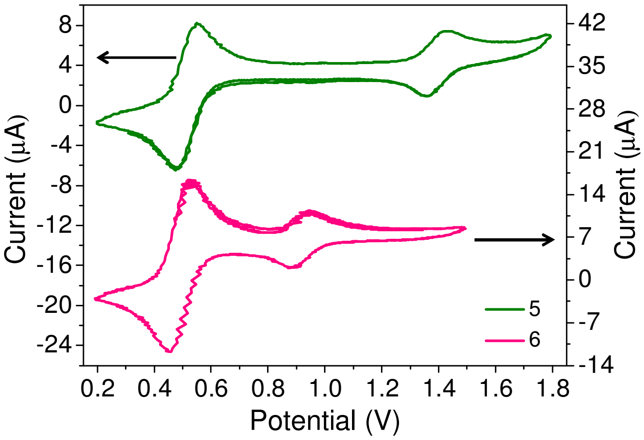

Figure 2: Cyclic voltammogram of **5** (olive, left-hand side layer in figure) and **6** (pink, right-hand side layer in figure) in acetonitrile. Ag/AgCl (saturated KCl) has been used as the reference electrode. Scan rate for both of the scans is 100 mV/s. Ligand-based reductions are omitted because only the metal-based redox potentials have been used in the interpretation of data throughout this chapter. The peak on the left side in both of the voltammograms is due to the ferrocene/ ferrocenium couple, which has been added as an internal standard.

Cyclic voltammograms recorded in acetonitrile (Figure 2) show the reversible Ru^{2+}/Ru^{3+} redox couple for **5** to be appearing at 1.26 V (*vs*. NHE in water; please refer to Appendix A) (ΔE = 70 mV); the corresponding Os^{2+}/Os^{3+} reversible redox couple for **6** appears at

0.8 V (ΔE = 70 mV). In the + 2V to − 2V potential window available, only two bipyridyl centered reductions could be obtained, − 1.4 V and − 1.64 V for **5** and − 1.32 V and − 1.57 V for **6**. For the reference complexes **8** and **9**, the metal based $E_{1/2}$ values are found to be 1.38 V and 0.98 V and are well corroborated by existing literature reports.[15] These potentials are significantly negative as compared to those for the corresponding reference complexes because of the previously discussed separation of the carboxylic moieties from the chromophoric centre by saturated spacers.

Table 1: Transition energy and excited state potentials for the sensitizers

	$E_{0\text{-}0}$(eV)		$[E(S^+/S^*)]$ (V)	
Sensitizer	**^{1}MLCT**	**^{3}MLCT**	**^{1}MLCT**	**^{3}MLCT**
5	2.48	2.11	-1.22	-0.85
6	2.25	1.80	-1.45	-1.00
8	2.39	2.01	-1.01	-0.63
9	2.19	1.74	-1.29	-0.76

In order to gain idea about the thermodynamic feasibility of electron injection into the TiO_2 semiconductor nanoparticles, knowledge of the excited state potentials of the newly designed sensitizer dyes is necessary. $E_{0\text{-}0}$ transition energy for the ^{3}MLCT states of **5**, **6**, **8** and **9** has been estimated from their excitation and emission spectral profiles. The corresponding values for the ^{1}MLCT states are, on the other hand, estimated from the onset of optical absorption.[16] The excited state potentials, $[E(S^+/S^*)]$ are thus calculated according to the equation $[E(S^+/S^*)] = [E(S^+/S)] - E_{0\text{-}0}$ and are tabulated in Table 1.[17] The potential of TiO_2 conduction band edge is ~ − 0.2 V.[18] The excited state potentials of the sensitizers being quite higher than this value, electron injection into TiO_2 conduction band is thermodynamically feasible.

The undeniable superiority of carboxylic acids as binding groups is discussed in the introductory section. However, such moieties have adversities; in the sense that there is an overt possibility of the dye getting desorbed at higher pHs due to the low ground state *p*Ka. Thus one needs to design dyes with pH stable anchoring units while still retaining the previously discussed advantages of carboxylate mode of binding.

With this idea and following the available literature, we substituted a single carboxylic acid binding unit with a *geminal dicarboxylic acid* one in a new *dye-spacer-anchor* arrangement. The present anchoring unit is thus a substituted malonic acid which is known to have unique ground state acid base properties. The first pK_a of malonic acid is reported to be 2.83 while the second *p*Ka value of 5.69 is significantly higher.[19] This is because the removal of the second proton from a negatively charged species containing an electron releasing (+I) $-COO^-$ group is difficult as the resulting dianion, due to unfavourable interaction between like charges, is destabilized with respect to the monoanion. Viewing alternatively, the electron releasing $-COO^-$ group exerts its +I effect and disfavours the release of the second proton. In order to verify whether this trend is indeed followed in our newly designed sensitizer molecules, the protonation changes in **5** and **6** have been monitored by conventional pH titration on a pH potentiostat and the results are shown in Figure 3. The pK_a values, equal to the pH at the respective half equivalence points, are calculated to be 2.95, 5.3 and 2.8, 5.4 for **5** and **6**, respectively.

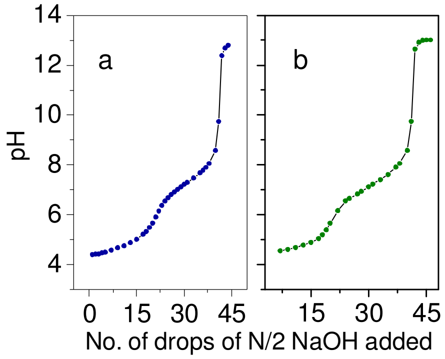

Figure 3: pH titration of (a) **5** and (b) **6** against 0.5 N NaOH in water.

In sharp contrast, the ground state pK_a values for the carboxylic acid groups in **8** and **9** are reported to be < 1, 2.7-2.9 and < 1, 2.7, respectively.[20] Thus it can be seen that even the first pK_a values in **5** and **6** are higher than the second pK_a values for the corresponding reference complexes. Therefore, this *geminal* dicarboxylic acid binding will undoubtedly be superior in terms of stability of the dye-TiO_2 linkage and hence longevity of the resulting dye sensitized solar cell.

Having established so, we set out to study the photophysical properties of the dye sensitized TiO_2 systems to ensure that the fundamental kinetic processes at the molecular level are not the limiting factor in any case.

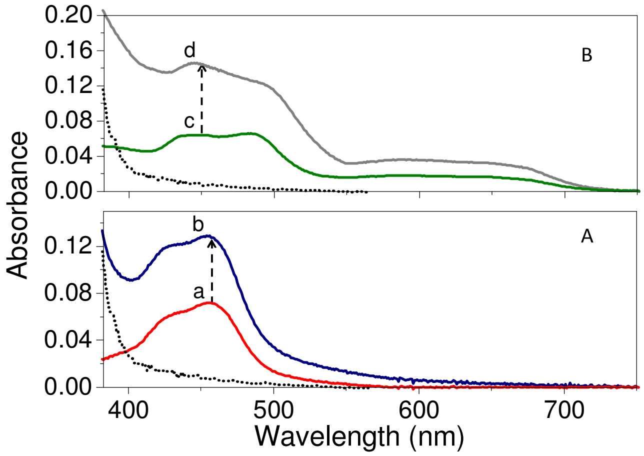

Figure 4: Changes in absorbance of (A) **5** (6.6×10^{-6} M) on addition of TiO_2 (0.031 g/L) (a → b) and (B) **6** (6.3×10^{-6} M) on addition of TiO_2 (0.031 g/L) (c → d) in water. Shown as a dashed line is the spectral profile of TiO_2 (15 g/L) in water.

The absorption spectrum becomes broad with simultaneous increase in absorbance on addition of an aqueous solution of TiO_2 nanoparticles to the aforesaid complexes (Figures 4a and b) which indicates significant interaction of the dye molecules with TiO_2. While no new CT band appears,[21] the MLCT absorption does become broad and the absorbance does increase which indicates weak electronic coupling of the dyes to TiO_2 similar to those reported for the conventional carboxylate bound dyes.[17] This conclusion is further supported by the fact that the emission spectrum of **5** and **6** in solution are identical to that on TiO_2.

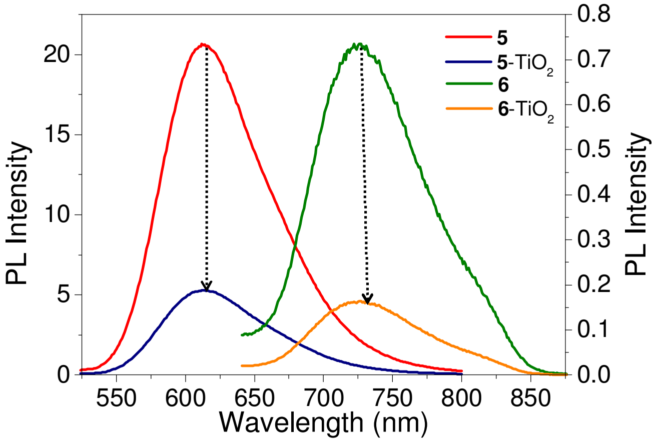

Figure 5: Fluorescence quenching of (a) **5** (6.6×10^{-6} M) and (b) **6** (6.3×10^{-6} M) on addition of TiO_2 (0.05 g/L) in water.

The emission intensity is also substantially diminished on TiO_2 surface (Figure 5) suggesting quenching of the excited state by electron injection.[16,17,21-23,24a.b]

Femtosecond transient absorption spectroscopic studies were then performed in water in order to identify the kinetic processes at the interface. For a comprehensive understanding of the electron transfer dynamics of **5** and **6** on TiO_2 nanoparticle surface, a detailed study of the excited state dynamics of the free sensitizer molecules is essential. Transient absorption spectra of **5** and **6** have been recorded in water and are shown in Figures 6 and 7, respectively.

The spectrum of **5** shows a broad absorption ranging from 530 to 850 nm. Recent work by Chergui *et al.* employing broadband fluorescence spectroscopy has revealed that ISC in ruthenium polypyridyl complexes occurs in 15 ± 10 fs.[25] Therefore, the absorption feature in the transient absorption spectrum can be assigned to excited triplet state absorption.[16] This is accompanied by a simultaneous negative absorption due to the ground state bleach below 500 nm.

The individual kinetic trace of **5** in water at 600 nm is found to be fitting with 1 ps (10.8%) and 7 ps (8.1%) rise times after initial population of hot excited states which takes place in pulse width limited time (< 120 fs, 81.1%). Following earlier works by McCusker and coworkers[26] and by us[16] on the excited state dynamics of similar ruthenium(II)-polypyridyl complexes, the 1 ps component is assigned to vibrational relaxation in the ^{3}MLCT manifolds. This assignment is strengthened by the fact that the

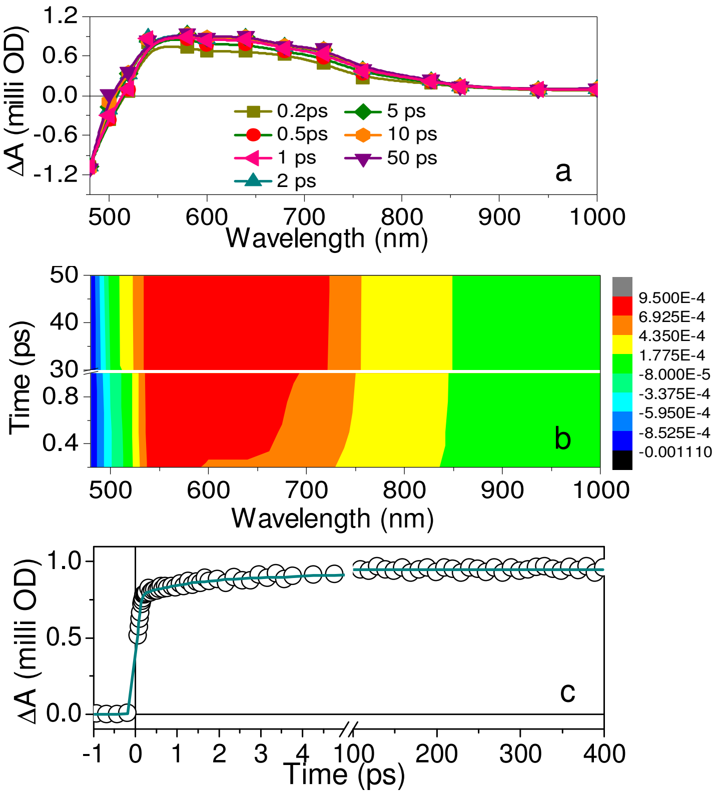

Figure 6: (a) Transient absorption spectrum of **5** at different delay times in water measured after 400 nm (fwhm < 120 fs) excitation. Concentration of **5** is ~ 200 μM, (b) Three dimensional contour plot of the transient absorption spectrum showing the evolution of the excited states with time, (c) The kinetic trace for **5** monitored at 600 nm.

amplitude of this component increases as one moves towards the blue side where the probe pulse is of higher energy. In addition, the average solvation relaxation time, $<\tau_s>$, in water and in acetonitrile is reported to be ~500-600 fs[27] and so the possibility of this component in the free dye to be arising due to solvation can be safely ruled out. The aforesaid average solvation time also rules out the possibility of the 7 ps component to be arising due to solvation. Considering the fact that the kinetic trace has been recorded upon excitation with a very high energy 400 nm light which simultaneously populates all the three bipyridine ligands, it would not be injudicious to assign this 7 ps component presumably to interligand electron redistribution in the ^{3}MLCT manifolds. Such an assignment is further corroborated by works carried out by Kelly and co-workers[28a] and Kohler and co-workers.[28b] However, recent studies by Hammarstrom and co-workers demonstrate that already after one picosecond, the molecule has no reminiscence of which bipyridine was initially photoexcited.[29a] The presence of a slow 15 ps component has also been observed very recently by Chergui and co-workers in $[Re(L)(CO)_3(bpy)]$ complexes that cannot go through interligand electron redistribution.[29b] This component was proposed to be originating from restructuring of solvent molecules lying close to the metal center and inserted amid the ligands. Thus, our assignment of the 7 ps component to interligand electron redistribution is only a tentative one and much further studies need to be done in order to confirm its true origin. Further, the lifetime of the MLCT state of Ru^{II}-polypyridyl complexes, known to be > 100 ns, is mirrored in the decay trace for **5** that does not decay until 400 ps.

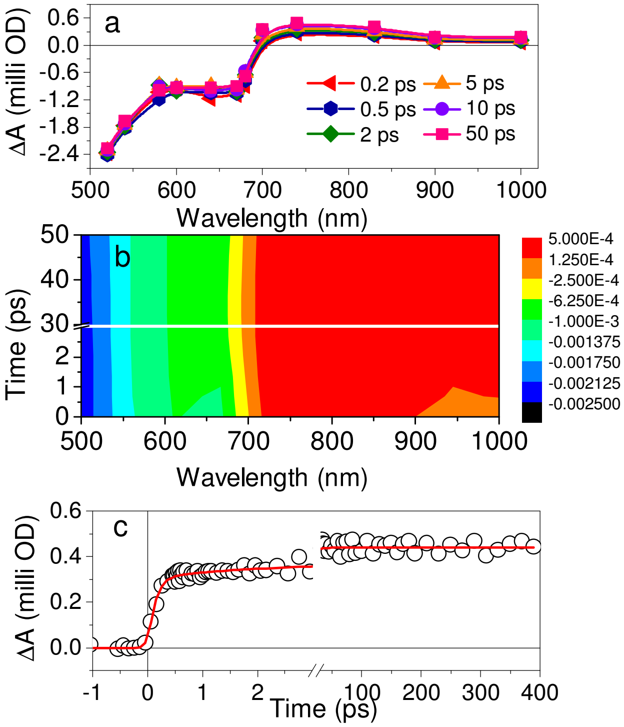

Figure 7: (a) Transient absorption spectrum of **6** at different delay times in water measured after 400 nm (fwhm < 120 fs) excitation. Concentration of **6** is ~ 200 µM, (b) Three dimensional contour plot of the transient absorption spectrum showing the evolution of the excited states with time, (c) The kinetic trace for **6** monitored at 740 nm.

The transient absorption spectrum of **6** in water (Figure 7) shows a broad positive absorption in the range 720-1000 nm. Following similar arguments as that for the spectrum of **5**, this feature can be safely assigned to excited triplet state absorption. However, unlike for **5** where only one bleach band is seen, two negative absorption features can be seen in the transient absorption spectrum for **6**, the positions of which can be seen to be corresponding exactly with the positions of the singlet and the triplet ground state MLCT absorptions (Figure 1).The negative absorptions at 500-580 nm and at 580-700 nm in the transient absorption spectrum of **6** can be therefore assigned to be arising due to bleach because of ^{1}MLCT and ^{3}MLCT ground state absorptions, respectively.[22]

Similar to the kinetic trace of the free dye **5** at 600 nm, the kinetic trace of **6** in water at 740 nm is found to be fitting with 0.9 ps (7%) and 10 ps (25%) rise times after initial population of hot excited states which again takes place in pulse width limited time (< 120 fs, 68%). Following similar analogy as discussed above, the aforesaid components are assigned respectively to vibrational relaxation and interligand electron redistribution in the ^{3}MLCT manifolds. The assignment of the 7 ps component for **5** and the 10 ps component for **6** to interligand electron transfer seems to be corroborated by the fact that the first two successive bipyridine reductions for both **5** and **6** are equally apart by ~ 240 mV which perhaps results in similar time constants for the electron transfer process involved. This is contrary to our observation (please see Chapter 3, Section 3.A.3) of almost double the value of the associated time constant for **3**-TiO_2 (for which the difference in the aforesaid potential values is 130 mV) than for **4**-TiO_2 (for which the difference in the aforesaid potential values is 210 mV).

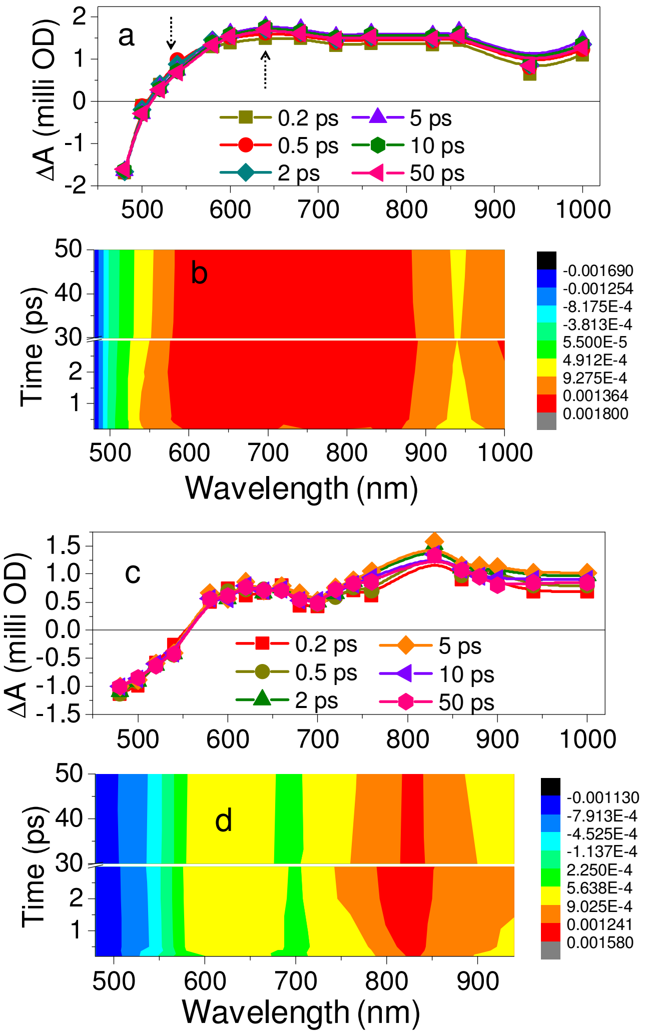

Figure 8: (a) Transient absorption spectrum of **5** on TiO_2 (15 g/L) in water at different delay times measured after 400 nm (fwhm < 120 fs) excitation, (b) Three dimensional contour plot of the transient absorption spectrum of **5** on TiO_2 showing the evolution of the excited states with time, (c) Transient absorption spectrum of **6** on TiO_2 (15 g/L) in water at different delay times measured after 400 nm (fwhm < 120 fs) excitation, (d) Three dimensional contour plot of the transient absorption spectrum of **6** on TiO_2 showing the evolution of the excited states with time Concentrations of **5** and **6** are ~ 200 μM.

Transient absorption spectrum of **5** on TiO_2 nanoparticle surface in water is shown in Figure 8a and b. The spectrum shows a broad absorption in the 500-1000 nm region consisting of overlapping cation radical absorption (**5**$^{\cdot+}$) in the range 520-750 nm and absorption due to electrons in the conduction band in the range 750-1000 nm. Assignment of the cation radical absorption is done on the basis of the results obtained in a complementary pulse radiolysis experiment where **5**$^{\cdot+}$ is generated selectively by the reaction of N_3 radical with **5** in N_2O-saturated aqueous solution (5% acetonitrile + 95% water) (Figure 9a). Numerous other studies on similar ruthenium polypyridyl complexes corroborate this assignment.[16] The excited state absorption profile of the free dye **5** in water shows that the absorption peaks at 541 nm (*vide supra*). In the transient absorption spectrum of **5** on TiO_2 nanoparticles, the signal amplitude corresponding to this excited state of **5** can be seen to be decreasing with concomitant increase in the signal assigned to that for the cation radical (Figure 8a). As expected, the time constant for the formation of the cation radical is reflected in this process. The lower energy absorption band in the 750-1000 nm region can be assigned to electrons in the conduction band of TiO_2 nanoparticles. Again, this assignment is corroborated by previous literature reports where it has been shown that electrons in the conduction band can be detected by visible, near IR and mid IR absorption.[3,16,22,24a,30] In addition to these bands, a negative absorption can be seen below 500 nm due to the ground state bleach.

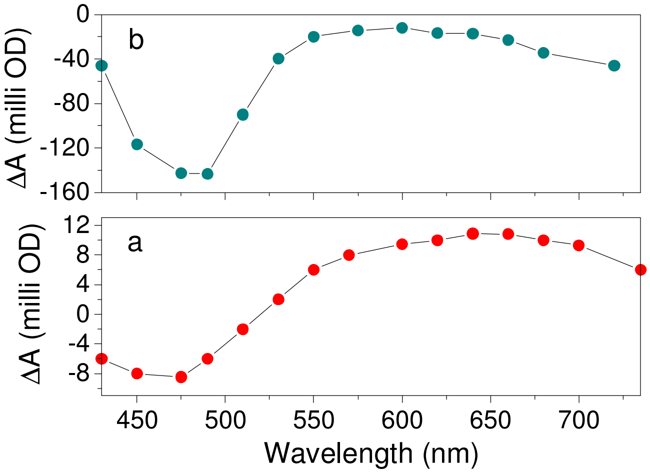

Figure 9: Uncorrected transient absorption spectrum of the cation radical of (a) **5** and (b) **6** obtained from one-electron oxidation in pulse radiolysis.

The transient absorption spectrum of **6** on TiO_2 (Figure 8c and d) presents two distinct absorption bands between 560-690 nm and 700-1000 nm in addition to a bleach due to ground state absorption below 550 nm. The first absorption band can again be assigned to the formation of cation radical (**6**$^{\cdot+}$) based on our complementary pulse radiolysis experiment to generate **6**$^{\cdot+}$ selectively as described above (Figure 9b) and also by previous results from our group on similar osmium complexes.[16,22]

The excited state charge separation process, involving electron injection from the MLCT excited state into nanocrystallite anatase, is a subject of immense interest. Ultrafast spectroscopists working all over the globe have experimentally proved that this charge separation process occurs on a femto- to picoseconds time scale.[2] It has also been proved that excited-state electron injection into TiO_2 is non-exponential and this behaviour is attributed to the surface heterogeneity of TiO_2 and its density of states, a distribution of the binding modes, strengths and interactions of the sensitizer. Also responsible are multiple injection processes taking place from an assortment of states in the thermal relaxation trail, *i.e.* from FC singlet states, internally converted singlet states and triplet state(s) formed by ISC.[2]

However, of greater importance in our case, in terms of interfacial charge separation and recombination, is the fact that the anchoring functionality is separated from the chromophoric unit by three saturated C-C bonds (Scheme 1). This is because of the well known exponential dependence of the electron transfer rate on the length of the bridge between the electron donor and acceptor in the nonadiabatic limit.[2,31a] The room-temperature injection rate constant exhibits an exponential dependence on distance following the equation (1):

$$k = k_o \exp[-\beta x],$$

β being the dampening factor. This exponential dependence can be accounted for by simple models of tunnelling in through space mechanism or by superexchange in the through-bond mechanism. A dampening factor ~ $1.0\ \text{Å}^{-1}$ often indicates saturated-hydrocarbon, through-bond superexchange tunnelling behaviour.[31b] Such distance dependence of electron injection rate on distance has been demonstrated in dye-sensitized systems by numerous researchers.[31c] The study carried out by Lian and co-workers bears most importance in the present context.[31d] Lian and co-workers studied a series of rhenium(I)-polypyridyl complexes bound to TiO_2 by carboxy linkage which was separated from the chromophoric core by saturated methylene linkers of varying lengths. They found that in the nonadiabatic limit, the electron injection rate exactly followed the aforesaid exponential dependence on bridge length. Most interestingly, on introduction of a single methylene spacer between the carboxy and the chromophore unit, the electron transfer rate decreased by > 200 times. This observation was attributed to a transition from the adiabatic limit (due to a strong coupling between the

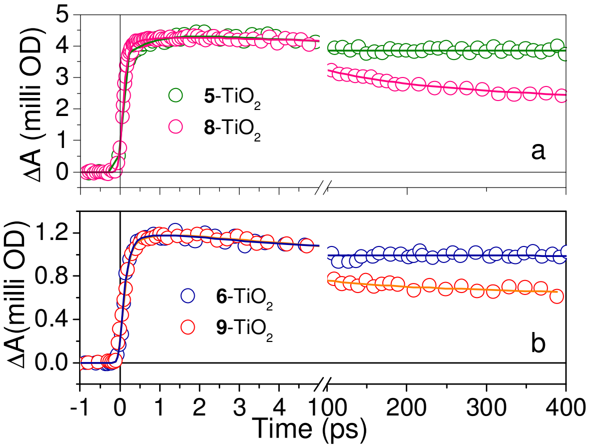

Figure 10: (a) Comparison of the kinetic traces of (a) **5** and (b) **6**, respectively with **8** and **9** adsorbed on TiO_2 at 1000 nm. The kinetic traces have been normalized with respect to the total signal amplitude.

donor and the acceptor units) to a nonadiabatic one.

Electron injection rate in our dye sensitized systems is determined by monitoring the time of appearance of the electron signal at 1000 nm (Figure 10). A comparison of the transient absorption spectrum of the free dyes **5** and **6** with their respective spectrum on TiO_2 would very easily reveal that at this wavelength there is least possible interference of the dye excited states in the respective transient absorption data on TiO_2. The time constants obtained upon fitting the electron signal at 1000 nm for **5**, **6**, **8** and **9** are shown in Table 2. It can be seen that in each case the electron injection process, defined to be complete at the maximum signal amplitude, can be fitted with two time constants, of which one is pulse width limited. This pulse width limited component is attributed to electron injection from thermally unrelaxed singlet/triplet MLCT states.[2,32] The origin of the second component is quite debatable. Benkö *et al.* explained the fast and the slow components as electron injection from the singlet and the triplet states, respectively.[33] Wenger *et al.*, on the other hand, extended their model by assigning the multiphasic dynamics to inhomogeneous dye adsorption.[34] A very recent work by Grätzel and co-workers on the interfacial electron injection dynamics under photovoltaic operating conditions has revealed that this component is indeed arising from the ^{3}MLCT states of aggregates or loosely bound forms of the sensitizer molecules.[32] Our observation also corroborates this assignment. This is because the slow component observed in case of **5**-TiO_2 and **6**-TiO_2 systems corresponds with the free dye ^{3}MLCT vibrational relaxation component. However, the correspondence of this time constant in the free dye and that on TiO_2 in our measurements implies the fact that the vibrational relaxation in the ^{3}MLCT states is the rate determining electron transfer step and hence this injection component arises presumably from the ^{3}MLCT states of the tightly bound dyes predominantly and not from any aggregated states or loosely bound dyes as suggested in earlier examples.

Table 2: Electron transfer parameters for **5**-, **6**- **8**- and **9**-TiO_2 systems

System	**Injection times (as monitored at 1000 nm)**	**Average injection time, τ_{av} (fs)**	**Decay times (as monitored at 1000 nm)**	**Recovery times for the signal at 480 nm**	**$-\Delta G^0$ (eV)**
5-TiO_2	< 120 fs (74.7%), 0.8 ps (25.3%)	277.1	4.2 ps (17.1%), > 400 ps (82.9%)	5.2 ps (20%), > 400 ps (80%)	1.46
6-TiO_2	< 120 fs (76%), 1 ps (24%)	331.2	2 ps (27%), 20 ps (5.4%), > 400 ps (67.6%)	2 ps (9%), 20 ps (6%), > 400 ps (85%)	1
8-TiO_2	< 120 fs (90.9%), 0.7 ps (9.1%)	154.6	6 ps (7%), 120 ps (29.5%), > 400 ps (63.5%)	6 ps (7%), 120 ps (30%), > 400 ps (63%)	1.58
9-TiO_2	< 120 fs (84.3%), 0.7 ps (15.7%)	211.1	6.5 ps (26%), 70 ps (15.7%), > 400 ps (58.3%)	6 ps (19%), 80 ps (12%), > 400 ps (69%)	1.18

One way to compare multiexponential functions is to define an amplitude-weighted-average-time constant (τ_{av}) as follows (Equation 2):

$$\tau_{av} = \frac{\sum A_i \tau_i}{\sum A_i}$$

Following this equation, τ_{av} for the injection process in each of the aforesaid systems is calculated and is shown in Table 2. It can be seen that the average time constant for injection in our newly designed dyes **5** and **6** is *only* 1.8 and 1.6 times slower, respectively, with respect to that for the reference dyes **8** and **9**. Following the earlier work by Lian and co-workers, the injection rate for the bridged systems should have been profoundly less (by atleast a factor of 1000) as compared to our reference systems. This is because of the fact that as compared to our reference systems, in dyes **5** and **6**, there should have been a sharp drop in the injection rate due to transition to the nonadiabatic limit followed by further slowing down as a result of exponential dependence of electron transfer rate on bridge length. No such effect is observed in our case and the injection rate decreases only marginally. It must however be pointed out that the rise time of the fast component depends on both the injection rate from the unrelaxed state and the excited-state relaxation rates. Thus, the two injection components originate from different states and have different physical meanings and consequently it is not very accurate and hence informative to define an average time. However, since the respective injection time constants for our newly synthesized dyes and those of the reference dyes do not differ much (this is also reflected in similar average lifetimes), we believe this approach is not that imprecise in the present context.

In an effort to understand the underlying reason for this unexpected fast injection rate, the frontier molecular orbitals have been calculated at the (DFT) GGA/PBE/DNP level of theory (Figure 11 and Figure 12). The frontier molecular orbitals show significant electron densities residing on the metal center; on Ru^{II} (in **5** and **8**) and on Os^{II} (in **6** and **9**) in the HOMO levels. On the other hand, while the LUMO orbitals are found to be localized predominantly on the unsubstituted 2,2′-bipyridine ligands for **5** and **6**, in case of **8** and **9**, the LUMO is largely localized on the bipyridine ligand with the anchoring carboxylic groups. The frontier molecular orbitals of single TiO_2 bound **5**-TiO_2, **6**-TiO_2, **8**-

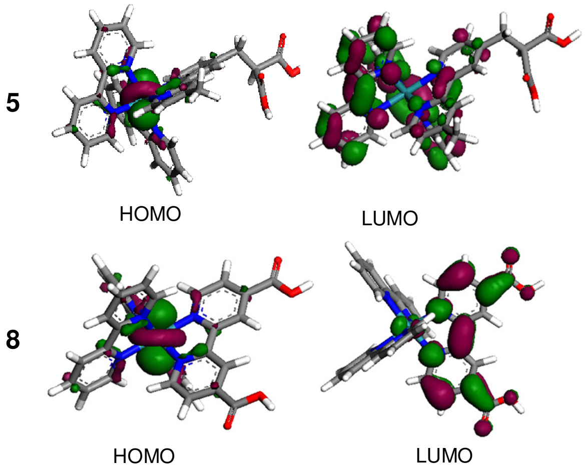

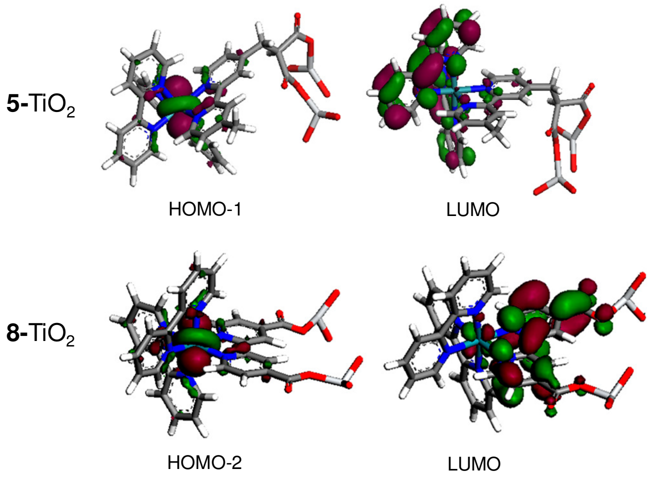

Figure 11: GGA/PBE/DNP calculated frontier molecular orbitals for **5**, **8**, **5**-TiO$_2$ and **8**-TiO$_2$ systems in water (white = hydrogen, gray = carbon, blue = nitrogen, red = oxygen, floral-white = titanium, and blue-green = ruthenium).

TiO$_2$ and **9**-TiO$_2$ systems have further been examined and orbital analysis shows similar trend as observed with the bare complexes. The HOMO coefficients mainly reside on Ru^{II} (in **5**-TiO$_2$ and **8**-TiO$_2$) and on Os^{II} (**6**-TiO$_2$ and **9**-TiO$_2$). The LUMO coefficients are again localized predominantly on the unsubstituted 2,2′-bipyridine ligands in **5**-TiO$_2$ and **6**-TiO$_2$, whereas for **8**-TiO$_2$ and **9**-TiO$_2$, it is found to be localized on the bipyridine ligand with the anchoring carboxylic groups.

Therefore, most likely, in the random mesoporous environment of the dye in the dye-TiO$_2$ solution, presumably the orientation of the dye is such that it parks one or both of the unsubstituted bipyridine moieties very close to the semiconductor surface such that electronic coupling of the excited state with the Ti 3d conduction band manifold is strong enough to mediate electron transfer through space or through bond by a superexchange tunnelling mechanism *via* appropriate orbitals of the intervening solvent molecules. Such through space electron injection has previously been postulated in the literature.[35]

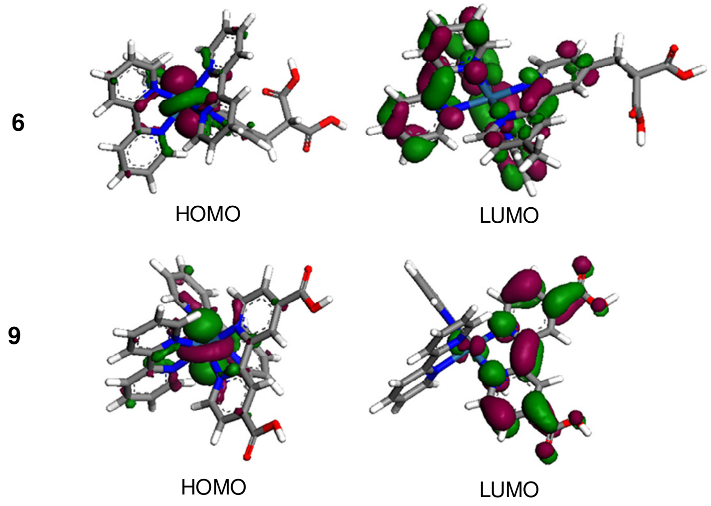

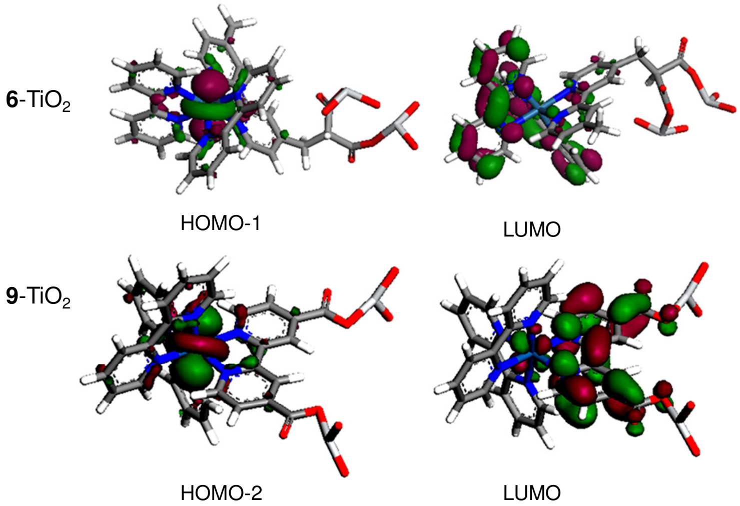

Figure 12: GGA/PBE/DNP calculated frontier molecular orbitals for **6**, **9**, **6**-TiO_2 and **9**-TiO_2 systems in water (white = hydrogen, gray = carbon, blue = nitrogen, red = oxygen, floral-white = titanium, and blue-green = ruthenium).

In order to examine this possibility further, DFT calculations on the {101} surface of anatase TiO_2 cluster have been undertaken. **5** and **8** have been anchored to this {101} surface and their geometries have been optimized keeping the TiO_2 cluster fixed. Frontier molecular orbital analysis suggests that in case of **5**-TiO_2, the orbital coefficients are largely localized on the Ru^{II} center (HOMO–5) and the bipyridine ligand closer to the

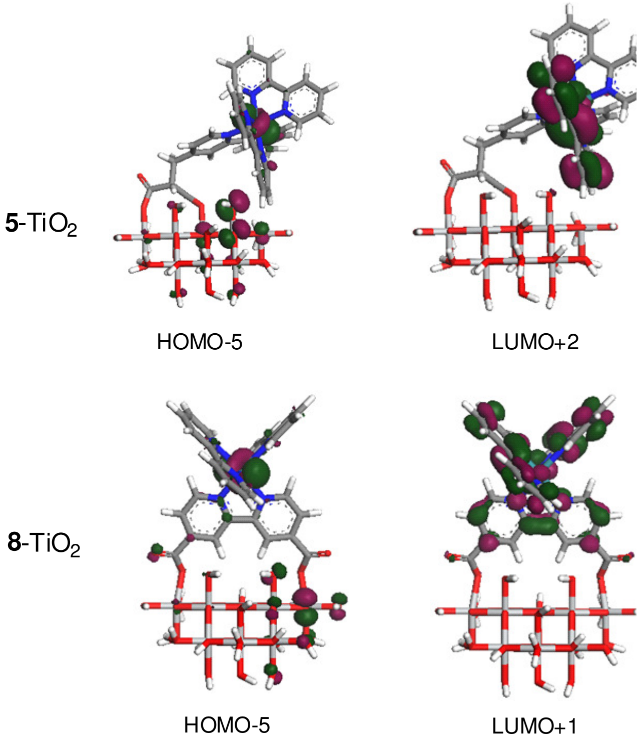

Figure 13: GGA/PBE/DNP calculated frontier molecular orbitals for clusters of **5**-TiO_2 and **8**-TiO_2 systems in water (white = hydrogen, gray = carbon, blue = nitrogen, red = oxygen, floral-white = titanium, and blue-green = ruthenium).

TiO_2 surface (LUMO+2) (Figure 13). However, in case of **8**-TiO_2, though the pattern of the frontier molecular orbitals is similar as in **5**-TiO_2 discussed above, the orientation of the anchoring groups (*i.e.* the –COOH units) moves the bipyridine ligands away from the TiO_2 surface (Figure 13).

For **5**-TiO_2, our frontier orbital analysis thus again suggests that electron transfer to TiO_2 would have significant through space contributions than that in **8**-TiO_2. This is because, as discussed above, the optimized geometry of **5**-TiO_2 shows significant orbital contributions on the unsubstituted bipyridine ligand lying very close to the semiconductor surface and thus there is an immense possibility of through space electron transfer, or electron injection through superexchange tunnelling mechanism *via* appropriate orbitals of the intervening solvent molecules. However, in case of **8**-TiO_2 the bipyridine ligands are farther away from the TiO_2 surface and hence the aforesaid through space interaction, if any, would be much weaker. Thus, the augmented electron injection rates observed for **5**-TiO_2 and **6**-TiO_2 systems, in spite of saturated linkers present, are presumably due to this through space electron transfer mechanism. The conventional through bond electron transfer can occur in both the systems.

While it is true that a quantitative injection yield could occur due to the long lived nature of the MLCT excited states even if the injection dynamics are slowed to the few nanosecond time scale, it has also been argued that fast injection rates can lead to higher solar energy conversion efficiencies.[36] In this regard, we believe that the newly designed sensitizer dyes **5** and **6** will be immensely useful. Our study also proves that with astute design, injection rates fast enough not to interfere with short MLCT lifetimes can be obtained without inducing a planar configuration of the binding moiety with respect to the connecting bipyridine unit.[8]

Of equal importance is the knowledge of the charge recombination rates in the concerned dye-TiO_2 conjugates. Fast recombination rates are justly detrimental to the resulting cells however fast the injection rates be. Therefore, provided the charge separation at the dye–semiconductor interface is maintained efficiently, the dye-sensitized solar cell can be made to work ingeniously. Charge recombination, *i.e.* backward electron transfer dynamics, therefore becomes necessary to be very slow as it is one of the major pathways for loss of the effective electron concentration in the conduction band. In this regard, dyes bound to the semiconductor surface through carboxylic anchoring groups demonstrate much supremacy than the dyes with other possible anchors. The inherent charge recombination rates in carboxylic bound dyes are very slow and generally occur in the order of milliseconds. The newly designed sensitizer dyes **5** and **6** therefore must have a slower charge recombination rate than the conventional carboxylic mode of binding as in **8** and **9** in order to establish any possible competitiveness in performance.

Inferences on the charge recombination dynamics have been drawn based upon a conventional comparison of the decay of the electron signal at 1000 nm (Table 2) where the interference from the excited states is minimum.[37] Interestingly, the charge recombination rate in **5**-TiO_2 system is about 20% slower than that in **8**-TiO_2 system while for the related osmium based **6**-TiO_2 system, it is no less than 10% slower than **9**-TiO_2 system. Interestingly, similar to that observed in the electron signal, the bleach recovery signal monitored at 480 nm follows a similar trend (Table 2 and Figure 14), though this contains obvious contribution from excited states.

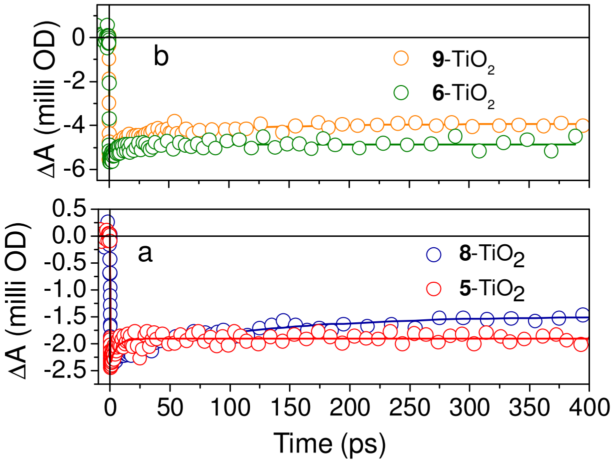

Figure 14: Recovery of the bleach signal at 480 nm for **5**-, **6**-, **8**- and **9**-TiO_2 systems.

This slowing down is because of the following reason. The charge recombination, known to be inherently slow than the electron injection process due to less spatial overlap of the TiO_2 conduction band with the t_{2g} orbital of the metal centre of the dye,[16] is further lessened as a result of the intervening saturated spacer groups that disposes the positively charged metal centre further away from the electrons located in the conduction band. Such behaviour has been observed for several other dye-semiconductor systems.[2,38] The distance dependence of charge recombination has been studied thoroughly by many workers.[2] A similar thorough comparison of the distance dependence of recombination rates and the concerned dampening factors for the electron transfer process could not be done in our systems as our probe delay rail does not allow measurements beyond 400-500 ps.

Another factor might play an important role in determining the charge recombination rate. The highly exergonic recombination reaction generally lies deeply within the Marcus kinetic inverted region and is characterized by reorganization energy values very small as compared to the driving force ($-\Delta G^0 \gg \lambda$, respective values for the classical **N719** dye being 1.5 and 0.3 eV).[16] The changes in the reorganization energy values, if any, will be consequently insignificant. Following Marcus semi-classical electron transfer theory, the BET rate can be expressed as a function of the driving force, reorganization energy, and the coupling element in the following way (Equation 3):[16]

$$k_{BET} = \left(\frac{2\pi}{\hbar}\right)[H_{AB}]^2 \frac{1}{\sqrt{4\pi\Lambda kT}} \exp\left\{-\frac{(\Delta G^0 + \Lambda)^2}{4\Lambda kT}\right\}$$

Now, if the coupling element for **5**-TiO_2, **8**-TiO_2 systems and for **6**-TiO_2, **9**-TiO_2 systems are supposed to be similar, the recombination rate is expected to vary considerably with changes in the driving force ($-\Delta G^0$) values only. Now, ΔG^0 is $E_C - E_{S/S+}$, where E_C is the potential of the conduction band edge (− 0.2 V) and $E_{S/S+}$ is the ground-state redox potential of the dye. The $-\Delta G^0$ values are thus summarised in Table 2.

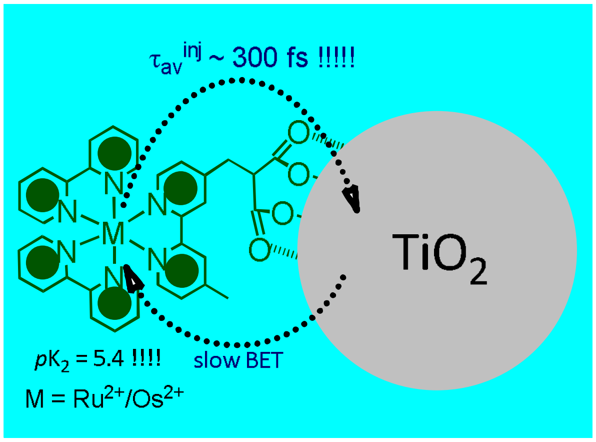

Scheme 3: Schematic illustration of the interfacial electron transfer processes in **5**- and **6**-TiO_2 systems.

It can be seen that for the *geminal* dicarboxylic acid bound dyes, **5** and **6**, the $-\Delta G^0$ values are considerably smaller than the values for the corresponding reference complexes, **8** and **9** respectively. This means that the electron recombination rate in **5**-TiO_2 and **6**-TiO_2 systems should have instead been faster than the corresponding reference dyes **8** and **9**, respectively. In addition, the through space interaction discussed in the preceding section could also have affected the electron recombination rates. The proximal orientation of the molecules on the TiO_2 nanosurface, in addition to securing fast injection, might also have led to faster recombination by placing the electron rich TiO_2 (conduction band) close to the accepting orbitals of the oxidized dye.[39] However, superseding all these factors, the electron recombination rate is still significantly slower in our distinctively designed *dye-spacer-gem-dicarboxy anchor* arrangement (Scheme 3).

4.D. Conclusion

To conclude therefore, two new Ru^{II}-/Os^{II}-polypyridyl based sensitizer dyes have been synthesized with *geminal* dicarboxylic acid anchoring group for binding of the dye to TiO_2 till significantly higher pHs as compared to the conventional monocarboxy linkages. Extremely fast electron injection rates are seen, in spite of multiple saturated C-C linkages present and are suggested to be probably due to electron injection through space or through bond by a superexchange tunnelling mechanism *via* appropriate orbitals of the intervening solvent molecules. The charge recombination rates are also significantly slower in spite of possible influences of through space recombination and smaller $-\Delta G^0$ values in the inverted region. These observations give insinuation about this novel *dye-spacer-gem-dicarboxy anchor* arrangement to be tremendously prospective towards the development of robust solar dyes for use in regenerative dye solar and aqueous photoelectrochemical fuel cells. This study further proves that with judicious design, even without forcing a planar configuration of the binding moiety with respect to the connecting bipyridine unit, sufficiently fast injection rates can be obtained such that these do not interfere with short MLCT lifetimes.

4.E. References

1. Hagfeldt, A.; Boschloo, G.; Sun, L.; Kloo, L.; Pettersson, H. *Chem. Rev.* **2010**, *110*, 6595.

2. Ardo, S.; Meyer, G. J. *Chem. Soc. Rev.* **2009**, *38*, 115 and references therein.

3. Ramakrishna, G.; Jose, D. A.; Krishna Kumar, D.; Das, A.; Palit, D. K.; Ghosh, H. N. *J. Phys. Chem. B* **2005**, *109*, 15445.

4. Galoppini, E. *Coord. Chem. Rev.* **2004**, *248*, 1283.

5. Works from the Solar Fuels EFRC centered at UNC, Chapel Hill, on the use of dye-sensitized architectures for aqueous photoelectrochemical fuel-forming applications can be found at http://www.efrc.unc.edu/

6. Campbell, W. M.; Jolley, K. W.; Wagner, P.; Wagner, K.; Walsh, P. J.; Gordon, K. C.; Schmidt-Mende, L.; Nazeeruddin, M. K.; Wang, Q.; Grätzel, M.; Officer, D. L. *J. Phys. Chem. C* **2007**, *111*, 11760.

7. Aranyos, V.; Grennberg, H.; Tingry, S.; Lindquist, S.-E.; Hagfeldt, A. *Sol. Energy Mater. Sol. Cells* **2000**, *64*, 97.

8. Heuer, W. B.; Xia, H.-L.; Ward, W.; Zhou, Z.; Pearson, W. H.; Siegler, M. A.; Sarjeant, A. A. N.; Abrahamsson, M.; Meyer, G. J. *Inorg. Chem.* **2012**, *51*, 3981.

9. (a) *Materials Studio* DMOL3 Version 4.1, Accelrys Inc., San Diego, CA. (b) Delley, B. *J. Chem. Phys.* **2000**, *113*, 7756.

10. (a) Wu, Z.; Cohen, R. E.; Singh, D. *J. Phys. Rev. B* **2004**, *70*, 104112. (b) Ziesche, P.; Kurth, S.; Perdew, J. P. *Comput. Mater. Sci.* **1998**, *11*, 122. (c) Kohn, W.; Becke, A. D.; Parr, R. G. *J. Phys. Chem*. **1996**, *100*, 12974.

11. (a) Klamt, A. COSMO and COSMO-RS. In *Encyclopedia of Computational Chemistry*; von Rague Schleyer, P., Allinger, N. L., Eds.; Wiley: New York, **1998**; Vol. *2*, p 604. (b) Klamt, A. *J. Phys. Chem*. **1995**, *99*, 2224.

12. (a) Redfern, P. C.; Zapol, P.; Curtiss, L. A.; Rajh, T.; Thurnauer, M. C. *J. Phys. Chem. B* **2003,** *107,* 11419. (b) Kaniyankandy, S.; Rawalekar, S.; Sen, A.; Ganguly, B.; Ghosh, H. N. *J. Phys. Chem. C* **2012**, *116*, 98.

13. Gould, S.; Strouse, G. F.; Meyer, T. J.; Sullivan, B. P. *Inorg. Chem.* **1991**, *30*, 2942.

14. Nazeeruddin, M. K.; Zakeeruddin, S. M.; Humphry-Baker, R.; Jirousek, M.; Liska, P.; Vlachopoulos, N.; Shklover, V.; Fischer, C.-H.; Grätzel, M. *Inorg. Chem.* **1999**, *38*, 6298.

15. Meyer, T. J.; Meyer, G. J.; Pfennig, B. W.; Schoonover, J. R.; Timpson, C. J.; Wall, J. F.; Kobusch, C.; Chen, X.; Peek, B. M.; Wall, C. G.; Ou, W.; Erickson, B. W.; Bignozzi, C. A. *Inorg. Chem.* **1994**, *33,* 3952.

16. Banerjee, T.; Kaniyankandy, S.; Das, A.; Ghosh, H. N.. *Inorg. Chem*. **2013**, *52*, 5366.

17. Banerjee, T.; Rawalekar, S.; Das, A.; Ghosh, H. N. *Eur. J. Inorg. Chem.* **2011**, 4187.

18. Duonghong, D.; Ramsden, J.; Grätzel, M. *J. Am. Chem. Soc.* **1982**, *104*, 2977.

19. Brown, H.C. *et al. In Determination of Organic Structures by Physical Methods*; Braude E. A.; Nachod, F. C., Eds.; Academic Press, New York, **1955**.

20. O'Connor, M. B.; Killard , A. J.; O'Kennedy, R.; Forster, R. J.; Smyth, M. R. *J Inorg. Biochem.* **2006**, *100*, 1252.

21. Pan, J.; Xu, Y.; Benko, G.; Feyziyev, Y.; Styring, S.; Sun, L.; Akermark, B.; Polivka, T.; Sundstrom, V. *J. Phys. Chem. B* **2004**, *108*, 12904.

22. Verma, S.; Kar, P.; Das, A.; Ghosh, H. N. *Chem. Eur. J.* **2011**, *17*, 1561.

23. Verma, S.; Kar, P.; Banerjee, T.; Das, A.; Ghosh, H. N. *J. Phys. Chem. Lett.* **2012**, *3*, 1543.

24. (a) Banerjee, T.; Kaniyankandy, S.; Das, A.; Ghosh, H. N. *J. Phys. Chem. C* **2013**, *117*, 3084. (b) Banerjee, T.; Das, A.; Ghosh, H. N. *New J. Chem.* DOI:10.1039/C3NJ00550J.

25. Cannizo, A.; Mourik, F. V.; Gawelda, W.; Zgrablic, G.; Bressler, C.; Chergui, M. *Angew. Chem.* **2006**, *118*, 3246; *Angew. Chem., Int. Ed.* **2006**, *45*, 3174.

26. Damrauer, N. H.; McCusker, J. K. *J. Phys. Chem. A* **1999**, *103*, 8440.

27. (a) Jarzeba, W.; Walker, G. C.; Johnson, A. E.; Barbara, P. F. *Chem. Phys.* **1991**, *152*, 57. (b) Ramakrishna, G.; Jose, D. A.; Kumar, D. K.; Das, A.; Palit, D. K.; Ghosh, H. N. *J. Phys. Chem. B* **2006**, *110*, 10197.

28. (a) Malone, R. A.; Kelley, D. F. *J. Chem. Phys.* **1991**, *95*, 8970. (b) Henrich, J. D.; Zhang, H.; Dutta, P. K.; Kohler, B. *J. Phys. Chem. B* **2010**, *114*, 14679.

29. (a) Wallin, S.; Davidsson, J.; Modin, J.; Hammarstrom, L. *J. Phys. Chem. A* **2005**, *109,* 4697. (b) El Nahhas, A.; Cannizzo, A.; van Mourik, F.; Blanco-Rodriguez, A. M.; Zalis, S.; Vlcek, Jr. A.; Chergui, M. *J. Phys. Chem. A* **2010**, *114,* 6361.

30. Kar, P.; Banerjee, T.; Verma, S.; Sen, A.; Das, A.; Ganguly, B.; Ghosh, H. N. *Phys. Chem. Chem. Phys.* **2012**, *14*, 8192.

31. (a) Barbara, P. F.; Meyer, T. J.; Ratner, M. A. *J. Phys. Chem.* **1996**, *100,* 13148. (b) References 263-266 of reference 2. (c) References 72, 104, 105, 267-279 of reference 2. (d) Asbury, J. B.; Hao, E.; Wang, Y.; Lian, T. *J. Phys. Chem. B*, **2000**, *104*, 11957.

32. Teuscher, J.; Decoppet, J.-D.; Punzi, A.; Zakeeruddin, S. M.; Moser, J.-E.; Grätzel, M. *J. Phys. Chem. Lett.* **2012**, *3*, 3786.

33. (a) Benko, G.; Kallioinen, J.; Korppi-Tommola, J. E. I.; Yartsev, A. P.; Sundstrom, V. *J. Am. Chem. Soc.* **2002**, *124*, 489. (b) Kallioinen, J.; Benko, G.; Sundstrom, V.; Korppi-Tommola, J. E. I.; Yartsev, A. P. *J. Phys. Chem. B* **2002**, *106*, 4396.

34. Wenger, B.; Grätzel, M.; Moser, J.-E. *J. Am. Chem. Soc.* **2005**, *127*, 12150.

35. (a) Luo, L.; Chang, C.-W.; Lin, C.-Y.;E. Diau, W.-G. *Chem. Phys. Lett.* **2006**, *432*, 452. (b) Argazzi, R.; Chiarati, A. R.; Indelli, M. T.; Scandola, F.; Bignozzi, C. A. Book of Abstracts L-

09, Eleventh International Conference on Photochemical Conversion and Storage of Solar Energy, Bangalore, India, **1996**. (c) Chang, C.-W.; Chou, C. K.; Chang, I-J.; Lee, Y.-P.; Diau, E. W.-G. *J. Phys. Chem. C* **2007,** *111,* 13288. (d) Imahori, H.; Kang, S.; Hayashi, H.; Haruta, M.; Kurata, H.; Isoda, S.; Canton, S. E.; Infahsaeng, Y.; Kathiravan, A.; Pascher, T.; Chabera, P.; Yartsev, A. P.; Sundstrom, V. *J. Phys. Chem. A* **2011**, *115*, 3679.

36. McFarland, S. A.; Lee, F. S.; Cheng, K. A. W. Y.; Cozens, F. L.; Schepp, N. P. *J. Am. Chem. Soc.* **2005**, *127*, 7065.

37. Tachibana, Y.; Moser, J. E.; Grätzel, M.; Klug, D. R.; Durrant, J. R. *J. Phys. Chem.* **1996**, *100*, 20056.

38. Heimer, T. A.; D'Arcangelis, S. T.; Farzad, F.; Stipkala, J. M.; Meyer, G. J. *Inorg. Chem.* **1996**, *35*, 5319.

39. Chang, C.-W.; Luo, L.; Chou, C.-K.; Lo, C.-F.; Lin, C.-Y.; Hung, C.-S.; Lee, Y.-P.; Diau, E.W.-G. *J. Phys. Chem. C* **2009,** *113,* 11524.

Chapter 5

Optimal Interfacial Electron Transfer Rates for *dye-spacer-anchor* Arrangement in Newly Designed Acetylacetonate Based Ru(II)- and Os(II)-polypyridyl Sensitizer

To be communicated

5.A. Foreword

Acetylacetone anchoring units have been shown to have high water resistance and oxidative stability.[1] Acetylacetones were first reported as potential anchoring groups by Meyer and co-workers in the year 1996.[2] Further studies were carried out with Mn^{II}-terpyridine acetylacetone complexes and very recently on coumarin moieties by Batista and co-workers.[1,3-5] Such anchoring units have also been recently explored as potential binding units on ZnO surfaces by Bahers *et al.* and by Warnan *et al.*[6,7] In addition, the synthesis of acetylacetone-linked BODIPY dyes have been reported by Ziessel and co-workers.[8] The search for novel sensitizer systems based on such anchoring groups therefore continues.

In the last chapter, we have explored the possibility of using *geminal* dicarboxylic acids as pH stable anchoring units for binding of Ru^{II}-polypyridyl dyes on TiO_2. Most importantly, the binding *geminal* dicarboxylic acid unit was separated from the chromophoric unit by multiple saturated spacers. To our surprise, in spite of this fact, the electron injection rate was *extremely* fast. The backward electron transfer mentioned before was also very slow.

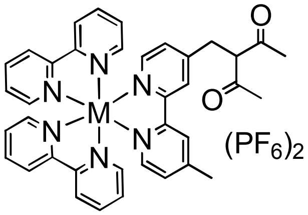

M = Ru^{2+}, **3**
= Os^{2+}, **4**

Scheme 1: Molecular structures of the dyes.

With this knowledge, similar acetylacetone based Ru^{II}- and Os^{II}-polypyridyl dyes, **3** and **4**, respectively, where the binding unit and the sensitizer core are again separated by exactly the same number of saturated spacers, have been synthesized following notoriously simple synthetic protocols. The interfacial electron transfer rates have been accurately quantified by femtosecond transient absorption spectroscopic studies and are the focus of the present study.

Meyer and co-workers,[2] in their aforesaid report on Ru^{II}-polypyridyl dye with acetylacetone anchor, used an 8 ns fwhm pulse to excite the samples and so many of the initial electron transfer processes could not be quantified. For the Mn^{II}-terpyridine acetylacetone complex carried out by Batista and co-workers,[1] a ~500 fs resolution pulse was used to excite the samples and so their photoinjection process was limited completely by the width of the pulse. As discussed above, in the recently studied coumarin-acetylacetone based sensitizer,[4] again studied by Batista and co-workers, the electron injection was found to be ultrafast but was only theoretically calculated.

In view of these facts, the present study is the only femtosecond pump-probe spectroscopic study till date that thoroughly characterizes the interfacial electron transfer processes. Furthermore, in view of the similar results obtained as for our previous studies using *gem*-dicarboxylic acid bound system, the efficacy of the newly derived *dye-spacer-anchor* arrangement towards the possible development of novel sensitizer systems is most authoritatively established.

5.B. Experimental Section (please see Appendix A for details)

5.B.1. Synthesis of TiO_2 nanoparticles

TiO_2 nanoparticles have been prepared by controlled hydrolysis of titanium (IV) tetraisopropoxide as discussed in Appendix A. TiO_2 nanoparticles at neutral pH are obtained by following the procedure reported by Wachtveitl and co-workers. To a 15 g/L solution of such nanoparticles, the stabilizing agent PVA (0.1% solution) is added. The pH is then raised to about 6 by removing the protons *via* treatment with Dowex MR-3 mixed bed ion-exchange resin. The final adjustment to neutral pH is done by adding aqueous NaOH dropwise.

5.B.2. Computational Methodologies

All DFT calculations have been performed with the program package DMol^3 in Materials Studio (version 4.1) from Accelrys Inc.[9] We have used DND (double numerical with *d* polarization) and DNP (double numerical with *d* and *p* polarization) basis sets which are comparable to 6-31G* and 6-31G** Gaussian-type basis sets, respectively. The optimization of additive on the surface has been performed with LDA/PWC/DND level of theory. The single point calculations have been reported with GGA/PBE/DNP level of theory while the frontier molecular orbitals have been calculated at GGA/PBE/DNP level of theory.[10] The implicit conductor like screening model (COSMO) has been employed using the dielectric constant of water (dielectric constant = 78.54) to take into account the solvent effect in these calculations.[11] To improve the computational performance, a Fermi smearing of 0.002 hartree (1 Ha = 27.212 eV) and a global cutoff of 4.5 Å has been employed. The tolerance of the energy, gradient, and displacement convergences are 2×10^{-5} Ha, 4×10^{-3} Ha.Å^{-1} and 5×10^{-3} Å, respectively. In this study, a previously reported titanium dioxide cluster [Ti_8O_{32}] has been used for the TiO_2 anatase {101} surfaces.[12] The charge of the cluster is made neutral by adding hydrogen atoms on oxygen atoms with dangling bonds.

5.B.3. Synthesis

5.B.3.1. 4-(bromomethyl)-4'-methyl-2,2'-bipyridine (1): This is prepared following the procedure used in the last chapter. To 4,4′-dimethyl-2,2′-bipyridine (1.8 g, 9.78 mmol) and N-bromosuccinimide (1.8 g, 10.1 mmol) in a 100 ml round bottomed flask, 40 ml dry CCl_4 is added under an inert Ar atmosphere. The reaction mixture is then set to reflux. As soon as boiling starts, a pinch (~ 50 mg) of azobisisobutyronitrile is added. The reaction mixture is refluxed for exactly 2 hours after which it is cooled to room temperature and the precipitated succinimide is filtered through a grade III sintered glass crucible. The filtrate is evaporated to near dryness in a rotary evaporator at a temperature not more than 50 ^{0}C. The viscous liquid so obtained is purified over 230-400 mesh silica using dichloromethane/acetone as the eluent to obtain pure **1** as a white solid which is stored at low temperature under hexane. Yield: 0.772 g, 30%. ESI-MS (*m/z*): Calculated for $C_{12}H_{11}BrN_2$ – 262.01, Observed – 263.01, 265.01 $[M + 1]^+$; ^{1}H NMR (500 MHz, $CDCl_3$): δ (ppm) 8.66 (1H, d, *J* = 5 Hz, H^6 (bpy)); 8.54 (1H, d, *J* = 5 Hz, $H^{6'}$ (bpy)); 8.41 (1H, s, H^3 (bpy)); 8.24 (1H, s, $H^{3'}$ (bpy)); 7.34 – 7.33 (1H, m, H^5 (bpy)); 7.15 (1H, d, *J* = 5 Hz, $H^{5'}$ (bpy)); 4.48 (2H, s, –C**H**$_2$Br); 2.44 (3H, s, bpy–C**H**$_3$). IR (KBr pellet, cm^{-1}) 1199 (ν_{bend}(C–Br)). Elemental Analysis: Calculated for $C_{12}H_{11}BrN_2$: C, 54.77; H, 4.21; N, 10.65. Found: C, 54.75; H, 4.24; N, 10.61.

5.B.3.2. 3-((2-(4-methylpyridin-2-yl)pyridin-4-yl)methyl)pentane-2,4-dione (2):

To a 10 ml dry THF solution of NaH (50%, 70 mg, 1.47 mmol) at 0 ^{0}C, acetylacetone (0.15 ml, 1.47 mmol) is added. A turbid suspension results to which a 10 ml tetrahydrofuran solution of **1** (386 mg, 1.47 mmol) is added drop-wise over a period of 20 minutes. The reaction mixture is then stirred for 24 hrs at room temperature. After completion of the reaction, a minimum quantity of water is added to the reaction mixture and stirred for 5 minutes. THF is then evaporated and solvent extraction is performed with chloroform; the organic layer is collected, dried with anhydrous sodium sulphate and evaporated to dryness to obtain a crude solid. This is finally purified by column chromatography over silica gel 200-400 mesh using $CHCl_3$/MeOH as the eluent to obtain pure **2**. Yield – 310.5 mg, 75%. ESI-MS (*m/z*): Calculated for $C_{17}H_{18}N_2O_2$ – 282.14, Observed – 283.16 $[M + H]^+$; ^{1}H NMR (500 MHz, CD_3CN): δ (ppm) 8.54 – 8.48 (2H, m, H^6 (bpy), $H^{6'}$ (bpy)); 8.26 – 8.22 (2H, m, H^3 (bpy), $H^{3'}$ (bpy)); 7.21 – 7.19 (2H, m, H^5 (bpy), $H^{5'}$ (bpy)); 4.30 (1H, t, *J* = 7 Hz, -C**H**-CH$_2$); 3.16 (2H, d, *J* = 7 Hz, -CH-C**H**$_2$); 2.41 (3H, s, bpy-CH$_3$); 2.16 (6H, s, -COCH$_3$). IR (KBr pellet, ν (cm^{-1})): 2924 (*sp^2* C-H), 1744 (C=O). Elemental Analysis: Calculated for $C_{17}H_{18}N_2O_2$: C, 72.32; H, 6.43; N, 9.92; Found: C, 72.30; H, 6.40; N, 9.97.

5.B.3.3. {bis-(2,2′-bpy)-(3-((2-(4-methylpyridin-2-yl)pyridin-4-yl)methyl)pentane-2,4-dione)} ruthenium(II) hexafluorophosphate (3):

$Ru(bpy)_2Cl_2.2H_2O$ (200 mg, 0.3846 mmol) and **2** (108.5 mg, 0.3846 mmol) are refluxed in ethanol for 8 hours with continuous stirring. The solvent is then evaporated and the product is made soluble in a minimum volume of water. Saturated aqueous NH_4PF_6 (10 mole equivalents) is added to the resulting solution to precipitate the desired Ru^{II}-polypyridyl complex as the hexafluorophosphate salt. This is kept as such for 4-5 hours in a refrigerator to ensure complete precipitation after which it is filtered, washed with large volumes of cold water and dried in a vacuum desiccator. The crude compound so obtained is purified by column chromatography over silica using acetonitrile/water/saturated aqueous KPF_6 as the eluent. The second fraction is collected and the solvent is removed to isolate a red solid which is redissolved in dichloromethane and two drops of acetonitrile and solvent extraction is done to remove the excess KPF_6 used in the eluent. The organic phase is dried over anhydrous sodium sulphate and is evaporated to dryness to give the desired product in pure form. Yield: 150 mg (39.6%). ESI-MS (*m/z*): Calculated for $C_{37}H_{34}N_6O_2PF_6Ru$ – 841.1 $[M - PF_6^-]^+$, Observed 841.46 $[M - PF_6^-]^+$; ^1H NMR (500 MHz, CD_3CN): δ (ppm) 8.51 (4H, d, *J* = 8.5 Hz, H^6 (bpy) and $H^{6'}$ (bpy)); 8.41 – 8.38 (1H, m, H^3 (bpy-acac)); 8.06 – 8.03 (4H, m, H^3 (bpy) and $H^{3'}$ (bpy)); 7.74 – 7.71 (3H, m, H^6 (bpy-acac) and $H^{6'}$ (bpy-acac), $H^{3'}$ (bpy-acac)); 7.69 – 7.68 (1H, m, H^4 (bpy) or $H^{4'}$ (bpy)); 7.57 (1H, d, *J* = 5 Hz, H^5 (bpy-acac)); 7.54 (1H, d, *J* = 6 Hz, $H^{5'}$ (bpy-acac)); 7.41 – 7.37 (5H, m, H^5 (bpy) and/or $H^{5'}$ (bpy) and/or H^4 (bpy) and/or $H^{4'}$ (bpy)); 7.25 – 7.22 (2H, m, H^5 (bpy) and/or $H^{5'}$ (bpy) and/or H^4 (bpy) and/or $H^{4'}$ (bpy)); 4.38 (1H, t, *J* = 7 Hz, -C**H**-CH_2); 3.22 (2H, d, *J* = 7.5 Hz, -CH-C**H**$_2$); 2.55 (3H, s, bpy-CH_3); 2.19 (6H, s, -$COCH_3$). IR (KBr pellet, cm^{-1}) 1708 (ν(C=O)), 840 (ν(PF_6)). Elemental Analysis: Calculated for $C_{37}H_{34}N_6O_2P_2F_{12}Ru$: C, 45.08; H, 3.48; N, 8.53; Found: C, 45.0; H, 3.55; N, 8.52.

5.B.3.4. {bis-(2,2′-bpy)-(diethyl 2-((4'-methyl-2,2'-bipyridin-4-yl)methyl)malonate)} osmium(II) hexafluorophosphate (**4**): This is prepared by a similar procedure as adopted for the synthesis of **3**. $Os(bpy)_2Cl_2.2H_2O$ (200 mg, 0.328 mmol) and **2** (114 mg, 0.333 mmol) are refluxed in ethanol for 8 hours withs continuous stirring. Then the solvent is evaporated and the product is made soluble in a minimum volume of water. Saturated aqueous KPF_6 (10 mole equivalents) is added to the resulting solution to precipitate the desired Os^{II}-polypyridyl complex as the hexafluorophosphate salt. This is kept as such for 4-5 hours in a refrigerator to ensure complete precipitation after which it is filtered, washed with cold water and dried in a vacuum desiccator. The crude compound so obtained is purified by column chromatography over alumina using acetonitrile/toluene as the eluent. The last fraction is collected and the solvent is removed to isolate a greenish-black solid which is redissolved in dichloromethane and two drops of acetonitrile and solvent extraction is done to remove the excess KPF_6 used in the eluent. The organic phase is dried over anhydrous sodium sulphate and is evaporated to dryness to give the desired product. Yield: 196 mg (52.5%). ESI-MS (*m/z*): Calculated for $C_{37}H_{34}N_6O_2PF_6Os$: 931.16 $[M - PF_6^-]^+$, Observed 931.80 $[M - PF_6^-]^+$. ^1H NMR (200 MHz, CD_3CN): δ (ppm) 8.45 (4H, d, *J* = 8 Hz, H^6 and $H^{6'}$ (bpy)); 8.32 (2H, d, *J* = 6 Hz, H^6 and $H^{6'}$ (bpy-acac)); 7.87 – 7.79 (4H, m, H^3 and $H^{3'}$ (bpy)); 7.65 - 7.55 (4H, m, H^4 and $H^{4'}$ (bpy)); 7.47 – 7.41 (2H, m, H^3 and $H^{3'}$ (bpy-acac)); 7.33 – 7.23 (4H, m, H^5 and $H^{5'}$ (bpy)); 7.16 – 7.11 (2H, m, H^5 and $H^{5'}$ (bpy-acac)); 4.31 (1H, t, *J* = 7 Hz, -C**H**-CH_2); 3.25 (2H, d, *J* = 7.4 Hz, -CH-C**H**$_2$); 2.60 (3H, s, bpy-CH_3); 2.06 (6H, s, -$COCH_3$). IR (KBr pellet, cm^{-1}) 1710 (ν(C=O)), 839 (ν(PF_6)). Elemental Analysis: Calculated for $C_{37}H_{34}N_6O_2P_2F_{12}Os$: C, 41.34; H, 3.19; N, 7.82; Found: C, 41.38; H, 3.23; N, 7.75.

5.C. Results and Discussion

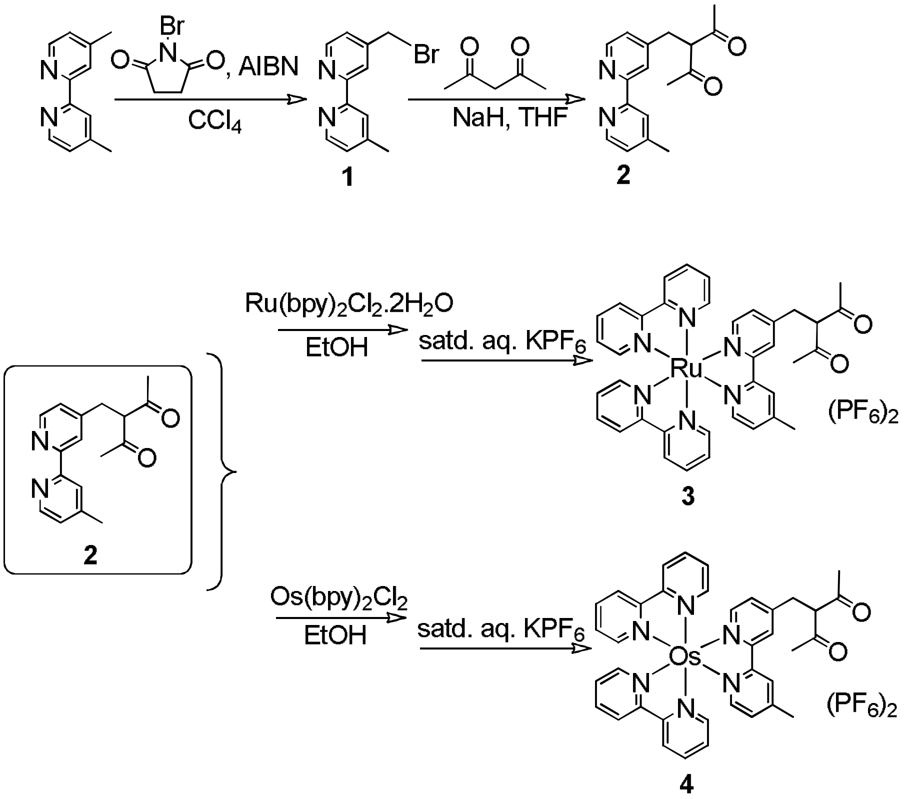

Scheme 2: Synthesis of **3** and **4**.

The synthetic methodology adopted is shown in Scheme 2. 4,4′-dimethyl-2,2′-bipyridine is first monobrominated at one of the methyl groups using N-bromosuccinimide to give **1**. This is then allowed to react with acetylacetone; a nucleophilic substitution reaction takes place in presence of sodium hydride as the base to yield **2** which is subsequently allowed to react with Ru(bpy)$_2$Cl$_2$ and Os(bpy)$_2$Cl$_2$ in ethanol, respectively, to give the complexes, **3** and **4**.

Figure 1 shows the absorption and emission spectra of **3** and **4** in water. The absorption spectrum is characterised by strong ligand centered π-π* transitions at 286 nm and 288 nm for **3** and **4**, respectively. The metal to ligand charge transfer comprising of overlapping ^{1}MLCT based $d_{M(II)} \rightarrow \pi^*_{bpy}$ [M = Ru^{II}/Os^{II}] appears at 453 nm for **3** ($\varepsilon = 1.63 \times 10^4$ M^{-1} cm^{-1}) and at 487 nm for **4** ($\varepsilon = 1.68 \times 10^4$ M^{-1} cm^{-1}). For **4**, the spin forbidden ^{3}MLCT based $d_{Os(II)} \rightarrow \pi^*_{bpy}$ transition appears as a broad absorption between 550-710 nm for **4** (ε_{630} = 4400 M^{-1} cm^{-1}). The emission spectrum of **3** consists of a broad ^{3}MLCT based emission with λ_{max} at 615 nm when excited at 453 nm. For **4**, this emission peaks at λ_{max} = 726 nm when excited at either 487 nm or at 630 nm.

Electrochemical study of **3** reveals a reversible Ru^{2+}/Ru^{3+} redox couple at 1.26 V (ΔE = 74 mV) while for **4**, the Os^{2+}/Os^{3+} reversible redox couple appears at 0.8 V (ΔE = 71 mV) (Figure 2). Knowledge about the position of the excited state of the dye with respect to the conduction band of TiO_2 is again necessary in order to follow the feasibility of electron injection from the dye to the semiconductor nanoparticles. E_{0-0} transition energy for the ^{3}MLCT states of **3** and **4** are calculated to be 2.34 eV and 1.89 eV, respectively, from the respective excitation and emission spectra. The excited state potentials $E(S^+/S^*)$ are thus -1.08 V and -1.09 V for **3** and **4**, respectively following the equation $[E(S^+/S^*)] = [E(S^+/S)] - E_{0-0}$.[13] The E_{0-0} values for the ^{1}MLCT states are approximated to be 2.50 eV and 2.31 eV for **3** and **4**, respectively, from the onset of optical absorption (unlike the estimation of E_{0-0} for ^{3}MLCT states which have been done as stated above).[14] The corresponding excited state potentials are thus -1.24 V and -1.51 V for **3** and **4**. The excited state potentials being above the conduction band level (E_{CB} = -0.5 V),[15] electron injection from the excited state of the sensitizers into the conduction band of TiO_2 becomes thermodynamically feasible.

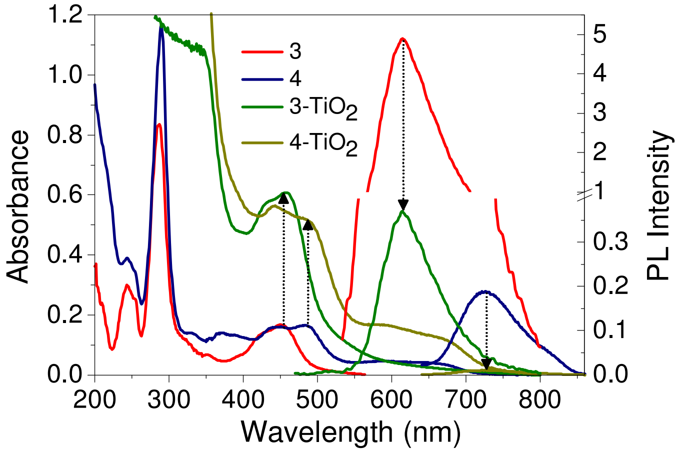

Figure 1: Absorption and emission spectra of **3**, **4**, **3**-TiO_2 and **4**-TiO_2 in water. The concentrations of both **3** and **4** are 1×10^{-5} M while the concentration of TiO_2 is 5.06 g/L for **3**-TiO_2 and 4.66 g/L for **4**-TiO_2.

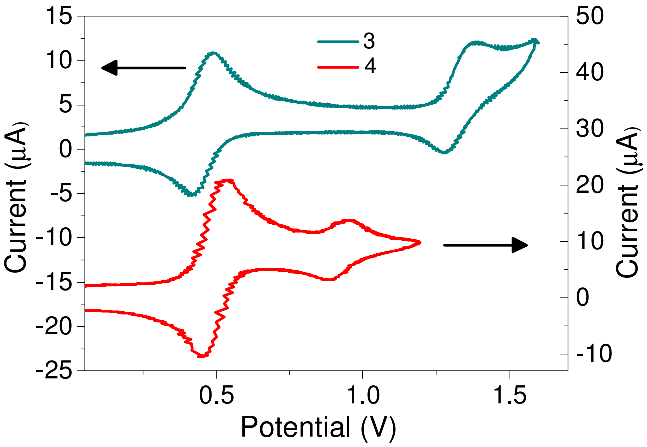

Figure 2: Cyclic Voltammogram of **3** (cyan, left hand side layer in figure) and **4** (red, right hand side layer in figure) in acetonitrile. Ag/AgCl (saturated KCl) has been used as the reference electrode. Scan rate for both the scans shown above is 100 mV/s. Ligand based reductions are omitted since only the metal based redox potentials have been used in the interpretation of data throughout the chapter. The peak on the left side in both the voltammograms is due to the ferrocene/ferrocenium couple which has been added as an internal standard.

The absorption spectrum becomes broad with simultaneous increase in absorbance on addition of an aqueous solution of TiO_2 nanoparticles to the aforesaid complexes (Figure 1) which indicates significant interaction of the dye molecules with TiO_2. While no new charge transfer band appears,[16] the MLCT absorption does become broad and the absorbance does increase which indicates weak electronic coupling of the dyes to TiO_2 similar to those reported for the conventional carboxylate bound dyes.[16,17] This conclusion is further supported by the fact that the emission spectrum of **3** and **4** in solution are identical to that on TiO_2. Also, the emission intensity is radically diminished on TiO_2 surface (Figure 1) suggesting substantial quenching of the excited state by electron injection and hence negligible contribution of excited state features in the transient absorption data on TiO_2 (*vide infra*).[14,16-19]

For a comprehensive understanding of the electron transfer dynamics of **3** and **4** on TiO_2 surface, a study of the excited state dynamics of the free sensitizer molecules is essential. Transient absorption spectra of **3** and **4** have been recorded in water and are shown in Figures 3 and 4, respectively. The transient absorption spectrum of **3** shows a broad absorption ranging from 530 to 950 nm and this is attributed to excited triplet state absorption[14] following the recent work by Chergui *et al.* employing broadband fluorescence spectroscopy that revealed intersystem crossing in ruthenium polypyridyl complexes to be occuring in 15 ± 10 fs.[20] This is accompanied by a simultaneous negative absorption due to the ground state bleach below 500 nm. The individual kinetic trace of **3** in water at 940 nm is found to be fitting with 5 ps (10.4%) rise time after initial population of hot excited states[14] which takes place in pulse width limited time (< 120 fs, 89.6%) (Figure 3c). The origin of the 5 ps component is uncertain. One possibility might be interligand electron redistribution following excitation with a very high energy

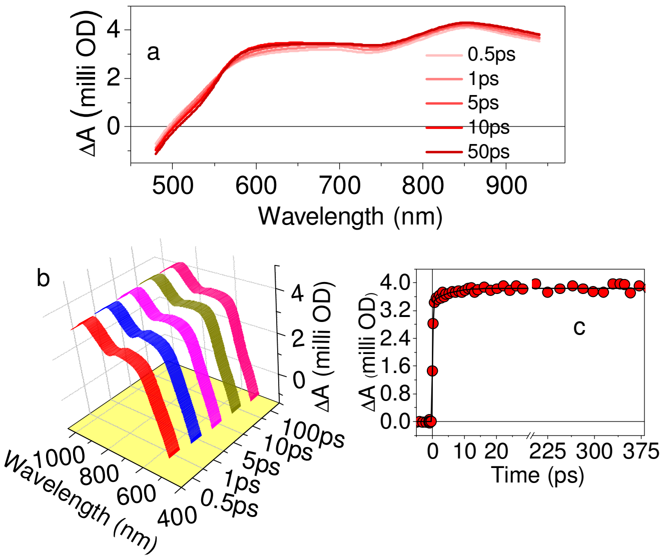

Figure 3: (a) Transient absorption spectrum of **3** at different delay times in water measured after 400 nm (fwhm < 120 fs) excitation. Concentration of **3** is ~ 200 µM, (b) Three dimensional plot of the transient absorption spectrum, and (c) The kinetic trace for **3** monitored at 940 nm.

400 nm light simultaneously populating all the three bipyridine ligands.[14,21] Such an assignment is corroborated by works carried out by Kelly and co-workers and Kohler and co-workers.[22] However, there are many more reports contradicting this assignment. As discussed in the previous chapters, recent studies demonstrate that already after one picosecond, the molecule has no recollection of which bipyridine was initially photoexcited.[23a] The presence of a slow 15 ps component has also been observed by Chergui and co-workers for complexes that cannot go through the aforesaid interligand electron redistribution.[23b] This component was proposed to be originating from restructuring of solvent molecules inserted amid the ligands and lying close to the metal center. Further, the lifetime of the MLCT state of Ru^{II}-polypyridyl complexes, known to be > 100 ns, is mirrored in the decay trace for **3** that does not decay until 400 ps.

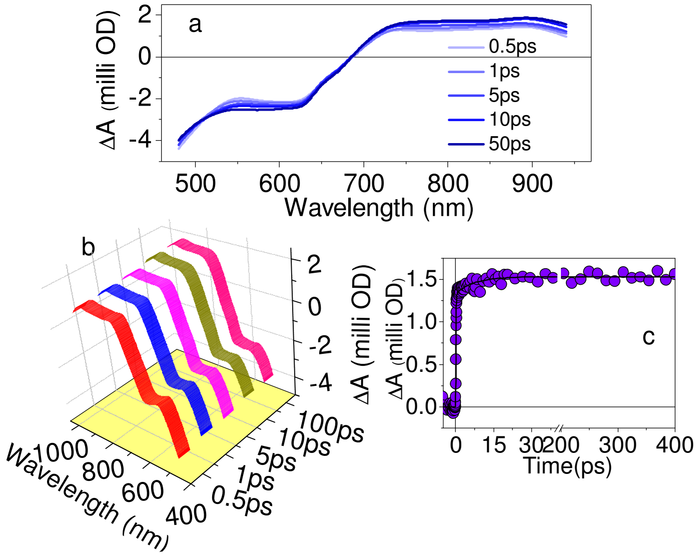

Figure 4: (a) Transient absorption spectrum of **4** at different delay times in water measured after 400 nm (fwhm < 120 fs) excitation. Concentration of **4** is ~ 200 µM, (b) Three dimensional plot of the transient absorption spectrum, and (c) The kinetic trace for **4** monitored at 900 nm.

The transient absorption spectrum of **4** in water (Figure 4) shows a broad positive absorption in the range 730-950 nm. Following arguments alike, this feature can be assigned to excited triplet state absorption. The negative absorptions at 480-550 nm and at 560-680 nm in the transient absorption spectrum of **4** can be assigned to bleach because of ^{1}MLCT and ^{3}MLCT ground state absorptions, respectively.[18a]

The kinetic trace of **4** in water at 900 nm is found to be fitting with 7.2 ps (13.1%) rise time after initial population of hot excited states which again takes place in pulse width limited time (< 120 fs, 86.9%). Following similar analogy as discussed above, the 7.2 ps component is assigned tentatively to interligand electron redistribution in the ^{3}MLCT manifolds.

Transient absorption spectrum of **3** on TiO_2 nanoparticle in water is shown in Figure 5. The spectrum shows a broad absorption in the 520-1000 nm region consisting of

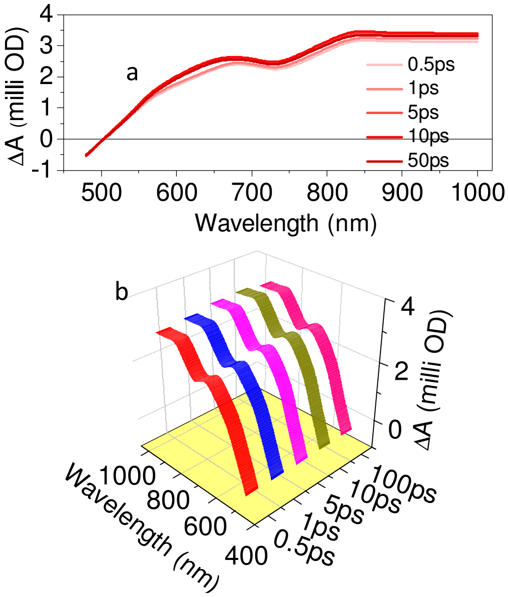

Figure 5: (a) Transient absorption spectrum of **3**-TiO$_2$ at different delay times in water measured after 400 nm (fwhm < 120 fs) excitation. Concentration of **3** is ~ 200 µM while that of TiO$_2$ is 15 g/L. (b) Three dimensional plot of the transient absorption spectrum.

overlapping cation radical absorption (**3**$^{\cdot+}$) in the range 520-720 nm and absorption due to electrons in the conduction band in the range 750-950 nm. Assignment of the former band to cation radical absorption is done on the basis of the results obtained in a complementary pulse radiolysis experiment where **3**$^{\cdot+}$ is generated selectively by the reaction of N$_3$ radical with **3** in N$_2$O-saturated aqueous solution (5% acetonitrile + 95% water) (Figure 6). Several other studies on similar ruthenium polypyridyl complexes corroborate this assignment. The lower energy absorption band in the 750-1000 nm region can be assigned to electrons in the conduction band of TiO$_2$ nanoparticles. This assignment is also corroborated by previous literature reports where it has been shown

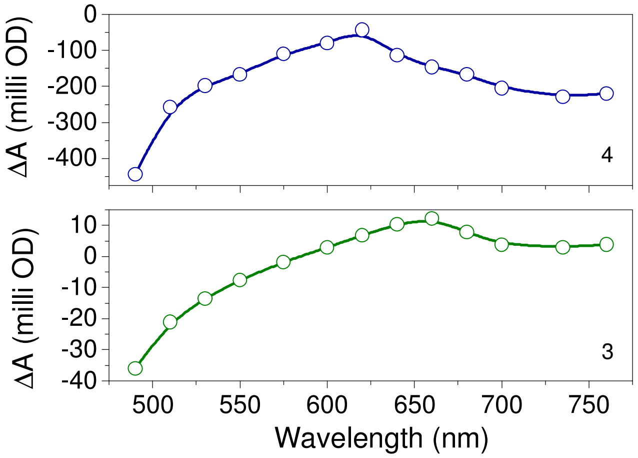

Figure 6: Uncorrected transient absorption spectrum of the cation radical of **3** and **4** obtained from one-electron oxidation in pulse radiolysis.

that electrons in the conduction band can be detected by visible, near IR and mid IR absorption.[13,14,18,19a,24,25] In addition to these bands, a negative absorption can be seen below 500 nm due to the ground state bleach.

The transient absorption spectrum of **4** on TiO_2(Figure 7) again presents two distinct absorption bands between 560-690 nm and 700-1000 nm in addition to a bleach due to ground state absorption below 550 nm. The first absorption band can again be assigned to the formation of cation radical (**4**$^{\cdot+}$) based on our complementary pulse radiolysis experiment to generate **4**$^{\cdot+}$ selectively as described above (Figure 6) and also by previous results from our group on similar osmium complexes.[14,18a] However, the signal in this cation radical absorption range contains obvious overlap with ^{3}MLCT ground state bleach.

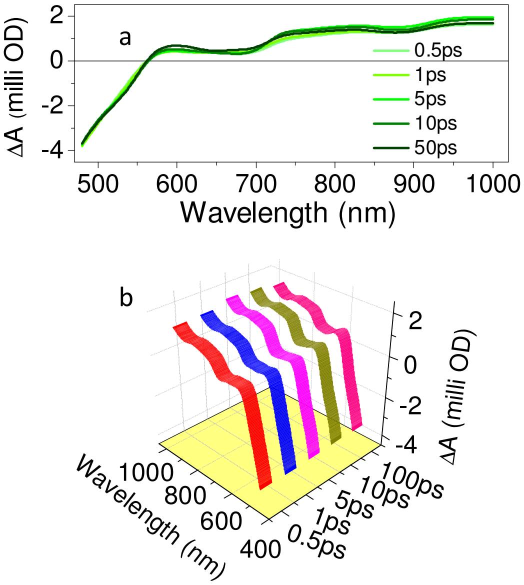

Figure 7: (a) Transient absorption spectrum of **4**-TiO_2 at different delay times in water measured after 400 nm (fwhm < 120 fs) excitation. Concentration of **4** is ~ 200 µM while that of TiO_2 is 15 g/L. (b) Three dimensional plot of the transient absorption spectrum.

Electron injection rate in the dye sensitized **3**- and **4**-TiO_2 systems is determined by monitoring the time of appearance of the electron signal at 1000 nm (Figure 8). The time constants obtained upon fitting the electron signal at 1000 nm are given in Table 1. The electron injection process can be fitted with two time constants, of which one is pulse width limited. This pulse width limited component is attributed to electron injection from thermally unrelaxed singlet/triplet MLCT states.[26,27] The slower second component is attributed to injection from thermalized ^{3}MLCT states.[26-29] An amplitude-

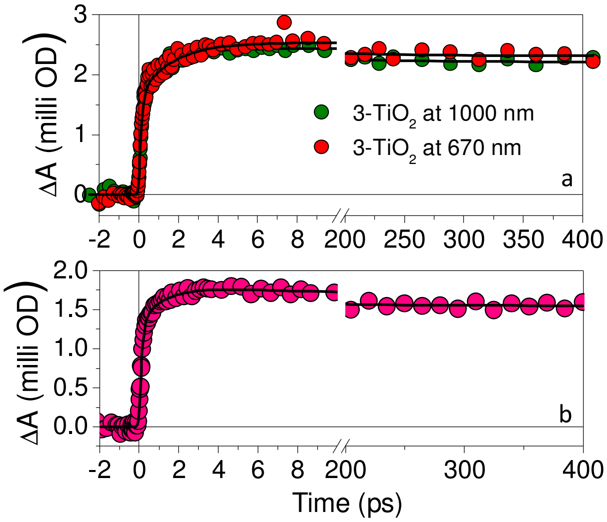

Figure 8: (a) Kinetic traces for **3**-TiO_2 and (b) **4**-TiO_2 at 1000 nm. The kinetic traces have been normalized with respect to the total signal amplitude for **3**-TiO_2. The cation radical signal at 670 nm for **3**-TiO_2 system can be fitted with < 120 fs (+64.7%), 1.7 ps (+35.3%), 123 ps (-9.6%), > 400 ps (-90.4%).

weighted-average-time constant (τ_{av}) for the injection process in each of the aforesaid systems is calculated and is shown in Table 1.[30] It can be seen that the average time constant for injection for both **3** and **4** is quite fast; much faster than that expected for a dye for which the anchoring unit and the chromophore centre is separated by multiple saturated C-C linkages.[26,31]

Table 1: Electron transfer parameters for **3**- and **4**-TiO_2 systems

System	Injection times (as monitored at 1000 nm)	Average injection time, τ_{av} *(fs)*	Decay times (as monitored at 1000 nm)	Recovery times for the signal at 480 nm
3-TiO_2	< 120 fs (67.3%), 1.4 ps (32.7%)	538.6	120 ps (10%), > 400 ps (90%)	120 ps (15%), >400 ps (85%)
4-TiO_2	< 120 fs (71.4%), 1.2 ps (28.6%)	429.8	12 ps (8.25%), 109 ps (6.73%), > 400 ps (85.02%)	12.5 ps (7.5%), 109 ps (5.5%), >400 ps (87%)

However, the point of greater interest is the fact that the electron injection rate is about 2 times and 1.3 times slower, respectively, for the ruthenium and the osmium dyes,

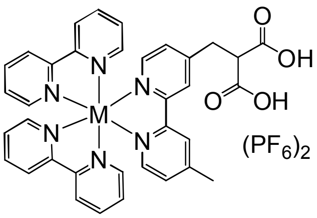

5, M = Ru^{2+}
6, M = Os^{2+}

Scheme 3: Molecular structures of dyes **5** and **6**.

when compared with our previously studied *gem-dicarboxy* bound dyes, **5** and **6** (Scheme 3), for which the average injection lifetimes were 277.1 and 331.2 fs.

In an attempt to explain the injection rates observed, the frontier molecular orbitals have been calculated at the (DFT) GGA/PBE/DNP level of theory. The frontier molecular orbitals show significant electron densities residing on Ru^{II} (in **3**) (Figure 9) and on Os^{II} (in **4**) in the HOMO levels. The LUMO is however largely localized on the unsubstituted bipyridine ligands instead of the bipyridine ligand with the anchoring acetylacetone groups. In a similar way as for the *gem-dicarboxy* bound dyes, therefore, presumably the orientation of the dye parks one or both of the unsubstituted bipyridine moieties very close to the semiconductor surface such that electronic coupling of the excited state with the Ti 3d conduction band manifold is strong enough to mediate electron transfer through space or through bond by a superexchange tunnelling mechanism *via* the intervening solvent molecules.[26,32] This is probably the reason for the observed fast electron injection in **3** and **4**-TiO_2 systems in spite of multiple saturated linkers.

DFT calculations on the {101} surface of anatase TiO_2 cluster have then been undertaken. **3** and **4** have been anchored to this {101} surface and their geometries have been optimized keeping the TiO_2 cluster fixed. Frontier molecular orbital analysis suggests that in case of **3**- and **4**-TiO_2, the orbital coefficients are largely localized on the metal center (HOMO–1) and the bipyridine ligand closer to the TiO_2 surface (LUMO+3) (Figure 10). This again suggests that electron transfer to TiO_2 would perhaps have significant through space contributions.

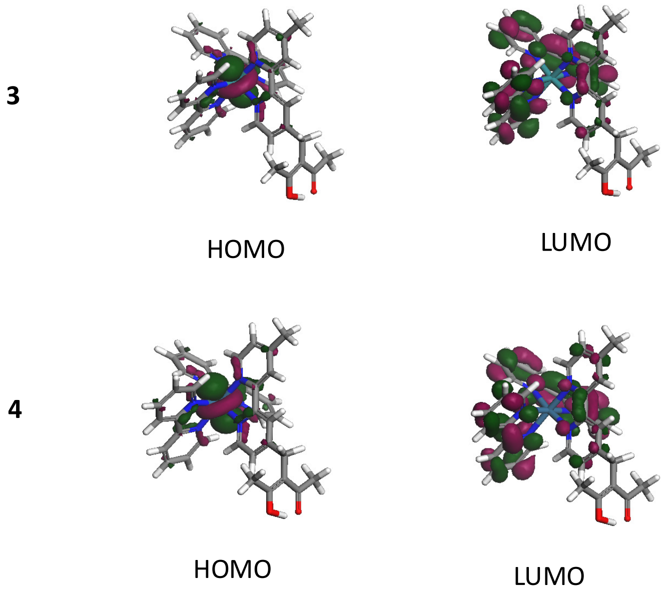

Figure 9: GGA/PBE/DNP calculated frontier molecular orbitals for **3** and **4** in water (white = hydrogen, gray = carbon, blue = nitrogen, red = oxygen and blue-green = ruthenium).

Incidentally, the optimized cluster geometry of **3**-TiO_2 shows that the distance between the TiO_2 surface and the middle point of the bipyridine ligand closer to the TiO_2 surface (this is being called the distance of closest approach) is 5.84 Å. This distance of closest approach was seen to be 4.70 Å for **5**-TiO_2. Thus, it seems that an increase of the distance between the LUMO electron density and the TiO_2 surface is manifested as slower electron injection rate in **3**-TiO_2 as compared to **5**-TiO_2. The aforesaid distance of closest approach is seen to be 5.76 Å for **4**-TiO_2 and thus the observed faster injection for **4**-TiO_2 than that in **3**-TiO_2 falls quite well in line with our explanations (Scheme 4). The conventional through bond electron transfer can occur in all the systems.

It must however be noted that this comparison between **3**- and **5**-TiO_2 systems is only a very crude one. The reason is that the two systems involve two entirely different anchoring moieties. However, such a comparison has been made in light of the fact that the LUMO coefficients are completely localized in the unsubstituted bipyridine ligands both for the dyes **3** and **5** (Figure 9) and so conventional through bond electron injection pathway seems to be a very indifferent one.

BET rates have been determined by monitoring the recovery of the ground state bleach at 480 nm (Table 1 and Figure 11). This is unlike the *gem-dicarboxy* bound **5**- and **6**-TiO_2 systems where the recombination had to be compared crudely at the electron signal at 900 nm due to significant excited state being present on TiO_2 surface.

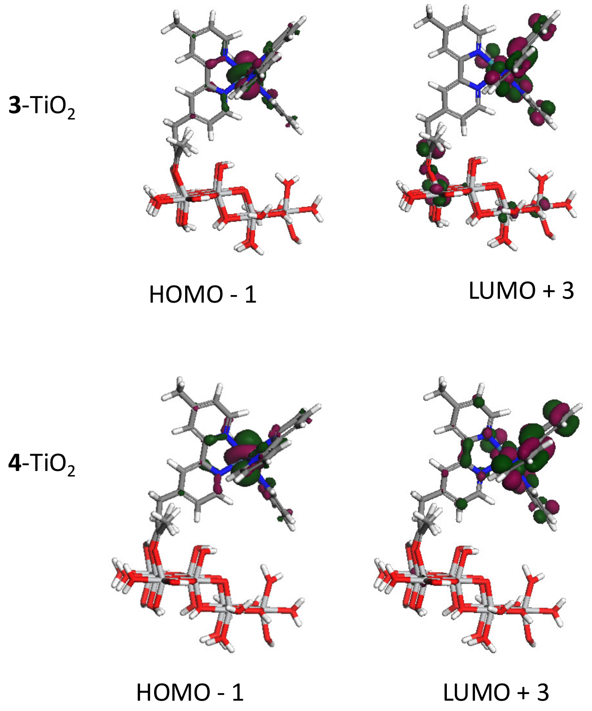

Figure 10: GGA/PBE/DNP calculated frontier molecular orbitals for clusters of **3**-TiO_2 and **4**-TiO_2 systems in water (white = hydrogen, gray = carbon, blue = nitrogen, red = oxygen, floral-white = titanium, and blue-green = ruthenium).

The bleach recovery is very slow, again due to the effect of the intervening saturated spacer groups which result in a greater separation of the positively charged metal centre

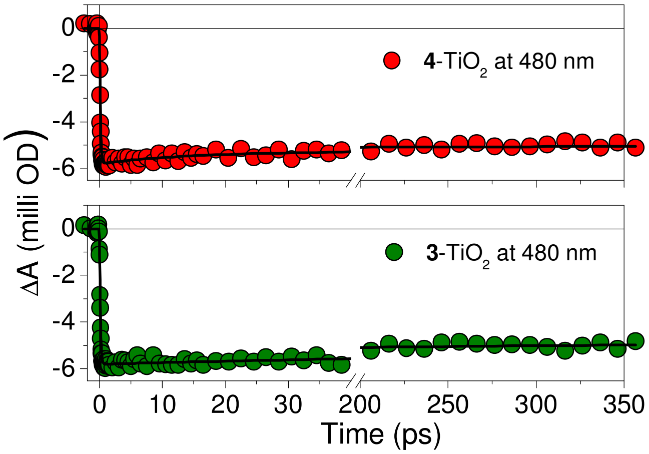

Figure 11: Recovery of the ground state bleach for **3**- and **4**-TiO$_2$ systems.

and the electrons located in the conduction band.[14] Such behaviour has been observed for many dye-semiconductor systems.[2,26]

The decay of the electron signal at 1000 nm for **5**- and **6**-TiO$_2$ systems had been seen to be fitting with 4.2 ps (17.1%), > 400 ps (82.9%) and 2 ps (27%), 20 ps (5.4%), > 400 ps (67.6%), respectively. Thus, a comparison of the rate of the decay of this electron signal for the *gem-dicarboxy* and the acetylacetone bound dyes reveals slower BET rates in both of our newly designed acetylacetone bound ruthenium(II)- and osmium(II)-polypyridyl systems. Though the electron signal at 1000 nm cannot be designated as the true recombination, one can assume that this slow backward electron transfer in **3**-/**4**-TiO$_2$ systems is due to a greater separation of the metal centre from the TiO$_2$ surface than that in **5**-/**6**-TiO$_2$ systems (*vide supra*).

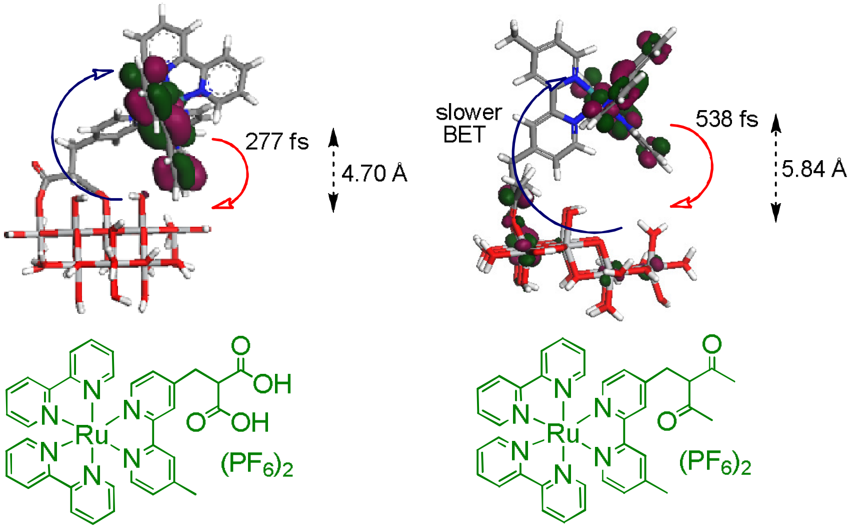

Scheme 3: Schematic diagram of the electron transfer processes in **5**- and **3**-TiO$_2$ sensitized systems.

5.D. Conclusion

Two new Ru^{II}-/Os^{II}-polypyridyl based sensitizer dyes have been synthesized with acetylacetone anchoring group for binding of the dye to TiO_2 in a novel *dye-spacer-anchor* arrangement and femtosecond time-resolved spectroscopic studies have been carried out. By comparison of the results obtained with our previous dyes with *gem-dicarboxy* anchors in the same arrangement, the efficacy of this *dye-spacer-anchor* arrangement, in manifesting a desired extremely fast electron injection rate while still maintaining very slow backward electron transfer rate in spite of multiple saturated C-C linkers present, is authoritatively established thus permitting future development of highly efficient dyes for use in regenerative dye solar and aqueous photoelectrochemical fuel cells.

5.E.References

1. McNamara, W. R.; Snoeberger III, R. C.; Li, G.; Schleicher, J. M.; Cady, W. C.; Poyatos, M.; Schmuttenmaer, C. A.; Crabtree, R. H.; Brudvig, G. W.; Batista, V. S. *J. Am. Chem. Soc.* **2008**, *130*, 14329.

2. Heimer, T. A.; D'Arcangelis, S. T.; Farzad, F.; Stipkala, J. M.; Meyer, G. J. *Inorg. Chem.* **1996**, *35*, 5319.

3. Abuabara, S. G.; Cady, C. W.; Baxter, J. B.; Schmuttenmaer, C. A.; Crabtree, R. H.; Brudvig, G. W.; Batista V. S. *J. Phys. Chem. C* **2007,** *111,* 11982.

4. Xiao, D.; Martini, L. A.; Snoeberger III, R. C.; Crabtree, R. H.; Batista V. S. *J. Am. Chem. Soc*. **2011**, *133*, 9014.

5. Snoeberger III, R. C.; Young, K. J.; Tang, J.; Allen, L. J.; Crabtree, R. H.; Brudvig, G. W.; Coppens, P.; Batista, V. S.; Benedict, J. B. *J. Am. Chem. Soc.* **2012**, *134*, 8911.

6. Bahers, T. L.; Pauporte, T.; Labat, F.; Lefevre, G.; Ciofini I. *Langmuir* **2011**, *27*, 3442.

7. Warnan, J.; Guerin, V.-M.; Anne, F. B.; Pellegrin, Y.; Blart, E.; Jacquemin, D.; Pauporté, T.; Odobel, F. *J. Phys. Chem. C* **2013**, *117*, 8652.

8. Olivier, J.-H.; Haefele, A.; Retailleau, P.; Ziessel, R. *Org. Lett.* **2010**, *12*, 408.

9. Campbell, W. M.; Jolley, K. W.; Wagner, P.; Wagner, K.; Walsh, P. J.; Gordon, K. C.; Schmidt-Mende, L.; Nazeeruddin, M. K.; Wang, Q.; Grätzel, M.; Officer, D. L. *J. Phys. Chem. C* **2007**, *111*, 11760.

10. Aranyos, V.; Grennberg, H.; Tingry, S.; Lindquist, S.-E.; Hagfeldt, A. *Sol. Energy Mater. Sol. Cells* **2000**, *64*, 97.

11. Heuer, W. B.; Xia, H.-L.; Ward, W.; Zhou, Z.; Pearson, W. H.; Siegler, M. A.; Sarjeant, A. A. N.; Abrahamsson, M.; Meyer, G. J. *Inorg. Chem.* **2012**, *51*, 3981.

12. Sullivan, B. P.; Salmon, D. J.; Meyer, T. J. *Inorg. Chem.* **1978**, *17*, 3334.

13. Banerjee, T.; Rawalekar, S.; Das, A.; Ghosh, H. N. *Eur. J. Inorg. Chem.* **2011**, 4187.

14. Banerjee, T.; Kaniyankandy, S.; Das, A.; Ghosh, H. N. *Inorg. Chem*. **2013**, *52*, 5366.

15. Duonghong, D.; Ramsden, J.; Grätzel, M. *J. Am. Chem. Soc.* **1982**, *104,* 2917.

16. Pan, J.; Xu, Y.; Benko, G.; Feyziyev, Y.; Styring, S.; Sun, L.; Akermark, B.; Polivka, T.; Sundstrom, V. *J. Phys. Chem. B* **2004**, *108*, 12904.

17. Tachibana, Y.; Moser, J. E.; Grätzel, M.; Klug, D. R.; Durrant, J. R. *J. Phys. Chem.* **1996**, *100*, 20056.

18. (a) Verma, S.; Kar, P.; Das, A.; Ghosh, H. N. *Chem. Eur. J.* **2011**, *17*, 1561. (b) Verma, S.; Kar, P.; Banerjee, T.; Das, A.; Ghosh, H. N. *J. Phys. Chem. Lett.* **2012**, *3*, 1543.

19. (a) Banerjee, T.; Kaniyankandy, S.; Das, A.; Ghosh, H. N. *J. Phys. Chem. C* **2013**, *117*, 3084. (b) Banerjee, T.; Das, A.; Ghosh, H. N. *New J. Chem.* DOI:10.1039/C3NJ00550J.

20. Cannizo, A.; Mourik, F. V.; Gawelda, W.; Zgrablic, G.; Bressler, C.; Chergui, M. *Angew. Chem.* **2006**, *118*, 3246; *Angew. Chem., Int. Ed.* **2006**, *45*, 3174.

21. Damrauer, N. H.; McCusker, J. K. *J. Phys. Chem. A* **1999**, *103*, 8440.

22. (a) Malone, R. A.; Kelley, D. F. *J. Chem. Phys.* **1991**, *95*, 8970. (b) Henrich, J. D.; Zhang, H.; Dutta, P. K.; Kohler, B. *J. Phys. Chem. B* **2010**, *114*, 14679.

23. (a) Wallin, S.; Davidsson, J.; Modin, J.; Hammarstrom, L. *J. Phys. Chem. A* **2005**, *109,* 4697. (b) El Nahhas, A.; Cannizzo, A.; van Mourik, F.; Blanco-Rodriguez, A. M.; Zalis, S.; Vlcek, Jr. A.; Chergui, M. *J. Phys. Chem. A* **2010**, *114,* 6361.

24. Ramakrishna, G.; Jose, D. A.; Krishna Kumar, D.; Das, A.; Palit, D. K.; Ghosh, H. N. *J. Phys. Chem. B* **2005**, *109*, 15445.

25. Kar, P.; Banerjee, T.; Verma, S.; Sen, A.; Das, A.; Ganguly, B.; Ghosh, H. N. *Phys. Chem. Chem. Phys.* **2012**, *14*, 8192.

26. Ardo, S.; Meyer, G. J. *Chem. Soc. Rev.* **2009**, *38*, 115.

27. Teuscher, J.; Decoppet, J.-D.; Punzi, A.; Zakeeruddin, S. M.; Moser, J.-E.; Grätzel, M. *J. Phys. Chem. Lett.* **2012**, *3*, 3786.

28. (a) Benko, G.; Kallioinen, J.; Korppi-Tommola, J. E. I.; Yartsev, A. P.; Sundstrom, V. *J. Am. Chem. Soc.* **2002**, *124*, 489. (b) Kallioinen, J.; Benko, G.; Sundstrom, V.; Korppi-Tommola, J. E. I.; Yartsev, A. P. *J. Phys. Chem. B* **2002**, *106*, 4396.

29. Wenger, B.; Grätzel, M.; Moser, J.-E. *J. Am. Chem. Soc.* **2005**, *127*, 12150.

30. She, C.; Guo, J.; Irle, S.; Morokuma, K.; Mohler, D. L.; Zabri, H.; Odobel, F.; Youm, K.-T.; Liu, F.; Hupp, J. T.; Lian, T. *J. Phys. Chem. A* **2007**, *111*, 6832.

31. Asbury, J. B.; Hao, E.; Wang, Y.; Lian, T. *J. Phys. Chem. B*, **2000**, *104*, 11957.

32. (a) Luo, L.; Chang, C.-W.; Lin, C.-Y.;E. Diau, W.-G. *Chem. Phys. Lett.* **2006**, *432*, 452. (b) Argazzi, R.; Chiarati, A. R.; Indelli, M. T.; Scandola, F.; Bignozzi, C. A. Book of Abstracts L-09, Eleventh International Conference on Photochemical Conversion and Storage of Solar Energy, Bangalore, India, **1996**. (c) Chang, C.-W.; Chou, C. K.; Chang, I-J.; Lee, Y.-P.; Diau, E. W.-G. *J. Phys. Chem. C* **2007,** *111,* 13288. (d) Imahori, H.; Kang, S.; Hayashi, H.; Haruta, M.; Kurata, H.; Isoda, S.; Canton, S. E.; Infahsaeng, Y.; Kathiravan, A.; Pascher, T.; Chabera, P.; Yartsev, A. P.; Sundstrom, V. *J. Phys. Chem. A* **2011**, *115*, 3679.

Appendix A

1. Materials and methods

Titanium (IV) tetraisopropoxide (97%), isopropyl alcohol, 4,4'-dimethyl-2,2'-bipyridine, *n*-butyl lithium, 3,4-dimethoxybenzaldehyde, 2,2'-bipyridine, 4-methoxybenzaldehyde, 2-acetylpyridine, L-tyrosine ethyl ester hydrochloride, isopropyl alcohol, 3,5-dimethoxybenzaldehyde, ruthenium trichloride hydrate, ammonium hexachloro osmate, Dowex MR-3 mixed bed ion-exchange resin, oleic acid, $Re(CO)_5Cl$, N-bromosuccinimide, sodium hydride, hexafluorophosphoric acid solution (55 wt. %), ammonium hexafluorophosphate and potassium hexafluorophosphate were obtained from Sigma-Aldrich and used as received. Solvents like THF, acetonitrile, isopropyl alcohol, pyridine, carbon tetrachloride, acetone, toluene, dichloromethane, methanol, ethanol and isopropyl alcohol were dried and distilled prior to use. Nanopure water (Barnsted System, USA) was used for making all aqueous solutions. All other reagents (AR grade) were procured from S.D. Fine Chemicals (India). Solvents were degassed thoroughly with IOLAR grade dinitrogen gas before use in the preparation of standard solutions. $Ru(bpy)_2Cl_2$,[1] $Os(bpy)_2Cl_2$,[2] **7** (from chapter 2),[3] **6**[4] and **8**[5] (from chapter 3) have been prepared following previously reported procedures.

2. Analytical Methods

FTIR spectra have been recorded as KBr pellets in a cell fitted with a KBr window, using a Perkin-Elmer Spectra GX 2000 spectrometer. ^{1}H NMR spectra have been recorded on a Bruker 200 MHz FT NMR (Model: Avance-DPX 200) or on a Bruker 500 MHz FT NMR (Model: Avance-DPX 500) using TMS as an internal standard. ESI-MS measurements have been carried out on a Waters QTof-Micro instrument. Microanalyses (C, H, N) have been performed using a Perkin-Elmer 4100 elemental analyzer. Electronic spectra have been recorded with a Shimadzu UV-3101 PC or a Varian Cary 500 UV-Vis-NIR spectrophotometer, room-temperature luminescence spectra have been recorded with either Fluorolog (Horiba Jobinyvon) or a Perkin-Elmer LS 50B or an Edinburgh FS P920 luminescence spectrofluorimeter, fitted with a red-sensitive photomultiplier tube. pH titrations have been done on a Mettler Toledo S20 pH meter. Electrochemical experiments have been performed in acetonitrile on a CH-660A or an AFCPBI, PINE Instrument Co. electrochemical instrument with a conventional three-electrode cell assembly, with SCE or an Ag/AgCl, saturated KCl as the reference electrode and a platinum working electrode. Ferrocene has been used as an internal standard. Unless otherwise specified, all potentials have been corrected and quoted with respect to NHE in water.[6]

3. Femtosecond Visible Spectrometer

The femtosecond tunable visible spectrometer has been developed based on a multipass amplified femtosecond Ti:sapphire laser system supplied by Thales, France.[7] The pulses of 20 fs duration and 4 nJ energy per pulse at 800 nm, obtained from a self mode-locked

Ti:sapphire laser oscillator (Synergy 20, Femtolaser, Austria) is amplified in a regenerative and two-pass amplifier pumped by a 20 W DPSS laser (JADE) to generate 40 fs laser pulses of about 1.2 mJ energy at a repetition rate of 1 kHz. The 800 nm output pulse from the multipass amplifier is split into two parts to generate pump and probe pulses. Frequency doubled 400 nm has been used as the excitation source. To generate pump pulses at 400 nm, one part of the 800 nm output with ~50 μJ/pulse is frequency doubled in BBO crystals. The crystal angle and the focus spot are kept such a way that one gets energy ~ 5-6 μJ/pulse at 400 nm (second harmonic). Finally the energy at the sample spot is kept ~ 1-1.5 μJ/pulse with pump diameter ~ 500 μm to avoid any multiple excitation processes. To generate visible probe pulses, about 3 μJ of the 800 nm beam is focused onto a 1.5 mm thick sapphire window. The intensity of the 800 nm beam is adjusted by iris size and ND filters to obtain a stable white light continuum in the 400 nm to the 1000 nm region. The probe pulses are split into the signal and reference beams and are detected by two matched photodiodes with variable gain. The spot sizes of the pump beam and probe beam at the crossing point have been kept around 500 and 300 μm, respectively. The noise level of the white light is about ~0.5% with occasional spikes due to oscillator fluctuation. Most laser noise is low-frequency noise and can be eliminated by comparing the adjacent probe laser pulses (pump blocked *vs.* unblocked using a mechanical chopper). The typical noise in the measured absorbance change is about <0.3%. The IRF for 400 nm excitation has been obtained by fitting the rise time of the bleach of sodium salt of meso-tetrakis(4-sulfonatophenyl)porphyrin (TPPS) at 710 nm and has been found to be 100-120 fs. The data analysis and fitting at individual wavelengths have been done with the LabView program.

4. Preparation of sample solution

The complexes discussed are insoluble in water and so sensitization has been done (unless otherwise specified) by dissolving the complexes in least possible volume of acetonitrile (this volume is less than 1% of the total volume) and then adding the dissolved dye into the aqueous colloidal solution of the nanoparticles. Throughout the text, therefore, water:acetonitrile (99:1, *v/v*) is abbreviated as water. The resulting solutions have been stirred for half an hour and then kept in dark overnight for the dye to covalently bind to TiO_2. For all the measurements the sample solutions have deoxygenated by continuously bubbling high purity nitrogen (99.95 IOLAR grade from Indian Oxygen Co. Ltd., India) through the solutions.

5. Synthesis of TiO_2 nanoparticles

TiO_2 nanoparticles have been prepared by controlled hydrolysis of titanium (IV) tetraisopropoxide.[8] A solution of 5 ml $Ti[OCH(CH_3)_2]_4$ (Aldrich, 97%) in 95 ml isopropyl alcohol is added dropwise (1ml/min) to 900 mL of nanopure water (2 ^{0}C) at pH 1.5 (adjusted with HNO_3). The solution is continuously stirred for 10-12 hours till the formation of a transparent colloid. The colloidal solution is concentrated at 35-40 ^{0}C with a rotary evaporator and then dried with nitrogen stream to yield a white powder. In the present work all colloidal samples have been prepared after dispersing the dry TiO_2 nanoparticles in water (15g/L). The TEM images show the particle size to be ~3 nm and SAED pattern confirm the particles to be crystalline anatase (Figure 1).

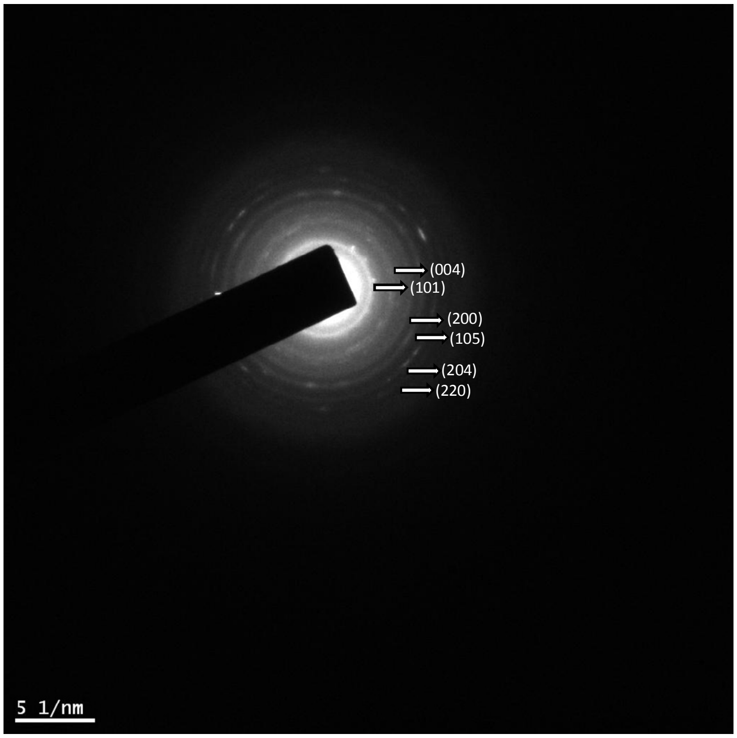

Figure 1: SAED pattern of TiO_2 nanoparticles showing the different planes of anatase phase.

6. References

1. Sullivan, B. P.; Salmon, D. J.; Meyer, T. J. *Inorg. Chem.* **1978**, *17*, 3334.

2. Kober, E. M.; Caspar, J. V.; Sullivan, B. P.; Meyer, T. J. *Inorg. Chem.* **1988**, *27*, 4587.

3. Ramakrishna, G.; Jose, D. A.; Krishna Kumar, D.; Das, A.; Palit, D. K.; Ghosh, H. N. *J. Phys. Chem. B* **2005**, *109*, 15445.

4. Verma, S.; Kar, P.; Das, A.; Palit, D. K.; Ghosh, H. N. *J. Phys. Chem. C* **2008**, *112*, 2918.

5. Kaniyankandy, S.; Rawalekar, S.; Verma, S.; Palit, D. K.; Ghosh, H. N. *Phys. Chem. Chem. Phys.* **2010**, *12*, 4210.

6. (a) Nazeeruddin, M. K.; Zakeeruddin, S. M.; Kalyanasundaram, K. *J. Phys. Chem.* **1993**, *97*, 9607. (b) Pavlishchuk, V. V.; Addison, A. W. *Inorg. Chim. Acta* **2000**, *298*, 97.

7. Kaniyankandy, S.; Rawalekar, S.; Verma, S.; Palit, D. K.; Ghosh, H. N. *Phys. Chem. Chem. Phys.* **2010**, *12*, 4210.

8. Ghosh, H. N. *J. Phys. Chem. B* **1999**, *103*, 10382.

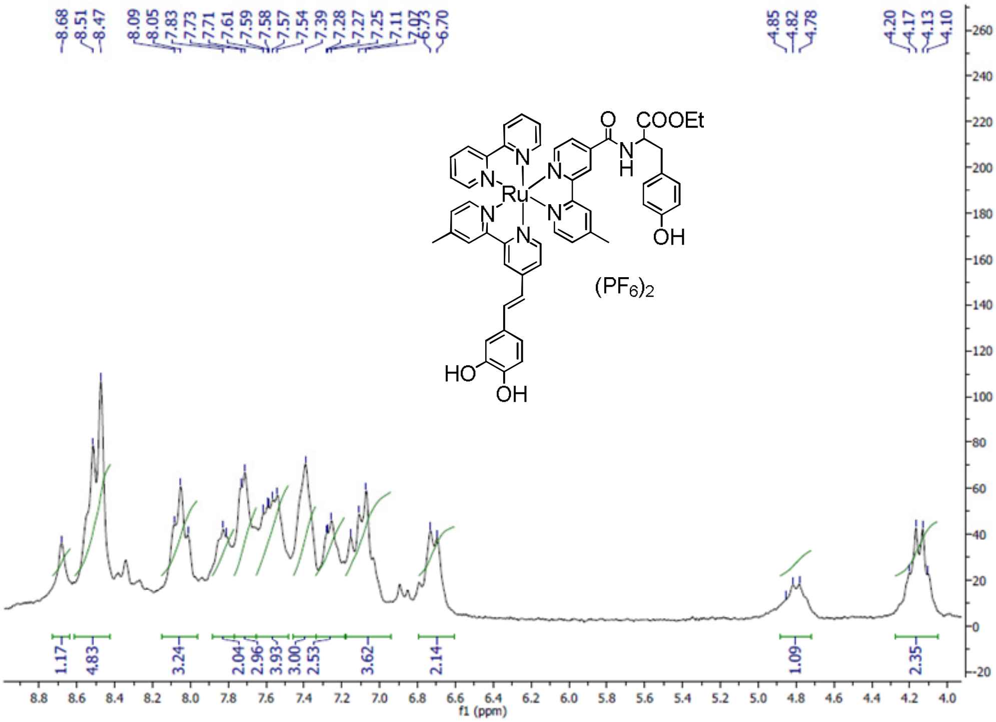
8.68
8.51
8.47
8.09
8.05
7.83
7.73
7.71
7.61
7.59
7.58
7.57
7.54
7.39
7.28
7.27
7.25
7.11
7.07
6.73
6.70
4.85
4.82
4.78
4.20
4.17
4.13
4.10
O
COOEt
N
H
N
N
Ru
N
N
N
N
OH
(PF6)2
HO
OH
1.17
4.83
3.24
2.04
2.96
3.93
3.00
2.53
3.62
2.14
1.09
2.35
8.8 8.6 8.4 8.2 8.0 7.8 7.6 7.4 7.2 7.0 6.8 6.6 6.4 6.2 6.0 5.8 5.6 5.4 5.2 5.0 4.8 4.6 4.4 4.2 4.0
f1 (ppm)
260 240 220 200 180 160 140 120 100 80 60 40 20 0 -20

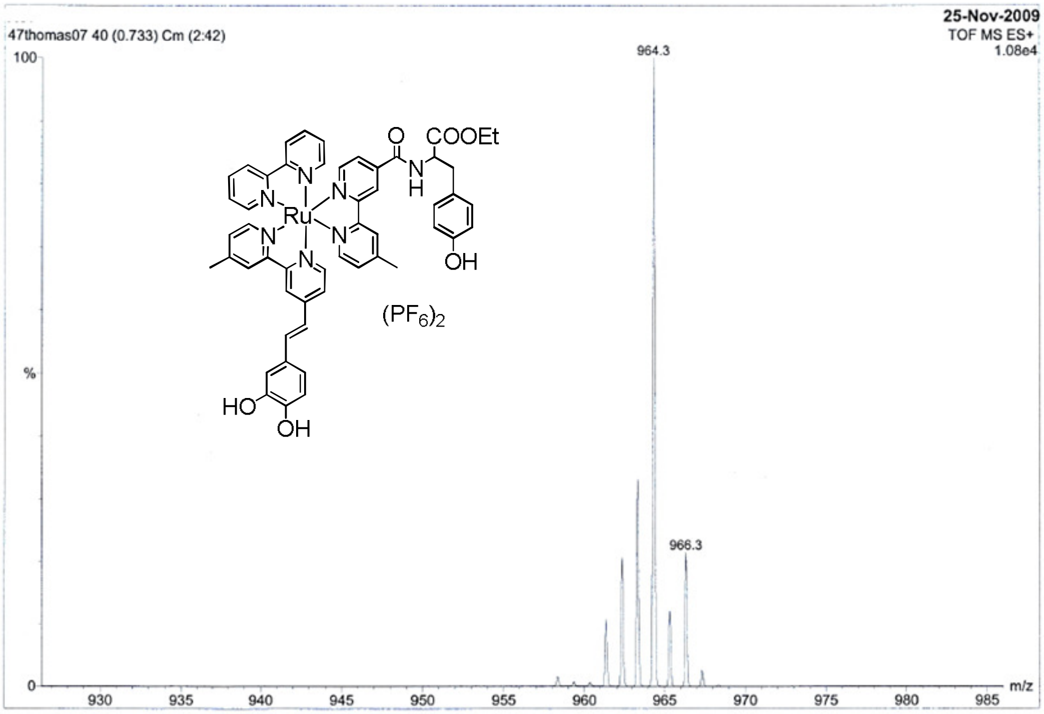
47thomas07 40 (0.733) Cm (2:42)
25-Nov-2009
TOF MS ES+
1.08e4
964.3
966.3
100
%
0
O
COOEt
N
H
Ru
OH
(PF6)2
HO
OH
930 935 940 945 950 955 960 965 970 975 980 985
m/z

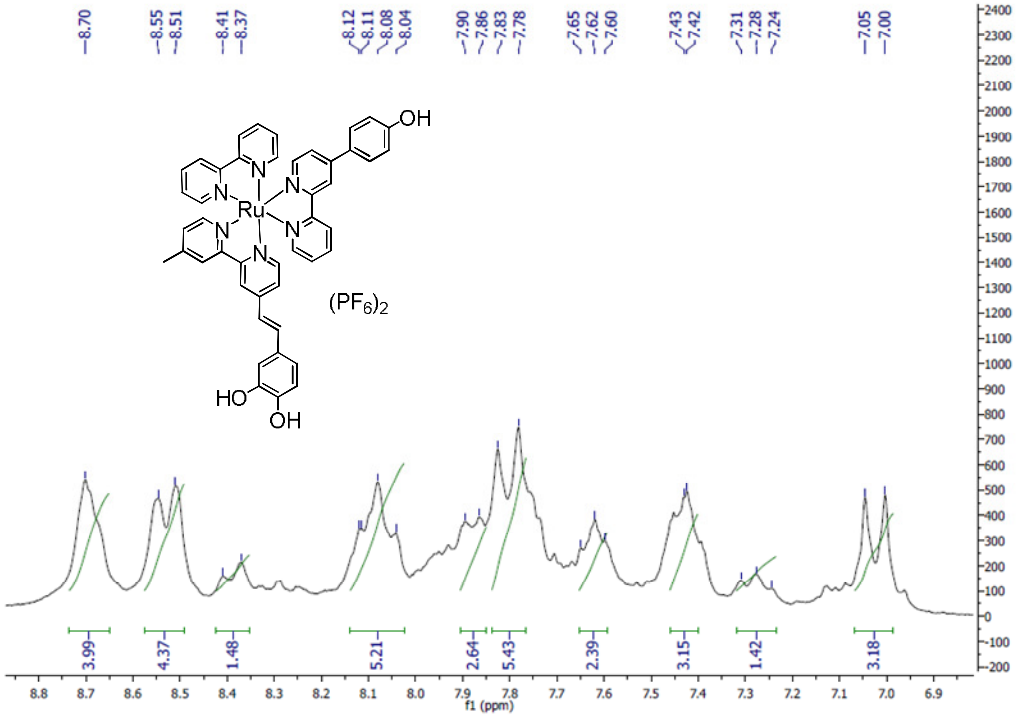
8.70
8.55
8.51
8.41
8.37
8.12
8.11
8.08
8.04
7.90
7.86
7.83
7.78
7.65
7.62
7.60
7.43
7.42
7.31
7.28
7.24
7.05
7.00
OH
N
N
Ru
N
N
N
N
(PF6)2
HO
OH
3.99
4.37
1.48
5.21
2.64
5.43
2.39
3.15
1.42
3.18
f1 (ppm)

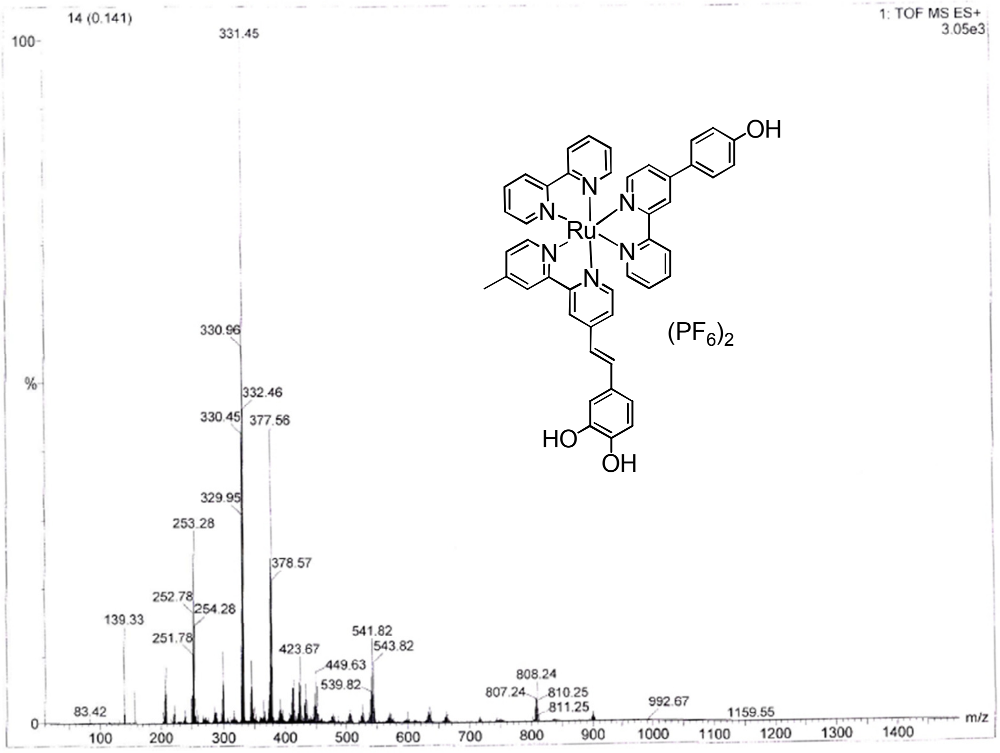
14 (0.141)
1: TOF MS ES+
3.05e3
100
%
0
331.45
330.96
332.46
330.45
377.56
329.95
253.28
378.57
252.78
254.28
139.33
251.78
423.67
541.82
543.82
449.63
539.82
808.24
807.24
810.25
811.25
992.67
1159.55
83.42
m/z
OH
N
Ru
(PF6)2
HO
OH

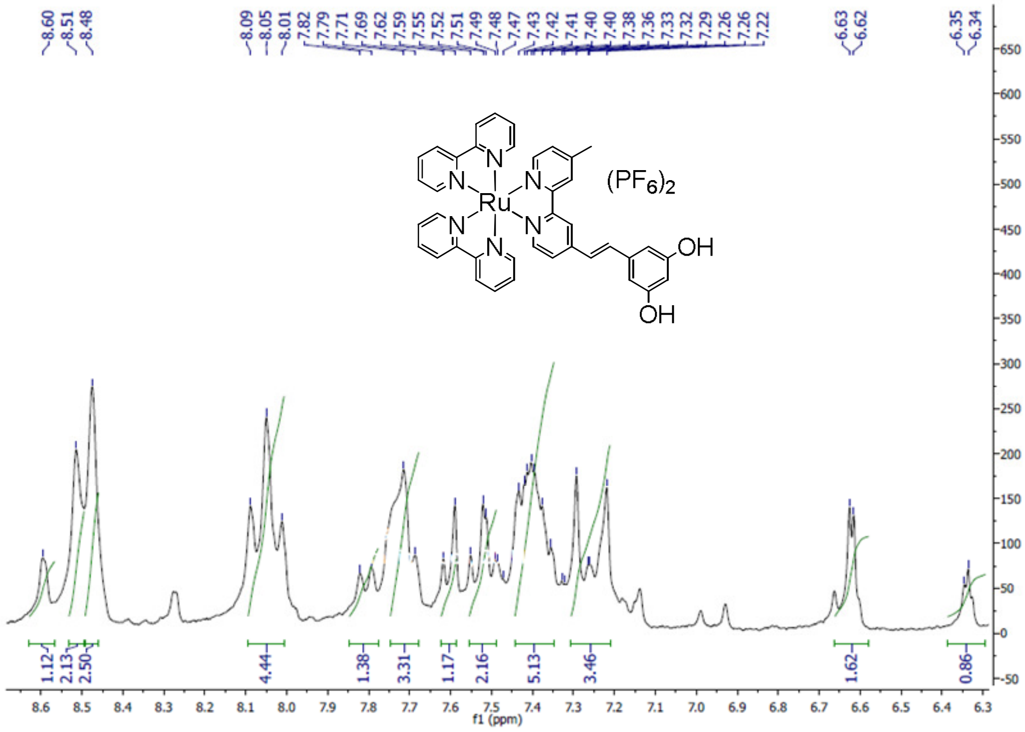
8.60
8.51
8.48
8.09
8.05
8.01
7.82
7.79
7.71
7.69
7.62
7.59
7.55
7.52
7.51
7.49
7.48
7.47
7.43
7.42
7.41
7.40
7.40
7.38
7.36
7.33
7.32
7.29
7.26
7.26
7.22
6.63
6.62
6.35
6.34
Ru
N
OH
OH
(PF6)2
1.12
2.13
2.50
4.44
1.38
3.31
1.17
2.16
5.13
3.46
1.62
0.86
f1 (ppm)
8.6 8.5 8.4 8.3 8.2 8.1 8.0 7.9 7.8 7.7 7.6 7.5 7.4 7.3 7.2 7.1 7.0 6.9 6.8 6.7 6.6 6.5 6.4 6.3
650 600 550 500 450 400 350 300 250 200 150 100 50 0 -50

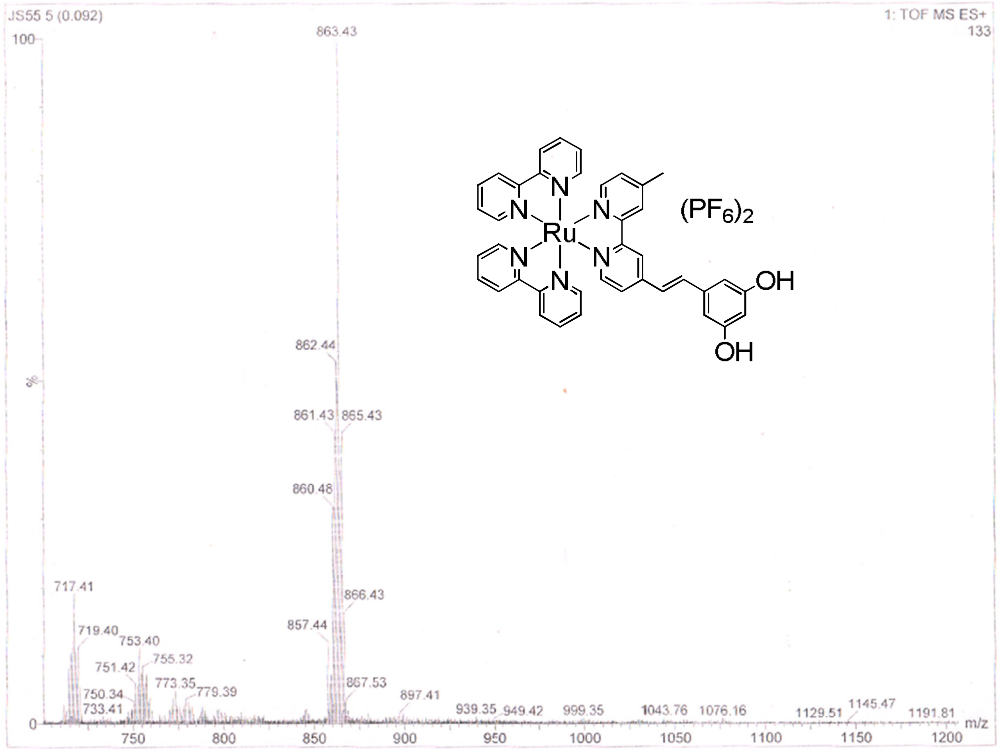
JS55 5 (0.092)
1: TOF MS ES+
133
100
%
0
863.43
862.44
861.43
865.43
860.48
866.43
857.44
867.53
717.41
719.40
753.40
751.42
755.32
773.35
779.39
750.34
733.41
897.41
939.35
949.42
999.35
1043.76
1076.16
1129.51
1145.47
1191.81
m/z
750 800 850 900 950 1000 1050 1100 1150 1200
Ru
N
OH
OH
(PF6)2

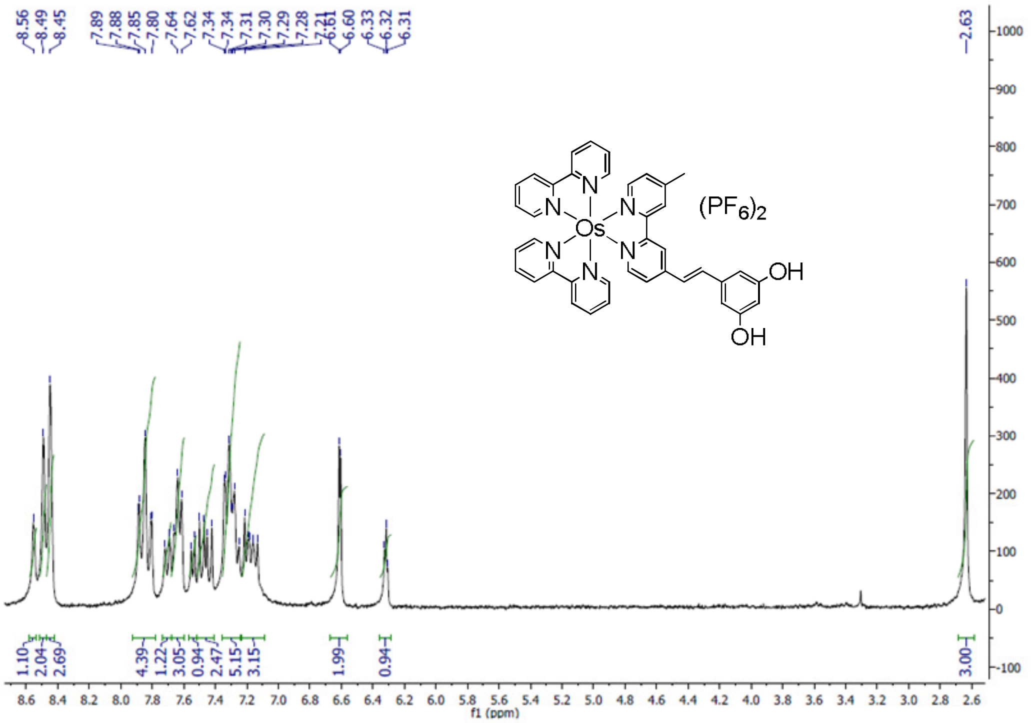
8.56
8.49
8.45
7.89
7.88
7.85
7.80
7.64
7.62
7.34
7.34
7.31
7.30
7.29
7.28
7.21
6.61
6.60
6.33
6.32
6.31
2.63
(PF6)2
Os
N
OH
1.10
2.04
2.69
4.39
1.22
3.05
0.94
2.47
5.15
3.15
1.99
0.94
3.00
1000
900
800
700
600
500
400
300
200
100
0
-100
8.6 8.4 8.2 8.0 7.8 7.6 7.4 7.2 7.0 6.8 6.6 6.4 6.2 6.0 5.8 5.6 5.4 5.2 5.0 4.8 4.6 4.4 4.2 4.0 3.8 3.6 3.4 3.2 3.0 2.8 2.6
f1 (ppm)

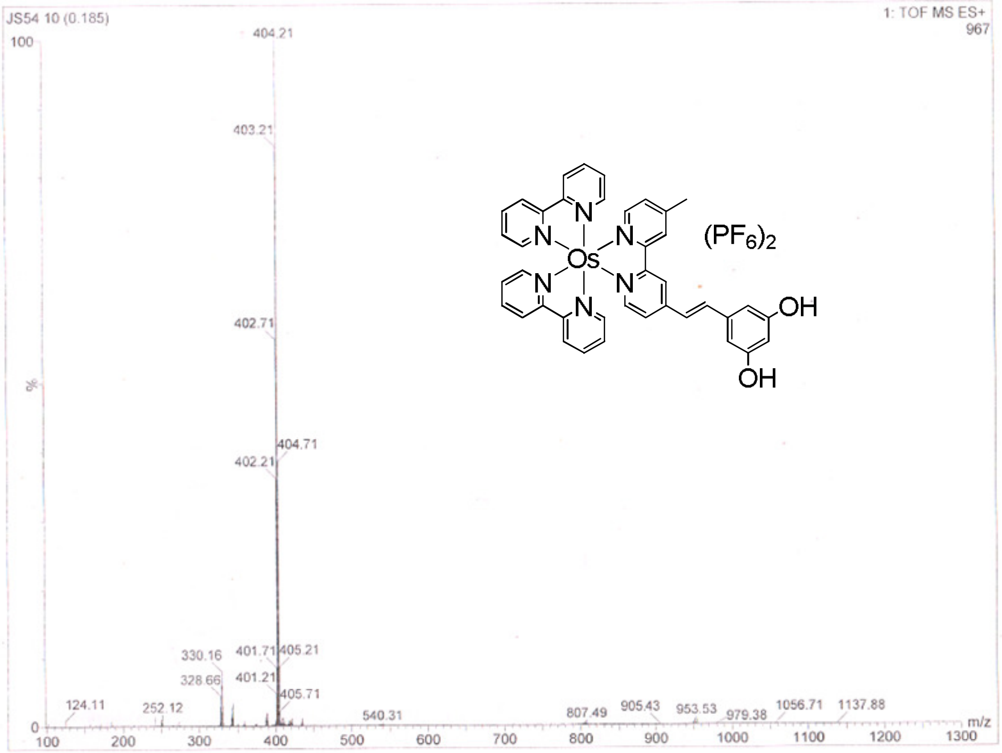
JS54 10 (0.185)
1: TOF MS ES+
967
100
%
0
404.21
403.21
402.71
404.71
402.21
330.16
328.66
401.71
405.21
401.21
405.71
124.11
252.12
540.31
807.49
905.43
953.53
979.38
1056.71
1137.88
(PF6)2
Os
N
OH
100 200 300 400 500 600 700 800 900 1000 1100 1200 1300
m/z

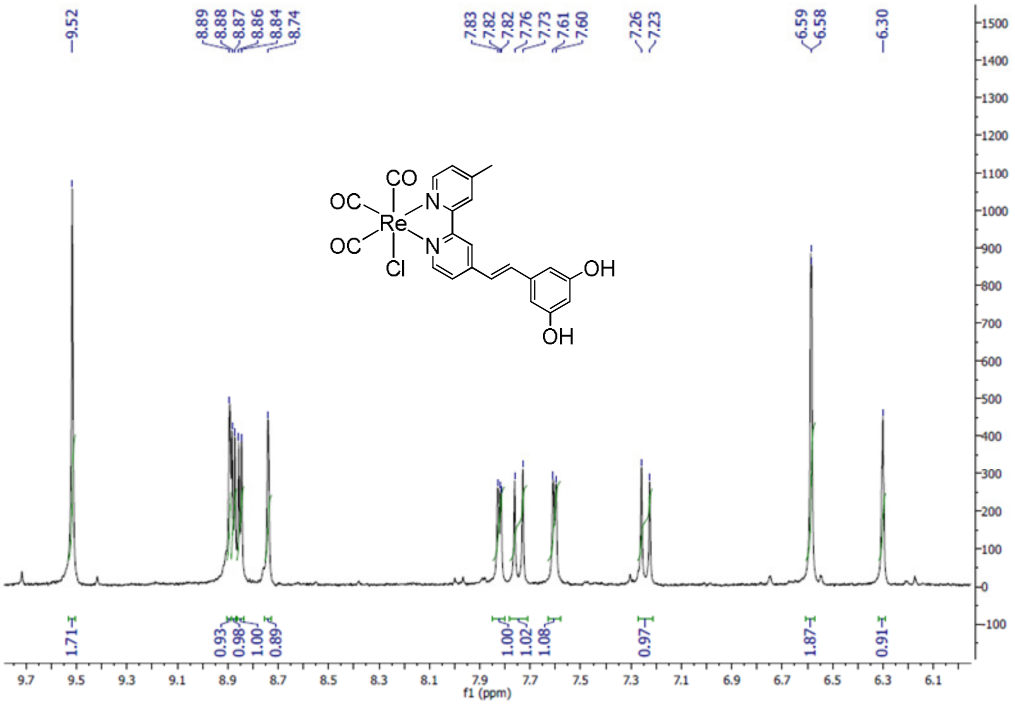
9.52
8.89
8.88
8.87
8.86
8.84
8.74
7.83
7.82
7.82
7.76
7.73
7.61
7.60
7.26
7.23
6.59
6.58
6.30
CO
OC
Re
OC
Cl
N
N
OH
OH
1.71
0.93
0.98
1.00
0.89
1.00
1.02
1.08
0.97
1.87
0.91
1500
1400
1300
1200
1100
1000
900
800
700
600
500
400
300
200
100
0
-100
9.7
9.5
9.3
9.1
8.9
8.7
8.5
8.3
8.1
7.9
7.7
7.5
7.3
7.1
6.9
6.7
6.5
6.3
6.1
f1 (ppm)

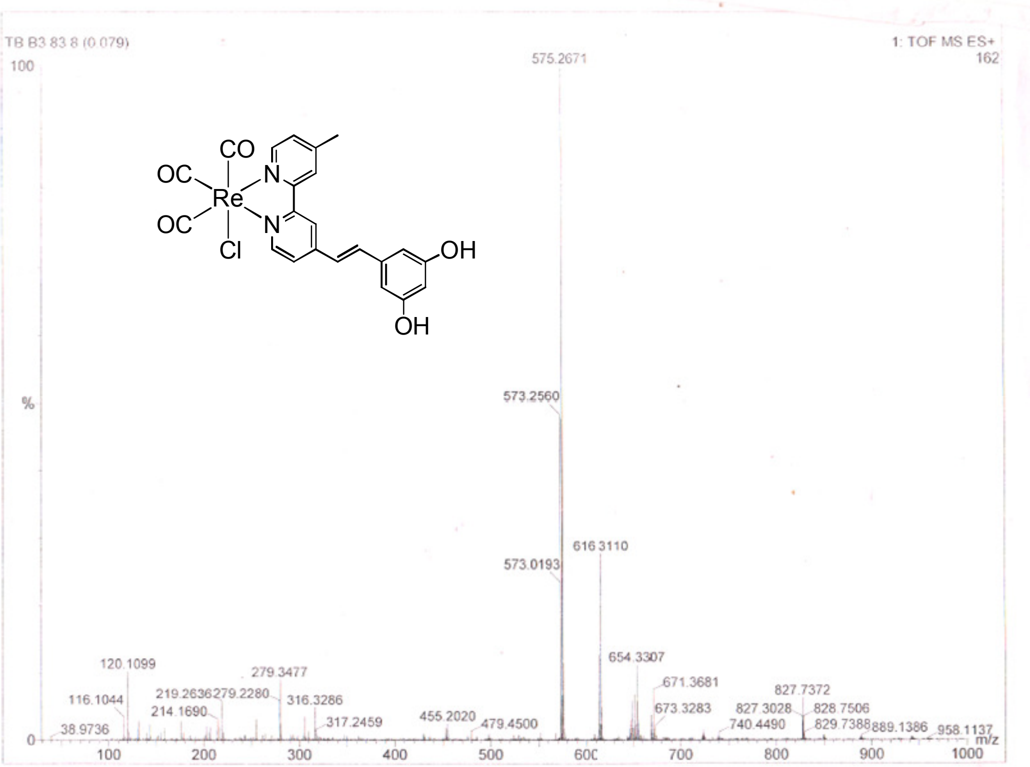
TB B3 83 8 (0.079)
1: TOF MS ES+
162
100
%
0
575.2671
573.2560
573.0193
616.3110
654.3307
671.3681
673.3283
827.7372
827.3028
828.7506
740.4490
829.7388
889.1386
958.1137
120.1099
116.1044
38.9736
219.2636
279.2280
214.1690
279.3477
316.3286
317.2459
455.2020
479.4500
CO
OC
Re
OC
Cl
N
N
OH
OH
m/z
100
200
300
400
500
600
700
800
900
1000

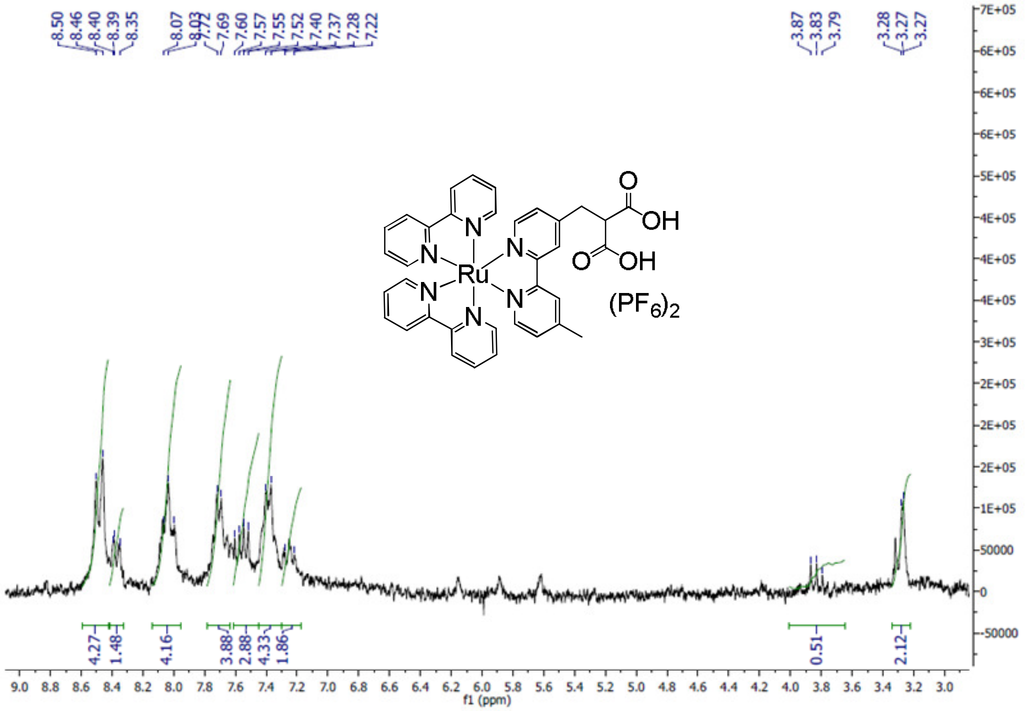
8.50
8.46
8.40
8.39
8.35
8.07
8.03
7.72
7.69
7.60
7.57
7.55
7.52
7.40
7.37
7.28
7.22
3.87
3.83
3.79
3.28
3.27
3.27
7E+05
6E+05
6E+05
6E+05
6E+05
5E+05
4E+05
4E+05
4E+05
3E+05
2E+05
2E+05
2E+05
1E+05
50000
0
-50000
O
OH
O
OH
N
N
N
Ru
N
N
N
(PF6)2
4.27
1.48
4.16
3.88
2.88
4.33
1.86
0.51
2.12
9.0 8.8 8.6 8.4 8.2 8.0 7.8 7.6 7.4 7.2 7.0 6.8 6.6 6.4 6.2 6.0 5.8 5.6 5.4 5.2 5.0 4.8 4.6 4.4 4.2 4.0 3.8 3.6 3.4 3.2 3.0
f1 (ppm)

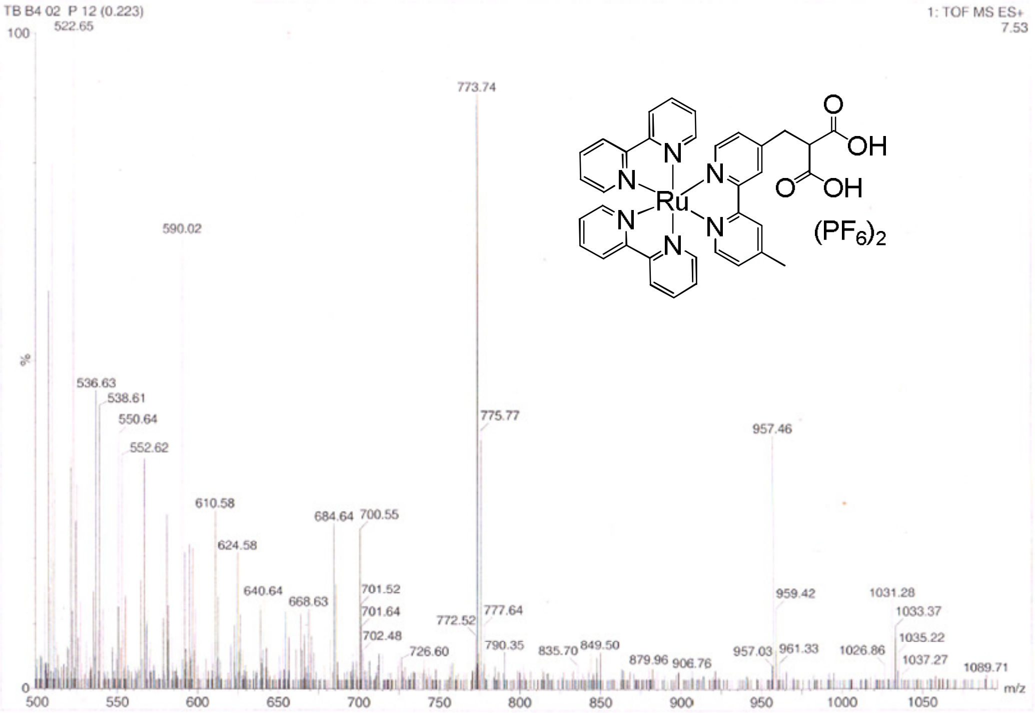
TB B4 02 P 12 (0.223)
1: TOF MS ES+
7.53
100
%
0
522.65
773.74
590.02
536.63
538.61
550.64
552.62
775.77
957.46
610.58
624.58
684.64
700.55
640.64
668.63
701.52
701.64
702.48
726.60
772.52
777.64
790.35
835.70
849.50
879.96
906.76
957.03
959.42
961.33
1026.86
1031.28
1033.37
1035.22
1037.27
1089.71
m/z
500 550 600 650 700 750 800 850 900 950 1000 1050
O
OH
O
OH
N
N
N
Ru
N
N
N
(PF6)2

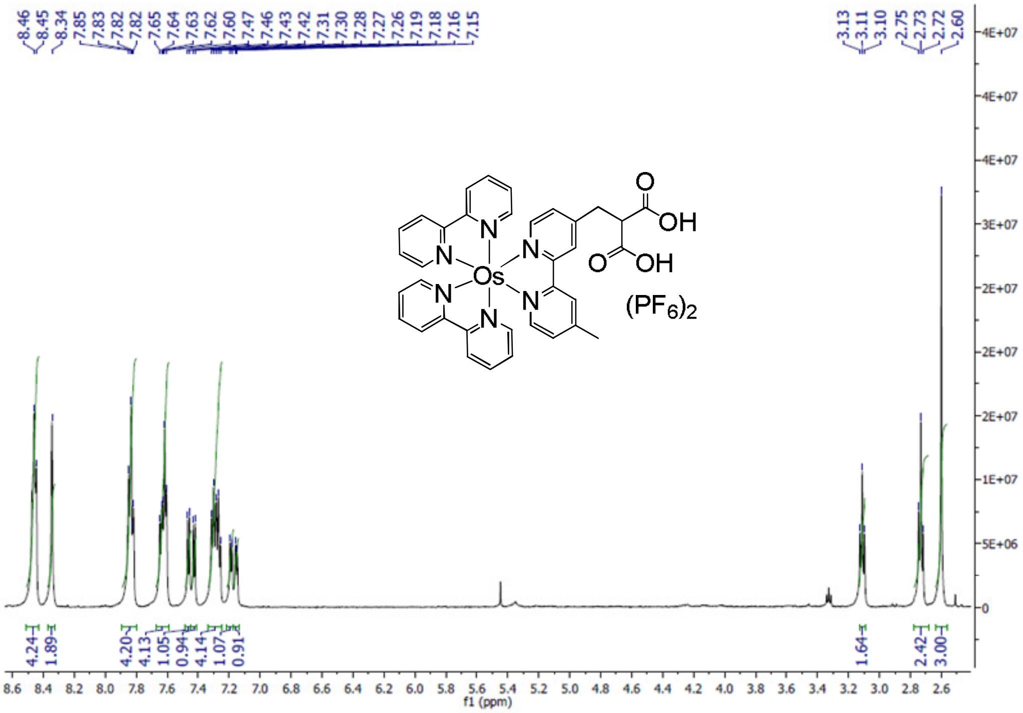
8.46
8.45
8.34
7.85
7.83
7.82
7.82
7.65
7.64
7.63
7.62
7.60
7.47
7.46
7.43
7.42
7.31
7.30
7.28
7.27
7.26
7.19
7.18
7.16
7.15
3.13
3.11
3.10
2.75
2.73
2.72
2.60
4E+07
4E+07
4E+07
3E+07
2E+07
2E+07
2E+07
1E+07
5E+06
0
N
N
N
N
N
N
Os
O
OH
O
OH
(PF6)2
4.24
1.89
4.20
4.13
1.05
0.94
4.14
1.07
0.91
1.64
2.42
3.00
8.6 8.4 8.2 8.0 7.8 7.6 7.4 7.2 7.0 6.8 6.6 6.4 6.2 6.0 5.8 5.6 5.4 5.2 5.0 4.8 4.6 4.4 4.2 4.0 3.8 3.6 3.4 3.2 3.0 2.8 2.6
f1 (ppm)

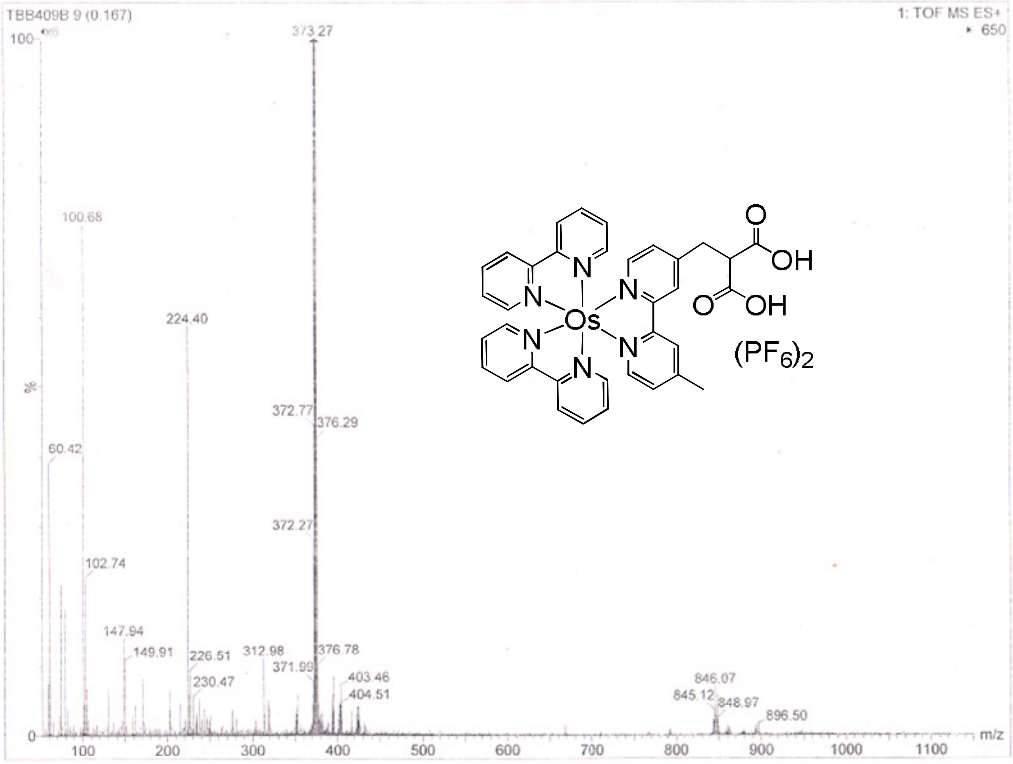
TBB409B 9 (0.167)
1: TOF MS ES+
650
100
373.27
%
100.68
224.40
60.42
372.77
376.29
372.27
102.74
147.94
149.91
226.51
312.98
376.78
371.99
230.47
403.46
404.51
846.07
845.12
848.97
896.50
0
100 200 300 400 500 600 700 800 900 1000 1100
m/z
N
N
N
N
N
N
Os
O
OH
O
OH
(PF6)2

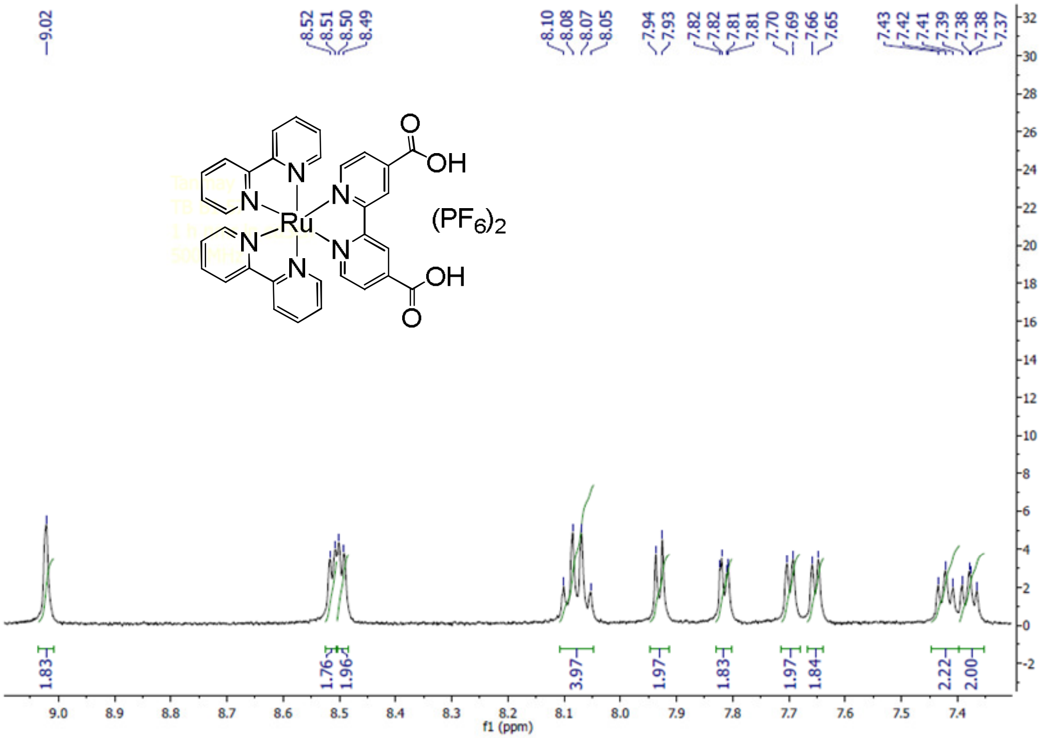
9.02
8.52
8.51
8.50
8.49
8.10
8.08
8.07
8.05
7.94
7.93
7.82
7.82
7.81
7.81
7.70
7.69
7.66
7.65
7.43
7.42
7.41
7.39
7.38
7.38
7.37
1.83
1.76
1.96
3.97
1.97
1.83
1.97
1.84
2.22
2.00
9.0
8.9
8.8
8.7
8.6
8.5
8.4
8.3
8.2
8.1
8.0
7.9
7.8
7.7
7.6
7.5
7.4
f1 (ppm)
32
30
28
26
24
22
20
18
16
14
12
10
8
6
4
2
0
-2
N
Ru
O
OH
(PF6)2

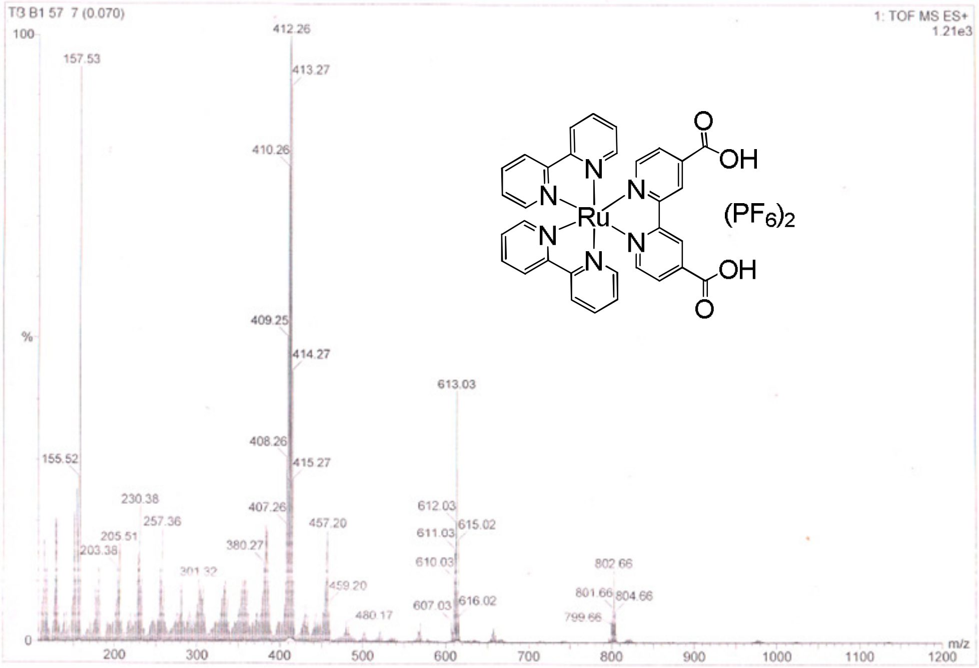
TB B1 57 7 (0.070)
1: TOF MS ES+
1.21e3
100
%
0
412.26
413.27
157.53
410.26
409.25
414.27
613.03
408.26
415.27
155.52
230.38
257.36
407.26
457.20
612.03
615.02
205.51
203.38
380.27
611.03
610.03
301.32
459.20
802.66
801.66
804.66
480.17
607.03
616.02
799.66
200
300
400
500
600
700
800
900
1000
1100
1200
m/z
N
Ru
O
OH
(PF6)2

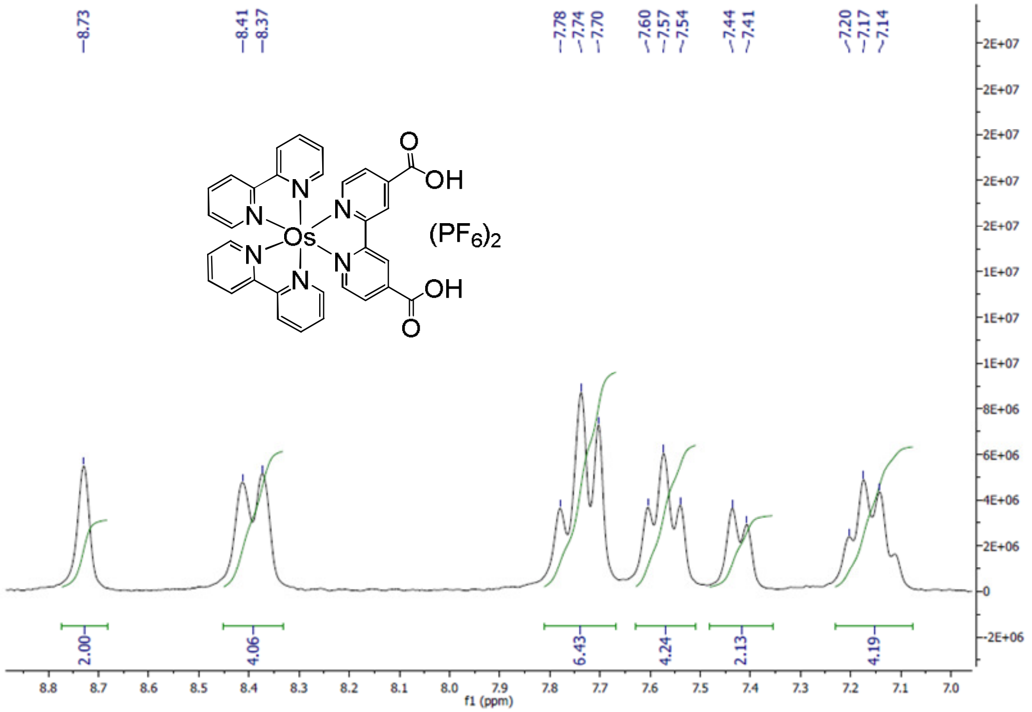
8.73
8.41
8.37
7.78
7.74
7.70
7.60
7.57
7.54
7.44
7.41
7.20
7.17
7.14
Os
N
OH
O
(PF6)2
2.00
4.06
6.43
4.24
2.13
4.19
2E+07
1E+07
8E+06
6E+06
4E+06
2E+06
0
-2E+06
8.8
8.7
8.6
8.5
8.4
8.3
8.2
8.1
8.0
7.9
7.8
7.7
7.6
7.5
7.4
7.3
7.2
7.1
7.0
f1 (ppm)

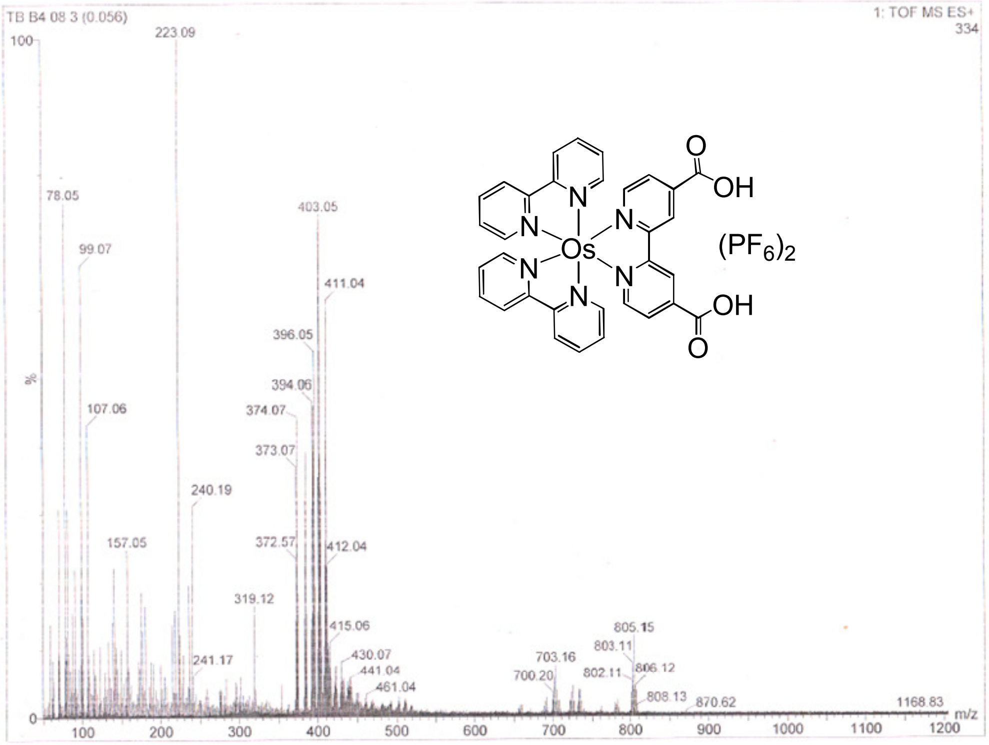
TB B4 08 3 (0.056)
1: TOF MS ES+
334
100
%
0
223.09
78.05
99.07
107.06
157.05
240.19
241.17
319.12
372.57
373.07
374.07
394.06
396.05
403.05
411.04
412.04
415.06
430.07
441.04
461.04
700.20
703.16
802.11
803.11
805.15
806.12
808.13
870.62
1168.83
Os
N
OH
O
(PF6)2
100
200
300
400
500
600
700
800
900
1000
1100
1200
m/z

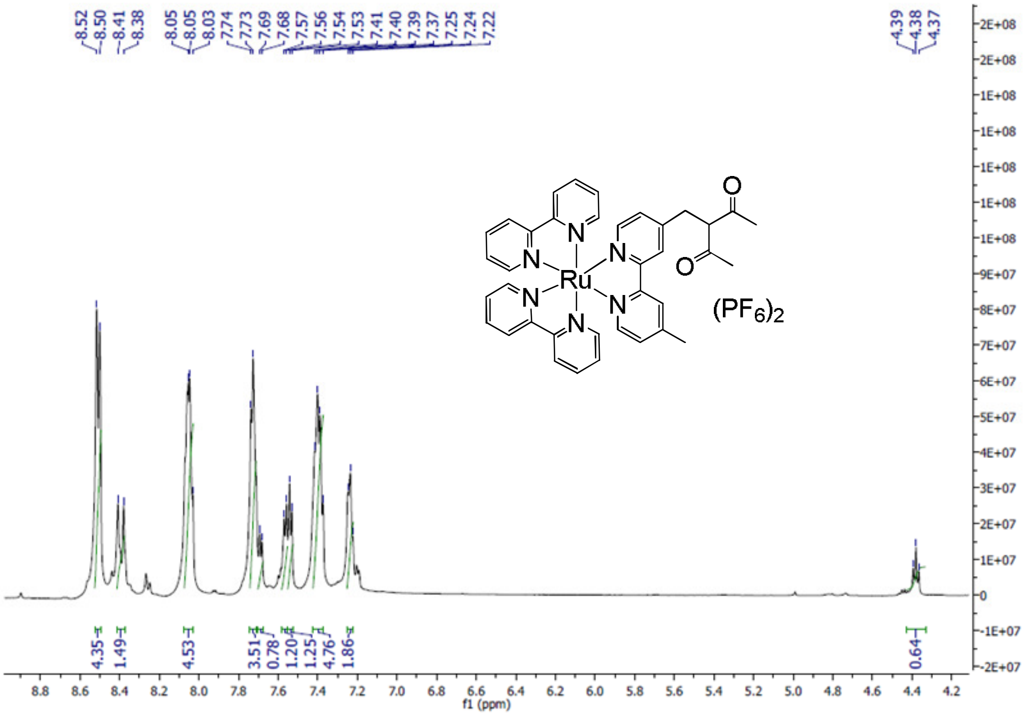
8.52
8.50
8.41
8.38
8.05
8.05
8.03
7.74
7.73
7.69
7.68
7.57
7.56
7.54
7.53
7.41
7.40
7.39
7.37
7.25
7.24
7.22
4.39
4.38
4.37
4.35
1.49
4.53
3.51
0.78
1.20
1.25
4.76
1.86
0.64
N
Ru
O
(PF6)2
f1 (ppm)

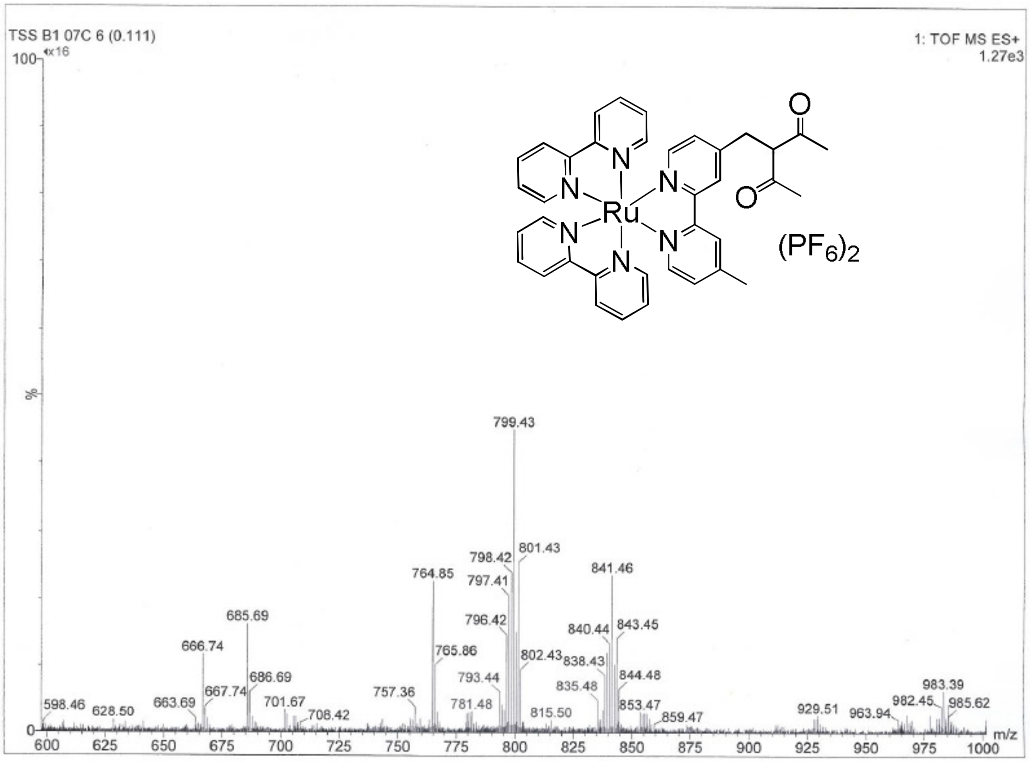
TSS B1 07C 6 (0.111)
1: TOF MS ES+
1.27e3
100
x16
%
N
Ru
O
(PF6)2
799.43
801.43
798.42
797.41
764.85
841.46
685.69
796.42
840.44
843.45
666.74
765.86
802.43
838.43
793.44
686.69
835.48
844.48
667.74
757.36
983.39
598.46
628.50
663.69
701.67
708.42
781.48
815.50
853.47
859.47
929.51
963.94
982.45
985.62
m/z

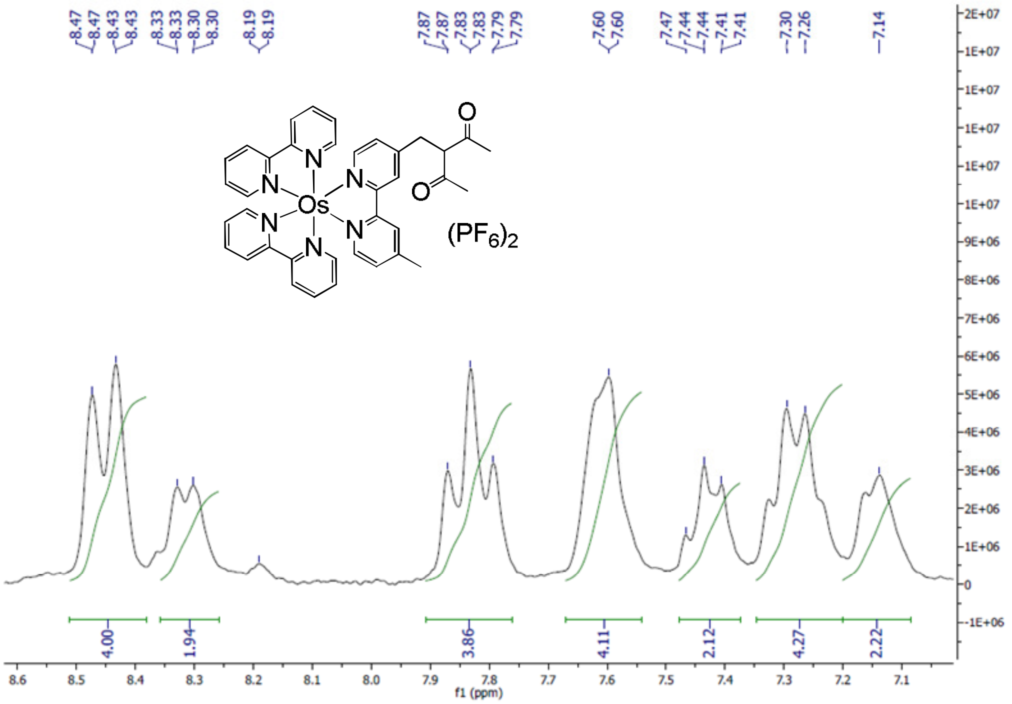
8.47
8.47
8.43
8.43
8.33
8.33
8.30
8.30
8.19
8.19
7.87
7.87
7.83
7.83
7.79
7.79
7.60
7.60
7.47
7.44
7.44
7.41
7.41
7.30
7.26
7.14
N
Os
O
(PF$_6$)$_2$
2E+07
1E+07
9E+06
8E+06
7E+06
6E+06
5E+06
4E+06
3E+06
2E+06
1E+06
0
-1E+06
4.00
1.94
3.86
4.11
2.12
4.27
2.22
8.6
8.5
8.4
8.3
8.2
8.1
8.0
7.9
7.8
7.7
7.6
7.5
7.4
7.3
7.2
7.1
f1 (ppm)

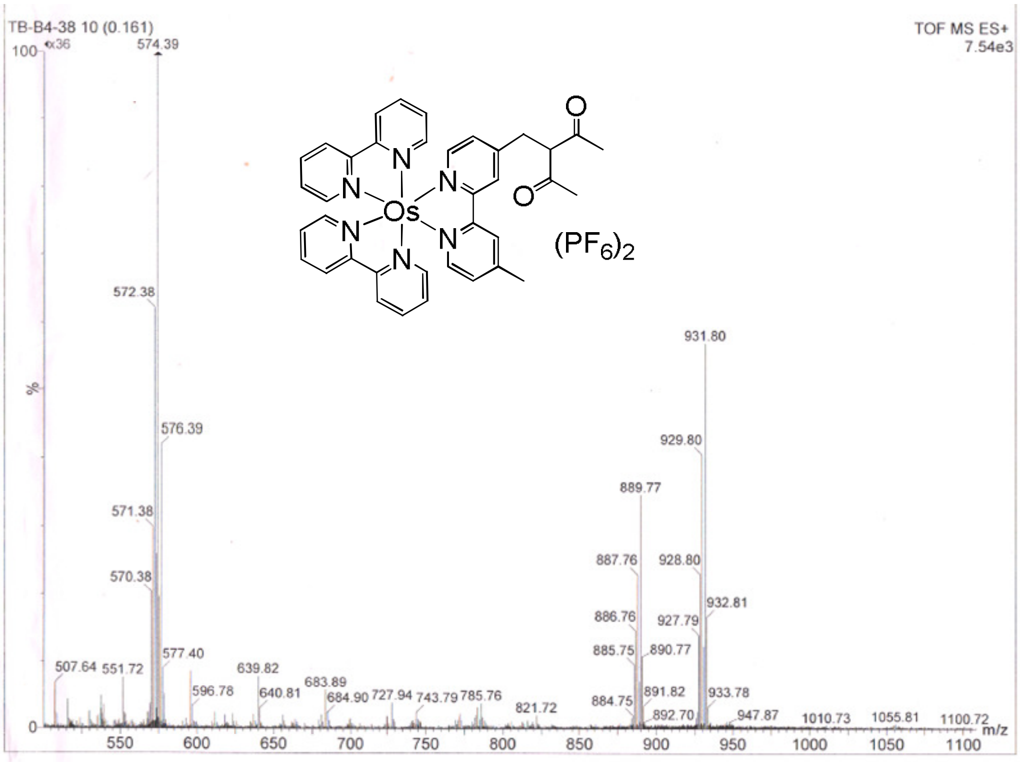
TB-B4-38 10 (0.161)
TOF MS ES+
7.54e3
100
x36
574.39
572.38
576.39
571.38
570.38
577.40
507.64
551.72
596.78
639.82
640.81
683.89
684.90
727.94
743.79
785.76
821.72
884.75
885.75
886.76
887.76
889.77
890.77
891.82
892.70
927.79
928.80
929.80
931.80
932.81
933.78
947.87
1010.73
1055.81
1100.72
%
0
550
600
650
700
750
800
850
900
950
1000
1050
1100
m/z
N
Os
O
(PF$_6$)$_2$

List of Publications Related to the Thesis

1. **Banerjee, T.**; Rawalekar, S.; Das, A.; Ghosh, H. N. Interfacial Electron Transfer Dynamics of Two Newly Synthesized Catecholate Bound Ru^{II} Polypyridyl-Based Sensitizers on TiO_2 Nanoparticle Surface – A Femtosecond Pump Probe Spectroscopic Study, *European Journal of Inorganic Chemistry* **2011**, 4187–4197.
2. **Banerjee, T.**; Kaniyankandy, S.; Das, A.; Ghosh, H. N. Newly Designed Resorcinolate Binding for Ru(II)– and Re(I)– Polypyridyl Complexes on Oleic Acid Capped TiO_2 in Nonaqueous Solvent: Prolonged Charge separation and Substantial Thermalized ^{3}MLCT Injection, *Journal of Physical Chemistry C* **2013**, *117*, 3084-3092.
3. **Banerjee, T.**; Kaniyankandy, S.; Das, A.; Ghosh, H. N. Synthesis, Steady-State, and Femtosecond Transient Absorption Studies of Resorcinol Bound Ruthenium(II)- and Osmium(II)- polypyridyl Complexes on Nano-TiO_2 Surface in Water, *Inorganic Chemistry* **2013**, *52*, 5366-5377.
4. **Banerjee, T.**; Das, A.; Ghosh, H. N. Interfacial charge recombination of Os(II)–polypyridyl– resorcinol complex on oleic acid capped TiO_2 surface: what determines the dynamics?, *New Journal of Chemistry* **2013**, *37*, 3100-3108.
5. **Banerjee, T.**; Biswas, A. K.; Reddy, G. U.; Sahu, T. S.; Ganguly, B.; Das, A.; Ghosh, H. N. Superior Grafting and State-of-the-art Interfacial Electron Transfer Rates for Newly Designed Geminal Dicarboxylate Bound Ru(II)- and Os(II)-polypyridyl Dyes on TiO_2 Nanosurface, ***Communicated to J. Phys. Chem. C***
6. **Banerjee, T.**; Biswas, A. K.; Sahu, T. S.; Ganguly, B.; Das, A.; Ghosh, H. N. State-of-the-art interfacial electron transfer rates for *dye-spacer-anchor* arrangement in newly designed acetylacetonate based Ru(II)- and Os(II)-polypyridyl sensitizer, ***To be communicated***

List of Other Publications

1. **Banerjee, T.**; Suresh, M.; Das, A.; Ghosh, H. N. Competitive binding of $Ba^{2+}$and Sr^{2+} to 18-Crown-6 in a Receptor with a 1-Methoxyanthraquinone Analogue as the Other Binding Site, *European Journal of Inorganic Chemistry* **2011**, 4680–4690.
2. Kar, P.; **Banerjee, T.**; Verma, S.; Sen, A.; Das, A.; Ganguly, B.; Ghosh, H. N. Photosensitization of nanoparticulate TiO_2 using a Re(I)-polypyridyl complex: studies on interfacial electron transfer in the ultrafast time domain, *Physical Chemistry Chemical Physics* **2012**, *14*, 8192–8198.
3. Verma, S.; Kar, P.; **Banerjee, T.**; Das, A.; Ghosh, H. N. Sequential Energy and Electron Transfer in Polynuclear Complex Sensitized TiO_2 Nanoparticles, *Journal of Physical Chemistry Letters* **2012**, *3*, 1543-1548.
4. Reddy, G. U.; Lo, R.; Roy, S.; **Banerjee, T.**; Ganguly, B.; Das, A. A New Receptor with a FRET Based Fluorescence Response for Selective Recognition of Fumaric and Maleic Acid in Aqueous Medium, *Chemical Communications* **2013**, DOI - *10.1039/C3CC45051A*.

5. Ghosh, A.; Das, P.; Saha, S.; **Banerjee, T.**; Bhatt, H. B.; Das, A. Diamine derivative of a ruthenium(II)-polypyridyl complex for chemodosimetric detection of nitrite ion in aqueous solution, *Inorganica Chimica Acta* **2011**, *372*, 115–119.
6. Das, P.; Mahato, P.; Ghosh, A.; Mandal, A. K.; **Banerjee, T.**; Saha, S.; Das, A. Urea/thiourea derivatives and Zn(II)-DPA complex as receptors for anionic recognition—A brief account, *Journal of Chemical Sciences* **2011**, *123*, 175–186.
7. **Banerjee, T.**; Das, A.; Ghosh, H. N. Dye Sensitized Solar Cells: A Brief Review of the Design and the Mechanistic Principles, ***To be communicated***
8. Verma, S,; **Banerjee, T.**; Das, A.; Ghosh, H. N. Interfacial electron transfer dynamics and photovoltaic studies of a newly designed N,N-dimethylamine Donor-Porphyrin-catechol sensitizer on TiO_2 nanosurface. ***Manuscript under preparation***

Conferences Attended, Paper/Poster Presented During PhD

- Attended **International Conference on Photochemical Conversion of Solar Energy** in March 2010 at Amrita Vishwa Vidyapeetham, Coimbatore, Tamilnadu, India.
- Participated and **presented poster** entitled 'Effect of Electron Donating Ligand in Ru(II)-Polypyridyl Complex Sensitized TiO_2 Nanoparticles: A Time-Resolved Ultrafast Study' in **3rd Asia Pacific Symposium on Radiation Chemistry and DAE-BRNS 10th Biennial Trombay Symposium on Radiation and Photochemistry** in September 2010 at Lonavala, Maharashtra, India.
- Participated and **presented poster** entitled 'Competitive binding of Ba^{2+} and Sr^{2+} to 18-Crown-6 in a Receptor with a 1-Methoxyanthraquinone Analogue as the Other Binding Site' in **DAE-BRNS 11th Biennial Trombay Symposium on Radiation and Photochemistry** in January 2012 at Mumbai, Maharashtra, India.